Modeling and regularization in tomographic reconstruction for Compton camera imaging

Yuemeng Feng

N°d'ordre NNT : 2019LYSEI084

THESE de DOCTORAT DE L'UNIVERSITE DE LYON
opérée au sein de
L'INSA LYON

Ecole Doctorale N° ED160
Electronique, Electrotechnique, Automatique

Spécialité/ discipline de doctorat :

STIC Santé

Soutenue publiquement le 25/10/2019, par:
Yuemeng FENG

Modeling and regularization in tomographic reconstruction for Compton camera imaging

---

Devant le jury composé de :

RAFECAS Magdalena	Professeur, Institute of Medical Engineering	Rapporteure
IDIER Jérôme	DR CNRS, Ecole Centrale de Nantes	Rapporteur
RESMERITA Elena	Associate Professor, Alpen-Adria Univ.Klagenfurt	Examinatrice
MOREL Christian	Professeur, Université de Aix-Marseille	Examinateur
LETANG Jean Michel	Maître de Conférences, INSA-LYON	Examinateur
SARRUT David	DR CNRS, INSA-LYON	Directeur de thèse
MAXIM Voichiţa	Maître de Conférences HDR, INSA-LYON	Co-directrice de thèse

Remerciements

Je commence à rédiger mes remerciements en français mais je vais changer pour anglais dans quelques phrases car je mélange toujours ces deux langues.

Tout d'abord je voudrais dire un gros merci à tous mes encadrants. Vous êtes la salle sur demande (Room of Requirement) à CREATIS (see Harry Potter for more explications) ! Merci à Voichiţa de m'avoir donné plein d'idées sur la thèse et m'avoir permis d'aller aux confs internationales. Sans les opportunités que tu m'as proposées (le projet de fin d'études, le sujet de thèse, les cours intéressants etc.) cette thèse n'aurait jamais été réalisée. Merci à David et Jean Michel, qui sont toujours patients et m'ont donné beaucoup d'idées pendant chaque discussion. Merci à tous mes encadrants de m'avoir fait confiance, de cette bonne entente et merci à vos efforts pendant cette thèse.

Je voudrais également ajouter des remerciements à tous les membres du jury de ma soutenance : merci aux rapporteurs, Magdalena Rafecas et Jérôme Idier, pour vos précieux conseils, merci aussi à Elena Resmerita et Christian Morel, d'avoir accepté d'être examinateur.

Merci à Ane et Thomas, qui ont développé le logiciel Gate et qui m'ont appris à l'utiliser. Merci à Claire et Michaël, qui ont parallélisé le code de reconstruction. Merci à Étienne et Mattia pour le partage de vos données pour que je puisse tester les méthodes de reconstruction. Merci à Pierre et Fabrice pour m'avoir offert les ressources informatiques. Vos aides ont vraiment contribué en grande partie dans cette thèse.

Merci à tous les collègues dans ce labo pour l'ambiance sympa de travail. Merci à Emeline, qui est toujours gentille avec moi et qui m'a aidée à corriger le résumé en français de ma thèse. Pourtant on pourrait faire moins de bêtises. Merci à Maxime (tes dessins sont géniaux même si je ne t'en ai jamais parlé), Nina (on peut essayer un autre restaurant chinois avec Emeline si elle reste encore à Lyon après sa soutenance), Sami (pour le café), Sarah (qui m'avais beaucoup aidé sur le travail quand on était à GE). En bref, vous n'avez rien fait sur ma thèse mais vous m'avez aidée à progresser sur mon niveau de français ! Merci à Zara, je ne comprends toujours pas l'importance de l'embrassement mais je sais que la compagnie est importante pour un humain. Thanks to Mo, the café machine you left in our office have saved several lives ! Thanks to Yunyun, Fei, Pei, Binqing, Ruifen, Zexian, Hao and all the other Chinese colleagues who had ever appeared in the past three years, without you I have no idea how can I survive during the Chinese New Year and Mid-Autumn Festival :)

Thanks to all my family members, especially to my parents, for always trusting me and supporting me.

Finally, I would like to say thank you, sincerely to Yonezu Kenshi and Akanishi Jin. Your singing waking me up every morning is more powerful than espresso !

Résumé

La caméra Compton est un dispositif d'imagerie gamma pour la tomographie par émission monophotonique (TEMP). Les améliorations qu'elle pourrait apporter aux applications médicales font l'objet de nombreuses études. Elles dépendent à la fois des développements instrumentaux et des techniques de traitement des données, dont la reconstruction tomographique est une étape-clé. Le but de cette thèse est d'améliorer les performances des algorithmes de reconstruction itératifs calculant le maximum de vraisemblance en mode liste (LM-MLEM). En imagerie avec une caméra Compton, le modèle d'acquisition est basé sur l'intégrale de l'intensité de la source sur des projections coniques. La modélisation des incertitudes de mesure influence fortement le résultat de LM-MLEM. L'une des contributions de cette étude est de montrer qu'un modèle plus précis de l'élargissement Doppler, validé avec la simulation Monte-Carlo, conduit à des images plus quantitatives. Une autre contribution est une méthode de régularisation par contrôle de la variation totale (TV) pour des données distribuées selon une loi de Poisson. La régularisation TV permet d'améliorer fortement la qualité des images pour les acquisitions à faible statistique rencontrées dans les applications de ce type d'imagerie. Nous avons également étudié l'apport de la déconvolution avec la fonction d'étalement du point dans le domaine de l'image, en conjonction avec la régularisation. Cette approche est utilisée pour corriger les effets physiques trop difficile à modéliser dans la fonction de transfert. Toutes les méthodes ont été validées avec des simulations Monte-Carlo.

Abstract

The Compton camera is an imaging device for SPECT (Single Particle Emission Computed Tomography) of increased sensitivity compared to the Anger camera as it does not require mechanical collimation. The goal of this thesis is to evaluate the improvements that Compton camera may bring for nuclear medicine applications, depending both on technological developments and data processing techniques, among which the tomographic reconstruction is currently a bottleneck. In Compton camera imaging, the acquisition model is based on the integral of the intensity of the source on conical shapes. Modeling the measurement uncertainties in the system matrix can strongly influence the result of the list mode MLEM iterative reconstruction algorithm. One of the contributions of this study is a more precise model validated by Monte Carlo simulation. Another contribution concerns regularization methods. We developed a total variation denoising algorithm for Poisson distributed data that we introduced in the MLEM reconstruction as a regularization step, which allows to improve the image quality in low-counts experiments. A total variation regularized EM reconstruction with PSF deconvolution in the image space is also proposed for ameliorating the conditioning of the inverse problem and restoring the resolution of reconstructed images. All the proposed methods were validated on Monte Carlo simulation.

Département FEDORA – INSA Lyon - Ecoles Doctorales – Quinquennal 2016-2020

SIGLE	ECOLE DOCTORALE	NOM ET COORDONNEES DU RESPONSABLE
CHIMIE	**CHIMIE DE LYON** **http://www.edchimie-lyon.fr** Sec. : Renée EL MELHEM Bât. Blaise PASCAL, 3e étage **secretariat@edchimie-lyon.fr** INSA : R. GOURDON	M. Stéphane DANIELE Institut de recherches sur la catalyse et l'environnement de Lyon IRCELYON-UMR 5256 Équipe CDFA 2 Avenue Albert EINSTEIN 69 626 Villeurbanne CEDEX **directeur@edchimie-lyon.fr**
E.E.A.	**ÉLECTRONIQUE, ÉLECTROTECHNIQUE, AUTOMATIQUE** **http://edeea.ec-lyon.fr** Sec. : M.C. HAVGOUDOUKIAN **ecole-doctorale.eea@ec-lyon.fr**	M. Gérard SCORLETTI École Centrale de Lyon 36 Avenue Guy DE COLLONGUE 69 134 Écully Tél : 04.72.18.60.97 Fax 04.78.43.37.17 **gerard.scorletti@ec-lyon.fr**
E2M2	**ÉVOLUTION, ÉCOSYSTÈME, MICROBIOLOGIE, MODÉLISATION** **http://e2m2.universite-lyon.fr** Sec. : Sylvie ROBERJOT Bât. Atrium, UCB Lyon 1 Tél : 04.72.44.83.62 INSA : H. CHARLES **secretariat.e2m2@univ-lyon1.fr**	M. Philippe NORMAND UMR 5557 Lab. d'Ecologie Microbienne Université Claude Bernard Lyon 1 Bâtiment Mendel 43, boulevard du 11 Novembre 1918 69 622 Villeurbanne CEDEX **philippe.normand@univ-lyon1.fr**
EDISS	**INTERDISCIPLINAIRE SCIENCES-SANTÉ** **http://www.ediss-lyon.fr** Sec. : Sylvie ROBERJOT Bât. Atrium, UCB Lyon 1 Tél : 04.72.44.83.62 INSA : M. LAGARDE **secretariat.ediss@univ-lyon1.fr**	Mme Emmanuelle CANET-SOULAS INSERM U1060, CarMeN lab, Univ. Lyon 1 Bâtiment IMBL 11 Avenue Jean CAPELLE INSA de Lyon 69 621 Villeurbanne Tél : 04.72.68.49.09 Fax : 04.72.68.49.16 **emmanuelle.canet@univ-lyon1.fr**
INFOMATHS	**INFORMATIQUE ET MATHÉMATIQUES** **http://edinfomaths.universite-lyon.fr** Sec. : Renée EL MELHEM Bât. Blaise PASCAL, 3e étage Tél : 04.72.43.80.46 **infomaths@univ-lyon1.fr**	M. Luca ZAMBONI Bât. Braconnier 43 Boulevard du 11 novembre 1918 69 622 Villeurbanne CEDEX Tél : 04.26.23.45.52 **zamboni@maths.univ-lyon1.fr**
Matériaux	**MATÉRIAUX DE LYON** **http://ed34.universite-lyon.fr** Sec. : Stéphanie CAUVIN Tél : 04.72.43.71.70 Bât. Direction **ed.materiaux@insa-lyon.fr**	M. Jean-Yves BUFFIÈRE INSA de Lyon MATEIS - Bât. Saint-Exupéry 7 Avenue Jean CAPELLE 69 621 Villeurbanne CEDEX Tél : 04.72.43.71.70 Fax : 04.72.43.85.28 **jean-yves.buffiere@insa-lyon.fr**
MEGA	**MÉCANIQUE, ÉNERGÉTIQUE, GÉNIE CIVIL, ACOUSTIQUE** **http://edmega.universite-lyon.fr** Sec. : Stéphanie CAUVIN Tél : 04.72.43.71.70 Bât. Direction **mega@insa-lyon.fr**	M. Jocelyn BONJOUR INSA de Lyon Laboratoire CETHIL Bâtiment Sadi-Carnot 9, rue de la Physique 69 621 Villeurbanne CEDEX **jocelyn.bonjour@insa-lyon.fr**
ScSo	**ScSo*** **http://ed483.univ-lyon2.fr** Sec. : Véronique GUICHARD INSA : J.Y. TOUSSAINT Tél : 04.78.69.72.76 **veronique.cervantes@univ-lyon2.fr**	M. Christian MONTES Université Lyon 2 86 Rue Pasteur 69 365 Lyon CEDEX 07 **christian.montes@univ-lyon2.fr**

*ScSo : Histoire, Géographie, Aménagement, Urbanisme, Archéologie, Science politique, Sociologie, Anthropologie

Contents

Résumé **v**

Abstract **vii**

I General introduction 1

Résumé en français **3**
Objectifs . . . 3
Organisation du manuscrit . . . 4

1 Introduction **5**
1.1 Objectives . . . 5
1.2 Thesis organisation . . . 6

II Compton camera imaging in nuclear medicine 7

Résumé en français **9**

2 Compton camera in nuclear medicine **11**
2.1 Gamma ray detection in nuclear medicine . . . 11
2.1.1 Gamma ray generation following radioactive decay . . . 11
2.1.2 Interaction of gamma rays . . . 12
2.1.3 γ-ray imaging modalities . . . 16
2.2 Compton scattering based imaging detectors . . . 18
2.3 Compton tomographic reconstruction : state of the art . . . 20
2.3.1 Analytic methods . . . 20
2.3.2 Iterative methods . . . 21
2.4 Simulation by Monte Carlo method . . . 22
2.4.1 MEGAlib . . . 22
2.4.2 GATE . . . 25
2.5 Conclusion . . . 25

III MLEM reconstruction 27

Résumé en français 29

3 MLEM implementation for Compton camera imaging 35
3.1 The list-mode MLEM algorithm . . . 35
3.2 Model for the Compton camera . . . 37
3.3 Sensitivity estimation by analytic models . . . 38
3.3.1 Simulation geometry . . . 41
3.3.2 Results and discussions . . . 42
3.4 System matrix estimation . . . 43
3.5 Influence of Doppler broadening on the scattering angle . . . 48
3.6 Event uncertainties on realistic data . . . 55
3.7 Reconstruction results . . . 56
3.8 Conclusion . . . 59

IV Resolution recovery of MLEM reconstruction for Compton camera imaging 61

Résumé en français 63

4 Resolution recovery of MLEM reconstruction 69
4.1 Image restoration and total variation regularization . . . 69
4.1.1 TV denoising for Gaussian noise . . . 70
4.1.2 TV regularized tomography with Poisson noise . . . 72
4.1.3 Results of TV denoising and TV-EM reconstruction for 2D RADON projections . . . 75
4.1.4 Results of dual TV-MAP-EM-FISTA reconstruction for Compton camera imaging . . . 79
4.2 Image-based PSF deconvolution . . . 82
4.2.1 Results of RL deconvolution on image deblurring . . . 83
4.2.2 EM-RL reconstruction for Compton camera imaging . . . 89
4.2.3 TV-EM-RL with known PSF . . . 90
4.2.4 TV-EM-RL with unknown PSF . . . 91
4.3 Related publications . . . 93
4.4 Conclusion . . . 96

V Reconstruction of prompt gamma ray in hadron therapy 99

Résumé en français 101

5 Compton camera imaging reconstruction for proton monitoring 103
5.1 Hadron therapy and Bragg peak identification . . . 103
5.2 Methods . . . 106

5.3 Results and discussions 106

VI Conclusion **111**

Résumé en français **113**

6 Conclusion and perspectives **115**
6.1 Conclusion 115
6.2 Perspectives 116

Bibliography **118**

Appendix **129**
3D reconstruction benchmark of a Compton camera against a parallel hole gamma-camera on ideal data 133

List of Symbols and abbreviations

List of Symbols

E_0, E_γ	initial photon energy
E_e	energy delivered to the electron during the Compton scattering process
E'_γ	remaining energy of Compton scattered photon
E_1, E_2	recorded energy by the camera
V_1, V_2	recorded position of photon by camera
β	Compton scattering angle, half-opening angle of cone
h	spatial kernel of the uncertainty of Compton scattering angle β
σ_β	standard variation of calculated scattering angle β
i	index of events
j	index of voxels
l	index of iterations
e_i	event i with the set of parameters (V_1, V_2, E_1, E_2)
v_j	voxel j
λ_j	mean number of photon emitted by voxel j
$S = (s_j)$	sensitivity of detection
$T = (t_{ij})$	system matrix
P, k	kernel matrix of point spread function
$R = (r_j)$	back projection

Abbreviations

PET	Positron Emission Tomography

SPECT	Single Photon Emission Computed Tomography
CC	Compton camera
CPPM	Centre de Physique des Particules de Marseille, France
IN2P3	Institut national de physique nucléaire et de physique des particules, France
IPNL	Institut de Physique Nucléaire de Lyon, France
HZDR	Helmholtz-Zentrum Dresden–Rossendorf, Germany
NCRO	OncoRay–National Center for Radiation Research in Oncology, Germany
IFIC	Instituto de Física Corpuscular, Spain
ISAS/JAXA	Institute of Space and Astronautical Science, Japan Aerospace Exploration Agency
NIRS	National institute of radiological sciences, Japan
RIKEN	Rikagaku Kenkyujo, National Institute of Physical and Chemical Research, Japan
CZT	Cadmium zinc telluride
CdTe	Cadmium telluride
$LaBr_3$	Lanthanum bromide
LSO	Lutetium orthosilicate
LYSO	Lutetium-yttrium orthosilicate
NaI	Natrium iodide
$CeBr_3$	Cerium Bromide
Si	Silicon
Ge	Germanium
Ce	Cerium
GATE	GEANT4 Application for Emission Tomography
MEGAlib	Medium Energy Gamma-ray Astronomy Library
GEANT4	GEometry ANd Tracking
CERN	European Organization for Nuclear Research
LM-MLEM	List-Mode Maximum Likelihood Expectation Maximization

SOE	Stochastic Origin Ensemble
MAP	Maximum A Posterior
FWHM	Full Width Half Maximum
MSE	Mean Square Error
PSF	Point Spread Function
TV	Total Variation
FISTA	Fast iterative shrinkage/thresholding algorithm

Part I

General introduction

Introduction

Objectifs

La médecine nucléaire dont application est largement exploitée en oncologie, neurologie et cardiologie, consiste à utiliser des composés radioactifs. Une fois le produit radiopharmaceutique injecté au patient, le rayonnement ionisant (habituellement un rayonnement gamma) sera émis, et détecté par un système d'imagerie. En montrant l'évolution temporelle (pharmacocinétique) et la biodistribution spatiale du radiotraceur dans le corps, l'imagerie en médecine nucléaire peut aider les médecins à diagnostiquer, à planifier ou à évaluer le traitement. L'invention des équipements d'imagerie et l'amélioration des technologies informatiques ont donné lieu à plusieurs avancées en médecine nucléaire. Aujourd'hui, les deux principales modalités d'imagerie en médecine nucléaire sont : la tomographie par émission de positons (TEP) et la tomographie par émission monophotonique (TEMP) avec systèmes de gamma-caméra. Le système TEP est utilisé pour exploiter la corrélation directionnelle entre les photons d'annihilation de l'émission de positons, tandis que le système TEMP est utilisé pour imager les rayonnements γ émis par le nucléide. Deux dispositifs d'imagerie différents sont proposés pour l'imagerie dans le système TEMP. L'un est la caméra collimatée basée sur une collimation mécanique, l'autre est la caméra Compton basée sur la collimation électronique. Seule la caméra collimatée est actuellement implémentée en clinique. Comparé à la caméra collimatée, l'avantage de la caméra Compton est la possibilité d'augmenter la sensibilité et la possibilité d'imager un grand spectre d'énergie. L'étude des améliorations que la caméra Compton pourrait apporter aux applications de médecine nucléaire est toujours en cours. Elle dépend à la fois des développements technologiques et des techniques de traitement des données, dont la reconstruction tomographique est nécessaire et difficile. En imagerie par caméra Compton, le modèle d'acquisition est basé sur l'intégrale de l'intensité de la source sur des projections coniques. En d'autres termes, la reconstruction de la distribution de la source n'est plus basée sur des projections linéaires comme dans la caméra collimatée, mais sur des projections coniques.

Le sujet de cette thèse est l'étude de la capacité de l'imagerie par caméra Compton en apportant des améliorations à l'algorithme itératif de reconstruction qui correspond au MLEM (*Maximum Likelihood Expectation Maximization* en anglais) en mode liste. Plus précisément, cette étude vise à améliorer la qualité des images reconstruites. Lors de la détection d'un photon, plusieurs facteurs influencent la qualité de la mesure, comme par exemple les processus physiques tels que l'atténuation, la diffusion et l'élargissement Doppler, la résolution imparfaite du détecteur, etc.. La modélisation des incertitudes de mesure dans la matrice du système influence le résultat de LM-MLEM fortement. L'une des contributions de cette étude est un modèle plus précis d'élargissement Doppler validé par la simulation Monte Carlo. Une autre

contribution concerne une méthode de régularisation par la variation totale (TV) développée pour les données distribuées selon une loi de Poisson. Le débruitage TV est introduit dans la reconstruction MLEM comme une étape de régularisation, ce qui permet d'améliorer la qualité de l'image dans l'acquitision à statistique faible. Nous avons également proposé une méthode de déconvolution par la fonction d'étalement ponctuel régularisée (PSF) pour la récupération de la résolution dans l'espace image. Cette méthode permet d'améliorer le conditionnement du problème inverse en imagerie TEMP et TEP. Toutes les méthodes ont été validées par simulation Monte Carlo.

Organisation du manuscrit

Ce manuscrit est composé de quatre parties. La première partie présente certains processus physiques qui peuvent se produire pendant la détection du rayon γ. Ensuite elle introduit les deux modalités d'imagerie principales de médecine nucléaire : TEP et TEMP, et fait un état de l'art de plusieurs prototypes de caméra Compton. Ensuite, nous illustrons les algorithmes les plus utilisés pour la reconstruction tomographique de la caméra Compton. A la fin, nous présentons la simulation Monte Carlo que nous avons utilisée dans cette étude.

La deuxième partie présente les différents modèles mathématiques utilisés dans la reconstruction LM-MLEM. Nous décrivons d'abord l'algorithme LM-MLEM. Puis nous présentons quelques méthodes analytiques pour estimer la matrice de sensibilité. Après avoir résumé certains des modèles probabilistes pour l'estimation de la matrice du système, nous nous concentrons sur l'étude des incertitudes sur l'angle de diffusion introduite par l'effet Doppler. La fin de cette partie montre quelques résultats de reconstruction à partir de données obtenues par la simulation Monte Carlo.

La troisième partie présente les méthodes pour améliorer la résolution dans l'espace image de la reconstruction MLEM en trois étapes. Nous présentons d'abord les méthodes de débruitage TV dans la littérature et la régularisation TV adaptée à MLEM. Ensuite, nous étudions la déconvolution par la PSF pour récupérer la déformation de la reconstruction causée par la résolution de détection et d'autres effets physiques sauf l'effet Doppler. Enfin, nous présentons la combinaison de la reconstruction TV-EM et de la déconvolution PSF et montrons quelques résultats de reconstruction.

La quatrième partie traite de l'imagerie par caméra Compton pour le contrôle de qualité en hadronthérapie. Nous présentons d'abord la mise en place de la simulation de source γ-prompt et le prototype de caméra Compton développé par l'Institut de Physique Nucléaire de Lyon, puis le résultat de la reconstruction obtenue par l'algorithme TV-MLEM de l'émission de γ-prompts produits lors de l'irradiation d'un faisceau de protons. Dans cet exemple le nombre d'événements mesurés est très faible et nous n'avons pas appliqué toutes les méthodes développées pendant cette thèse. Cela aurait nécessité un travail de modélisation de l'effet Doppler à différentes énergies et le calcul des PSF pour cette configuration spécifique. Nous nous sommes concentrés sur l'application de la régularisation TV, ce qui permet déjà une amélioration de la qualité des images reconstruites.

Chapter 1

Introduction

1.1 Objectives

Nuclear medicine means to use radioactive compounds in medicine to image and treat human disease, of which the application is largely exploited in oncology, neurology and cardiology. After introducing the radio-pharmaceutical into the patient, the ionizing radiation (usually a gamma ray) will be emitted and detected by a γ imaging system. By showing the temporal course of the radiotracer in the body, nuclear medicine imaging can help physicians to diagnose, to plan or evaluate the treatment. The inventions of imaging equipment and the improvements in computing technologies have led to several breakthroughs in nuclear medicine. Nowadays the two major imaging modalities are: the positron emission tomography (PET), and the gamma camera system single photon emission computed tomography (SPECT). The PET system is used to exploit the directional correlation between annihilation photons emitted by positron decay, while the SPECT system is used to image gamma rays emitted by nuclide. Two different imaging devices are proposed for imaging in SPECT, one is the Anger camera based on mechanical collimation, another is the Compton camera based on electronic collimation. Compared to Anger camera, the advantage of Compton camera is the possibility of increasing the sensitivity and the possibility of imaging a wide range of energy spectrum sources. The detection of gamma radiation sources is now carried on by Anger cameras, and the investigation of the improvements that Compton camera may bring for nuclear medicine applications is still ongoing. It depends both on technological developments and data processing techniques, among which the tomographic reconstruction is currently a bottleneck. In Compton camera imaging, the acquisition model is based on the integral of the intensity of the source on conical shapes. In other words the reconstruction of distribution of the source is no longer based on linear projections like for Anger camera, but on conical projections.

The goal of this thesis is to investigate the capability of Compton camera imaging by improving the reconstruction performance of the most employed iterative algorithm, the List Mode Maximum Likelihood Expectation Maximization (LM-MLEM). More precisely, this study aims to ameliorate the quality of reconstructed images. During the detection of γ photons, several factors will influence the quality of measurement, e.g. physical processes such as attenuation, scattering and Doppler broadening, the imperfect detector resolution, etc. Modeling the measurement uncertainties in the system matrix can strongly influence the result of LM-MLEM. One of the contributions of this study is a more precise model for Doppler broadening validated by Monte Carlo simulation. Another contribution concerns a total variation (TV) regularization method developed for Poisson distributed data. The TV introduced in the MLEM reconstruction as a regularization step allows to improve the image quality in low-counts experiments. We also proposed a TV regularized EM reconstruction with point spread function

(PSF) deconvolution for resolution recovery in the image space. This method can ameliorate the conditioning of the inverse problem for SPECT and PET modalities.

1.2 Thesis organisation

This manuscript is composed of four parts. The first part presents several common physical processes that might occur during the γ ray detection. Then introduces two main imaging modalities in nuclear medicine: PET and SPECT, and summarizes the state of the art on existing prototypes of Compton camera. Afterwards we illustrate some of the most used algorithms for Compton tomographic reconstruction. At the end, we will present the Monte Carlo simulation we used in this study.

The second part introduces the different mathematical models used in the LM-MLEM reconstruction. We first describe the LM-MLEM algorithm. Then propose and analyze different methods for calculating the sensitivity matrix. After summarizing some of the probabilistic models for the system matrix estimation, we focus on the investigation of uncertainties on the scattering angle and models for Doppler broadening. The end of this part investigates the validity of the different models with some reconstruction result obtained from simulated data.

The third part presents the resolution recovery methods in image space of MLEM reconstruction for Compton camera imaging by three steps. We first present the TV denoising methods in the literature and then introduce the TV regularization adapted to MLEM. Then we investigate the PSF deconvolution for recovering the deformation of reconstruction caused by the limited detection resolution and other physical effects except Doppler broadening. Finally, we present the combination of TV regularized EM reconstruction and PSF deconvolution on Compton camera imaging and show some reconstruction results.

The fourth part serves as a perspective of applying Compton camera imaging in hadron therapy. We first demonstrate the simulation setup of prompt gamma sources with the prototype of Compton camera developed by IPNL. Then present the reconstruction result obtained by the ameliorated algorithm TV-MLEM of γ emitted by secondary radiation of a pencil proton beam. In this configuration few events were measured and we didn't apply all the methods developed in this thesis. This would have required modeling the Doppler broadening at different energies and calculating PSF for this specific configuration. We only focused on the TV regularization, which already allowed to improve the quality of the reconstructed images.

Part II

Compton camera imaging in nuclear medicine

Résumé en français

La médecine nucléaire consiste à utiliser des substances radioactives pour le diagnostic et le traitement de maladies, dont l'application est largement exploitée en oncologie, en neurologie et en cardiologie. En montrant le métabolisme de la radio-pharmaceutique in vivo, l'imagerie en médecine nucléaire permet d'évaluer le fonctionnement des organes et d'aider les médecins à diagnostiquer et à désigner ou surveiller le traitement. Les inventions d'appareils d'imagerie et les améliorations des technologies de l'information ont conduit à plusieurs progrès en médecine nucléaire. Lors de la détection des rayons γ, plusieurs processus physiques peuvent se produire. Ce chapitre présente d'abord les principales interactions photon-matière, puis deux modalités d'imagerie essentielles en médecine nucléaire : la tomographie par émission de positons (TEP) et la tomographie par émission monophotonique (TEMP). La caméra Compton est proposée comme une nouvelle option pour les détecteurs de rayons γ en TEMP. Après avoir résumé certains prototypes de la caméra Compton existants au monde, nous présentons les algorithmes de reconstruction des images. À la fin de ce chapitre, nous nous concentrons sur la simulation Monte Carlo que nous avons utilisée dans cette thèse.

Détection du rayons γ en médecine nucléaire

La détection du rayon γ est obtenue par l'interaction entre la particule γ et le matériau de l'équipement d'imagerie. Plusieurs processus physiques ont lieu lorsque le photon γ voyage dans la matière, dépendant à la fois du matériau et de l'énergie initiale des photons. La fonction générale d'un système d'imagerie par rayons γ est de fournir une image de la distribution de la radioactivité chez le patient à partir des rayons γ sortant du corps. Il existe deux principaux types de rayonnements d'intérêt pour la détection des rayons γ : les rayonnements d'annihilation qui surviennent après l'émission de positons, et les rayonnements γ émis par les noyaux excités. Les paires de photons d'annihilation suivant l'émission de positons sont détectés en TEP, tandis que les photons γ sont détectés par une caméra γ en TEMP. L'imagerie TEMP est réalisée par les caméras collimatées, dont un rayon γ passant par le trou du collimateur interagit avec le détecteur sensible. L'efficacité de detection pour la caméra collimatée peut être faible, car un certain nombre de photons frappant les collimateurs sont diffusés ou absorbés. La caméra Compton est donc proposée pour améliorer l'efficacité et la sensibilité.

Détecteur basé sur la diffusion Compton

La caméra Compton est une gamma caméra sans collimation mécanique qui permet d'imager des sources de photons en 3D. Dans un premier temps, un photon interagit dans le diffuseur où il transmet une partie de son énergie à un électron. Le photon diffusé peut encore interagir dans le premier détecteur, et est finalement absorbé dans le second détecteur. Une fois l'acquisition des photons terminée, on obtient un ensemble d'évènements qui définissent chacun un cone. A

la différence de la tomographie classique, on a ici des projections sur des surfaces coniques.

La caméra Compton a été proposée dans les années 70 simultanément pour des applications d'imagerie astronomique (Schönfelder et al. [1973]) et nucléaire (Todd et al. [1974]). Plusieurs prototypes (Schonfelder et al. [1984], Schindler et al. [1997], Zoglauer et al. [2009a], Bandstra et al. [2011], Tatischeff et al. [2016]) ont été construits et exploités non seulement pour l'observation des sources γ cosmiques, mais aussi pour la surveillance des centrales nucléaires et des déchets avec le développement de détecteurs portatifs γ dopés suite au récent accident de Fukushima au Japon (Harayama et al. [2015], Iltis et al. [2018]).

La caméra simulée dans cette thèse est basée sur le prototype développé par l'Institut de physique nucléaire de Lyon (IPNL) en France (Krimmer et al. [2018]). Leur prototype est réalisé en Si/$LaBr_3$. Nous allons détailler la géométrie, la résolution spatiale et énergétique dans la section 5.2 où nous montrons une reconstruction de gamma prompts détectés par ce prototype.

Tomographie Compton

Les méthodes de reconstruction tomographique pour l'imagerie par caméra Compton peuvent être classées en méthodes analytiques et itératives. Un algorithme analytique vise à reconstruire les images de distribution des sources directement à partir de projections. Au contraire de celui-ci, l'algorithme itératif vise à trouver la solution en utilisant l'évaluation par calcul itératif à partir de projections. La reconstruction par technique analytique permet de trouver rapidement la solution exacte pour un modèle continu. Cependant pour une acquisition réelle en imagerie radio-isotopique, la capacité de reconstruction est limitée. Les contraintes sont dues à un champ de vision limité, à des bruits importants et à d'autres facteurs supplémentaires, ce qui rend les méthodes itératives plus attrayantes en raison de la possibilité de modéliser tous ces facteurs. Notre contribution vise à l'algorithme itératif par maximisation de la vraisemblance (MLEM). Avant d'approfondir la méthode MLEM, cette section présente un bref aperçu de plusieurs méthodes analytiques et itératives existantes.

Simulation Monte Carlo

La simulation Monte Carlo est une technique d'échantillonnage statistique visant à résoudre des problèmes complexes en générant des expériences pseudo-aléatoires. Cette méthode suppose que le système à problèmes peut être exprimé par plusieurs densités de probabilités tirées de l'ajustement des données et de la théorie. Formellement développé par Stan Ulma et Von Neumann en 1947 Eckhardt [1987], il est maintenant largement utilisé en physique, ingénierie, biologie, intelligence artificielle, etc. Dans l'étude de la physique des particules, cette méthode est utilisée pour concevoir des détecteurs, comprendre leur comportement et comparer les données expérimentales à la théorie Rogers [2006]. GEANT4 (GEometry and Tracking) est une boîte à outils conçue pour la simulation du passage des particules dans la matière à l'aide des méthodes de Monte Carlo, développées au CERN (Organisation européenne pour la recherche nucléaire). Il implique une fonctionnalité complexe comprenant des modèles physiques, la géométrie (l'information des détecteurs), le suivi (la trajectoire des particules dans la matière, y compris les désintégrations et les interactions) et la visualisation. Cette section présente deux outils de simulation Monte Carlo basés sur la plateforme GEANT4 : MEGAlib (Medium Energy Gamma-ray Astronomy Library) et GATE (GEANT4 Application for Emission Tomography). Nous avons utilisé ces deux outils de simulation pour générer les données utilisées dans cette thèse. Dans le chapitre 3 toutes les données simulées sont générées par MEGAlib. Les données de sources voxélisées dans le chapitre 4 sont générées par GATE.

Chapter 2

Compton camera in nuclear medicine

Nuclear medicine means to use radioactive materials for diagnosis and treatment of illnesses, of which the application is largely exploited in oncology, neurology and cardiology. By showing the metabolism of radio-pharmaceutical in vivo, nuclear medicine imaging can assess how organs function and help physicians to diagnose and plan or evaluate the treatment. Radioisotope decays are used to visualize specific internal processes or particular tissues. The measurement of gamma ray is important for radionuclide imaging diagnostics, in which the radio-pharmaceutical is injected into the patient and the emitted ionizing radiation (usually a γ ray) will be detected by imaging system. The detection of radiation is also used for monitoring in hadron therapy, in which the γ ray is generated by the nuclear reaction of the hadron within the body.

The inventions of imaging equipment and the improvements in computing technologies have led to several breakthroughs in nuclear medicine. This chapter first presents briefly the creation of γ ray during the radionuclide imaging and hadron therapy, then several common photon interactions that might occur during the γ detection are presented. We then describe the two main imaging modalities in nuclear medicine: the positron emission tomography (PET) and the gamma camera system single photon emission computed tomography (SPECT), among which the Compton camera (CC) is proposed as a new option for γ ray detectors. After summarizing several existing prototypes of CC, we will illustrate some of the most used algorithms for reconstruction. The end of this chapter introduces the Monte Carlo simulation we employed in this study.

2.1 Gamma ray detection in nuclear medicine

2.1.1 Gamma ray generation following radioactive decay

Radioactive decay is a process during which an unstable nucleus (parent) loses energy by emitting a particle or electromagnetic radiation and transforms into a stable or unstable nucleus (daughter). The unstable daughter will further decay until to be stable, which forms a decay chain. In nuclear medicine the three main categories of decay processes are: α decay, β decay and γ decay. γ photon is one of the particles that can be generated, or emitted during these processes. More precisely, the emitted particles in different decay modes can be distinguished as follows (Chandra and Rahmim [2017]):

- Alpha particles in α decay;
- Electrons in β^- decay;
- Positrons in β^+ decay;

- Neutrinos in β^+ decay;
- Antineutrinos in β^- decay;
- Gamma rays in γ decay;
- Atomic orbital electrons in internal conversion;
- Neutrons in spontaneous fission and in neutron emission decay;
- Heavier nuclei in spontaneous fission;
- Protons in proton emission decay.

In radionuclide imaging modalities such as SPECT, a radio-tracer containing radioisotope is injected into the patient, the short-lived excited nucleus decays into a more stable form and releases γ ray photons. The emitted γ photon will then travel through the body and interacts with the collimated detectors. In PET, the measured photons are generated by the annihilation of a positron emitted by the β^+ decay of the radioisotope that interacts with an atomic electron.

Moreover, in hadron therapy, the heavy charged particles, e.g. protons, carbon ions will be delivered into the patient, travel through matter (e.g. organ, tissue, blood) and lose their energy by ionization and nuclear interactions with the nuclei of matter. Two types of γ might be produced by the interactions: pairs of γ photons of specific energy generated by the annihilation of positron produced by the fragments, and prompt-γ emitted by the excited nuclear fragments in picosecond. The measurement of annihilated back-to-back photons can be carried out with PET, and the detection of prompt-γ can be realized by SPECT, for which Compton cameras are also under investigation. The measurement of γ generated by the nuclear reactions of the hadrons within the body is an option for monitoring the hadron therapy and assuring the quality of treatment.

2.1.2 Interaction of gamma rays

The detection of γ ray is achieved through the interaction between the γ particles and the imaging devices. Several physical processes will take place when the γ photon travels through the matter, which depend both on the material and the initial energy of the photon. Figure 2.1(a) shows the different interactions that might occur related to different initial energy in silicon.

- **Compton scattering**

  The Compton scattering is also called incoherent scattering, during this process the photon interacts with an electron loosely bound to the nucleus. The photon has energy E_γ much larger than the binding energy E_b. The photon transfers energy E_e to the electron which recoils, then the photon scatters as $E'_\gamma = E_\gamma - E_e$ through a scattering angle β. The scattering angle β can be deduced from energies E_γ and E'_γ:

$$cos(\beta) = 1 - m_e c^2 (\frac{1}{E'_\gamma} - \frac{1}{E_\gamma}) \tag{2.1}$$

  where m_e is the mass of an electron at rest and c is the speed of light.

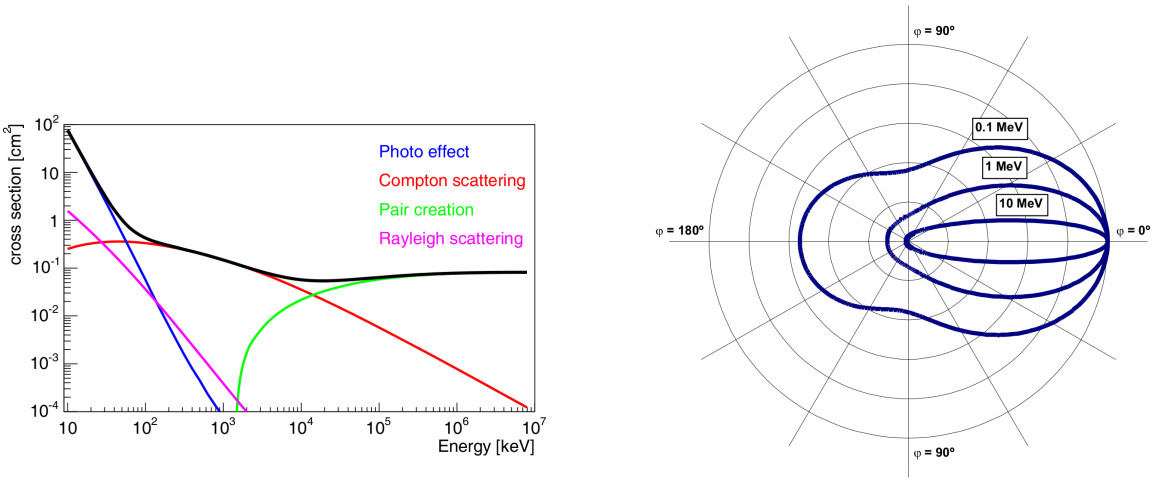

(a) Cross section for photon interactions

(b) Klein-Nishina cross section at different energies

Figure 2.1: Cross section for photon interactions in silicon according to the energy of the γ ray (left) and the Klein-Nishina differential cross section as a function of Compton scatter angle β for different initial energies of photon (right). Image source: A. Zoglauer [2005].

The probability that a photon with an energy E_γ undergoes a Compton scattering through an angle β is given by the Compton scattering cross section. The Klein-Nishina formula enables to calculate this probability as a function of β, E_γ and E'_γ:

$$K(\beta, E_\gamma) = \frac{r_e^2}{2}(\frac{E'_\gamma}{E_\gamma})^2(\frac{E'_\gamma}{E_\gamma} + \frac{E_\gamma}{E'_\gamma} - \sin^2\beta) \tag{2.2}$$

where r_e is the classical electron radius given by $r_e = \frac{e^2}{4\pi\epsilon_0 m_e c^2}$ with e the elementary charge and ϵ_0 the permittivity of free space. The electron is loosely bound to the nucleus of an absorber atom, so the cross section can only be approximated. Figure 2.1(b) shows the Klein-Nishina cross section as a function of Compton scattering angle β at different initial energies of photon. The higher the initial energy is, the higher is the possibility to have a smaller scattering angle β. In CC imaging the reconstruction of photon emission is based on conical projections. The half-opening angle of cone β is deduced from the energies E_γ, E_e. Since the electrons are in motion around the nucleus, which leads to the Doppler broadening, the measurement of energies will not reflect only one Compton scattering angle, but various angles around it. The half-opening angle can only be approximated and this actuality should be considered in the modeling of imaging. We will detail the modeling in CC imaging in the following.

Figure 2.2 is the general diagram of Compton scattering.

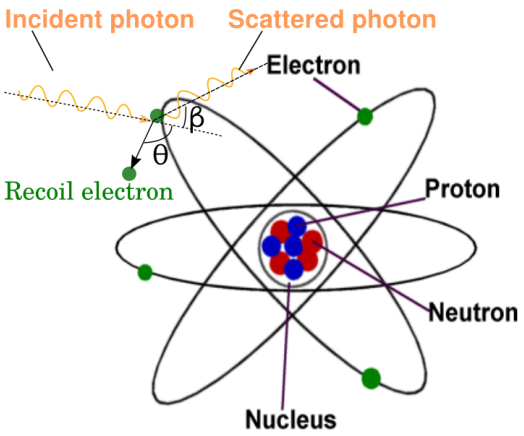

Figure 2.2: Diagram of the Compton scattering. An incident photon with initial energy E_γ transfers an energy E_e to an electron and is scattered through the Compton scattering angle β with a remaining energy E'_γ. The scattering angle β is the angle between the direction of the scattered photon E'_γ and the positive abscissa axis (represented by the dashed line). The recoil angle θ is the angle between the direction of the recoil electron and the positive abscissa axis.

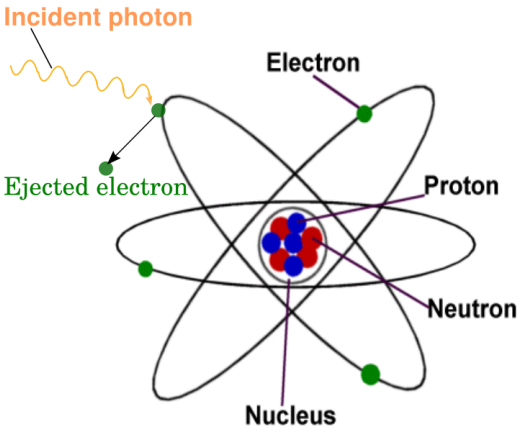

Figure 2.3: Diagram of the photo-electric effect. An incident photon with initial energy E_γ transfers all its energy and is absorbed by one of the orbital electrons of the atom. The electron is then ejected with kinetic energy E_e.

- **Photo-electric absorption**

  In photo-electric absorption the photon interacts with a tightly bound orbital electron of an absorber atom. This process occurs when the γ photon has energy E_γ from a few eV to over 1 MeV. The γ energy E_γ largely exceeds the binding energy E_b of electron, which will lead to the ejection of the electron. Figure 2.3 shows the diagram of photo-electric absorption. During the absorption the photon will transfer all its energy to the electron and disappear, and the electron will be ejected with kinetic energy E_e:

$$E_e = E_\gamma - E_b \tag{2.3}$$

- **Rayleigh scattering**

  Rayleigh scattering is also called coherent scattering, during this process the photon interacts with the total atom and loses none of its energy. No energy is transferred

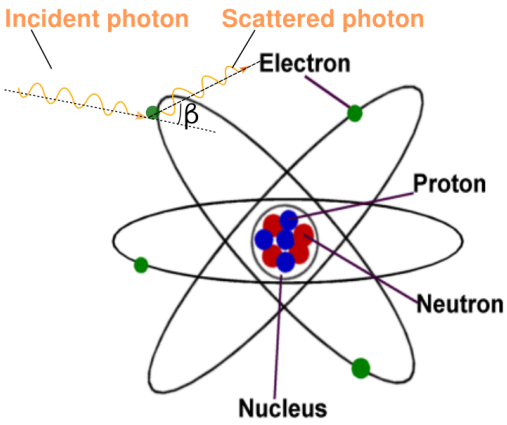

Figure 2.4: Diagram of the Rayleigh scattering. An incident photon with initial energy E_γ is scattered through a relatively small scattering angle β, no energy is transferred to the electron.

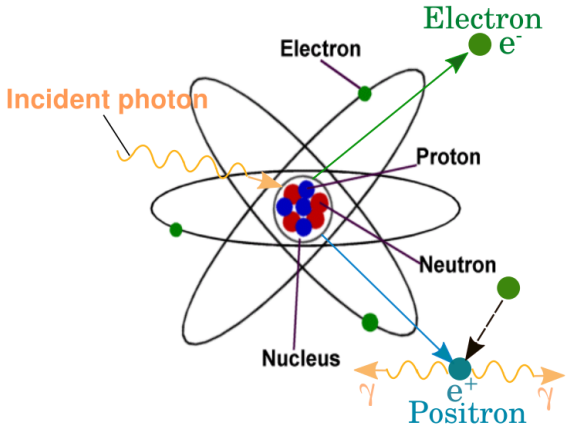

Figure 2.5: Diagram of positron creation and further positron annihilation.

from the photon to the electron, and the photon is scattered through a relatively small scattering angle β. Figure 2.4 shows the general diagram of Rayleigh scattering.

Although Rayleigh scattering is often ignored in radiation dosimetry because there is no energy transferred, it might plays a relevant role at low energies, as the scattered photon deviates from the original trajectory.

- **Electron-positron pair creation**

  This process happens when the incident photon energy E_γ exceeds $2m_ec^2 = 1.022$ MeV. During this process the photon only interacts in the Coulomb electric filed of atomic nucleus or orbital electrons and creates an electron-positron pair. In some cases triplet production might also occur. The photon will be fully absorbed, a part of its energy transfers to a mass of an electron-positron pair, the rest energy transfers in the form of kinetic energy to the created pair. The momentum is transferred to the nucleus or the electron. The positron combines with an electron and both annihilate, producing two γ rays of 511 keV in opposite direction. Figure 2.5 shows the diagram of nuclear pair production and further positron annihilation. The electron-positron pair creation is the basic process in PET.

2.1.3 γ-ray imaging modalities

The general function of a γ ray imaging system is to provide an image of the radioactivity distribution in the patient from γ rays exiting the body. There are two main types of radiation of interest in γ ray detection: annihilation radiation ($\gamma\pm$) arising after positron emission, and the γ ray emission from excited nuclei. The annihilation photons from positron emission are detected with PET, and the single γ photons are detected with a γ camera in SPECT.

- **PET**

  PET uses a radiotracer labeled with some radioactive material, e.g. ^{18}F, ^{15}O, ^{13}N, ^{11}C, being chosen by which organ and function are supposed to be observed, that decays by β^+ and emits positrons. One emitted positron will annihilate with one electron and then gives two back-to-back 511 keV photons. The coincidence detection is based on the arrival times of the two photons. The pair of photons in coincidence defines a line of response (LOR) through the point of annihilation, so-called as electronic collimation. The source position is located along the LOR which connects the two detector elements and projections are obtained by several detectors placed around the patient. The image can then be reconstructed from the projections. The width of LOR is non-zero because of the spatial and time resolution. Not all the recorded coincidence events are true coincidences, but can be scattered, random or multiple coincidence. The figure 2.6 shows the detection of two back-to-back photons. Scattered coincidence takes place when one or both of the photons from a single positron annihilation is scattered by the patient. Random coincidence occurs when two photons originating from different annihilations are detected as a true coincidence. The aim of PET is to record the true coincidence. Other physical processes such as attenuation will also contribute to noise in PET. Several techniques are developed to meet the need of accurate datasets. The fusion of two medical imaging devices into one physical unit, e.g. PET/MR, PET/CT were developed. A combined CT/PET technique benefits from an additional anatomy information that helps to correct the scatter and attenuation and can provide more precise location of the lesion (Beyer et al. [2000]). The time-of-flight (TOF) PET were built in the 1980s (Ter-Pogossian et al. [1982], Gariod et al. [1982]) and a number of TOF-PET were developed to reduce statistic noises in the reconstruction and the random coincidence event rates (Lewellen [1998], Mazoyer et al. [1990], Surti [2015]). More recently, the digital photon counting (DPC) PET system developed by Philips has allowed to count photons directly without analog post-processing. Therefore the information for image reconstruction are collected with high efficiency and accuracy (Miller et al. [2015]) and makes better lesion detection possible. Compared with SPECT, the main advantage of PET imaging is the higher sensitivity and spatial resolution, as well as its capability to perform quantitative measurements within shorter scan times.

- **SPECT**

  SPECT is an imaging system to image γ rays emitted by radionuclide, usually designed for detecting energies in the order of tens to few hundreds of keV. In contrast to PET where pairs of photons are imaged, in gamma cameras single photons are imaged. The gamma camera, or Anger camera (Anger [1952]), is composed of four basic elements (Cherry et al. [2012]): the collimator, which defines the LOR; the radiation detector, which counts incident γ photons; the computer system, which reconstructs the 3D images from the projections; the gantry system, which supports and moves the gamma camera and patient. Figure 2.7 illustrates the geometry of Anger camera. A γ photon passes through the hole of collimator and interacts with the sensitive material. Usually, the

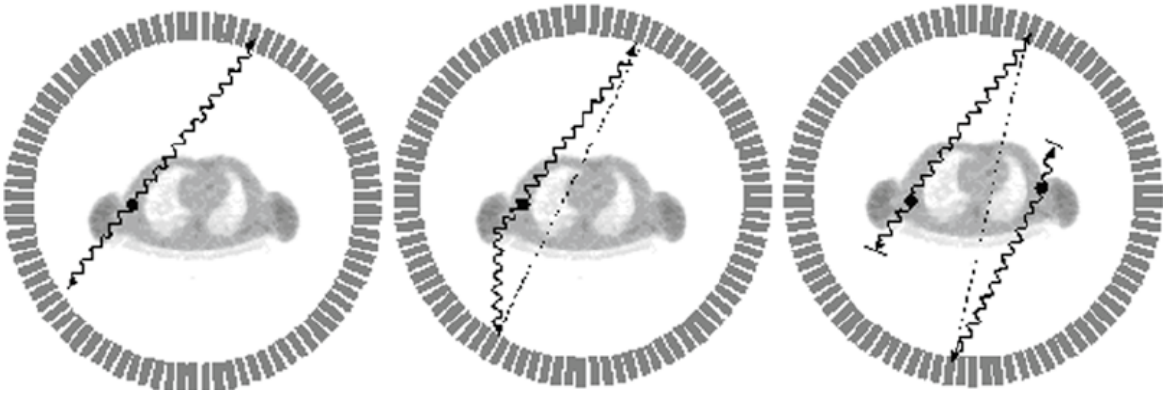

(a) true coincidence (b) scattered coincidence (c) random coincidence

Figure 2.6: Diagram of the detection of a pair of photons in PET with types of coincidence events. Image source: Livieratos [2012].

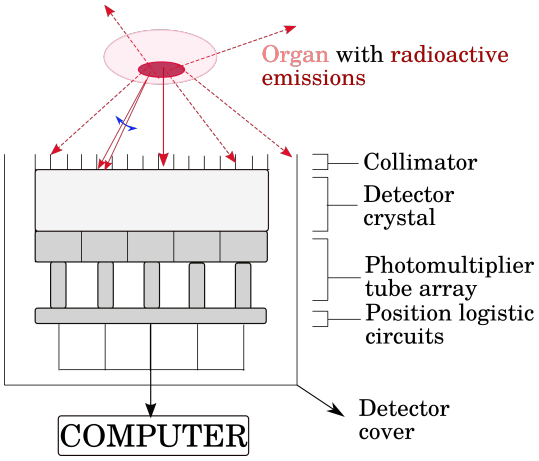

Figure 2.7: Diagram of the detection of photons in SPECT by collimated camera.

detection is based on photoelectric absorption of the photon in a scintillating crystal, followed by measurement of visible light.

Since physical collimators are needed in order to reject photons that are not within a small angular range, the efficiency can be low as a large number of photons hits the collimators are scattered or absorbed. The sensitivity of detection depends largely on the collimators, which makes the optimal design of the collimators essential. Another possible solution for improving the efficiency and the sensitivity is to use a Compton camera (CC).

A CC is composed of several position sensitive γ ray detectors. In the model of detection by CC, the incident γ ray first interacts with the element of one of these detectors and undergoes a Compton scattering, then the escaped γ ray will interact with another detector which records the position and deposited energy of second interaction. If the scattered γ ray transfers all its energy to the second detector, the initial energy can be determined by the sum of the two energies detected. The direction of the scattered γ ray can be determined from the two recorded positions, the scattering angle is determined from the initial and the first recorded energy, and the emission position of the γ ray is located on a cone shell centered on the scattered ray direction with half-opening angle that equals to the scattering angle.

The idea of using a CC is to have a large acceptance angle and identify the direction

of an incoming γ ray by using a coincidence mechanism based on Compton scattering instead of using the collimator based mechanism. However, in CC imaging the reconstruction is based on the conical projection defined by Compton scattering angle and photon trajectory, which makes the reconstruction process more complex than the one based on line projection. Previous works attempted to benchmark the CC with respect to the collimated camera from the point of view of detection efficiency and imaging capabilities. It is widely acknowledged that at energies superior to three or four hundred of keV, CC devices allow an increase in efficiency of one or two orders of magnitude (Gormley et al. [1997], Han et al. [2008]). Recently, a factor of 20 was found in simulations when compared the General Electric HealthCare Infinia SPECT with a CC prototype currently under development (Fontana et al. [2017]).

Although CCs could be of interest (Singh and Doria [1983], Takeda et al. [2012], Motomura et al. [2013], Krimmer et al. [2015], Pausch et al. [2016], Kishimoto et al. [2017], Fontana et al. [2017]), imaging of γ sources in nuclear medicine is actually carried out with collimator-based gamma cameras. CCs have recently regained interest as they may allow ion-range monitoring for proton and hadron-therapy using prompt-γ emission generated by nuclear interactions of the ions with tissue (Frandes et al. [2010], Richard et al. [2012], Ortega et al. [2015], Taya et al. [2016], Schoene et al. [2016], Hueso-González et al. [2016], Aldawood et al. [2017], Rohling et al. [2017], Krimmer et al. [2018]).

2.2 Compton scattering based imaging detectors

The CC was proposed during the 70's simultaneously for astronomical (Schönfelder et al. [1973]) and nuclear medicine (Todd et al. [1974]) imaging applications. Several prototypes (Schonfelder et al. [1984], Schindler et al. [1997], Zoglauer et al. [2009a], Bandstra et al. [2011], Tatischeff et al. [2016]) have been built and exploited for the observation of cosmic γ sources, or for monitoring nuclear plants and waste with the development of handheld γ-detectors boosted by the recent accident in Fukushima, Japan (Harayama et al. [2015], Iltis et al. [2018]). A research group at the University of Michigan (Du et al. [2001]) built a prototype of camera based on two 3D position-sensitive CZT detectors. The prototype is then developed in Lee et al. [2014] and Wahl et al. [2015], and has been widely used in US nuclear power plants for monitoring. The group of Kyushu University, in collaboration with the Cyclotron Center in Institute of Physical and Chemical Research (RIKEN) in Japan and the Institute of Modern Physics of Chinese Academy of Sciences, built a camera for multi-tracer imaging (Yang et al. [2001]). Their prototype is composed by two detectors made of Germanium and the detected energy is from 100 keV to 2 MeV. Another prototype made of Si/CdTe is developed by Takeda et al. [2012] in the Institute of Space and Astronautical Science, Japan Aerospace Exploration Agency (ISAS/JAXA), the University of Tokyo and the RIKEN Center for Molecular Imaging Science in Japan, the detected energy is several hundreds keV. The same group had built a portable commercial camera (Harayama et al. [2015]) and field test had gone through in Fukushima for particle detection. Their prototype consists of 2 layers of Si double-sided strip detectors and 3 layers of CdTe double-sided strip detectors and the angular resolution at 662 keV can reach a FWHM of 2.2%. In Kishimoto et al. [2017], a spatial resolution better than 3 mm FWHM and an intrinsic detection efficiency of 0.06% for 662 keV γ ray is achieved with Waseda University, Hamamatsu Photonics Central Research Laboratory, National Institutes for Quantum and Radiological Science and Technology (NIRS-QST) and Osaka University Graduate School of Medicine, Medical Imaging Center for Translational Research. Their prototype used Ce-doped $Gd_3Al_2Ga_3O_{12}$(GAGG) for both scatterer and absorber. An in-vivo detection of multi-tracer

(^{131}I-NaOH accumulated in the thyroid, $^{85}SrCl_2$-HCL in the bone and $^{65}ZnCl_2$-saline in the liver) was realized. In Iltis et al. [2018] a temporal imaging prototype made of $CeBr_3$ is developed for nuclear waste detection, and the energy range is from 200 keV to 2 MeV. Most recently, experiments in human body were realized by CC imaging in Gunma University Heavy Ion Medical Center, Japan (Nakano et al. [2019]) for two radiopharmaceuticals ^{99m}Tc-DMSA and ^{18}F-FDG. The investigated CC was made of Si/CdTe. Their study proved that the Compton camera as a new modality might enable the multi-tracer imaging in nuclear medicine diagnosis.

For γ energies above 1 MeV, the pair production cross-section increases rapidly and becomes comparable with the Compton cross section. This phenomenon is not desired in CC because it produces two annihilated photons which can escape the detection. $LaBr_3$ is capable to produce Compton processes even for these energies (Ortega et al. [2015]). Several proposed prototypes have used $LaBr_3$ for absorbers (Frandes et al. [2010], Fontana et al. [2017], Krimmer et al. [2018], Ortega et al. [2015], Taya et al. [2016]). The detectable energy can range from several hundreds keV to 50 MeV.

The prototype developed by the German group (Rohling et al. [2017]) in the OncoRay–National Center for Radiation Research in Oncology/Helmholtz-Zentrum Dresden–Rossendorf (HZDR) used CZT as scatter layer and LSO as absorber. Their prototype is built for in vivo range verification in proton therapy. The Spanish group Instituto de Física Corpuscular (IFIC) in Valencia, investigated a prototype based on Si/$LaBr_3$ for dose monitoring in hadron therapy (Llosá et al. [2010]) in collaboration with Laboratoire de l'Accélérateur Linéaire (LAL) in France. Another prototype was built by l'Institut de physique nucléaire de Lyon (IPNL) in France and several materials (LYSO, NaI, BGO, $LaBr_3$) for absorber were investigated (Richard et al. [2012]).

The CC simulated in this thesis is inspired from the prototype designed by IPNL (Krimmer et al. [2018]). The detectors are made of Si (scatterer) and $LaBr_3$ (absorber). We will detail the geometry, the spatial and energy resolution of the prototype in Krimmer et al. [2018] in section 5.2, in which we tried to reconstruct a prompt gamma distribution detected by this prototype.

The above prototypes of CC are summarized below:

Prototype of CC for nuclear waste detection			
Location	Institute	Material	Reference
France, Troyes	DAMAVAN imaging	$CeBr_3$	Iltis et al. [2018]
Japan, Kanagawa	ISAS/JAXA	Si/CdTe	Harayama et al. [2015]
USA, Michigan	University of Michigan	CZT	Du et al. [2001]

Prototype of CC for medical imaging			
Location	Institute	Material	Reference
France, Lyon	IPNL	Si/LYSO, Si/BGO, Si/$LaBr_3$	Krimmer et al. [2018],Richard et al. [2012]
German, Dresden	National Center for Radiation Research in Oncology	LSO/CZT	Rohling et al. [2017]
Japan, Fukuoka	Kyushu University	Ge	Yang et al. [2001]
Japan, Kanagawa	ISAS/JAXA	Si/CdTe	Takeda et al. [2012]
Japan, Maebashi	Gunma University	Si/CdTe	Nakano et al. [2019]
Japan, Tokyo	NIRS-QST	Ce-doped GAGG, Si/$LaBr_3$	Kishimoto et al. [2017]
Spain, Valencia	IFIC	Si/$LaBr_3$	Llosá et al. [2010]
USA, Michigan	University of Michigan	CZT	Lee et al. [2014], Wahl et al. [2015]

2.3 Compton tomographic reconstruction: state of the art

Tomographic reconstruction methods for CC imaging can be classified into two classes: analytic and iterative algorithms. The analytic algorithm aims to reconstruct in one step the source distribution images directly from projection, while the iterative algorithm aims to find the solution by using iterative computation. Analytic reconstruction can find the exact solution rapidly for continuous model, but for real acquisition in radioisotope imaging the capability of reconstruction is limited. The constraints come from the facts of limited field of view, significant noise and other additional factors, e.g. γ ray attenuation, scattering, etc., which makes the iterative methods more attractive because of the facility to model all those factors. Our study contributed to the iterative algorithm and mainly extended the maximum likelihood expectation maximization (MLEM). Before focusing on the MLEM method, this section will present a brief overview of several existing analytic and iterative methods.

2.3.1 Analytic methods

Analytic reconstruction technique intends to find the source distribution by a direct inversion of the projections. The image can be reconstructed from projections of a single scattering angle, or from the summation of projections over scattering angles. Several algorithms have been proposed since 1990. Cree and Bones [1994] presented two analytical algorithms based on integral transformation of a set of restricted cone-surface projection, only the γ rays scattered perpendicularly to the detectors are used. When the counting statistics are low the number of useful data is limited. This constraint was withdrawn in Maxim et al. [2009] by averaging the images reconstructed from each set of cone-surface projections defined by angles determined from the scattered γ ray with the detector. Since the useful data is augmented, the signal to noise ratio (SNR) is increased. Other methods that express the solution in terms of series expansion in spherical harmonics were proposed by Basko et al. [1998], Parra [2000], Tomitani and Hirasawa [2002] and Hirasawa and Tomitani [2003]. The cone surface projections are

transformed into plane projection by using spherical harmonic coordinates. An analytical inversion formula of Compton projections was first formulated by Basko et al. [1998] without considering the distribution of possible scattering angles. Then Parra [2000] developed a direct inversion from the full projections that cover all different scattering angles. Tomitani and Hirasawa [2002] proposed a practical analytical algorithm which is applicable to projection data for a limited range of scattering angles, the effect of the broadening of Compton scattering angle is not considered. The shortcoming of neglecting this uncertainty is that for low energy γ rays, the broadening of the Compton scattering angle can be very large, thus the reconstructed image will not have a satisfying spatial resolution. Then in Hirasawa and Tomitani [2003] authors developed an analytic method more adapted for low energy γ ray (approximately 150 keV) with the effect of broadening incorporated.

It was shown in Cree and Bones [1994] that an infinitely large planar detector offers a complete geometry, and the source can be perfectly reconstructed even from only events corresponding to cones with axes perpendicular to that plane. A method allowing to consider arbitrary axis directions was proposed in Maxim [2014], and the supplementary data is used for noise reduction. Despite some attempts to find a complete acquisition geometry and associated analytic reconstruction algorithms (Smith [2005], Kuchment and Terzioglu [2017], Palamodov [2017]), for the moment there is no realistic configuration guaranteeing complete data sets and perfect reconstruction. More recently, a new inversion formula for a weighted conical Radon transform modelling Compton camera data is developed in Maxim [2018].

Analytic reconstruction methods provide a direct mathematical solution and can be very fast compared to iterative methods. However, due to the limited capability of accurate modeling of emission and detection process, the reconstructed image often loses resolution and has high level of noise.

2.3.2 Iterative methods

Unlike the analytic methods, the iterative methods intend to approximate the solution by iteratively adapting the reconstruction to the measured projections. The first iterative reconstruction was proposed by Bracewell [1956] for radioastronomy and Gordon et al. [1970] for electron microscopy and X-ray photography. Iterative algorithms can be categorized in algebraic methods and statistical methods. The first class includes the algorithms like: the Algebraic Reconstruction Technique (ART) (Gordon et al. [1970], Knöös et al. [1986]), the Simulatenous Iterative Reconstruction Technique (SIRT) (Andersen and Kak [1984], Gilbert [1972]), and the iterative least-squares techniques. The second class includes algorithms with or without a priori information about the source, among which the MLEM (Shepp and Vardi [1982], Lange and Carson [1984], Wilderman et al. [2000], Sauve et al. [1999]) is one of the most used algorithms and ordered subset expectation maximization (OSEM) (Hudson and Larkin [1994]) as its variant. Alternative methods can be derived using Bayesian approach, e.g. Maximum A Posteriori (MAP) method (Lange and Carson [1984]), MAP-EM one step late (OSL) method (Green [1990]), Maximum Entropy (ME) method (Skilling et al. [1979]). In Andreyev et al. [2009] a different method is proposed by using a Stochastic Origin Ensemble (SOE) method based on Markov chain. The iterative methods are now carried out for PET and SPECT with sinogramed data, for CC imaging the iterative process is the same but the modeling of system matrix is different and the distribution of dose is reconstructed from list-mode data. The measurement space of CC is often much larger than that of PET or SPECT, which leads to a larger system matrix that cannot be stored and should be calculated in each iteration. The definition of system matrix and the modeling is detailed in the next chapter.

2.4 Simulation by Monte Carlo method

Monte Carlo simulation is a statistical sampling technique aiming to solve complex problems by generating stochastic experiments. This method assumed that the problem system can be expressed by several densities of probabilities driven from data fitting theory. Formally developed by Stan Ulma and Von Neumann in 1947 (Eckhardt [1987]), it is now widely used in physics, engineering, biology, artificial intelligence, etc. In the study of particle physics, this method is used for designing detectors, understanding their behavior and comparing experimental data to theory (Rogers [2006]). Among several other Monte Carlo codes, GEANT4 is a toolkit designed for the simulation of the passage of particles through matter using Monte Carlo methods, developed at CERN (European Organization for Nuclear Research). It involves a complex functionality, including physics models, geometry (the information of detectors), tracking (particle track through the matter including decays and interactions) and visualization. This section presents two Monte Carlo simulation toolkits based on the platform GEANT4 (GEometry ANd Tracking): MEGAlib (Medium Energy Gamma-ray Astronomy Library) and GATE (GEANT4 Application for Emission Tomography). We used these two simulation toolkits to generate the data employed in this thesis. In chapter 3 all the simulated data are generated by MEGAlib. The voxelized source data in chapter 4 are generated by GATE.

2.4.1 MEGAlib

MEGAlib is a set of software tools designed for simulation and analysis of the data of γ ray detectors. Originally developed by Zoglauer et al. [2009a] for astrophysics and expended in various domains such as medical imaging, environment monitoring, this toolkit comprises a set of necessary libraries for a complete data analysis chain, from data acquisition to image reconstruction. In our study the used programs are: Geomega, Cosima, Revan, Sivan.

Geomega

Geomega is the detector geometry package. The description of volume and materials are set in a *.geo file, the detector profile is set in a *.det file. The information of source is set in *.source file. The whole geometry is presented by a *.geo.setup file. The main reference for Geomega can be found in Zoglauer et al. [2009b].

Cosima

Cosima is a simulation tool based on the GEANT4. It produces an output *.sim file containing the pure hits, i.e. sequences of interactions in detectors without error. These events can be analyzed or transferred into interaction processes (Compton scattering, pair production, etc.) by the program Sivan and Revan.

Sivan

Sivan is one of the analysis programs for providing the event reconstruction from simulated data. It produces the ideal data from pure hits: no errors of energy or position are added. This program aims to determine responses and the maximum possible efficiency of an event reconstruction algorithm.

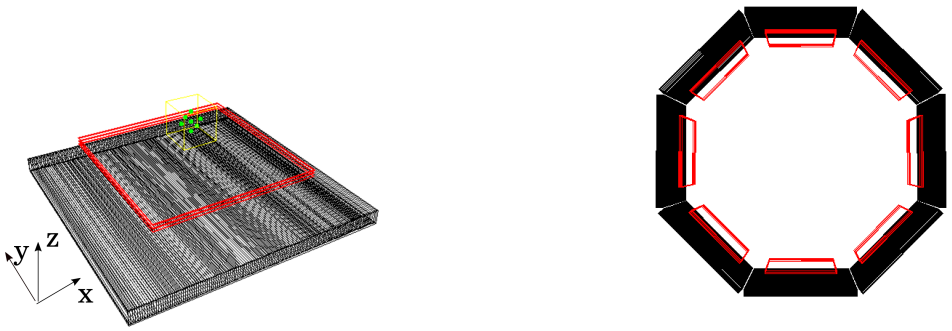

Figure 2.8: Geometry of CC composed of one single camera (left) and eight cameras (right). A source (green points) composed of seven point-like sources is positioned in front of the single camera. The reconstruction volume is indicated by the yellow cube.

Revan

Revan intends to provide a more realistic event reconstruction. It can transfer the events from pure hits to interaction processes, e.g. Compton, pair, etc. The uncertainties are introduced to the energy and position measurement according to the resolution of detector.

Mimrec

Mimrec is a reconstruction tool that can read the analyzed data and reconstruct the image of source by list-mode MLEM algorithm. Besides, Mimrec can also handle other analysis such as energy spectra, ARM resolution scatter-angle distribution, etc.

Simulation and reconstruction with MEGAlib

The interactive display of simulation geometry and reconstructed image is realized by ROOT's standard or openGL display. The figure 2.8 is a demonstration of two CC generated by the display of Geomega. The detail of the camera will be given in chapter 3 section 3.3.1.

A source composed of seven point-like sources emitted at 511 keV was simulated, the distance between two nearest neighbors was 3 cm. The center of the source was set 10 cm in front of the single camera. There were 2×10^6 photons emitted in total. After the analysis of Revan there were 39,636 triggered events (detected), among which the Compton event counts were 28,124. Figure 2.9 shows the energy spectrum and the Compton sequence reconstruction analyzed by Revan. Figure 2.10 is the reconstruction of images obtained and displayed by Mimrec.

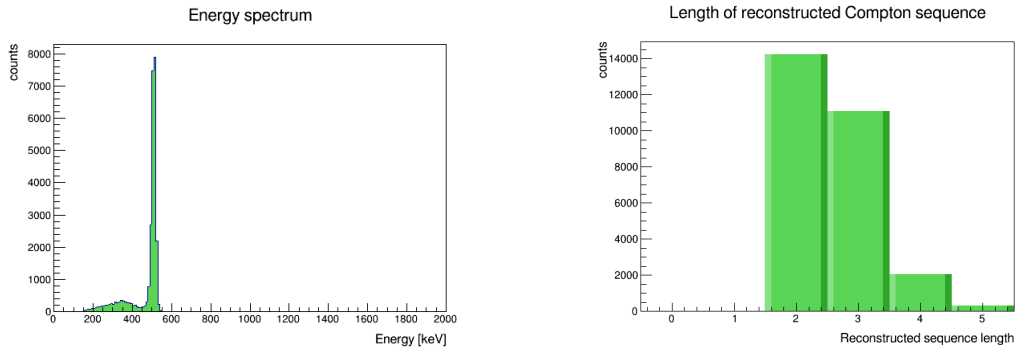

Figure 2.9: Energy spectrum and the reconstructed Compton sequence length, the length corresponds to the number of interactions in detectors.

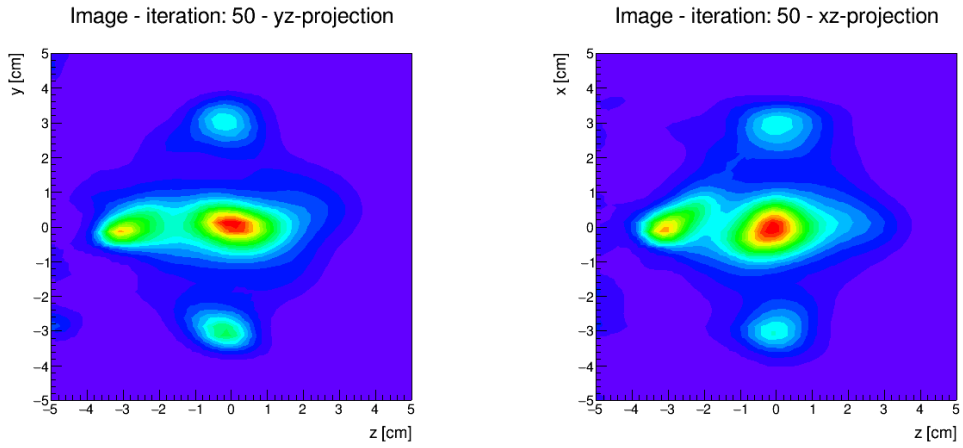

(a) Central slice on plane yz

(b) Central slice on plane xz

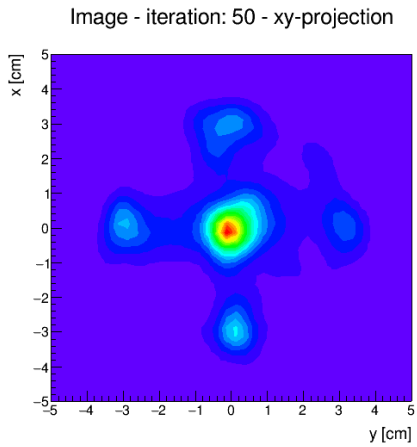

(c) Central slice on plane xy

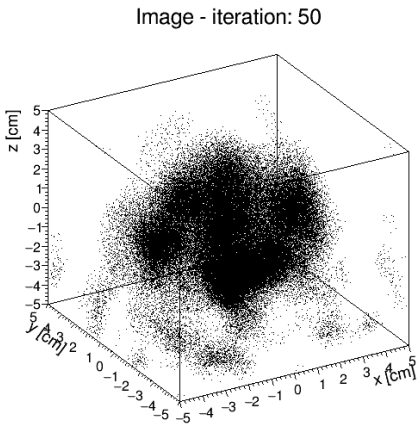

(d) 3D reconstruction

Figure 2.10: Reconstruction is obtained after 50 iterations from 2×10^6 simulated photons, after the analysis of Revan that leads to 39636 triggered events (detected), among which the Compton event counts are 28124. The simulated camera is placed on the plane xy.

2.4.2 GATE

GATE is an advanced open-source software developed by the international OpenGATE collaboration. Being designed for simulations in medical imaging and radiotherapy, it can handle the simulation of PET, SPECT, Computed Tomography (CT), Optical Imaging (Bioluminescence and Fluorescence) and Radiotherapy experiments. This toolkit contains the well-validated physics models in GEANT4, geometry description and visualization, and 3D rendering tools with original features specific to emission tomography. Like in MEGAlib, user needs to define the sources and the geometry of scanner and phantom, set up the physics processes and the detector model. Unlike the module Sivan in MEGAlib, where the detector is ideal but the energy uncertainties caused by Doppler broadening are modeled, GATE can reject the Doppler broadening by physics list 'emstandard'. The ideal detector with Doppler broadening can be selected by physics list 'emstandard_opt4'. Figures in 2.11 show some examples of simulation in GATE.

In this thesis the Compton camera module in GATE is used in chapter 4, the version is developed by Etxebeste et al. [2019]. This new version is validated against experimental data obtained by MACACO prototype built at IFIC in Valencia (Muñoz et al. [2017]). The interest of this new module in GATE is that one can compare the performance of different CC imaging systems under the same analysis in medical experimental setting. The simulated data of GATE in chapter 4 was generated by ideal mode with ideal detector: the measurement is supposed to be perfect without uncertainties.

2.5 Conclusion

We present the creation of γ ray during the radionuclide imaging and hadron therapy. Several common photon interactions that might occur during the γ detection are summarized. We also describe the two main imaging modalities in nuclear medicine: PET and SPECT, among which the CC is proposed as a new option for γ ray cameras. We summarize several existing prototypes of CC and illustrate some of the most used algorithms for reconstruction. The Monte Carlo simulation toolkits we employed in this study are also introduced. In the next chapter we will present the list-mode MLEM algorithm for reconstruction of CC imaging.

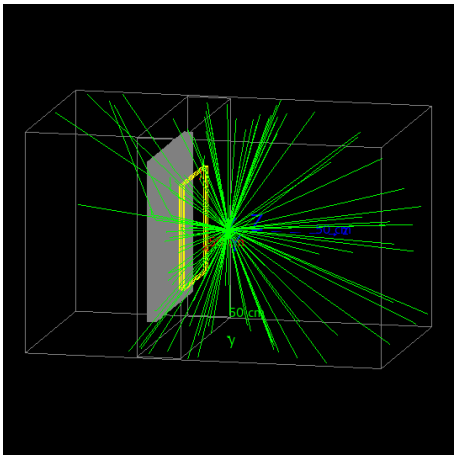

(a) An isotropic source is set in front of a double layers CC. The green lines indicate the γ ray emitted from the source, the number of events emitted is 100. The simulated source is composed of seven point-like sources at 511 keV.

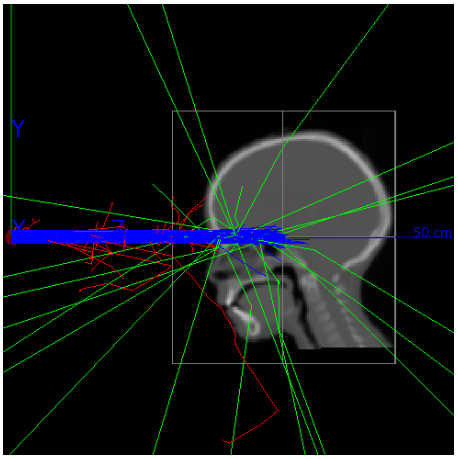

(b) A simplified simulation of proton therapy. The pencil beam emits proton at 100 MeV to the patient. The used physic list is QGSP_BERT_EMV. The high energy interactions create exited nuclei passing to the precompound model modeling the nuclear de-excitation.

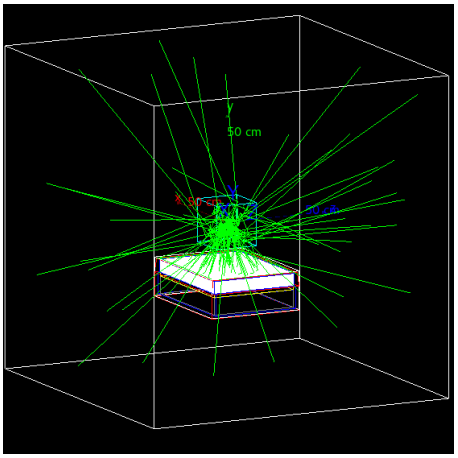

(c) A simplified simulation of a SPECT acquisition by a collimated camera. The emitted isotope is ^{111}I, the two emitted energies are 171 keV and 245 keV. The simulated phantom is water.

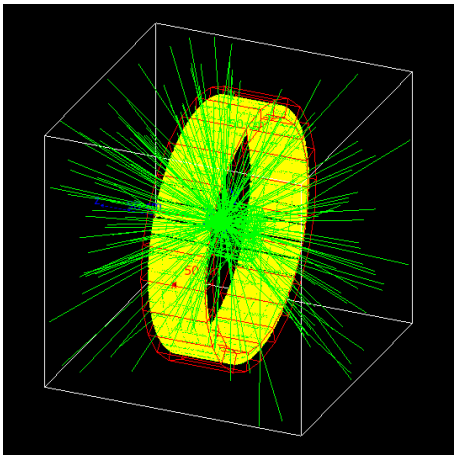

(d) A simplified simulation of PET acquisition. The camera is composed of a 46x4 crystal block as a ring. Each crystal block contains 12x12 crystal. The phantom is a water cylinder. The source is in the cylinder, not centered.

Figure 2.11: Illustrations of simulations in GATE.

Part III

MLEM reconstruction

Résumé en français

L'algorithme MLEM en mode liste

Nous considérons ci-après que le volume contenant la source des photons est divisé en voxels indexés sur $j = 1, \ldots, J$. Le nombre de photons émis par le voxel j est noté x_j. Nous échantillonnons l'espace de données par $i = 1, \ldots, I$ et nous notons y_i le nombre de photons détectés en i. t_{ij} représente la probabilité qu'un photon émis par un voxel j soit détecté en i,

$$t_{ij} = P(\text{detecté en } i \mid \text{émis par } j).$$

Si le nombre de photons émis par la source est suffisamment grand, l'équation linéaire $Tx = y$ est valable approximativement, avec $T = (t_{ij})_{1 \leq i \leq I, 1 \leq j \leq J}$ la matrice de transfert ou la matrice système. En pratique, le nombre de photons émis est souvent trop faible et cette équation n'est vérifiée qu'en moyenne. Avec λ le vecteur des moyennes des x_i et μ le vecteur des moyennes des y_i, nous avons

$$T\lambda = \mu.$$

Trouver le nombre de particules émises dans un voxel n'est pas possible, et les méthodes de reconstruction ont pour but d'estimer sa moyenne (MLEM, Lange and Carson [1984], Wilderman et al. [2000], Sauve et al. [1999]) ou de déterminer sa distribution a posteriori (SOE Andreyev et al. [2009]). Résoudre le problème précédent serait une tâche simple si μ était connu.

Cependant, seulement les y_i sont connus. L'émission radioactive suit une distribution de Poisson, par conséquent nous pouvons supposer que $y_i \sim \mathcal{P}(\mu_i)$, avec la densité de probabilité :

$$p(y_i) = e^{-\mu_i} \frac{\mu_i^{y_i}}{y_i!}.$$

A partir de là, la fonction de vraisemblance des données mesurées est la suivante :

$$L(Y|\lambda) = \prod_i p(y_i|\mu_i) = \prod_i e^{-\mu_i} \frac{\mu_i^{y_i}}{y_i!}.$$

Le vecteur inconnu λ (la solution de $T\lambda = \mu$) peut alors être déterminé en maximisant la fonction de vraisemblance, ou de façon équivalente :

$$\ln(L(Y|\lambda)) = \sum_i \left[-\sum_j t_{ij}\lambda_j + y_i \ln(\sum_j t_{ij}\lambda_j) - \ln(y_i!) \right].$$

Ce problème d'optimisation peut être résolu classiquement en déterminant les zéros du gradient car le logarithme de la vraisemblance est une fonction concave. Les conditions Karush-Kuhn-Tuker (KKT) qui imposent la positivité du λ_j peuvent être ajoutées. Enfin, la solution du maximum vérifie :

$$\widehat{\lambda}_j = \frac{\widehat{\lambda}_j}{\sum_i t_{ij}} \sum_i \frac{t_{ij} y_i}{\sum_k t_{ik} \widehat{\lambda}_k}.$$

Cependant, cette expression n'est pas très utile pour la détermination des intensités moyennes d'émission λ. Un algorithme numérique doit être utilisé pour résoudre le maximum de vraisemblance. La descente du gradient n'assure pas la positivité de la solution. Une meilleure approche consiste à appliquer l'algorithme de maximisation de l'espérance (EM) de Dempster et al. [1977].

L'estimation itérative de maximum de logarithme de vraisemblance à partir d'observations incomplètes par l'algorithme EM a d'abord été proposée par Dempster et al. [1977] puis adaptée à la tomographie par Shepp and Vardi [1982], Lange and Carson [1984]. Il a été adapté plus tard pour les données en mode liste dans Snyder and Politte [1983] et Wilderman et al. [1998].

On appellera Y le vecteur de mesures incomplètes, et X le vecteur de l'émission complète non observable. Avec x_{ij} comme le nombre de photons émis dans le voxel j et détectés dans l'index i, nous avons $t_{ij}\lambda_j$ la valeur moyenne de x_{ij}, $y_i = \sum\limits_j x_{ij}$. L'expression de la log-vraisemblance pour un ensemble de données complet devient :

$$\ln(L(X|\lambda)) = \sum_i \sum_j \left[x_{ij}\ln(t_{ij}\lambda_j) - t_{ij}\lambda_j - \ln(x_{ij}!)\right].$$

Suivant Lange and Carson [1984], l'étape (**E**) de l'algorithme EM consiste à calculer l'espérance conditionnelle de la log-vraisemblance par rapport aux données mesurées après renouvellement de $\ln(t_{ij}\lambda_j)$:

$$E(\ln(L(X|\lambda))|Y, \widehat{\lambda}^{(l)}) = \sum_i \sum_j (-t_{ij}\lambda_j + E(x_{ij}|y_i, \widehat{\lambda}^{(l)})\ln(t_{ij}\lambda_j)) + \text{constante}$$

où :

$$E(x_{ij}|y_i, \widehat{\lambda}^{(l)}) = \frac{t_{ij}\widehat{\lambda_j}^{(l)}}{\sum\limits_k t_{ik}\widehat{\lambda_k}^{(l)}} y_i$$

Le but de l'étape (**M**) est de trouver le $\widehat{\lambda}^{(l+1)}$ estimé qui maximise l'espérance $E(\ln(L(X|\lambda))|Y, \widehat{\lambda}^{(l)})$. Prendre les dérivées de cette espérance conduit à :

$$\frac{\partial E}{\partial \lambda_j} = -\sum_i t_{ij} + \frac{1}{\lambda_j}\sum_i \frac{t_{ij}\widehat{\lambda_j}^{(l)}}{\sum\limits_k t_{ik}\widehat{\lambda_k}^{(l)}} y_i = 0$$

qui mène finalement à la formule MLEM :

$$\widehat{\lambda}_j^{(l+1)} = \frac{\widehat{\lambda}_j^{(l)}}{s_j}\sum_i \frac{t_{ij}y_i}{\sum\limits_k t_{ik}\widehat{\lambda_k}^{(l)}}$$

où $s_j = \sum\limits_i t_{ij}$ est la sensibilité de détection, qui est la probabilité de détection pour un photon émis par le voxel j.

Pour les données en mode liste (LM), un échantillonnage très fin de l'espace de données conduit à mesure au plus un photon par classe. Nous avons alors $y_i = 1$ si un photon a été détecté en i, et $y_i = 0$ sinon. Les t_{ij} sont calculés uniquement dans l'espace de données détectés I. Puisque T est souvent une grande matrice qui ne peut pas être stockée et doit être calculée à chaque itération, le mode liste peut aider à réduire le coût du calcul. Nous avons $s_j = \sum_{I+\overline{I}} t_{ij}$, le $\overline{I}$ indique l'espace des évènements non réalisés. La valeur de s_j ne peut plus être calculée par la somme des t_{ij} car en mode liste t_{ij} sont calculés uniquement en I.

La formule LM-MLEM peut être exprimée comme :

$$\widehat{\lambda}_j^{(l+1)} = \frac{\widehat{\lambda}_j^{(l)}}{s_j} \sum_{i \in I} \frac{t_{ij}}{\sum\limits_k t_{ik} \widehat{\lambda}_k^{(l)}}$$

Modèle de l'imagerie par la caméra Compton

Comme mentionné précédemment, une caméra Compton est composée de deux détecteurs : le diffuseur et l'absorbeur. Une coïncidence Compton, ou un évènement Compton, se produit lorsqu'un photon émis par la source subit plusieurs interactions, parmi lesquelles au moins une interaction doit être la diffusion Compton. On note E_1 l'énergie déposée lors de la première diffusion Compton. Cette énergie peut également être notée E_e, avec e correspondant au fait que l'énergie est transférée à l'électron. L'angle β de diffusion Compton peut être calculé à partir de E_1 par :

$$\cos\beta = 1 - \frac{E_1 m_e c^2}{E_0(E_0 - E_1)}$$

Pour estimer β par cette equation, l'énergie initiale du photon E_0 doit être connue, ou au moins estimée par l'énergie totale déposée dans le détecteur. E_0 est notée E_γ dans le chapitre précédent. Nous ne présentons pas ici les évènements comportant trois interactions ou plus, dont il n'y a pas besoin de connaître l'énergie initiale : l'angle de diffusion peut être déduit à partir de l'information sur l'énergie et la position des interactions (Aprile et al. [2008], Boggs and Jean [2000], Kroeger et al. [2002], Ortega et al. [2015]).

Les positions de la première et de la deuxième interaction sont notées V_1 et V_2. Nous pouvons déduire que le photon a été émis quelque part sur la surface d'un cône $\mathscr{C}(V_1, V_2, \beta)$ avec le sommet V_1, l'axe de direction $\overrightarrow{V_2V_1}$ et le demi-angle d'ouverture β. Le modèle de projection conique est montré dans la figure 3.1. Cette forme conique apparaît alors dans la définition de la probabilité définissant les éléments dans la matrice du système t_{ij} dans la section 3.1. Notant qu'avec des incertitudes énergétiques considérées, la surface conique devient une coque. L'épaisseur et la consistance interne de la coque dépendent du modèle des incertitudes.

Dans les sections qui suivent, nous rappelons quelques-unes des formules trouvées dans la littérature sur le calcul du vecteur de sensibilité et de la matrice du système, puis nous nous concentrons sur la description des incertitudes d'énergie. Nous avons divisé ces dernières en deux classes selon la cause : l'effet Doppler inévitable, qui est lié au fait que la diffusion se produit sur un électron en mouvement ; et les incertitudes de mesure dues à la résolution imparfaite des détecteurs. La résolution imparfaite des détecteurs entraînera non seulement les incertitudes énergétiques, mais aussi des incertitudes spatiales. En outre, d'autres incertitudes peuvent également être introduites en raison de plusieurs effets physiques tels que la diffusion, l'atténuation, etc. Pour traiter les artefacts causés par des incertitudes autres que l'effet Doppler, nous proposons d'appliquer des méthodes pour récupérer la résolution des images, utilisant la deconvolution de la PSF et la régularisation.

Méthodes de calcul du vecteur de sensibilité

La sensibilité représente la probabilité qu'un photon émis par un volume soit détecté par la caméra. Le vecteur de sensibilité contient la valeur de cette probabilité pour chaque voxel du volume à reconstruire.

Une séquence d'évènements aléatoires doit être réalisée pour qu'un photon soit détecté par la caméra. Tout d'abord, le photon doit être émis dans l'angle solide sous-tendu par le diffu-

seur à la position de la source. Ensuite le photon a une probabilité de diffuser au moins une fois quelque part à l'intérieur du détecteur ou de quitter le diffuseur sans avoir été absorbé. L'angle sous lequel le photon est dévié est régi par la formule Klein-Nishina. Le photon qui s'est échappé du diffuseur a une certaine probabilité d'être dirigé vers l'absorbeur et d'interagir avec celui-ci. Avec une certaine probabilité, cette interaction se produit et est l'absorption du photon. D'autres évènements aléatoires peuvent survenir et peuvent compliquer encore l'évaluation de cette probabilité. La meilleure option peut-être de calculer la sensibilité par la simulation Monte-Carlo ou par l'acquisition réelle. Ceci peut être fait une seule fois pour une configuration de volume de reconstruction et réutilisé pour toutes les reconstructions d'images. Dans notre cas, comme pendant cette thèse nous devons souvent changer la géométrie de la caméra et la configuration du volume de reconstruction, nous avons besoin d'une méthode pour l'évaluer rapidement et les méthodes analytiques semblent les plus appropriées. Cependant, elles demandent des simplifications drastiques du modèle et doivent être comparées aux simulations de Monte Carlo.

Les méthodes de calcul de la sensibilité étudiées dans cette section sont résumées dans le tableau 3.1. Nous avons testé la validité de ces modèles de calcul de sensibilité à l'aide de simulations de Monte Carlo pour trois et six diffuseurs. Les géométries de simulation sont montrées dans la figure 3.3.

L'estimation de la matrice du système

Un élément t_{ij} dans la matrice du système représente la probabilité qu'un photon émis avec une énergie E_0 par le voxel v_j soit détecté comme évènement e_i. V_1 et V_2 présentent la position de la première et de la deuxième position, et E_1, E_2 présentent les première et seconde énergies enregistrées par les détecteurs. Nous supposons ici la relation $E_0 = E_1 + E_2$. À une énergie E_0 donnée, avec V_1, V_2, E_1 et E_2 connus, la probabilité qu'un photon émis par le centre M du voxel v_j soit détecté comme e_i peut être représentée comme $t_{ij} = P(V_1, E_1, V_2, E_2|M)$ et peut être calculée comme le produit de plusieurs probabilités. Les processus considérés pendant la détection sont présentés en figure 3.8. Les estimations de ces probabilités et les formules de calcul de la matrice du système ont été proposées dans la littérature et ils sont résumées dans le tableau 3.2. En dehors de ces processus d'autres processus peuvent également se produire, tels que la diffusion de Rayleigh, la retro-diffusion et la diffusion de Molière.

Le calcul de la matrice du système est toujours un problème dans l'imagerie par la caméra Compton pour plusieurs raisons. La première est que les phénomènes physiques à décrire sont beaucoup plus complexe qu'en TEP ou TEMP, surtout si l'on considère les interactions multiples d'un photon. La seconde est que le temps de calcul pour un cône de réponse est plus long que pour une ligne de réponse. Des simplifications drastiques des formules précédentes peuvent ainsi être vues dans la littérature. Et enfin, la recherche d'une meilleure modélisation est largement motivée par le fait que la modélisation ait relativement de faibles performances et des artefacts fréquents, par exemple l'allongement de reconstruction dans le sens vertical de l'axe de la caméra, des intensités différentes pour des sources identiques, etc. Dans ce chapitre, nous avons testé plusieurs modèles de la matrice du système et de la sensibilité. Notre objectif était d'identifier les facteurs qui influencent le plus la reconstruction et de trouver un compromis entre finesse de la modélisation et effort de calcul. Nous avons remarqué que la forme du noyau décrivant les incertitudes sur les énergies mesurées a une influence considérable sur les résultats. Nous discutons la forme de ce noyau pour deux types d'incertitudes, l'effet Doppler et les incertitudes dues au détecteur.

L'effet Doppler et son influence sur l'angle de diffusion

Le but de cette section est de montrer qu'une modélisation plus précise de l'effet Doppler a une influence déterminante sur la qualité de l'image reconstruite. L'effet Doppler est présenté pour la première fois par Christian Doppler en 1842. Il décrit le changement de fréquence ou de longueur d'onde d'une source d'ondes perçu par un observateur en mouvement. Dans Du Mond [1929], l'élargissement Doppler a été mesuré pour la distribution de la ligne des spectres de Compton. Dans la pratique, cet effet est inévitable et entraînera des incertitudes sur la mesure des énergies. Les incertitudes sur l'énergie affecteront donc la valeur calculée de l'angle de diffusion β. Dans cette section nous appelons cette valeur β_{energy}. Dans la pratique, l'énergie E_1 enregistrée est généralement associée à certaines incertitudes dues à la résolution énergétique limitée du détecteur. De plus, l'énergie déposée est également affectée par l'effet Doppler. Ces incertitudes signifient que la mesure E_1 ne correspond pas à l'angle de diffusion réel β mais à un angle de diffusion plus large autour de l'angle β. Pour modéliser ces incertitudes, plusieurs auteurs ont proposé d'utiliser la distribution gaussienne, comme dans Maxim et al. [2016], Muñoz et al. [2018], ou la distribution de Von-Mises, presque sous une forme gaussienne comme dans Sauve et al. [1999].

Les facteurs qui influencent le plus l'élargissement Doppler sont le matériau du détecteur et l'énergie du photon émis. Notre objectif est d'améliorer le modèle de la distribution gaussienne simple pour l'effet Doppler en silicium à 511 keV monoénergétique. L'étude de cette section est basée sur la simulation de Monte Carlo d'une source ponctuelle. La caméra simulée est composée d'un diffuseur à trois couches en silicium et d'un absorbeur en $LaBr_3$. Nous avons d'abord simulé une source ponctuelle de photons à 511 keV à 10 cm de la caméra. Les évènements ont été obtenus par le détecteur idéal. Seulement l'effet Doppler a été ajouté pendant la simulation. Nous n'avons simulé qu'une seule source ponctuelle, donc la position initiale M est fixe et connue. L'information exacte de la position de diffusion et d'absorption permet d'obtenir la vraie valeur de l'angle β_{geo} par le produit scalaire exprimé comme suit :

$$\cos(\beta_{geo}) = \frac{\overrightarrow{MV_1}.\overrightarrow{V_1V_2}}{|MV_1||V_1V_2|}$$

La résolution angulaire de la mesure (RAM) pour une observation (un évènement) i est calculée par :

$$\Delta\beta_i = \beta_i^{\text{geo}} - \beta_i^{\text{energy}},$$

La figure 3.11 montre la résolution angulaire de la mesure (RAM) pour la diffusion Compton de photons de 200 keV dans le silicium, sans sélection de l'angle de diffusion. Les données sont tirées de la thèse de A. Zoglauer [2005] et sont basées sur des simulations. D'après la figure 3.11 nous pouvons dire que le profil a un pic abrupt et une queue longue. Un modèle plus adapté pour l'effet Doppler pourrait être un mélange de cinq Gaussiennes avec des écart-types différents, correspondant aux sous-couches 1s, 2s, 2p, 3s, 3p. Ainsi le modèle gaussien simple ou la distribution de Von-Mises proche d'une Gaussienne ne sont pas bien adaptés. Ida et al. [2018] ont appliqué un modèle de gaussiennes mixtes précises spécifiques à leur matériau détecteur (Ge). Ce modèle est notre référence. En raison du coût du calcul, nous n'avons adapté qu'une combinaison de deux distributions gaussiennes à l'effet Doppler du silicium. Cela permet déjà d'observer une amélioration de la qualité de l'image reconstruite.

Incertitudes liées aux détecteurs réalistes

Cette section a pour but de montrer que, pour des données plus réalistes, les incertitudes causées par l'effet Doppler ont peu d'effet par rapport aux autres erreurs de mesure. Le modélisation précise de l'effet Doppler ne suffit plus. Pour la même simulation comme dans la section précédente, nous analysons maintenant les données plus réalistes générées par le module Revan de MEGAlib, ce qui permet d'ajouter des incertitudes énergétiques plus réalistes.

Résultat et conclusion

Nous avons simulé sept sources ponctuelles émettant simultanément des photons à 511 keV. Il s'agit d'évènements enregistrées un par un, les coïncidences aléatoires ne sont pas prises en compte. La source a été placée comme en figure 3.19, situé sur (0, 0, 0), (0, 0, 3), (0, 0, -3), (0, 3, 0), (0, -3, 0), (0, -3, 0), (3, 0, 0), (-3, 0, 0). Nous montrons les coupes centrales du résultat de la reconstruction dans la direction parallèle et orthogonale à la caméra. Le volume de reconstruction avait $(10.25 \times 10.25 \times 10.25)$ cm^3 divisé en $(41 \times 41 \times 41)$ voxels, les résultats sont obtenus avec 20000 évènements. Un résumé pour comparer l'influence de différents modèles de sensibilité et d'élargissement Doppler est illustré en figure 3.20. Pour plus de détails en 1D, le profil central de (b) et (d) dans la direction orthogonale à la caméra est représenté en figure 3.21.

Suivant des méthodes testées sur les données simulées par le détecteur idéal, on pourrait conclure que pour le modèle des incertitudes causées par l'effet Doppler, le modèle gaussien mixte améliorera la résolution de l'image reconstruite, par rapport à celle d'une distribution gaussienne simple. En outre, parmi les méthodes d'estimation de la matrice de sensibilité présentées, M_1 est la plus adaptée. La correction de l'intensité de l'objet reconstruit par la sensibilité la plus adaptée sera évidente si la résolution de la reconstruction est améliorée par le modèle de matrice de système. Ce résultat est accepté par la MIC 2019.

Nous avons aussi comparé la reconstruction à partir de données simulées par le détecteur idéal avec la reconstruction à partir de données plus réalistes générées par le module Revan dans MEGAlib. Ces dernières contiennent non seulement de l'effet Doppler, mais aussi les incertitudes causées par la mesure. La figure à gauche en 3.22 présente les coupes centrales de reconstruction à partir de données réalistes, la méthode utilisée pour la sensibilité est M_1 et le modèle utilisé pour les incertitudes énergétiques est une distribution gaussienne, avec écart-type estimé par des données réalistes. En comparant des résultats obtenus après 50 itérations aux résultats obtenus après 200 itérations, la reconstruction ne pourra pas converger vers la vérité terrain. Nous proposons de corriger les artefacts de reconstruction causés par les incertitudes de mesure dans le domaine spatial, avec la régularisation TV et la déconvolution PSF. Les méthodes seront présentées dans le prochain chapitre.

Chapter 3

MLEM implementation for Compton camera imaging

This chapter introduces the different mathematical models used in the list-mode MLEM reconstruction by four parts. The first part describes the list-mode MLEM algorithm. The second part analyzes different methods for calculating the sensitivity matrix. The third part presents some probabilistic models for the system matrix estimation. The fourth part investigates sources of uncertainties on the scattering angle and investigates models for Doppler broadening. At the end of this chapter we will investigate the validity of the different models with some reconstruction results obtained from ideal detectors. The intention of this chapter is to demonstrate that the modeling can have an obvious influence on the artifacts in the reconstruction result for ideal detectors. A combination of an accurate sensitivity estimation method and an accurate system matrix modeling has been proven effective to reduce artifacts. More realistic data are also investigated and the unsatisfactory results give us the motivation to investigate the image recovery methods in spatial domain, which will be further studied in the next chapter.

3.1 The list-mode MLEM algorithm

We consider hereafter that the volume containing the source of photons is divided in voxels indexed on $j = 1, \ldots, J$. We denote x_j the number of photons emitted from voxel j. We also sample the data space of measured events in bins indexed on $i = 1, \ldots, I$ and we denote y_i the number of photons detected in bin i. Denote t_{ij} the probability of a photon emitted from voxel j to be detected in bin i,

$$t_{ij} = P(\text{detected in } i \mid \text{emitted from } j). \tag{3.1}$$

Let Y denote the incomplete measurement vector, X the non observable complete emission. If the number of photons emitted by the source is sufficiently large, the linear equation $TX = Y$ approximately holds, with $T = (t_{ij})_{1 \leq i \leq I, 1 \leq j \leq J}$ the transfer matrix or system matrix. In practice, the number of emitted photons is too low and this equation holds only on average. We denote λ the vector of the averages of the x_i and μ the vector of the averages of the y_i:

$$T\lambda = \mu. \tag{3.2}$$

Finding the number of particles emitted in a voxel is not possible because not all the emissions can be detected, and the aim of the reconstruction methods is to estimate it in

average (MLEM) or to determine its posterior distribution (stochastic origin ensemble (SOE)). Now solving (3.2) would be a simple task if μ would be known.

However, only y_i is known, and they are modeled as the radioactive emission that follows a Poisson distribution. Thus $y_i \sim \mathcal{P}(\mu_i)$, with the density of probability:

$$p(y_i|\mu_i) = e^{-\mu_i}\frac{\mu_i^{y_i}}{y_i!}. \tag{3.3}$$

Since then, the likelihood function of the measured data is:

$$L(Y|\lambda) = \prod_{\mathbf{i}} p(y_i|\mu_i) = \prod_{\mathbf{i}} e^{-\mu_i}\frac{\mu_i^{y_i}}{y_i!}, \tag{3.4}$$

with λ and μ related through (3.2). The unknown vector λ can then be determined by maximizing the likelihood function, or equivalently its logarithm:

$$\ln(L(Y|\lambda)) = \sum_i \left[-\sum_j t_{ij}\lambda_j + y_i \ln(\sum_j t_{ij}\lambda_j) - \ln(y_i!)\right]. \tag{3.5}$$

This optimization problem can be classically solved by determining the zeroes of the gradient as the log-likelihood is concave. The Karush-Kuhn-Tuker (KKT) conditions accounting for the positivity of the λ_j can be added. Finally, the solution of the maximum verifies:

$$\widehat{\lambda}_j = \frac{\widehat{\lambda}_j}{\sum_i t_{ij}} \sum_i \frac{t_{ij} y_i}{\sum_k t_{ik}\widehat{\lambda}_k}. \tag{3.6}$$

However, this expression is not very helpful for the determination of the mean emission intensities λ. A numerical algorithm has to be employed to solve for the maximum of the likelihood. The gradient descent does not insure the positivity of the solution. A better approach consists to apply the expectation-maximization (EM) algorithm from Dempster et al. [1977].

Expectation maximization

Iterative estimation of the maximum log-likelihood with an incomplete observation by the expectation maximization (EM) algorithm was first proposed by Dempster et al. [1977] and then was adapted to emission tomography by Shepp and Vardi [1982], Lange and Carson [1984]. It has been extended for list mode data in Snyder and Politte [1983] and to CC imaging by Wilderman et al. [1998].

Denote x_{ij} the non observable complete data, representing number of photons emitted in voxel j and detected in index i. We have $E(x_{ij}) = t_{ij}\lambda_j$ and $y_i = \sum_j x_{ij}$. The log-likelihood expression for a complete data set becomes:

$$\ln(L(X|\lambda)) = \sum_i \sum_j \left[-t_{ij}\lambda_j + x_{ij}\ln(t_{ij}\lambda_j) - \ln(x_{ij}!)\right]. \tag{3.7}$$

Following Lange and Carson [1984], the (**E**) step of the EM algorithm consists to calculate the conditional expectation of the log-likelihood with respect to the measured data after renewal of λ:

$$E(\ln(L(X|\lambda))|Y, \widehat{\lambda}^{(l)}) = \sum_i \sum_j (-t_{ij}\lambda_j + E(x_{ij}|y_i, \widehat{\lambda}^{(l)})\ln(t_{ij}\lambda_j)) + \text{constant}, \tag{3.8}$$

where

$$E(x_{ij}|y_i, \widehat{\lambda}^{(l)}) = \frac{t_{ij}\widehat{\lambda_j}^{(l)} y_i}{\sum_k t_{ik}\widehat{\lambda_k}^{(l)}}. \tag{3.9}$$

The aim of the (**M**) step is to find the estimated $\widehat{\lambda}^{(l+1)}$ which maximizes the expectation ((3.8)). Taking the derivatives of expression ((3.8)) leads to:

$$\frac{\partial E}{\partial \lambda_j} = -\sum_i t_{ij} + \frac{1}{\lambda_j}\sum_i \frac{t_{ij}\widehat{\lambda_j}^{(l)}}{\sum\limits_k t_{ik}\widehat{\lambda_k}^{(l)}} y_i = 0, \tag{3.10}$$

which finally leads to the MLEM formula refers to sinogramed data:

$$\widehat{\lambda}_j^{(l+1)} = \frac{\widehat{\lambda}_j^{(l)}}{s_j}\sum_i \frac{t_{ij} y_i}{\sum\limits_k t_{ik}\widehat{\lambda_k}^{(l)}}, \tag{3.11}$$

where $s_j = \sum\limits_i t_{ij}$ is the so-called sensitivity of detection, i corresponds to a specific measurement element.

For list-mode data where the data space is highly sampled, we have $y_i = 1$ for an event detected, and $y_i = 0$ for no event detected. The t_{ij}s are calculated only in the detected data space I. Since T is often a large matrix that cannot be stored: for i events detected and j voxels of reconstructed volume, the size of T is $I \times J$. Thus T has to be calculated at each iteration and list mode can help to reduce the computation cost. We have $s_j = \sum_{I\cup\overline{I}} t_{ij}$, the $\overline{I}$ denotes the data space of not measured events. The value of s_j can no longer be calculated by the summation of the t_{ij}s for in list mode t_{ij} are calculated only in I. The list-mode (LM) MLEM formula can be expressed as:

$$\widehat{\lambda}_j^{(l+1)} = \frac{\widehat{\lambda}_j^{(l)}}{s_j}\sum_{i\in I} \frac{t_{ij}}{\sum\limits_k t_{ik}\widehat{\lambda}_k^{(l)}} \tag{3.12}$$

3.2 Model for the Compton camera

As mentioned before, a CC is composed of two detectors: the scatterer and the absorber. A Compton coincidence, or event, happens when a photon emitted by the source undergoes several interactions, among which at least one interaction must be Compton scattering. The energy deposited during the first Compton scattering recorded as E_1 allows to calculate the Compton scattering angle β by equation (3.13). This energy is also noted as E_e in the former chapter, e corresponds to the fact that the energy is transferred to electron. The equation (3.13) will appear several times in this chapter for readers convenience. To estimate β by this equation, the initial energy of the photon E_0 needs to be known, or at least estimated as the total energy deposited in the detection. E_0 is noted as E_γ in the former chapter. We do not present here the events with three or more interactions, which do not require to estimate the initial energy, but can deduce the scattering angle from the energy and position information about interactions (Aprile et al. [2008], Boggs and Jean [2000], Kroeger et al. [2002], Ortega et al. [2015]).

$$\cos\beta = 1 - \frac{E_1 m_e c^2}{E_0(E_0 - E_1)} \tag{3.13}$$

The positions of the first and second interaction are recorded as V_1 and V_2. It can be deduced that the photon was emitted somewhere on the surface of the cone $\mathscr{C}(V_1, V_2, \beta)$ with apex V_1, axis direction $\overrightarrow{V_2V_1}$ and half-opening angle β. Figure 3.1 is the illustration of the conical projection model.

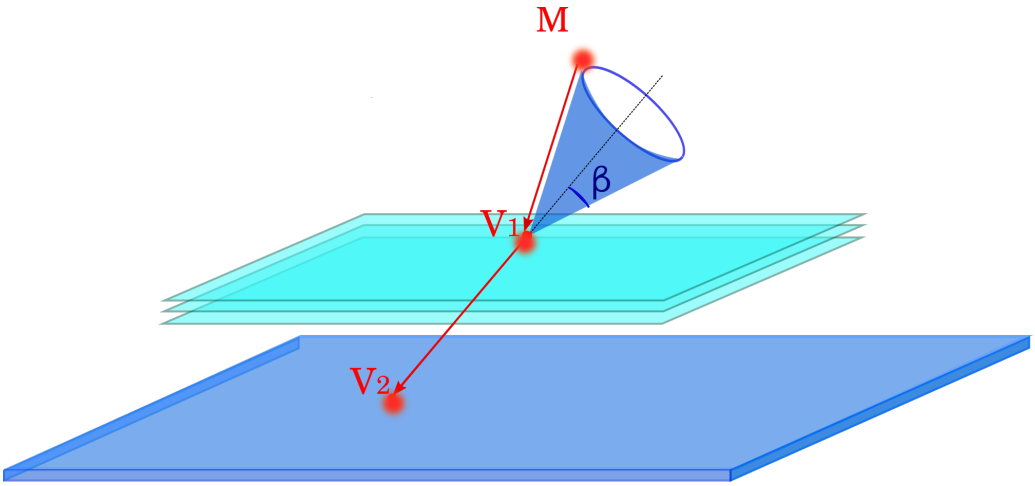

Figure 3.1: Illustration of the model for CC. The blue layer represents the absorber, the cyan layers represent the scatterers. M is the center of a voxel, V_1, V_2 are the positions of first and second interaction, β is the Compton scattering angle deduced from the detected energies.

This conical shape appears then in the definition of the probability defining the elements of the system matrix t_{ij} in section 3.1. Moreover, if the energy uncertainties are considered, the theoretic conical surface becomes a conical shell. The thickness and the internal consistency of the shell depend on the model of uncertainties.

In the following sections we recall some of the formulas provided in the literature for the calculation of sensitivity vector and system matrix, then we focus on the description of the energy uncertainties. We divided them into two classes by the cause: the unavoidable Doppler broadening that is related to the fact that the scattering occurs on a moving electron, and the measurement uncertainties caused by the imperfect resolution of the detectors. Except the energy uncertainties, the imperfect spatial resolution of detector will also leads to spatial uncertainties. Besides, other uncertainties may also be introduced due to several physical effects such as scattering, attenuation, etc. To deal with the artifacts caused by uncertainties other than Doppler broadening, we propose to apply some resolution recovery methods in image space.

3.3 Sensitivity estimation by analytic models

The probability of a photon emitted by some given volume to be detected by the camera is called sensitivity of detection. The term *volume* designates generally a voxel of a larger volume containing the source. A small voxel can be assimilated to a point. The sensitivity vector contains the value of this probability for each voxel of the volume to be reconstructed.

A sequence of random occurrences should be realized for a photon to be detected by the camera. First, the photon has to be emitted in the solid angle subtended by the scatterer at the source position. Then the photon has a probability to scatter at least once somewhere inside, probability is related to the thickness of media traveled by the photon, and to leave the scatterer without being absorbed. The angle at which the photon is deviated is governed by the Klein-Nishina cross-section. The photon that escaped from the scatterer has some probability to be directed towards the absorber and to interact with it. With some probability this interaction happens and refers to photo-absorption. Other occurrences may happen complicating even more the evaluation of this probability. The best option may be from then to calculate the sensitivity by Monte-Carlo simulation or by real acquisitions. This may be done once for a

given volume configuration and reused for all the image reconstructions. In our case, since in the development stage we need to change often the geometry of the camera and the volume configuration, we need a method to evaluate it rapidly and analytic methods seem the most appropriate. They need, however drastic simplifications of the model and have to be compared against Monte Carlo simulations.

Wilderman et al. [2001] made a pioneering study in the context of the MLEM algorithm for a camera composed of a single layer scatterer and an absorber. They proposed to calculate the sensitivity s_j for the j^{th} voxel as the sum over the K elements of the scatterer by

$$s_j \propto \sum_{k=1}^{K} \frac{\cos\theta_k}{l_{jk}^2} \left(1 - e^{-\mu d_{jk}}\right), \tag{3.14}$$

where the first factor stands for the solid angle subtended by the elementary detector k at the voxel j and the second factor is the probability of interaction in the scatterer. Here l_{jk} and θ_k are respectively the modulus and the polar angle of the vector connecting the center of the k^{th} elementary detector to the center of the j^{th} voxel, μ is the total cross-section in the scatterer and d_{jk} is the path length inside the scatterer along the ray from the center of voxel j to the center of the detector element k. For the notations see figure 3.2. For a camera that is small compared to the distance to the source, and only in this case, a good approximation is to reduce the sum to a single term (Maxim et al. [2016]).

The most general model we consider in this work is an extension of (3.14) where we also include a factor for the probability of the photon to passes through the previous layers without interaction. We assume that the probability of generating a Compton event is the same for all the photons once they were scattered somewhere. The sensitivity at some point $M(x_0, y_0, z_0)$ from the volume is then modeled as:

$$s(M) \propto \sum_{n=1}^{L} \int_a^b \int_c^d \frac{\cos\theta}{(x-x_0)^2 + (y-y_0)^2 + D^2} \left(1 - e^{-\mu_c d'}\right) e^{-(n-1)\mu_t d''} dydx, \tag{3.15}$$

with a, b, c, d the coordinates of detector (presented in figure 3.2) and L the number of layers. For simplicity, in the notations we omit the dependency of the angle θ and thickness d' on M and $N(x, y, z_0+D)$, and the dependency of D on M and n. The first factor accounts for the solid angle of the detector pixel seen from the (center of) the voxel, the second for the probability of interaction in the scattering layer and the last one accounts for the probability that the photon pass through the previous layers without interaction. The linear attenuation coefficients μ_c and μ_t stand respectively for Compton scattering and total attenuation, depending on the photon energy and the detector material. In the calculation they were set to 0.2, deduced from the data table in (Veigele [1973]). For silicon the density of element is $\rho = 2.32$ g/cm^3, the conversion factor for changing barns/atom to cm^2/g is 2.144^{-2}. The value $\mu_c = 0.2$ corresponds to an initial energy of photons of 511 keV and the Compton scattering factor $\mu_c/\rho = 4.04$ barns/atom, the value $\mu_t = 0.2$ corresponds to an initial energy of photon of 511 keV and the mass attenuation coefficient $\mu_t/\rho = 4.08$ barns/atom.

The numerical evaluation of (3.15) is relatively time consuming (order of minutes) but can be calculated once and saved on the disk. As the value $\mu_c d'$ is close to zero, we replaced the factor $1 - e^{-\mu_c d'}$ with its first order approximation $\mu_c d' = \mu_c \delta / cos\theta$, with $\delta = 0.2$ cm the thickness of the scattering layer. We note hereafter $M1$ this sensitivity model, calculated from:

$$s(M) \propto \int_a^b \int_c^d \frac{1}{(x-x_0)^2 + (y-y_0)^2 + D^2} e^{-(n-1)\mu_t d''} dydx, \tag{3.16}$$

proportionality factors are ignored.

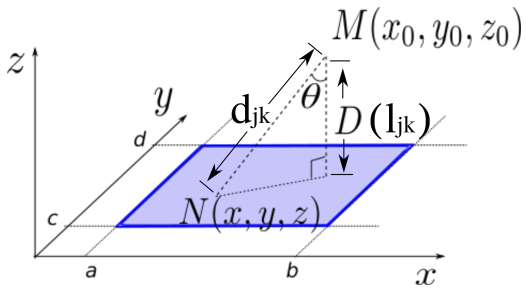

Figure 3.2: Scheme representing a point M from the volume and a scatterer layer (blue rectangle), with coordinates $x \in [a, b]$ and $y \in [c, d]$. The sensitivity is calculated at M, and N is a running point from the detector.

We also test some simpler versions. If we neglect the probability of absorption in the previous layers we get the model that we call $M2$, very similar to the one proposed in Wilderman et al. [2001], given as:

$$\begin{aligned} s(M) &\propto \int_a^b \int_c^d \frac{1}{(x-x_0)^2+(y-y_0)^2+D^2} dydx \\ &\propto \int_a^b \frac{1}{\sqrt{(x-x_0)^2+D^2}} \left(\text{atan}\left(\frac{d-y_0}{\sqrt{(x-x_0)^2+D^2}} \right) - \text{atan}\left(\frac{c-y_0}{\sqrt{(x-x_0)^2+D^2}} \right) \right) dx. \end{aligned} \tag{3.17}$$

This modification provides an important reduction of the computing time. If we neglect all the coefficients related to attenuation in (3.15) we obtain the model $M3$ defined as

$$\begin{aligned} s(M) &\propto \int_a^b \int_c^d \frac{\cos\theta}{(x-x_0)^2+(y-y_0)^2+D^2} dydx \\ &\propto \int_a^b \int_c^d \frac{1}{\left((x-x_0)^2+(y-y_0)^2+D^2\right)^{3/2}} dydx \\ &\propto \text{atan}\left(\frac{(b-x_0)(d-y_0)/D}{\sqrt{(b-x_0)^2+(d-y_0)^2+D^2}} \right) - \text{atan}\left(\frac{(b-x_0)(c-y_0)/D}{\sqrt{(b-x_0)^2+(c-y_0)^2+D^2}} \right) \\ &\quad -\text{atan}\left(\frac{(a-x_0)(d-y_0)/D}{\sqrt{(a-x_0)^2+(d-y_0)^2+D^2}} \right) + \text{atan}\left(\frac{(a-x_0)(c-y_0)/D}{\sqrt{(a-x_0)^2+(c-y_0)^2+D^2}} \right) \end{aligned} \tag{3.18}$$

We added to the comparison the simple model from Maxim et al. [2016], that we call $M4$, although this model is not adapted to large cameras close to the source. $M4$ is defined as:

$$s(M_j) \propto \frac{|\cos\theta|}{d_{jk}^2}, \tag{3.19}$$

where M_j is the center of voxel j. The other variables are defined in figure 3.2, with N the center of the scatterer block.

The methods of sensitivity calculation studied in this section are summarized in table 3.1. Compared to other methods, the most precise method $M1$ is more accurate, but the exponential term will increase the computing time. $M2$ neglecting the total attenuation and $M3$ neglecting all the attenuation are simpler versions of $M1$ and are more adapted to geometry compared to $M4$. The factors related to attenuation in $M1$ and $M2$ are energy dependent. $M4$ is the most simple and most rapid method, but the difference between computing time of $M4$, $M3$ and $M2$ is not evident (in several seconds.)

Table 3.1: sensitivity calculation model

$M1$	exponential attenuation model (3.16)
$M2$	attenuation (3.17)
$M3$	without attenuation (3.18)
$M4$	block model Maxim et al. [2016]

Except the methods presented above, other models were proposed in the literature. A formula for the evaluation of the sensitivity that also includes the probabilities of interaction in the absorber is given in Sullivan et al. [2009]. The probabilities for a photon to travel from the source to the first hit and from the first hit to the absorber is not considered. Also, the authors consider only two-site events. In Schoene et al. [2017] authors propose a formula that takes the volumes of both scatterer and absorber, with adding an estimation of the photon energies. The imaging result was improved. A formula considering the solid angles and the linear attenuation in the first and second interactions for three or multiple site events was proposed by Muñoz et al. [2018].

3.3.1 Simulation geometry

We tested the validity of these sensitivity calculation models with Monte Carlo simulations for two scatterer configurations, namely three or six layers. The simulated geometries are demonstrated in figure 3.3. The camera is composed of silicon strip scatterers (512 strips on each face) and a segmented $LaBr_3$ absorber. The prototype with three scattering layers and one absorber is also used in the next chapter.

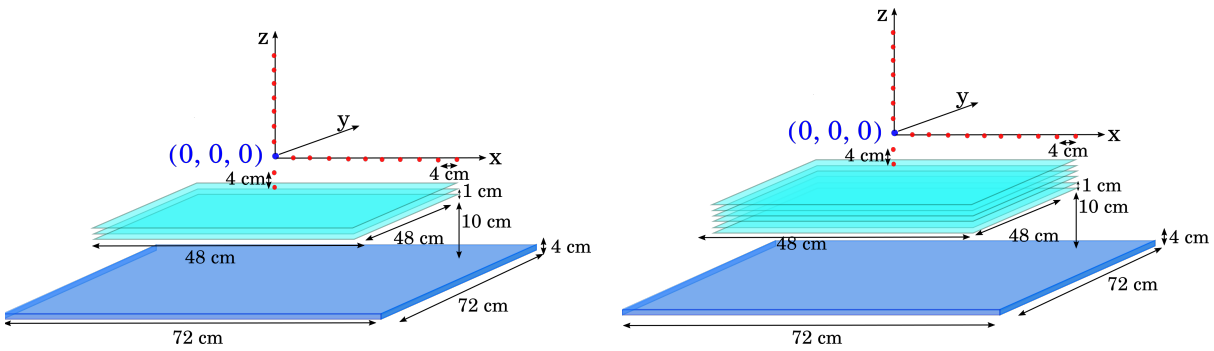

(a) 3 scatterers camera (b) 6 scatterers camera

Figure 3.3: The simulated geometry of 3 scattering layers (left) and 6 scattering layers (right), the closest layer was set 10 cm to the origin (0, 0, 0). The point sources were placed at different spatial positions, in the direction orthogonal to the camera (z axis) varying from (0, 0, -8) to (0, 0, 28), in the direction parallel to the camera (x axis) varying from (0, 0, 0) to (36, 0, 0). The distance between two neighbour sources was 4 cm.

A point-like source emitting $n = 2 \times 10^6$ photons with energy 511 keV was placed at different spatial positions chosen to realize a uniform sampling in the directions parallel to the camera (x axis) and orthogonal to it (z axis). The total number of considered positions was 20. The number of Compton events was recorded for each source simulated with ideal detectors (data generated by Sivan module in MEGAlib) and with realistic detectors (data generated by Revan module in MEGAlib). Only the uncertainties caused by Doppler broadening is considered in the simulation of ideal detectors. More realistic data were simulated adding Gaussian uncertainties

on the measured energies with $\sigma = 1$ keV for the scatterers and $\sigma = 11.4$ keV at 511 keV for the absorber. The position errors of realistic detectors are determined by the strip pitch (≈ 1 mm) and by the size of the crystals ($0.5 \times 0.5 \times 4$ cm^3).

3.3.2 Results and discussions

The red points in figure 3.4 represent the Compton event counts obtained from the emission in different position, which can also be taken as the detection efficiency. The lines in figure 3.4 provide the profile of methods $M1$ to $M4$.

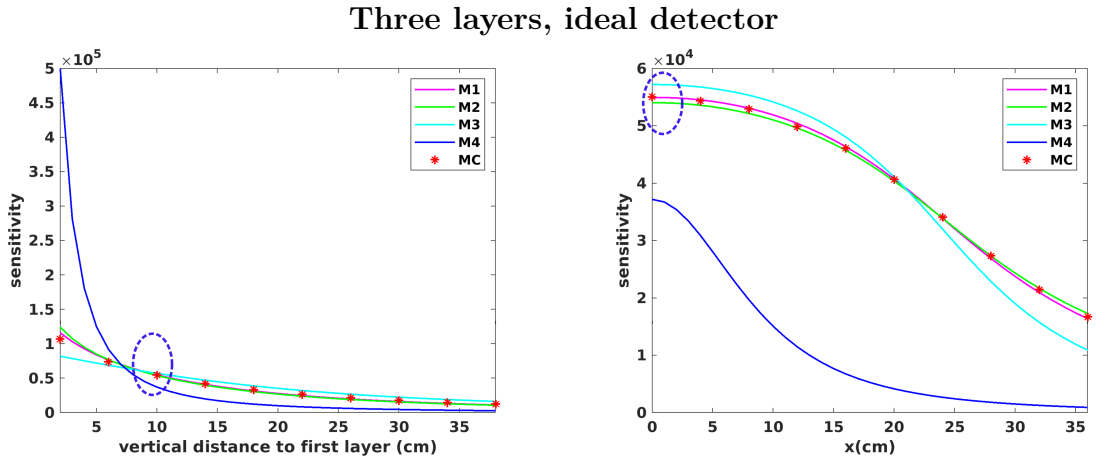

(a) Direction orthogonal to the camera (b) Direction parallel to the camera

Figure 3.4: Comparison of the sensitivity models for a camera composed of three layers (ideal detectors), the blue ellipse marks the origin (0, 0, 0).

The results for the two camera configurations, namely three or six layers, and for data simulated with ideal detectors are shown in figures 3.4 and 3.5. The upper layer is at $z = -10$ for all the figures. The values for $x = y = 0$ and $z \in [-8, 28]$ cm, giving a distance to the first layer in the range $[2, 38]$ cm, are plotted in (a). The values for $y = z = 0$ and $x \in [0, 36]$ are plotted in (b). The lines are normalized by first dividing the calculated value S_j by the sum of S_j, then multiplying it by the sum of the red points (total number of counts). One common point between the two plots was marked by a blue ellipse and corresponds to the source placed at (0, 0, 0).

Obviously the model $M4$ based on a solid angle approximation of a small-size detector is not adapted in our case. The model $M3$ also performs quite poorly. Models $M1$ and $M2$ give very similar results. The differences become visible as the number of layers increases where the model $M1$ slightly outperforms $M2$. Close to the camera the solid angle approximation is less valid and the fit is not as good as for further points. Increasing the sampling rate for the numerical integration has a small effect on the fitting quality close to the camera and has a sensible impact on the computing time. For a volume with $80 \times 80 \times 64$ voxels the calculation of sensitivity by $M1$ takes more than half an hour, while the other methods take only several seconds. Although based on some approximations, equation (3.16) is quite general and seems to cope reasonably well with the simulations.

The results for the two camera configurations, namely three or six layers, and for realistic data are shown in figures 3.6 and 3.7. Except for a diminution in the number of counts (for data simulated with realistic detector the efficiency is lower than for the ideal one), the plots are similar to the ideal case and the same conclusions may be drawn.

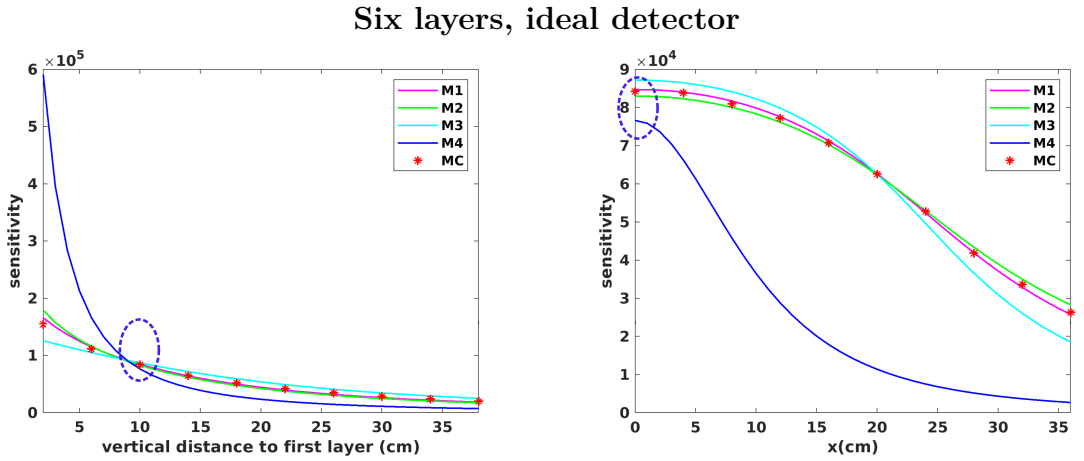

(a) Direction orthogonal to the camera (b) Direction parallel to the camera

Figure 3.5: Comparison of the sensitivity models for a camera composed of six layers (ideal detectors), the blue ellipse marks the origin (0, 0, 0).

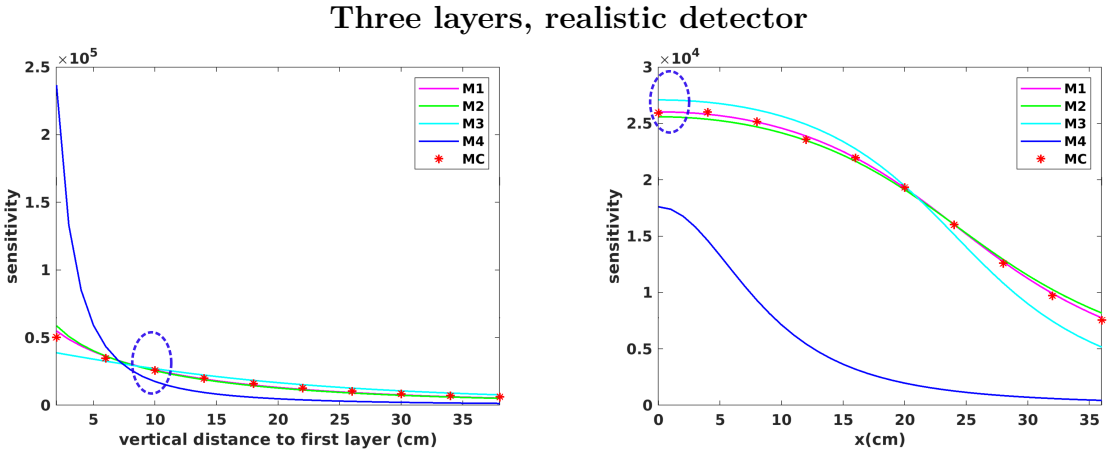

(a) Direction orthogonal to the camera (b) Direction parallel to the camera

Figure 3.6: Comparison of the sensitivity models for a camera composed of three layers (realistic detectors), the blue ellipse marks the origin (0, 0, 0).

This section investigates four different analytic methods for sensitivity matrix estimation. Although the most adapted method $M1$ needs more computation time, it can be calculated one time and saved for the following iterations. Besides, the estimated sensitivity vector can be stored for further use, as long as the CC does not change and stays in the same position regarding the field of view. Note that another way to calculate the sensitivity vector is to use $S = \sum_i t_{ij}$, since the sensitivity matrix represents the probability for a photon emitted from voxel j being detected by the camera. We propose to apply the analytic methods for estimating the sensitivity matrix. In the next section we will present the estimation methods for system matrix T.

3.4 System matrix estimation

The element t_{ij} in system matrix represents the probability for a photon emitted from voxel v_j (or from a point M) being detected as event e_i. Let V_1 and V_2 represent the position of first and second interactions, and E_1, E_2 represent the first and second energies recorded by the

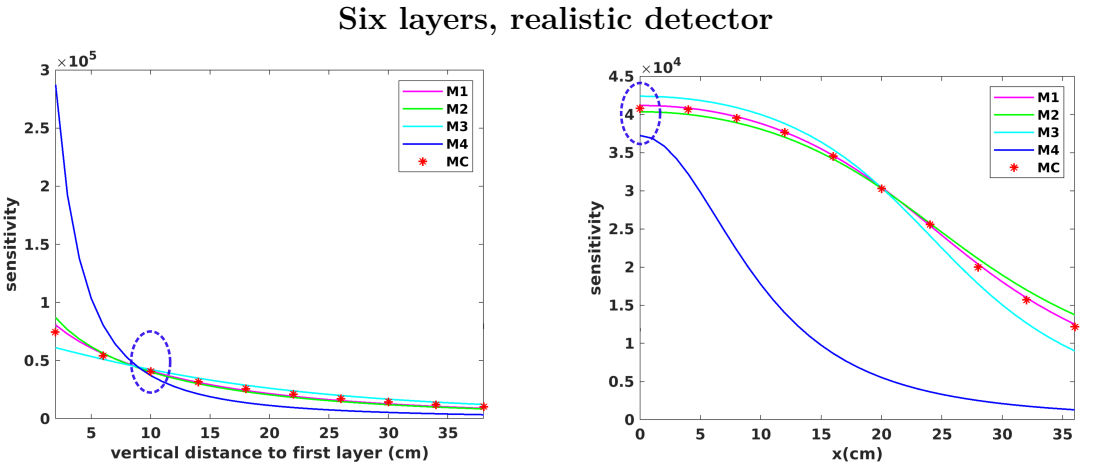

(a) Direction orthogonal to the camera (b) Direction parallel to the camera

Figure 3.7: Comparison of the sensitivity models for a camera composed of six layers (realistic detectors), the blue circle marks the origin (0, 0, 0).

detectors. Let E_e represent the energy transferred to the electron during the first interaction, and E'_γ represents the remaining γ photon energy. If we consider only two-site events, the second interaction should be a photo-electric absorption, the photon deposits all the remaining energy to the electron in the second interaction, thus we have $E'_\gamma = E_2$. Otherwise, if the event is three or multi-site, the second interaction will also be a Compton scattering, and the deposited energy E_2 will be smaller than E'_γ. Here we assume the relation $E_0 = E_1 + E_2$, the Compton scattering angle β can then be calculated by:

$$\begin{aligned} \cos\beta &= 1 - \frac{E_1 m_e c^2}{E_0(E_0 - E_1)} \\ &= 1 - \frac{E_1 m_e c^2}{(E_2 + E_1)E_2} \end{aligned} \tag{3.20}$$

At some given initial energy E_0, with V_1, V_2, E_1 and E_2 being known, the probability for a photon emitted from the center M of voxel v_j being detected as e_i can be represented as $t_{ij} = P(V_1, E_1, V_2, E_2|M)$ and can be calculated as the product of several probabilities. Figure 3.8 indicates the notations and the possible cases that may happen during the travel of a photon, where:

- P_1 is the probability that a photon emission takes place at voxel v_j,
- P_2 is the probability that the photon emitted from the position v_j reaches the position V_1,
- P_3 is the probability that the first interaction is a Compton scattering, this is where the Compton scattering process including the Doppler broadening occurs,
- P_4 is the probability that the photon reaches the position V_2,
- P_5 is the photo-electrical absorption probability in the second interaction,
- P_6 is the Compton scattering probability in the second interaction.

Except the cases considered in the figure 3.8, other possible processes may also happen, such as Rayleigh scattering, back scattering and Molière scattering.

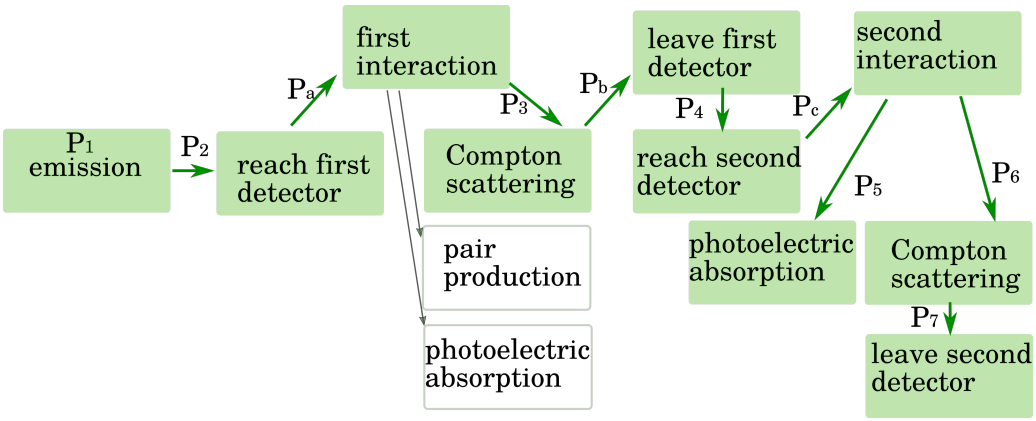

Figure 3.8: Detection process and the considered probabilities of different process (green blocks).

Estimations of these probabilities and formulas for the calculation of the system matrix have been proposed in the literature. With the notations indicated in figure 3.9, with only two-site events considered, Wilderman et al. [2000] suggest that:

$$P(V_1, V_2, E_1, E_2|M) = \frac{1}{8\pi^2}\frac{\mu_c}{\mu_t}\underbrace{(1-e^{-\mu_t d_1})}_{P_a}\underbrace{K(\beta, E_0)\delta(\beta_M - \beta)}_{P_3}\underbrace{e^{-\mu_t d}}_{P_b}\underbrace{(1-e^{-\mu_t d_2})}_{P_c} \times \underbrace{\frac{\cos\theta_m \cos\theta_g}{|\overrightarrow{V_1M}|^2|\overrightarrow{V_2V_1}|^2}}_{\text{solid angle}} \tag{3.21}$$

where:

- the solid angle factor gives the probability of the photon to reach an elementary surface, first at V_1 then at V_2,
- $K(\beta, E_0)$ is the Klein-Nishina cross section represents the probability for a photon with energy E_0 to undergo a Compton scattering with angle β,
- $\frac{\mu_C}{\mu_t}$ is the ratio of the Compton to total absorption cross section in the first detector.

Sauve et al. [1999] added a description of energy uncertainties taking the form of a von-Mises distribution. This model considers the emission points which are not on the cone, but close to its surface. Indeed, the scattering angle is often spread out due to physical process such as: multiple scattering, depth-dependent interactions and Doppler broadening. For narrow distributions, the von-Mises distribution can be approximated by a Gaussian. The advantage of the von-Mises distribution is that it depends on the cosine of the variable thus avoids calculation of arccos. On the opposite, the estimation of its parameters is more complicated. The factor

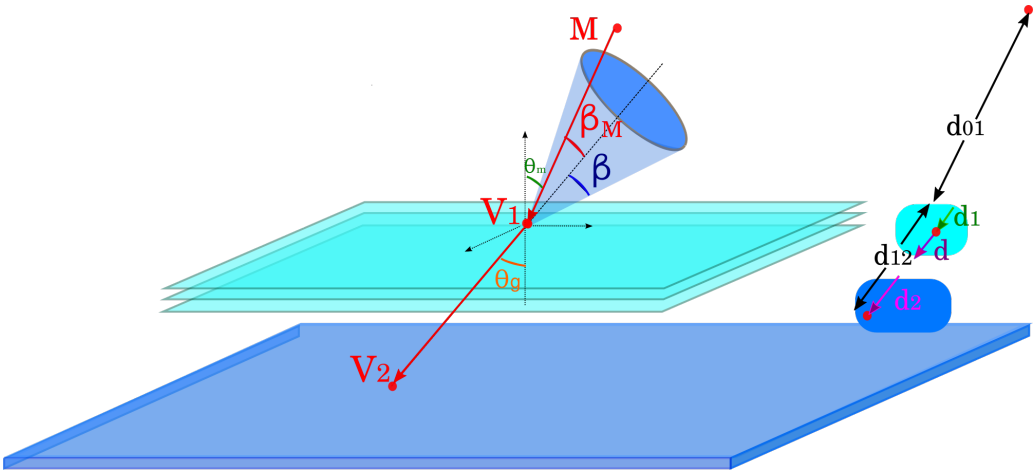

Figure 3.9: Illustration of parameters used for the probabilistic models.

$1/\sin\beta$ favours small Compton angles. The formula they proposed is:

$$P(V_1,V_2,E_1,E_2|M)=\frac{P_3\triangle E}{2\pi\sin\beta}\frac{\triangle S}{I_0(\eta)||\overrightarrow{V_2V_1}||^2}\underbrace{P(V_1|M)}_{P_2}\underbrace{P(E_1|V_1,M)}_{P_3}$$
$$\underbrace{\exp[-\eta(\cos\beta(1+\frac{(1-E_0/E_1)}{\tau})+\sin\beta\sqrt{1-(1+\frac{(1-E_0/E_1)}{\tau})^2})]}_{\text{energy uncertainties model}} \tag{3.22}$$

where:

- $\tau=\epsilon/511keV$ is the ratio of incident energy to electron rest mass,
- η is a factor proportional to the FWHM of the energy measurement, $I_0(\eta)$ is the Bessel function of the first kind of zero-th order,
- $\triangle E$ is the scattering detectors energy bin,
- $\triangle S$ is the projection of the detector cell surface element at location V_2 onto the plane perpendicular to vector $\overrightarrow{V_1M}$.

Xu and He [2007] proposed a method based on spectral deconvolution, considering two types of second interactions. Compared to the former two methods, here the solid angle is not taken into consideration.

If the second interaction is a photoelectric absorption, then we have $E_2=E_0-E_1$:

$$P(V_1,V_2,E_1,E_2|M)=\frac{1}{\sin\beta}\underbrace{e^{-\mu_{E_0}d_1}}_{\text{attenuation}}\underbrace{K(\beta,E_0)\frac{2\pi m_ec^2}{(E_0-E_1)^2}}_{P_3}\underbrace{e^{-\mu_{E_0-E_1}d}}_{P_b}$$
$$\times\underbrace{\frac{\sigma_p(E_2)}{\sqrt{2\pi(\sigma^2{}_{E_1}+\sigma^2{}_{E_2})}}e^{-\frac{(E_0-E_1-E_2)^2}{2(\sigma^2{}_{E_1}+\sigma^2{}_{E_2})}}}_{P_5} \tag{3.23}$$

and if the second interaction is a Compton scattering:

$$P(V_1,V_2,E_1,E_2|M) = \frac{1}{\sin\beta}\underbrace{e^{-\mu_{E_0}d_1}}_{\text{attenuation}}\underbrace{K(\beta,E_0)\frac{2\pi m_e c^2}{(E_0-E_1)^2}}_{P_3}\underbrace{e^{-\mu_{E_0-E_1}d}}_{P_b} \times \underbrace{K(\beta,E_0-E_1)\frac{2\pi m_e c^2}{(E_0-E_1-E_2)^2}}_{P_6}\underbrace{e^{-\mu_{E_0-(E_1-E_2)}d_2}}_{P_7} \tag{3.24}$$

Maxim et al. [2016] proposed a model which takes into account the energy uncertainties as a Gaussian distribution. Compared to the previous models, some factors (e.g. $\sin\beta$) that cancel in the MLEM reconstruction formula were withdrawn:

$$P(V_1,V_2,E_1,E_2|v_j) = \int_{M\in v_j}\underbrace{K(\beta,E_0)}_{P_3}\underbrace{\frac{\cos\theta_m\cos\theta_g}{|\overrightarrow{V_1M}|^2|\overrightarrow{V_2V_1}|^2}}_{\text{solid angles}}\overbrace{h(\beta_M|\beta,\sigma_\beta)}^{\text{energy uncertainties model}}\,dv. \tag{3.25}$$

The kernel h was taken as a Gaussian with mean the calculated value of the Compton angle and standard deviation evaluated according to the formula derived by Ordonez et al. [1997]:

$$\sigma_\beta = \frac{m_e c^2}{\sin\beta}\sqrt{\left(\frac{1}{{E_1}^2}-\frac{1}{{E_0}^2}\right)^2 d{E_1}^2 + \frac{d{E_2}^2}{{E_0}^4}}. \tag{3.26}$$

In the method proposed in Kishimoto et al. [2017] the elements of the system matrix are calculated as the following formula:

$$P(V_!,V_2,E_1,E_2|M) = \frac{1}{2\pi\sin\beta}\underbrace{\left(1-\frac{d_{01}}{\sqrt{d_{01}^2+a^2}}\right)}_{\text{solid angle}} \times \underbrace{exp\left(-\frac{1}{2}\left(\frac{\beta_M-\beta}{\sigma}\right)^2\right)}_{\text{energy uncertainties model}} \times \underbrace{f(E_1,E_2,\beta,d_1,d)}_{\text{reaction probability}}, \tag{3.27}$$

where:

- The formula of the solid angle can be approximated at small values as $1-\cos\delta \simeq \delta^2/2$. It stands for the solid angle of an element of volume at V_1.
- the energy uncertainties take a Gaussian form as in Maxim et al. [2016], the standard variance of the Gaussian is determined by the angular resolution of the detector material,
- the reaction probability of a photon is taken as

$$f(E_1,E_2,\beta,d_1,d) = \underbrace{exp(-\sigma_t(E_1+E_2)d_1)}_{P_aP_b}\underbrace{K(\beta,E_1+E_2)}_{P_3}\underbrace{exp(-\sigma_t(E_2)d)}_{P_c}\underbrace{\sigma_{p,C}}_{P_5}, \tag{3.28}$$

  The factor $f(E_1,E_2,\beta,d_1,d)$ gets canceled in the MLEM formula except for $exp(-\sigma_t(E1+E2)x_s) \approx 1$.

One of the most recent methods, proposed by Muñoz et al. [2018], is particularly well suited for using conventional ray-tracing techniques. Their considered probabilities are the same as in Sauve et al. [1999] but the energy uncertainties are modeled by a Gaussian kernel.

The above mentioned system matrix estimation methods are summarized in table 3.2.

Table 3.2: System matrix estimation model

Methods	**Doppler broadening uncertainties**
Wilderman et al. [2000]	neglected
Sauve et al. [1999]	von-Mises distribution
Xu and He [2007]	neglected
Maxim et al. [2016]	single Gaussian distribution
Kishimoto et al. [2017]	single Gaussian distribution
Muñoz et al. [2018]	single Gaussian distribution

As we can see from these examples, the system matrix calculation is still an issue in CC imaging, for several reasons. The first is that the physical phenomenon to describe are much more complicate than in PET or SPECT, especially if we consider multiple interactions of a single photon. The second is the computation time longer for a cone of response than for a line of response. Drastic simplifications of the previous formulas can thereby be seen in the literature. And finally, the research for a better modeling is largely motivated by the relatively low performances and frequent artifacts that are experimented with CC, e.g. reconstruction elongation in the vertical direction of the camera, different intensities for identical sources, etc..

In this chapter, we tested several models of system matrix and sensitivity vectors. Our purpose was to identify the factors that most influence the reconstruction in order to better focus on the modeling while preserving the model as simple as possible for balancing the fitness of modeling and the computational efforts. We noticed that the shape of the kernel describing the energy uncertainties has a considerable influence on the results. In the next section we will discuss Doppler broadening and the other uncertainties that affect the calculation of the scattering angle.

3.5 Influence of Doppler broadening on the scattering angle

The Doppler effect is a phenomenon first presented by Christian Doppler in 1842. It describes the change of frequencies or wavelengths of a wave source in relation to a moving observer. Due to the distribution of velocities of particles, Doppler effect will cause the broadening of spectral lines. In Du Mond [1929] the Doppler broadening was considered and measured for the distribution of Compton spectra line. In practice this effect is inevitable and will cause uncertainties in energies measurement. The uncertainties of energy will further affect the scattering angle β calculated by (3.20), in this section we call this value β_{energy}. In practice the recorded energy E_1 is usually associated with some uncertainties due to the limited energy resolution of detector. Besides, the deposited energy is also affected by Doppler broadening. This uncertainty means that the measured deposited energy E_1 does not correspond to the real scattering angle β but to a broaden angle of values around the angle β. To model this uncertainty, several authors proposed to use a Gaussian distribution, as in Maxim et al. [2016], Muñoz et al. [2018], or a Von-Mises distribution as in Sauve et al. [1999] nearly to a Gaussian form.

The purpose of this section is to show that a more accurate modeling of the Doppler broadening has a determinant influence on the quality of the reconstructed image. The goal is to ameliorate the simple Gaussian distribution model for Doppler broadening in silicon at mono-energy 511 keV. The investigation of this section is based on the Monte Carlo simulation of one

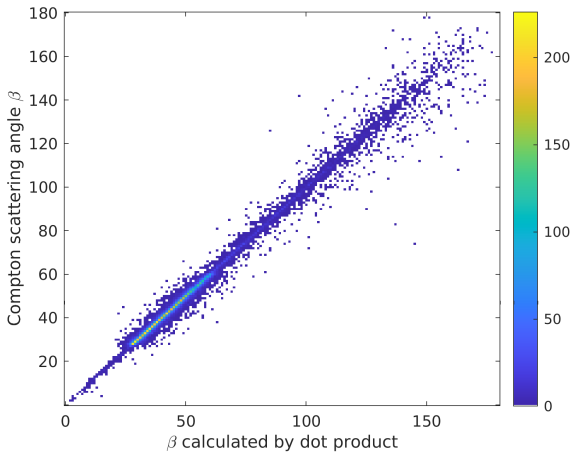

Figure 3.10: Uncertainties on Compton scattering angle for ideal detector, during the data analysis only the Doppler broadening was considered. The calculated value β_{energy} is plotted against the true value β_{geo}.

point source. The most important factors for Doppler broadening are the material of detector and the emitted photon energy. The simulated camera is composed by a three-layer scatterer made of silicon and one absorber made of $LaBr_3$. We first simulated a point source of 511 keV photons at (0, 0, 0), 10 cm to the first scattering layer of the simulated camera. The events were obtained by only adding the Doppler broadening during the simulation. We simulated just one point source so the emission position M is fixed and known, the exact scatter and absorption position information can be obtained by ideal detector. The measurement resolution of detector was considered ideal in simulation, thus there is no error on the interaction positions V_1 and V_2. The true scattering angle β_{geo} can then be deduced by the scalar product expressed in (3.29). The figure 3.10 shows the scattering angle calculated by using the energy information against the value obtained by using the exact position information. The number of considered events was nearly 20,000. This figure contains the events that first interact on the scatterers made with silicon, as well as the events first interacts on the absorber made with $LaBr_3$.

$$\cos(\beta_{geo}) = \frac{\overrightarrow{MV_1}.\overrightarrow{V_1V_2}}{|MV_1||V_1V_2|} \tag{3.29}$$

The angular resolution of measurement (ARM) for one observation (event) i is calculated by:

$$\Delta\beta_i = \beta_i^{\text{geo}} - \beta_i^{\text{energy}}, \tag{3.30}$$

this factor represents the distance between empirical and theoretical value. Figure 3.11 shows the ARM for Compton scattering of 200 keV photons in silicon, without scatter angle selection. The data is obtained from the thesis of A. Zoglauer [2005] and is based on simulations. From the figure 3.11 we can tell that the profile has a steep peak and a long tail. And a more adapted model for Doppler broadening might be a mixture of five Gaussian distributions with different standard deviation, corresponds to subshells 1s, 2s, 2p, 3s, 3p. Thus the Gaussian model (in Maxim et al. [2016] and Muñoz et al. [2018]) or the Von-Mises distribution not far from a Gaussian (Sauve et al. [1999]) are not well adapted. In order to approximate the long tails Ida et al. [2018] have applied a mixed Gaussian model and developed an accurate error distribution model specific to their detector material (Ge). This model is our reference. Due to the computation cost, we only adapted a combination of two Gaussian distributions to the Doppler broadening of silicon.

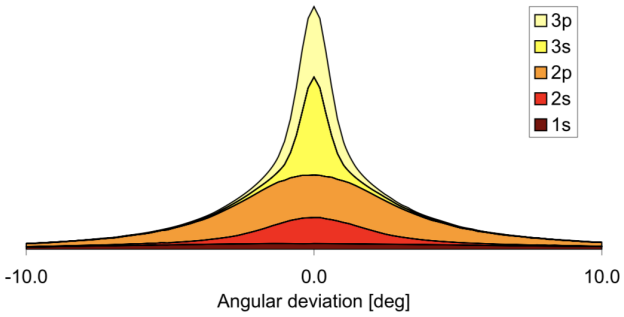

Figure 3.11: The profile of angular resolution measurement (ARM) for Compton scattering of 200 keV photons in silicon without scattering angle selections. During the simulation only Doppler broadening is considered, there is no uncertainty in energy and position measurement. The different areas represent the contributions of different shells of the silicon atom: in the outside shells, the electrons are less energetic and the distribution is sharper. This figure is obtained from A. Zoglauer [2005].

Table 3.3: FWHM of Doppler Broadening for different semiconductor materials, the data is obtained from A. Zoglauer [2005]

Material	200 keV [degree]	500 keV [degree]	1 MeV [degree]
Si	**1.8**	**0.80**	**0.40**
Ge	2.85	1.25	0.65
CdZnTe	3.50	1.55	0.85

The variance σ^2 of the dataset can be calculated from the sum of squares of ARM. If the ARM follows a Gaussian distribution the full width half maximum (FWHM) can be estimated from σ as FWHM $= 2.35\sigma$. Table 3.3 shows some FWHMs of Doppler broadening for different semiconductor materials, the data is obtained from A. Zoglauer [2005], for silicon the FWHM is 0.8° at 500 keV.

We separated the events in figure 3.10 by β_{geo} in bins of 1°. The set of events was partitioned in 180° in subsets $\mathscr{E}_k$. The subset $\mathscr{E}_k$ contains the events whose $\beta_{\text{geo}} \in [k-1, k[$ degrees. For each bin we calculated the standard deviation of the errors by:

$$\widehat{\sigma}_k = \sqrt{\frac{1}{\mathcal{I}_k}\sum_{i=1}^{\mathcal{I}_k}(\Delta\beta_i)^2} \tag{3.31}$$

where $\mathcal{I}_k$ is the number of events in subset $\mathscr{E}_k$. We assumed that the mean of ARM is zero.

Equation (3.26) allows to estimate the σ_β for each observation by the detected energy if the energies uncertainties are known. The Revan module in MEGAlib provides these uncertainties with more realistic detection measurement errors. We analysed the events with the uncertainties derived from the simulation setup by considering the detector measurement error, not only the Doppler broadening. As above for each 1° bin of exact scattering angle values β_{geo} we calculated the average value of the standard deviation by (3.26). We compared the σ_β calculated by (3.26) with the standard deviation of the data simulated with ideal detectors calculated by (3.31), the result is shown in figure 3.12. In this figure the uncertainties caused by Doppler broadening in different material are not distiguished: Doppler broadening exists either in the silicon or $LaBr_3$. The blue dots represent the standard deviation calculated from the data simulated with ideal

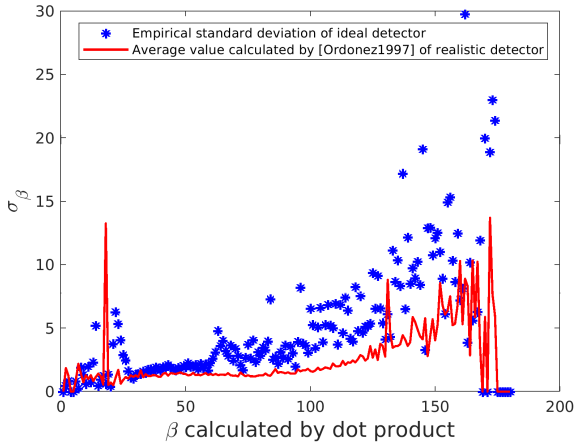

Figure 3.12: Standard deviation calculated from data simulated with ideal detectors (blue dots) and the σ_β calculated by the method proposed in Ordonez et al. [1997] obtained for realistic data simulated with realistic detectors. The standard deviation of β for data simulated with ideal detectors (uncertainties caused only by Doppler broadening) is as high as the one proposed for realistic data (uncertainties caused by Doppler broadening and the measurement resolution of detectors).

detectors, the bin of histogram was 1°, the red line is the average value of σ_β calculated from realistic data simulated with realistic detectors by method Ordonez et al. [1997]. The standard deviation for β larger than 170° is not presented for low counts reason. This figure proves that the Doppler broadening should not be neglected: the standard deviation of β for data simulated with ideal detectors is as high as the estimated σ_β for data simulated with realistic detectors, even if only the Doppler broadening was added. Furthermore, from figure 3.11 it can be noticed that the distribution of these uncertainties is not a simple Gaussian distribution, so the FWHMs from table 3.3 cannot be related to the standard deviation $\widehat{\sigma}_k$ with the factor 2.35.

We observed from figure 3.10 that the distribution of the uncertainties on β has different shapes which depend on the interval of the calculated scattering angle. This is mainly caused by the order of interactions with different material. To simplify we selected the events which only have 2 interactions and during the analysis of data simulated with ideal detectors we separated the events by the position of first interaction: first interaction occurring on the scattering detector, or occurring on the absorbing detector. If the first interaction occurs on the scatterers made of silicon, the ARM is mainly affected by the Doppler broadening in silicon, otherwise if the first interactions occurs on the absorber, the ARM reflects the Doppler broadening in $LaBr_3$. The Doppler induced uncertainties are then represented in figure 3.13 for the two materials. The colorbar in figures 3.13(a) and 3.13(b) represent the number of counts. For 4×10^5 counts the percentage of events that first interact in the absorber is only 2%, thus we concentrate on the Doppler broadening in silicon. Figure 3.13(a) also shows that for the events with first interaction on the scattering detector, the maximum value of β calculated by scalar product is 147°. This value can be explained by the simulation geometry and corresponds to the events that first interacted on the boundary of the first scattering layer and then were absorbed on the other side of the boundary of the absorbing layer, demonstrated in figure 3.14.

Figure 3.15 is a part of the histogram of ARM for photons emitted at 511 keV and interacting first on a silicon layer. The total considered counts are 20,000, the maximum of ARM is 57.1371° and the minimum is -53.9612°. The number of bins is 1440, each bin size is 0.077°. Figure 3.15 only shows a part of the histogram with the ARM range in $[-15°, 15°]$, the number of bins in figure 3.15 is 388.

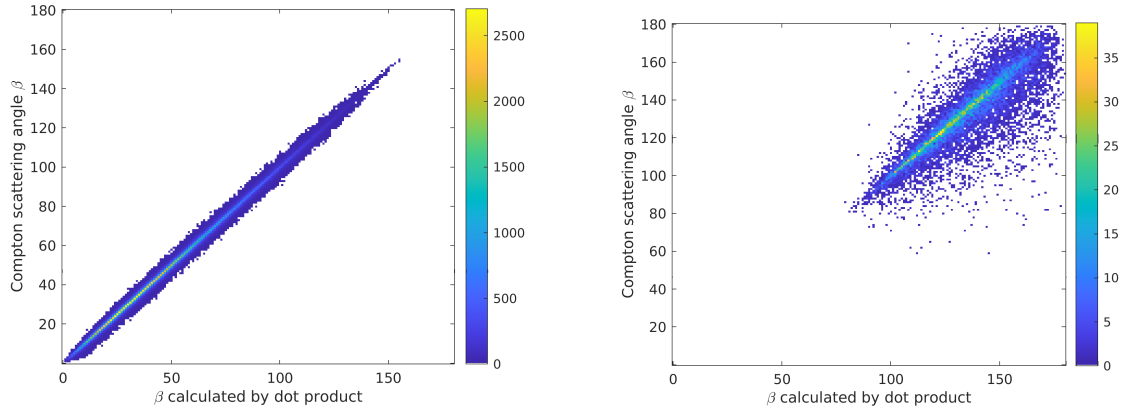

(a) First interaction occurs on the scatterers (sili- (b) First interaction occurs on the aborber ($LaBr_3$) con)

Figure 3.13: Uncertainties of Compton scattering angle for data simulated with ideal detector, the left plot is obtained from the events detected first by the scattering layers, the right plot is obtained by the events detected first by the absorber. The percentage of events in (b) is 2%.

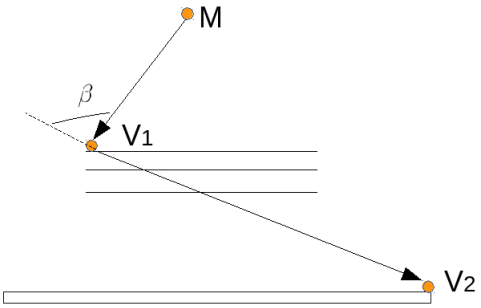

Figure 3.14: The maximum value of β deduced from the geometry of camera: the photon is emitted from position M and first interacts in the edge of the scatterer, then interacts in the edge of the absorber.

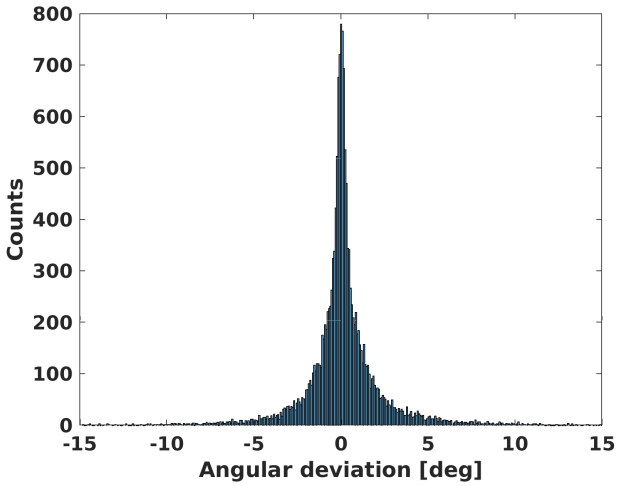

Figure 3.15: Histogram of ARM with the angular deviation range in $[-15°, 15°]$, the size of bin is 0.077°, the number of bins is 388. Events first scattered on silicon, source emitting at 511 keV.

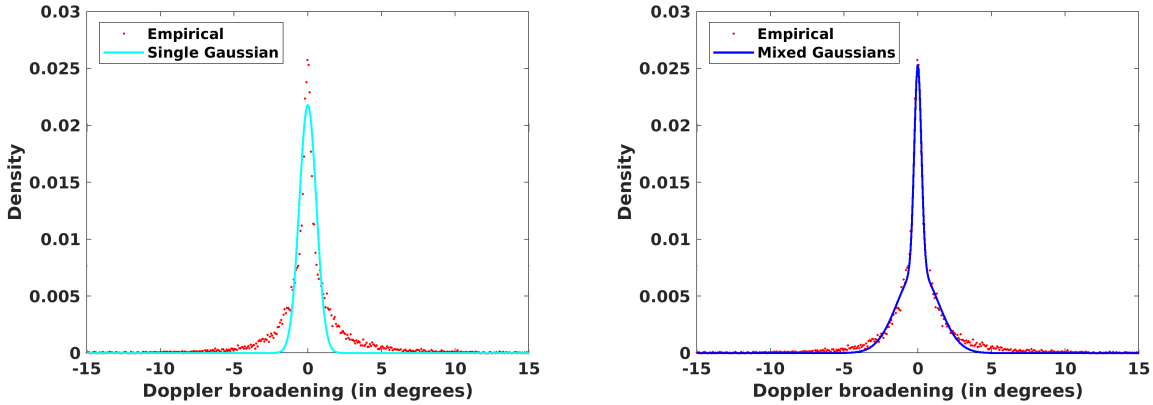

(a) Single Gaussian fit (b) Mixed Gaussian fit

Figure 3.16: Gaussian fitting of ARM distribution.

In order to fit the histogram of Doppler broadened ARM of silicon at 511 keV, we adjusted a Gaussian model:

$$g(\Delta\beta) = ke^{-\frac{\Delta\beta^2}{2\sigma^2}}, \tag{3.32}$$

and a combination of two Gaussian distributions:

$$g(\Delta\beta) = k_1 e^{-\frac{\Delta\beta^2}{2\sigma_1^2}} + k_2 e^{-\frac{\Delta\beta^2}{2\sigma_2^2}}. \tag{3.33}$$

Results are shown in figure 3.16. The dataset was the normalized histogram of ARM plotted in 3.15.

The uncertainties caused by Doppler broadening depend on the material of camera and the initial energy of photons. When the photon energy is low the uncertainties will be large. The initial position of source, however, has no evident influence on this type of uncertainties. As a proof we simulated four different sources. Figures in 3.17 show the results of fitting the model function to the angular uncertainties distribution. When the energy of the photons changes from 4 MeV to 511 keV, the FWHM of the ARM distribution changes as it can be seen when comparing the plots 3.17(a) and 3.17(b). When the position of the source changes, the shape of the distribution remains roughly the same, as shown by the plots 3.17(b), 3.17(c) and 3.17(d). The numerical values of the parameters k and σ are given in table 3.4 for the single Gaussian fit 3.32 and in table 3.5 for the Gaussian mixture fit 3.33. The parameters in table 3.4 and table 3.5 were found by using the matlab function *"optimoptions"*. The optimization was realized by solving the minimum difference between the dataset and the Gaussian model expressed in (3.32) and (3.33). The mean square error (MSE) is calculated by:

$$MSE = \frac{1}{N}\sum_{n=1}^{N}(g(\Delta\beta_n) - h(\Delta\beta_n))^2, \tag{3.34}$$

where $h(\Delta\beta, n)$ is the normalized value of the histogram of ARM, N is the number of bins (N = 1440).

Comparing table 3.4 and 3.5, the mixed Gaussian model reduces the MSE. In these two tables, the parameters we found for (b), (c) and (d) prove that Doppler broadening depends mainly on the energy. Compared to 511 keV, at high energy 4 MeV (a) Doppler broadening is reduced. Except 511 keV and 4 MeV we didn't investigate the other energy levels. One possible

Table 3.4: Parameters of single Gaussian fit

Plots in figure 3.17	(k,σ)		MSE
a	0.0503	0.1346	2.428e-06
b	0.0317	0.5438	1.5164e-06
c	0.0428	0.6097	2.0058e-06
d	0.0256	0.5699	1.1742e-06

Table 3.5: Parameters of mixed Gaussians fit

Plots in figure 3.17	(k_1,σ_1, k_2, σ_2)				MSE
a	0.0456	0.0621	0.0175	0.3490	1.1591e-07
b	0.0292	0.2350	0.0116	1.3424	2.1574e-08
c	0.0399	0.2497	0.0161	1.4675	3.3676e-08
d	0.0236	0.2335	0.0099	1.3215	2.3973e-08

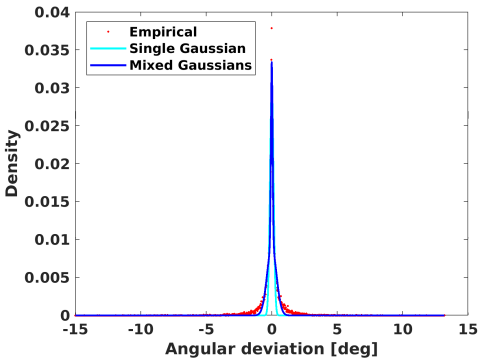

(a) source at (0, 0, 0), 10 cm to the camera, 4 MeV, FWHM= 0.5°

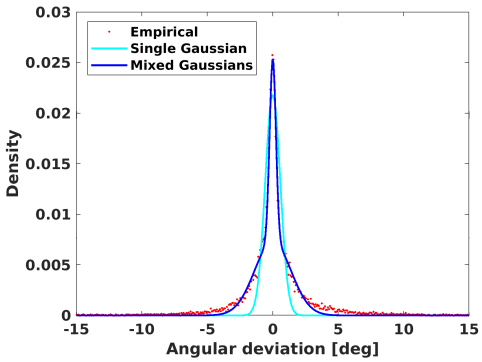

(b) source at (0, 0, 0), 10 cm to the camera, 511 keV, FWHM = 1°

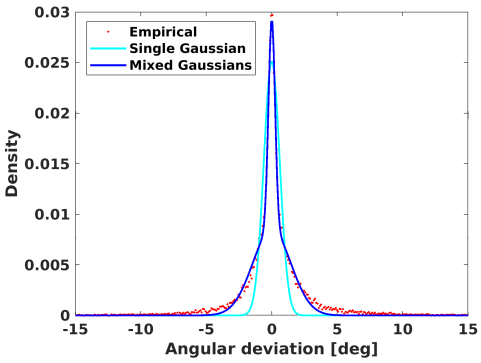

(c) source at (0, 0, -5), 5 cm to the camera, 511 keV, FWHM= 1°

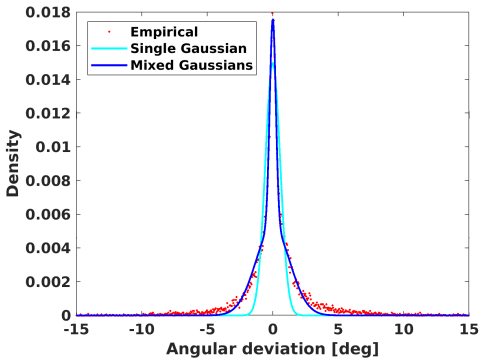

(d) source at (20, 20, 0), 10 cm to the camera, 511 keV, FWHM= 1°

Figure 3.17: Fitting model for the distribution of angular uncertainties due to the Doppler broadening, the uncertainties (red dot) are calculated by $\beta_{geo} - \beta_{energy}$, see table 3.4 and 3.5 for the parameters. The selected events first interacted on the scattering layer, then was absorbed by the absorber. The figures only show the adjustment with angular deviation in range [-15 °, 15°].

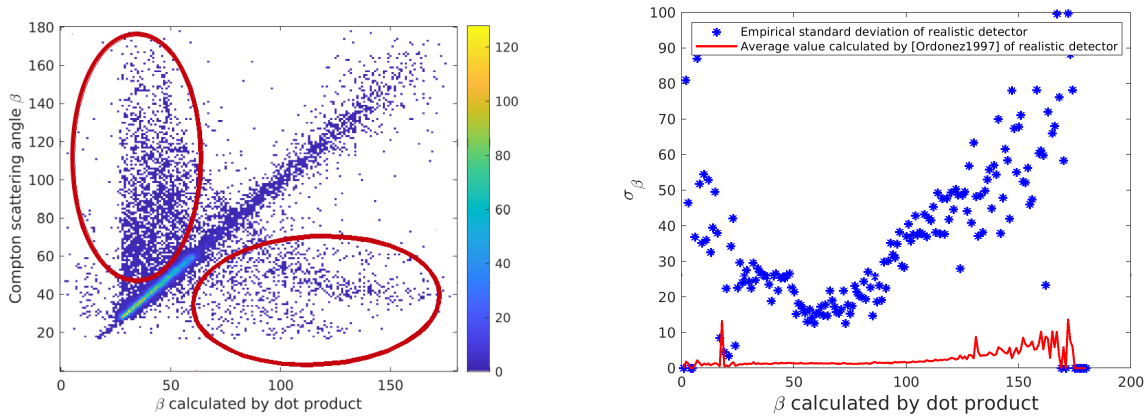

(a) (b)

Figure 3.18: (a): Uncertainties of Compton scattering angle for realistic data obtained by adding errors on the energies, (b): standard deviation calculated from realistic data (blue dot) and the σ_β calculated by the method proposed in Ordonez et al. [1997] for realistic data. In our simulation the standard deviation of β for realistic data is much higher than the one calculated as in Ordonez et al. [1997]. One reason is the large tail of the empirical distribution of errors (indicated by the two red ellipsoids).

foreseen of this work is to find a fitted model for σ changing with different energies. In section 3.7 a mono-energy source at 511 keV was simulated, we used the parameters (b) in the table 3.4 for the simple Gaussian distribution for modeling the Doppler broadening in system matrix, and used the parameter (b) in table 3.5 for the mixed Gaussian distribution for comparison.

3.6 Event uncertainties on realistic data

The intention of this section is to show that for more realistic data the uncertainties caused by Doppler broadening have little effects compared to other measurement errors. To ameliorate the image quality the accurate modeling for Doppler broadening is not enough. For the same simulation as in the former section, we now analyze the more realistic data generated by the Revan module of MEGAlib, which allows to add more realistic energy uncertainties.

Figure 3.18(a) shows the scattering angle β_{energy} calculated by using the energy information against the value β_{geo} obtained from the ideal position information of data simulated with ideal detector. The number of considered events is nearly 2×10^4. Compared to figure 3.10, for the realistic data the distribution of uncertainties caused by measurement are more complicated to model.

Figure 3.18(b) shows the standard deviation calculated from data simulated with realistic detector (blue dot) and the σ_β calculated by the method proposed in Ordonez et al. [1997] for realistic data. We can say that in our simulation the standard deviation of β for realistic data is much higher than the calculated σ_β in Ordonez et al. [1997], so the method proposed in Ordonez et al. [1997] is not adapted to our simulation. We used a simple Gaussian distribution with the standard deviation estimated from the data simulated with realistic detectors for modeling the energy uncertainties in section 3.7 for the reconstruction of realistic data.

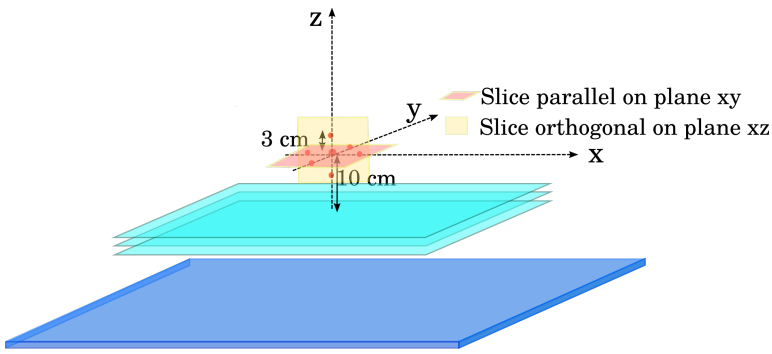

Figure 3.19: Simulation geometry of the seven points source, the central point is placed 10 cm from the camera. Central slices parallel and orthogonal to the camera are shown as reconstruction result in the following.

3.7 Reconstruction results

In this section we illustrate the previous conclusion on the reconstruction of a mono-energy source. We simulated seven point sources emitting simultaneously photons at 511 keV. The events were recorded one-by-one, random coincidences are not considered. The source was placed as in figure 3.19, located at (0, 0, 0), (0, 0, 3), (0, 0, -3), (0, 3, 0), (0, -3, 0), (3, 0, 0), (-3, 0, 0). We show the central slices in the direction parallel and orthogonal to the camera as the reconstruction result. The reconstruction volume had (10.25, 10.25, 10.25) cm^3 divided into (41, 41, 41) voxels, results are obtained with 20,000 events.

A summary to compare the influence of different models of sensitivity and Doppler broadening is shown in figure 3.20. We tested four different combination of methods in figure 3.20: single Gaussian distribution for Doppler broadening without sensitivity estimation ($s_j = 1$), results are shown in (a); single Gaussian distribution for Doppler broadening with sensitivity calculation methods $M1$, results are shown in (b); mixed Gaussian distribution for Doppler broadening with sensitivity calculation $M4$, results are shown in (c); mixed Gaussian distribution for Doppler broadening with sensitivity calculation $M1$, results are shown in (d). The single Gaussian kernel is not well adapted to the Doppler broadening. Note the difference in intensity between the sources located at different distances to detector in (a) and (b), the most adapted sensitivity method $M1$ will not help to compensate and to get the images of the points. Compare (c) to (d), with the application of the mixed Gaussian distribution which corresponds better to the Doppler broadening, the reconstruction is more sensitive to the sensitivity calculation. The intensities in the images are now similar for the seven-point sources, as it can be seen in figure 3.20 (c) and (d). The combination between the adapted Doppler broadening model and the most complicate sensitivity calculation method $M1$ in (d) gives the best result. For more details in 1D, the central profile of (b) and (d) in orthogonal direction to the camera is shown in figure 3.21.

So far from the tested methods on data simulated with ideal detector, we might draw the conclusion that for the model of uncertainties caused by Doppler broadening, the mixed Gaussian distribution will ameliorate the resolution of reconstructed images compared to the single Gaussian distribution. Besides, among the presented sensitivity matrix estimation methods, $M1$ is the most adapted. The correction of the intensity of reconstructed object by the most adapted sensitivity estimation method will be evident if the resolution of reconstruction is improved. These results will be presented in MIC 2019.

We also compared the reconstruction from data simulated with ideal detector with the reconstruction from more realistic data generated by the Revan module in MEGAlib, which

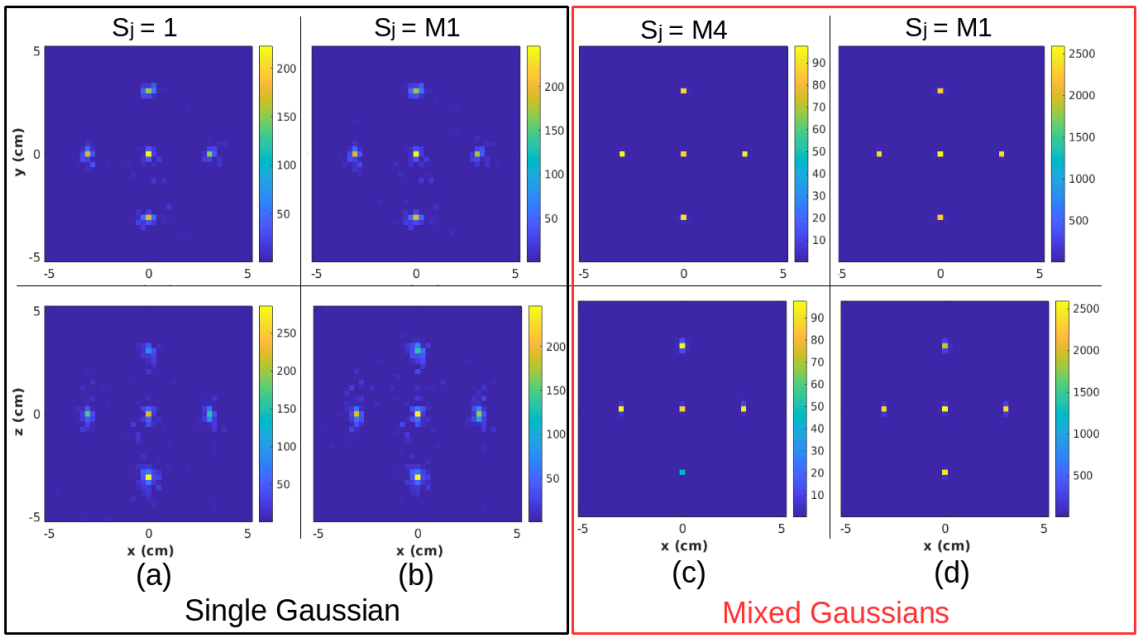

Figure 3.20: Central slices of the reconstructed volume obtained from different combination of models. The used data for reconstruction is simulated with ideal detector. The number of iterations is 50. Slices parallel to the camera are shown in the first line, slices orthogonal to the camera are shown on the second line. The combination of $M1$ and a mixed Gaussian distribution leads to a better result.

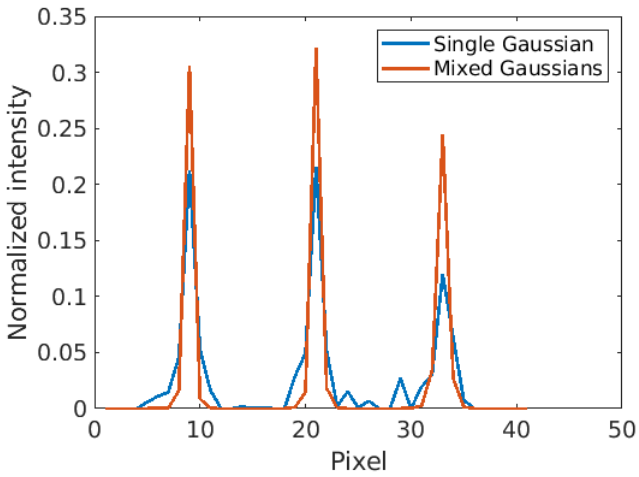

Figure 3.21: Central profile of reconstruction from data simulated with ideal detector through vertical direction. The sensitivity model used in the reconstruction is $M1$. The compared models for Doppler broadening are single Gaussian and a mixed Gaussian distribution.

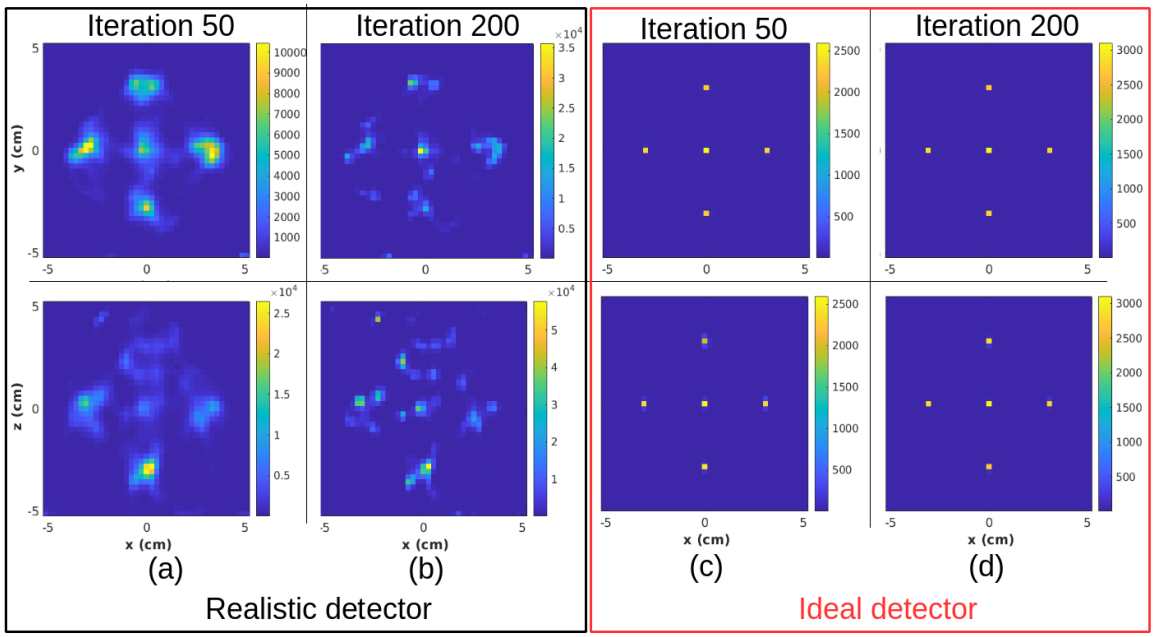

Figure 3.22: Central slices of reconstruction obtained from 20,000 events from realistic data and data simulated with ideal detectors. Slices parallel to the camera are shown in the first line, slices orthogonal to the camera are shown on the second line. The result on data simulated with ideal detector shows that a more adapted model leads the reconstructed image to the ground truth. Compare the result of data simulated with ideal detectors obtained after 50 iterations to 200 iterations, the reconstruction begins to converge. Meanwhile, with the more adapted sensitivity calculation, the reconstruction on data simulated with realistic detector still diverges after several iterations. To see the position of object the reconstruction should be stopped before divergent, and the resolution of reconstruction is not good enough to identify the point-like object.

contains not only the Doppler broadening but also the uncertainties caused by measurement. Figures on the left in 3.22 are the central slices of reconstruction from realistic data, the method used for sensitivity calculation is $M1$ and the model used for energy uncertainties is a Gaussian distribution, with standard deviation estimated by data simulated with realistic detector. The results were obtained with 20,000 events. The reconstruction obtained from realistic detector could not well recover the distribution of seven points as from the data simulated with ideal detector. Comparing the results obtained after 50 iterations to the results obtained after 200 iterations, the reconstruction will not be able to converge to the ground truth. We propose to correct the artifacts of reconstruction caused by the uncertainties of measurement in spatial domain, with TV regularization and PSF deconvolution. The methods will be presented in the next chapter.

3.8 Conclusion

This chapter investigated several models for the parameters used in the list mode MLEM reconstruction algorithm. We presented four analytic methods for the calculation of sensitivity matrix. We showed that the most adapted method for calculating the system matrix is the method taking with account the geometry and the size of the camera, as well as the attenuation factors. Therefore, we used this most adapted analytic method in the following reconstructions in this thesis.

Several methods for system matrix calculation were summarized. We showed that for modeling the uncertainties caused by the Doppler broadening, a mixed Gaussian distribution is more adapted than a single Gaussian. Elongation of the sources in the direction orthogonal to the camera, non uniform intensities and blur were observed for the single Gaussian fit. These artifacts were reduced for the mixture model where the sources were well identified and had similar reconstructed intensities. The conclusion we might draw is that improper modeling of the physical processes during the reconstruction might contribute to the elongation artifacts often observed in CC imaging. The contribution was validated on data simulated with ideal detectors, the detection resolution was supposed to be exact, no measurement uncertainties other than Doppler broadening were added. For more general uncertainties the Gaussian mixture considered before is insufficient and more complex models or even image-space resolution recovery methods should be employed. To correct the uncertainties caused by limited detection resolution and other physical effects, we propose to apply the total variation regularization and PSF deconvolution method presented in the next chapter.

Part IV

Resolution recovery of MLEM reconstruction for Compton camera imaging

Résumé en français

Ce chapitre étudie les méthodes de l'amélioration de la résolution dans les images en trois étapes : d'abord une méthode de régularisation par la variation totale (TV) adaptée à l'algorithme MLEM est développée, puis la déconvolution PSF pour récupérer la déformation de la reconstruction est étudiée, enfin la combinaison de la reconstruction TV régularisée EM et la déconvolution de la PSF sur la caméra Compton est présentée. Quelques résultats de reconstruction sur des données idéales et des données réalistes sont présentés à la fin pour comparaison.

Restauration d'images et régularisation par variation totale

Cette section donne d'abord une brève introduction sur les méthodes de restauration d'images, puis résume certaines méthodes de la régularisation TV existantes en matière de débruitage d'image, de défloutage et de reconstruction EM, et en fin illustre la méthode EM pour trouver le maximum a posteriori adapté à notre problématique.

La restauration d'image consiste à trouver l'image u à partir de l'image observée z, avec $z \sim \mathcal{D}(k*u)$, où k représente un opérateur de dégradation et $\mathcal{D}$ est une distribution probabiliste où la distribution gaussienne et la distribution de Poisson sont les plus communes. Dans le cas d'une distribution gaussienne et de la convolution, le modèle des bruits additifs s'écrit généralement comme suit :

$$k*u + n = z$$

avec n représentant les bruits additifs et $*$ représentant la convolution. L'estimation de u à partir de z sans avoir k et n connus est souvent liée au débruitage et au défloutage de l'image. Les bruits dans l'acquisition d'images peuvent généralement être classés en deux types : les bruits additifs n indépendants du signal et les bruits relatifs dépendants du signal. Les causes des bruits additifs sont le bruit thermique, les fluctuations du capteur et des circuits électroniques des appareils d'imagerie. Un modèle typique pour n est le bruit additif gaussien, dont la fonction de densité de probabilité (PDF) corresponds à la loi normale et n'est pas liée aux fréquences. En raison de sa traçabilité mathématique, ce modèle est souvent utilisé pour modéliser les processus aléatoires qui se produisent dans la nature. Le bruit dépendant du signal est généré par la nature stochastique du processus de comptage des photons. Le nombre de photons détectés suivant une loi de Poisson ($z \sim P(k*u)$) apportera les bruits distribués suivant une loi de Poisson à l'image. Contrairement aux bruits additifs gaussiens, le PDF des bruits de Poisson dépend du nombre de photons détectés. Dans la plupart des acquisitions d'imagerie médicale, les bruits dans l'image sont souvent un mélange de bruits additifs et du bruit de Poisson. De plus, en cas d'un faible nombre de photons détectés dans TEMP, le bruit de Poisson est beaucoup plus fort que le bruit additif et influencera certainement la qualité de l'image. Trouver une méthode de débruitage appropriée pour le bruit de Poisson est alors important pour la reconstruction.

Certains auteurs ont suggéré que le bruit de Poisson peut être transformé en bruit Gaussien (Anscombe [1948], Donoho [1993]), qui permet l'application d'un certain nombre de mesures de réduction du bruit (Zhang et al. [2008], Luisier et al. [2010], Luisier et al. [2011], Makitalo and Foi [2011]). Avant d'aborder la régularisation TV, remarquons que d'autres techniques de débruitage pour bruit Poisson existant, comme l'estimation multi-échelle de Haar (Fryzlewicz and Nason [2004], Nowak and Kolaczyk [2000]), le wedgelets et platelets (Willett and Nowak [2003]) ou minimum description length (Nowak and Figueiredo [1999]). Le but de notre travail n'est pas de comparer ces différents algorithmes, mais de développer une méthode adaptée à la reconstruction MLEM. Nous avons choisi la régularisation TV pour les raisons suivantes : premièrement, la méthode TV répond aux faibles coûts de calcul. Comparé aux autres algorithmes, TV peut réaliser le débruitage plus rapidement. Deuxièmement, la TV permet de réduire les bruits tout en préservant efficacement les bords de l'objet, ce qui est particulièrement intéressant en TEMP et TEP, où l'on doit conserver l'information des contours de l'objet. Troisièmement, la régularisation TV introduisant l'algorithme de lissage avant l'algorithme EM aidera à la convergence et améliorera la stabilité des résultats. Cet avantage a été prouvé expérimentalement dans notre travail.

Méthode de régularisation TV

La régularisation TV a été introduite pour la première fois par Rudin et al. [1992] et développée plus tard par Rudin and Osher [1994], Chan et al. [1995], Vogel and Oman [1996], Chan et al. [1996], Carter [2001], Chambolle [2004] pour le débruitage et la déconvolution. Lorsque l'opérateur k est une fonction de Dirac ($\delta(x, y)$), le système devient : $u + n = z$, ce qui correspond au débruitage de l'image pour $z \sim \mathcal{D}(u)$. Dans Rudin and Osher [1994], Chan and Wong [1998], Chan et al. [1996], Carter [2001] plusieurs algorithmes numériques basés sur la TV ont également été proposés pour la restauration des images contaminées par le flou et le bruit.

Dans la méthode de variation totale avec la bruit additif gaussien, le problème primal à résoudre est :

$$\min_u \underbrace{\alpha TV(u) + \frac{1}{2}||u - z||_2^2}_{\Phi(u)},$$

où $\mathrm{TV}(u) = \int_\Omega |\nabla u|_2 dxdy$, ∇ présente le gradient et $||u-z||_2$ représente la norme L_2 de l'erreur entre l'image vraie u et l'image observée z. La version discrète de la norme TV pour une image u (une matrice bidimensionnelle de taille $J = N \times N$) est la suivante :

$$TV(u) = \sum_{1 \le i,j \le N} |(\nabla u)_{(i,j)}|.$$

Ensuite la TV perturbée $\mathrm{TV}(u) = \int_\Omega \sqrt{|\nabla u|^2 + \epsilon} dxdy$ est proposée par plusieurs chercheurs (Rudin et al. [1992], Chan et al. [1995], Vogel and Oman [1996], Chan et al. [1996], Carter [2001]), le problème primal devient :

$$\min_u \alpha \int_\Omega \sqrt{|\nabla u|^2 + \epsilon} dxdy + \frac{1}{2}||u - z||_2^2.$$

Au lieu de résoudre directement le problème primal, Chan et al. [1996] et Carter [2001] ont proposé une méthode primal-dual pour résoudre le problème de régularisation de TV indépendante de ϵ. Ici le "dual" porte le nom d'un principe dual appliqué à la norme TV. Le $|\nabla u|$ peut se écrire :

$$|\nabla u| = \max_{|w|_2 \le 1} w \cdot \nabla u,$$

où w est la variable du problème dual qui représente le gradient normalisé de u. Leur problème primal-dual est :

$$\min_{u} \max_{|w|_2 \leq 1} \{ \underbrace{-\alpha \int_{\Omega} u \nabla \cdot w dx dy + \frac{1}{2} ||u - z||_2^2}_{\Psi(u,w)} \}.$$

En tomographie d'émission où l'acquisition suit la distribution de Poisson, les données acquises sont souvent contaminées par des bruits de Poisson. Ces bruits introduiront des hautes fréquences dans la reconstruction lorsque le MLEM est utilisé. En raison de la nature de l'estimation de la probabilité maximale, les fréquences élevées seront renforcées à chaque itération. Une solution possible est d'introduire le lissage a priori de l'information dans le processus de reconstruction. La méthode basée sur la norme de variation totale permet d'obtenir des régions lisses tout en préservant ses bords. Plusieurs techniques ont été proposées par Panin et al. [1999], Yan and Vese [2011], Anthoine et al. [2012], Sawatzky et al. [2008] pour la reconstruction EM régularisée par TV. L'introduction de la régularisation TV dans l'algorithme EM signifie que l'on ajoute un lissage avant l'EM, ce qui conduit à un TV régularisé maximum a posteriori (MAP).

L'objet de l'algorithme EM est de résoudre le maximum de vraisemblance, ce qui équivaut à résoudre le problème de minimisation suivant :

$$\min\{-L(\lambda|Y) \, : \, \lambda \in (\mathbb{R}_+)^J\},$$

où λ est le vecteur estimé de moyennes de distribution des émissions, Y est le vecteur des observations. Avec la régularisation TV, l'objectif devient :

$$\min\{-L(\lambda|Y) + G(\lambda) : \lambda \in (\mathbb{R}_+)^J\},$$

où $G(\lambda)$ représente le terme de variation totale, donc $G(\lambda) = \alpha \mathrm{TV}(\lambda)$.

Plusieurs méthodes numériques ont été proposées pour résoudre ce problème (Anthoine et al. [2012], Sawatzky et al. [2008]).Toutes ces méthodes ont été prouvées expérimentalement pour conduire la reconstruction TV-EM stable ainsi que préserver les contours de l'objet. Notre objectif est de rechercher la méthode la mieux adaptée à la reconstruction EM. Nous avons appliqué la méthode proposée dans Maxim et al. [2018] qui a fait ses preuves de convergence à la fois en théorie et expérimentalement.

Afin de comparer cette méthode proposée (Maxim et al. [2018]) avec d'autres méthodes, plusieurs tests numériques sont effectués. Pour le débruitage d'image de bruit de Poisson, nous avons comparé la méthode proposée par Chambolle and Pock [2011] et Maxim et al. [2018]. Pour la reconstruction tomographique, nous avons comparé les méthodes proposée dans Anthoine et al. [2012], Sawatzky et al. [2008] et Maxim et al. [2018]. Deux niveaux de bruit différents ont été testés en figure 4.1 pour les bruits faibles et les bruits forts. Les résultats de la reconstruction MLEM avec régularisation TV sont montrés en figure 4.3. Selon la comparaison numérique, la méthode proposée par Maxim et al. [2018] peut améliorer efficacement la résolution de reconstruction, en particulier pour les données avec les bruits faibles. L'algorithme est plus rapide que la méthode proposée par Anthoine et al. [2012] qui est basée sur l'algorithme de Chambolle and Pock [2011]. À l'exception de la reconstruction, pour le débruitage de Poisson uniquement, la méthode de Chambolle and Pock [2011] fonctionne à la fois pour les données à bruit élevé et à bruit faible. La méthode que nous proposons présente moins d'avantages pour le bruit élevé, mais elle est plus rapide que celle de Chambolle and Pock [2011] dans les premières itérations avec le bruit faible. Pour accélérer l'algorithme, nous avons également ajouté l'algorithme FISTA proposé par Beck and Teboulle [2009]. L'algorithme TV-FISTA-EM est résumé dans le tableau de l'algorithme 1.

Déconvolution de la PSF

La résolution spatiale des images de la caméra Compton souffre des incertitudes dues à la résolution imparfaite de la détection des photons, principalement sur les mesures de position et d'énergie. Pour corriger les artefacts introduits par ces incertitudes, nous avons étudié la méthode de la déconvolution par la fonction d'étalement du point (PSF). Nous illustrons d'abord l'algorithme de déconvolution Richardson-Lucy (RL) introduit par Richardson [1972], Lucy [1974], puis nous testons la déconvolution RL sur le défloutage d'image avec et sans le bruit de Poisson. Ensuite, nous rappelons la méthode de déconvolution PSF appliquée à la récupération de résolution pour l'imagerie médicale, et illustrons la déconvolution dans l'algorithme de reconstruction. Après l'étude de la déconvolution avec le filtre de convolution connu, nous présentons enfin la méthode de déconvolution développée où nous estimons la PSF inconnue pour la caméra Compton.

Nous modélisons les incertitudes de mesure par une convolution avec k, ce qui signifie que la mesure est maintenant $T(k \otimes \lambda)$. Si le k est invariant par rotation, la convolution avec k est aussi la corrélation avec k, l'algorithme général peut être exprimé comme suit :

$$\widehat{\lambda}^{(l+1)} = \frac{\widehat{\lambda}^{(l)}}{s}(R \otimes k), \quad \text{avec } R = T^T \left[\frac{1}{T(\widehat{\lambda}^{(l)} \otimes k)} \right].$$

Nous avons étudié la déconvolution de PSF variante spatiale par la simulation Monte Carlo avec un géométrie de la caméra présentée à la figure 4.19. La première simulation était une source voxélisée convoluée avec la PSF connue : un filtre gaussien ($\sigma = 2$) 3D. Aucune incertitude n'a été prise en compte au cours de la simulation, même l'effet Doppler a été désactivé. La deuxième simulation a été obtenue avec la PSF inconnue et les incertitudes sur la détection de l'énergie et de la position ont été prises en compte. Il convient donc d'estimer la PSF inconnue. L'estimation de la PSF est détaillée à la section 4.2.4.

La méthode proposée de débruitage par TV a été utilisée dans une étude présentée dans l'annexe (voir page 133). Le but de cette étude est d'évaluer la qualité d'imagerie par la caméra Compton dans une condition idéale. La reconstruction EM par la régularisation TV combinée avec la déconvolution de la PSF a été présentée dans MIC 2018, pour améliorer la qualité des images reconstruites à partir des données plus réalistes.

Conclusion

Dans la reconstruction de l'image par caméra Compton, en raison de l'influence des incertitudes des mesures angulaires et de position, les images semblent souvent très dégradées et déformées. Ces incertitudes sont difficiles à modéliser dans l'estimation de la matrice du système. Par ailleurs, le bruit de Poisson apparaît fréquemment lors de la reconstruction et est généré par des appareils de détection de photon. Nous avons étudié deux méthodes de récupération de résolution dans l'image pour améliorer la résolution spatiale limitée de la reconstruction : le débruitage TV et la déconvolution de PSF. Plusieurs conclusions peuvent être tirées du résultat obtenu.

Tout d'abord, la méthode TV régularisée EM contribue largement à la convergence de la reconstruction et permet d'obtenir un résultat lisse et sans bruit tout en préservant l'information sur les bords des objets. Cet avantage sera particulièrement utile en protonthérapie lorsqu'il s'agit d'identifier la chute dans le profil de γ prompt à la fin du parcours des protons. L'inconvénient de TV-EM est que le choix du paramètre définissant le poids de régularisation a une forte influence et est difficile à gérer. Deuxièmement, la déconvolution de la PSF basée

sur l'image pourrait être une solution pour récupérer la résolution spatiale. Si la PSF est bien connue, sans le bruit de Poisson, la déconvolution RL convergera vers la vérité terrain. Pour les données contaminées par le bruit de Poisson, la capacité de déconvolution est limitée, l'algorithme diverge après quelques itérations. La déconvolution régularisée par TV pourrait être une solution. Si le poids de régularisation est bien choisi, TV-RL produira un résultat acceptable. Troisièmement, dans le cadre de la reconstruction MLEM, la déconvolution ne pourra pas converger vers la vérité terrain même avec la PSF bien connue. La post-déconvolution peut réduire le temps de calcul mais la qualité du résultat est plus limitée par rapport au RL-EM. Pour combiner le débruitage et le défloutage de l'image tout en conservant le contour de l'objet, nous proposons d'appliquer la méthode TV-RL-EM pour la reconstruction. Nous pensons que le TV-RL-EM est une bonne solution pour la récupération de la résolution spatiale de la reconstruction MLEM pour l'imagerie caméra Compton. Étant donné que le calcul de régularisation et de déconvolution est ajouté dans l'espace image, cette méthode peut être facilement extensible à d'autres modalités d'imagerie et être adaptée à d'autres algorithmes de reconstruction, par exemple OSEM.

L'inconvénient de TV-RL-EM est que l'estimation de la PSF dans les images reconstruites dépend de la configuration de l'acquisition (le volume de reconstruction, le nombre d'événements, la géométrie de la caméra, matériaux, l'énergie de la source, etc.) Dans la pratique, le changement de l'un de ces facteurs nécessitera le changement de la PSF estimé. D'ailleurs, nous n'avons pas résolu le problème du coût de calcul. Une solution possible pour l'accélération est de paralléliser le calcul de la déconvolution dans chaque voxel.

Chapter 4

Resolution recovery of MLEM reconstruction

This chapter investigates resolution recovery methods in image space for Compton camera imaging in three steps: first a total variation (TV) regularization method adapted to MLEM algorithm is developed, then the PSF deconvolution for recovering the deformation of reconstruction is studied, and finally the combination of TV regularized EM reconstruction and PSF deconvolution on Compton camera imaging is presented. Some reconstruction results on data simulated with ideal detectors and data simulated with realistic detectors are shown for comparison.

4.1 Image restoration and total variation regularization

The contribution of this section is a total variation regularized EM reconstruction algorithm adapted to Compton camera imaging. This section first gives a brief introduction on image restoration methods, then summarizes some existing TV regularization methods in image denoising, deblurring and in EM reconstruction, finally illustrates a maximum a posteriori (MAP) EM method adapted to our problem.

Image restoration means to find the image u from the degraded image z, with $z \sim \mathcal{D}(\mathbf{k}*u)$, where $\mathbf{k}$ stands for a degradation, or a transfer operator and $\mathcal{D}$ is some probabilistic distribution. The most common, and with interest in our work are the Gaussian distribution and the Poisson distribution. In the case of a Gaussian distribution, the additive noise model is generally written as:

$$\mathbf{k}*u + n = z \tag{4.1}$$

with n represents the additive noise and $*$ the convolution. Recovering (or estimating) u from z without $\mathbf{k}$ and n being known is often related to image denoising and deblurring.

Noise in image acquisition can be categorized generally in two types: the additive noise n and the signal dependent noise. The cause of additive noise is the intrinsic thermal and electronic fluctuations of the sensor and electronic circuits of imaging devices. A typical model for n is Gaussian additive noise, of which the probability density function (PDF) equals to a normal distribution. Because of its mathematical tractability, Gaussian additive noise is often used to mimic the random processes that occur in nature.

The signal dependent noise is generated from the stochastic nature of the photon-counting process at the devices. The number of detected photons following a Poisson law ($z \sim P(\mathbf{k}*u)$) will bring the Poisson distributed noise to the image. Unlike the Gaussian additive noise, the

PDF of Poisson noise depends on the number of photons detected. In most acquisitions of medical imaging, the noise in image is often a mixture of additive and Poisson noise. In low photon counts such as SPECT, Poisson noise is much stronger than the additive noise and will definitely influence the image quality. Finding an appropriate denoising method for Poisson noise is thus important for resolution recovery of reconstruction.

Some researchers have suggested that Poisson noise can be transformed to Gaussian noise (Anscombe [1948], Donoho [1993]), which enables the application of a number of noise reduction algorithms (Zhang et al. [2008], Luisier et al. [2010], Luisier et al. [2011], Makitalo and Foi [2011]). Before investigating the TV regularization for denoising, we would like to mention that except TV methods there are also other denoising techniques for Poisson noise, such as multiscale Haar estimation (Fryzlewicz and Nason [2004], Nowak and Kolaczyk [2000]), wedgelets and platelets methods (Willett and Nowak [2003]) or minimum description length (Nowak and Figueiredo [1999]). The goal of our work is not to compare these different algorithms, but to develop a method adapted to MLEM reconstruction. We chose TV regularization because of the following reasons: firstly, TV meets the relatively low computational costs and memory requirements, so as to be able to handle large data sets. Compared to the other algorithms, TV may realize denoising faster. Secondly, TV allows to reduce the noise while preserving effectively the edges of object, which is especially interesting in SPECT and PET, where one should preserve the information of object contours. Thirdly, TV regularization introducing the smooth prior to EM algorithm will help the algorithm to converge and will improve the stability of results. This advantage was proved experimentally in this chapter.

4.1.1 TV denoising for Gaussian noise

TV regularization was first introduced by Rudin et al. [1992] and latterly be developed for image denoising and deblurring (in another word deconvolution).

Let u be the true image and z the observed image, both defined on the open and bounded domain Ω of $\mathbb{R}^2$. When the operator $\mathbf{k}$ is a Dirac delta function the system in (4.1) becomes:

$$u + n = z, \tag{4.2}$$

which leads to image denoising for $z \sim \mathcal{D}(u)$. Generally the problem is ill-posed with respect to u and a certain regularized condition should be imposed to transform it in a well-posed problem. In total variation method with Gaussian additive noise the primal problem to be solved is:

$$\min_u \underbrace{\alpha TV(u) + \frac{1}{2}||u - z||_2^2}_{\Phi(u)}, \tag{4.3}$$

where

$$TV(u) = \int_\Omega |\nabla u|_2 dxdy, \tag{4.4}$$

∇ is the gradient and $||u - z||_2$ represents the L_2-norm of the error between the true image u and the observed image z.

The discrete version of the TV norm for an image u (a two dimension matrix of size $J = N \times N$) is:

$$TV(u) = \sum_{1 \le i,j \le N} |(\nabla u)_{(i,j)}|. \tag{4.5}$$

Since the objective function $\Phi(u)$ is convex with respect to the variable u, we can minimize $\Phi(u)$ by solving the first order necessary and sufficient condition:

$$\nabla\Phi(u) = \overrightarrow{0}. \tag{4.6}$$

The corresponding Euler-Lagrange equation is:

$$-\alpha\nabla\cdot(\frac{\nabla u}{|\nabla u|}) + u - z = 0. \tag{4.7}$$

This equation is not well defined when $|\nabla u| = 0$. To overcome this barrier the perturbed TV norm is proposed by several researchers (Rudin et al. [1992], Chan et al. [1995], Vogel and Oman [1996], Chan et al. [1996], Carter [2001]):

$$TV(u) = \int_\Omega \sqrt{|\nabla u|^2 + \epsilon}\ dxdy, \tag{4.8}$$

where the ϵ is a small positive parameter, so now the primal problem becomes:

$$\min_u\ \alpha\int_\Omega \sqrt{|\nabla u|^2 + \epsilon}\ dxdy + \frac{1}{2}||u - z||_2^2. \tag{4.9}$$

The corresponding Euler-Lagrange equation is then:

$$-\alpha\nabla\cdot(\frac{\nabla u}{\sqrt{|\nabla u|^2 + \epsilon}}) + u - z = 0. \tag{4.10}$$

The main difficulty posed by this equation is the linearization of the non-linear term: $-\nabla\cdot\frac{\nabla u}{\sqrt{|u|^2+\epsilon}}$, which makes the denoising sensitive to the parameter ϵ. Several numerical algorithms have been proposed by Rudin et al. [1992], Chan et al. [1995], Vogel and Oman [1996] to solve iteratively the primal problem.

Instead of solving directly the primal problem (4.9), Chan et al. [1996] and Carter [2001] proposed a primal-dual method to solve the TV regularization problem independent on ϵ. Here the "dual" is named after a dual principle applied to the TV norm. Rewriting the $|\nabla u|$ as:

$$|\nabla u| = \max_{|w|_2\leq 1} w\cdot\nabla u, \tag{4.11}$$

where w is the variable of dual problem which stands for the normalized gradient of u. Their primal-dual problem is:

$$\min_u\max_{|w|_2\leq 1}\{\underbrace{-\alpha\int_\Omega u\nabla\cdot w\ dxdy + \frac{1}{2}||u - z||_2^2}_{\Psi(u,w)}\}. \tag{4.12}$$

The objective function $\Psi(u, w)$ is strictly convex in the primal variable u, the minimum can be found as a solution of:

$$\nabla_u\Psi(u, w) = 0 \Leftrightarrow u(w) = z + \alpha\nabla\cdot w. \tag{4.13}$$

Now replacing the primal variable u by writing u in terms of w, the dual problem is:

$$\max_{|w|_2\leq 1}\{\alpha\int_\Omega w\cdot\nabla z\ dxdy - \frac{\alpha^2}{2}||\nabla\cdot w||_2^2\}. \tag{4.14}$$

In Chambolle [2004] a purely dual method was also proposed. The first step consists to rewrite the Euler equation as follows (see Hiriart-Urruty and Lemaréchal [2013][Prop. 6.1.2] for properties of the complex conjugate):

$$(z-u)/\alpha \in \partial TV(u) \Longleftrightarrow u \in \partial TV^*((z-u)/\alpha), \tag{4.15}$$

where ∂ stands for the sub-gradient, the superscript $*$ denotes the complex conjugate. This leads to:

$$\frac{z}{\alpha} \in \frac{z-u}{\alpha} + \frac{1}{\alpha}\partial TV^*\left(\frac{z-u}{\alpha}\right), \tag{4.16}$$

and by introducing the variable $w = \frac{z-u}{\alpha}$, the problem turns to:

$$\min_w \frac{\|w-(z/\alpha)\|^2}{2} + \frac{1}{\alpha}TV^*(w). \tag{4.17}$$

An algorithm proved fast for solving this problem is proposed in Chambolle [2004].

Except denoising, in Rudin and Osher [1994], Chan and Wong [1998], Chan et al. [1996], Carter [2001] several numerical algorithms based on TV were also proposed for restoration of images corrupted both by blurring and noise. The model is expressed in (4.1), where $\mathbf{k}$ is an unknown transfer operator that stands for the blurring kernel and corresponds to a point spread function (PSF). The problem is ill-posed with respect to both u and $\mathbf{k}$, and regularization is needed for both. The goal is deblurring (in other words blind deconvolution since the PSF is unknown) as well as denoising. In Chan and Wong [1998] authors cited that the motivation of using the total variation regularization for PSF is that some PSFs can have edges. After adding TV regularization the problem to be solved is:

$$\min_u \underbrace{\alpha_1 TV(u) + \alpha_2 TV(\mathbf{k}) + \frac{1}{2}||\mathbf{k} * u - z||_2^2}_{\Phi(u,\mathbf{k})}. \tag{4.18}$$

where α_1, α_2 are parameters measuring the trade off between a good fit and the regularity of the solutions u and $\mathbf{k}$.

4.1.2 TV regularized tomography with Poisson noise

In emission tomography where the acquisition follows Poisson distribution, the acquired data is often contaminated with Poisson noise. Poisson noise will introduce high frequencies in the reconstruction when the MLEM is used. Due to the nature of estimating the maximum likelihood, high frequencies will be reinforced during each iteration. One possible solution is to introduce smoothing a priori information into the reconstruction process. The prior based on the total variation norm is suitable for obtaining smooth regions while preserving its edges. Several TV methods were proposed for tomographic reconstruction from data contaminated with Poisson noise (Panin et al. [1999], Yan and Vese [2011], Anthoine et al. [2012], Sawatzky et al. [2008]). Introducing the TV regularization in the MLEM algorithm means that we add a smoothing prior to the likelihood, which leads to a TV regularized maximum a posteriori (MAP) algorithm.

The object of MLEM algorithm is to solve for the maximum of likelihood, which equals to solve the following minimization problem:

$$\min\{-L(\lambda|Y) \,:\, \lambda \in (\mathbb{R}_+)^J\}. \tag{4.19}$$

where λ is the vector of means of the emission distribution, Y is the vector of observations. With the TV regularization, the objective becomes:

$$\min\{-L(\lambda|Y) + G(\lambda) : \lambda \in (\mathbb{R}_+)^J\}, \tag{4.20}$$

where $G(\lambda)$ represents the total variation term, thus:

$$G(\lambda) = \alpha \mathrm{TV}(\lambda). \tag{4.21}$$

The corresponding Euler-Lagrange equation of (4.20) is:

$$-\nabla_\lambda L(\lambda|y) + \alpha \partial \mathrm{TV}(\lambda) = 0. \tag{4.22}$$

The gradient of the log-likelihood is:

$$\nabla_\lambda L(\lambda|y) = T^*\mathbf{1} - T^*[\frac{y}{T\lambda}], \tag{4.23}$$

where T corresponds to the system matrix, T^* is the complex conjugate of T and $T^* = T^T$. The Euler-Lagrange equation that corresponds to (4.20) is then:

$$T^*\mathbf{1} - T^*[\frac{y}{T\lambda}] + \alpha \partial \mathrm{TV}(\lambda) = 0. \tag{4.24}$$

To solve (4.24), in Anthoine et al. [2012] a method based on the primal-dual algorithm introduced by Chambolle and Pock [2011] is proposed. The method can be summarized as follows: let $H(\mu) = \langle \mu - y\log\mu, 1\rangle$ be the negative log-likelihood for Poisson denoising, where μ is the mean of observation Y and $\mu = T\lambda$. The proposed algorithm consists to choose the constants $\sigma, \tau > 0$, and initial values $(\lambda^{(0)}, \mu^{(0)}) \in (X \times Y)$, where X is the Euclidean space $\mathbb{R}^{N\times N}$ and $Y = X \times X$, then to apply the Chambolle-Pock algorithm for Poisson denoising step. This gives:

$$\mu^{(l+1)} = (1 + \sigma \partial H^*)^{-1}(\mu^{(l)} + \sigma T\lambda^{(l)}), \tag{4.25}$$

$$\hat{\lambda}^{(l+1)} = (1 + \tau \partial G)^{-1}(\hat{\lambda}^{(l)} - \tau T^*\mu^{(l+1)}), \tag{4.26}$$

$$\lambda^{(l+1)} = 2\hat{\lambda}^{(l+1)} - \hat{\lambda}^{(l)}, \tag{4.27}$$

where H^* is the convex conjugate of H.

The TV-MAP-EM algorithm consists to solve (4.24) by two steps: expectation **(E)** step and maximization **(M)** step . The **(E)** step is same as MLEM:

$$\lambda^{(l+\frac{1}{2})} = \frac{\lambda^{(l)}}{T^*\mathbf{1}} T^*[\frac{y}{T\lambda^{(l)}}]. \tag{4.28}$$

The **(M)** step is a generalized TV Poisson denoising step, with the objective:

$$\lambda^{(l+1)} \in \arg\min_u \left\{ \langle u - \lambda^{(l+\frac{1}{2})}\log(u), T^*\mathbf{1}\rangle + \alpha ||u||_{\mathrm{TV}} \right\}. \tag{4.29}$$

This step becomes regular Poisson denoising when T^* is an identity matrix.

Several numerical methods have been proposed for solving the **(M)** step (Yan and Vese [2011], Sawatzky et al. [2008]). The method in Sawatzky et al. [2008] is based on the dual

formulation introduced by Chambolle [2004]. The Poisson denoising step can be resumed in the following formulas:

$$\lambda^{(l+1)} = \lambda^{(l+\frac{1}{2})} - \mathrm{div}\psi^k \cdot \alpha \frac{\lambda^{(l)}}{T^*\mathbf{1}}, \tag{4.30}$$

$$\psi^{k+1} = \frac{\psi^k + \tau\nabla\left(\mathrm{div}\,\psi^k - \lambda^{(l+\frac{1}{2})}/\alpha\right)}{1 + \tau|\nabla\left(\mathrm{div}\,\psi^k - \lambda^{(l+\frac{1}{2})}/\alpha\right)|}, \tag{4.31}$$

where the condition $0 < \tau < \frac{T^*\mathbf{1}}{4\alpha\lambda}$ should be ensured for convergence of the algorithm.

All these methods were experimentally proved to lead the reconstruction stable while preserving sharp edges of object. Our goal is to search a best suited method for EM reconstruction for Compton camera imaging. We developed a new TV-MAP-EM method, described in detail in Maxim et al. [2018]. This method is proved both theoretically and experimentally convergent. We name this method "dual" as it is based on a dual formulation. The idea is to iteratively reach the maximum of likelihood (the minimum of (4.20)) by solving a sequence of minimization problems lean on the Fenchel-Rockafellar duality theorem. The dual formulation is written as:

$$\varphi^* = \arg\min_{\varphi\in K} h(\varphi), \tag{4.32}$$

with

$$h(\varphi) = -\langle \log(T^*\mathbf{1} + \alpha\mathrm{div}\varphi), T^*\mathbf{1}\lambda^{(1+\frac{1}{2})}\rangle, \tag{4.33}$$

and $K = \{\varphi \in Y : |\varphi_{i,j}| \leq 1 \text{ and } T^*\mathbf{1} + \alpha\mathrm{div}\varphi > 0\}$.

The TV Poisson denoising step reads:

$$\lambda^{(l+1)} = \frac{T^*\mathbf{1}}{T^*\mathbf{1} + \alpha\mathrm{div}\varphi^*}\lambda^{(l+\frac{1}{2})}, \tag{4.34}$$

where φ^* is the limit of the sequence $(\varphi^{(k)})$ generated as:

$$\varphi^{(k+1)} = \frac{\varphi^{(k)} - \tau z^{(k)}}{1 + \tau|z^{(k)}|}, \tag{4.35}$$

with

$$z^{(k)} = \nabla\left(\frac{T^*\mathbf{1}}{T^*\mathbf{1} + \alpha\mathrm{div}\varphi^*}\lambda^{(l+\frac{1}{2})}\right). \tag{4.36}$$

Let $L_h = 8\alpha^2||T^*\mathbf{1}\lambda^{l+\frac{1}{2}}||_\infty/(\min(T^*\mathbf{1}) - 4\alpha)^2$, for 2D images it is proved that the sequence $(h(\varphi^{(k)}))$ is decreasing and converges to the minimum of h when $\alpha < \min(T^*\mathbf{1})/4$ and $\tau < \alpha/L_h$, for 3D images the condition becomes $\alpha < \min(T^*\mathbf{1})/6$ (see Maxim et al. [2018] for convergence proofs in detail).

With the sensitivity estimated by analytic methods introduced in the previous chapter, $T^*\mathbf{1}$ can be replaced by the sensitivity vector S. To accelerate the algorithm we also added the fast iterative shrinkage-thresholding algorithm (FISTA) proposed by Beck and Teboulle [2009]. The dual TV-MAP-EM-FISTA algorithm for reconstruction is summarized as Algorithm 1.

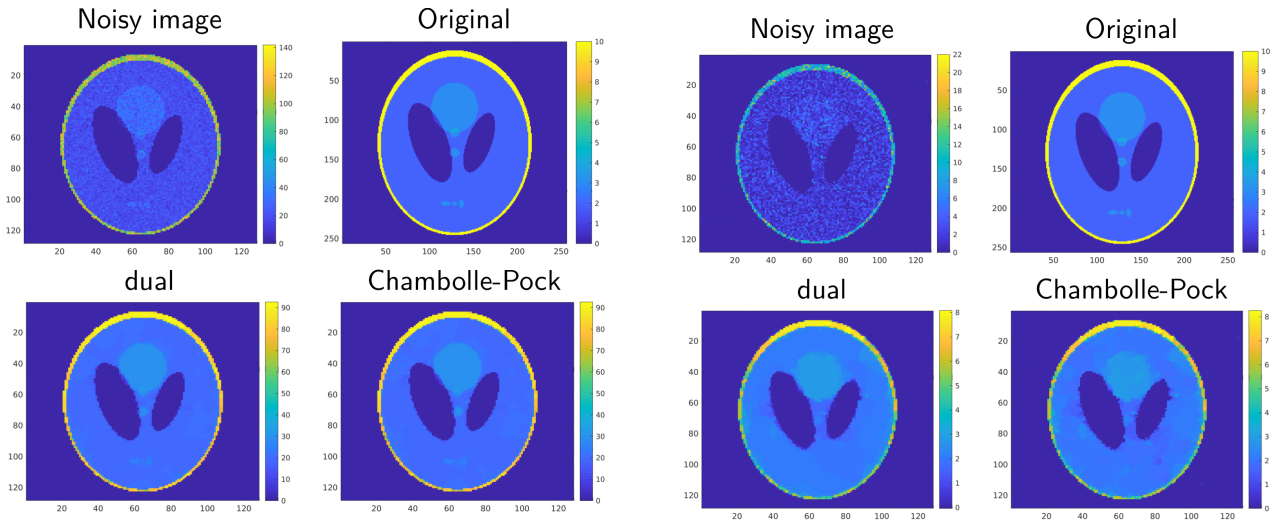

(a) Mild noise (b) Severe noise

Figure 4.1: Comparison of proposed dual method and Chambolle and Pock [2011] for Poisson denoising in different noise level.

4.1.3 Results of TV denoising and TV-EM reconstruction for 2D RADON projections

Several numerical tests are performed to compare the proposed method with some representative methods from the literature. The experiments are summarized below:

Tests	Algorithms compared to the dual method in Maxim et al. [2018]
Image denoising	Chambolle and Pock [2011]
Tomographic reconstruction	Anthoine et al. [2012] Sawatzky et al. [2008]

We first compared the method proposed by Maxim et al. [2018] (FISTA added) with Chambolle and Pock [2011] for image denoising. Two different noise levels were tested in figure 4.1 for mild noise and severe noise, the TV denoising was stopped at 2×10^4 iterations since the result is close to the ground truth f. To show the convergence of these two algorithms, we calculated the difference between result obtained after each iteration and result obtained after 2×10^4 iterations. The log-difference as a function of iteration is shown in figure 4.2 for 1×10^4 iterations. The ground truth f is the *Shepp-Logan* head phantom in Matlab, sampled in 256^2 pixels. We used Matlab function *"poissrnd"* to generate random numbers from the Poisson distribution, this function is also used in section 4.2.1 for generating image contaminated by Poisson noise. The severe noisy image is generated by using the *Shepp-Logan* phantom as the mean value of Poisson distributed noise, the mild noisy image is generated by multiplying the image intensity by 10.

The denoised images shown in figure 4.1 prove that the proposed Poisson denosing method and the Chambolle-Pock method work both for severe noise and mild noise data. Moreover, comparing the figures of merit shown in figure 4.2, the convergence of our proposed method was faster than the convergence of Chambolle-Pock method in the first iterations while the noise is mild, but was slower for severe noise, which requires a high regularization coefficient.

For tomographic reconstruction, we compared the method proposed in Anthoine et al. [2012], Sawatzky et al. [2008] and Maxim et al. [2018] (without FISTA). Ideal Radon projections of the *Shepp-Logan* phantom in Matlab were generated for angles running from 0° to 175° in steps

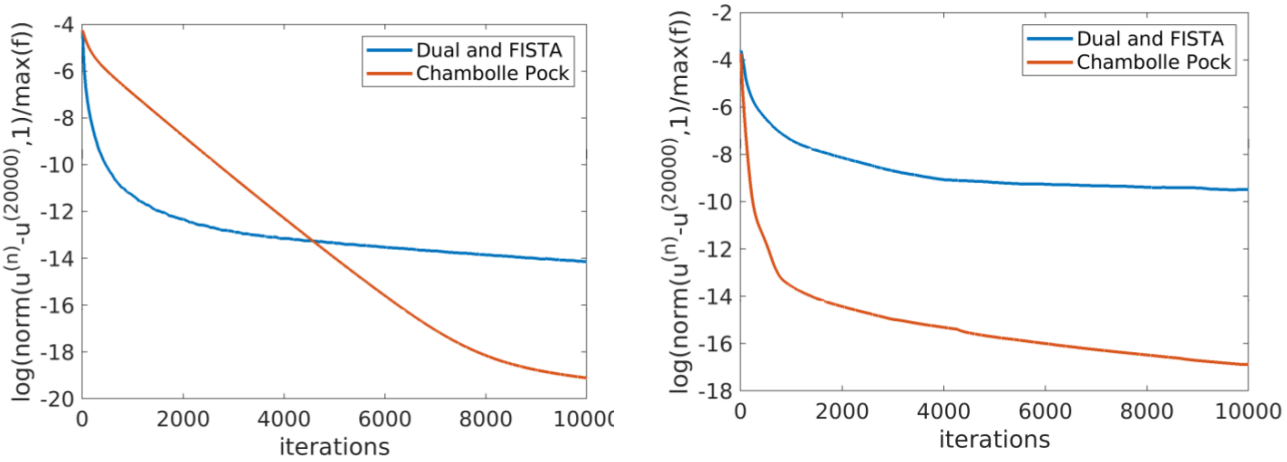

(a) Mild noise

(b) Severe noise

Figure 4.2: Figures of merit for the comparison of the proposed dual method (blue line) and Chambolle and Pock [2011] method (red line) for Poisson image denoising.

of 6°. Random values for empirical projections were drawn from *"poissrnd"* with the mean of Poisson distribution equal to the theoretical projection. The empirical total number of counts is then about 3×10^6. The results of MLEM reconstruction with TV regularization (dual TV-MAP-EM) are shown in figure 4.3. As figures of merit we used the total energy calculated by (4.20), shown on the left of figure 4.4, and the mean square error (MSE) shown on the right of figure 4.4, calculated as:

$$\mathrm{MSE}(\widehat{\lambda}) = \frac{1}{J} \left\| \widehat{\lambda_j} - \lambda_j \right\|^2. \tag{4.37}$$

The difference between the central slices of reconstruction (shown on left in figure 4.3) is not visually evident. Comparing the merit MSE shown in figure 4.4, the proposed dual method and Sawatzky method perform better than the method in Anthoine et al. [2012]. The total energy decreases faster when the dual method or the Sawatzky method are used, which corresponds to a faster convergence of reconstruction.

In this section an algorithm that combines a regular ML-EM step with a TV Poisson denoising step is presented and compared with other methods following the same objective. According to the numerical comparison, the TV regularization method proposed in Maxim et al. [2018] will help to reduce the high frequencies artifacts in MLEM reconstruction. This method can also be used for Poisson denosing only, but the performance is inferior to the Chambolle-Pock method when the noise level is severe, a situation that requires a stronger regularization weight.

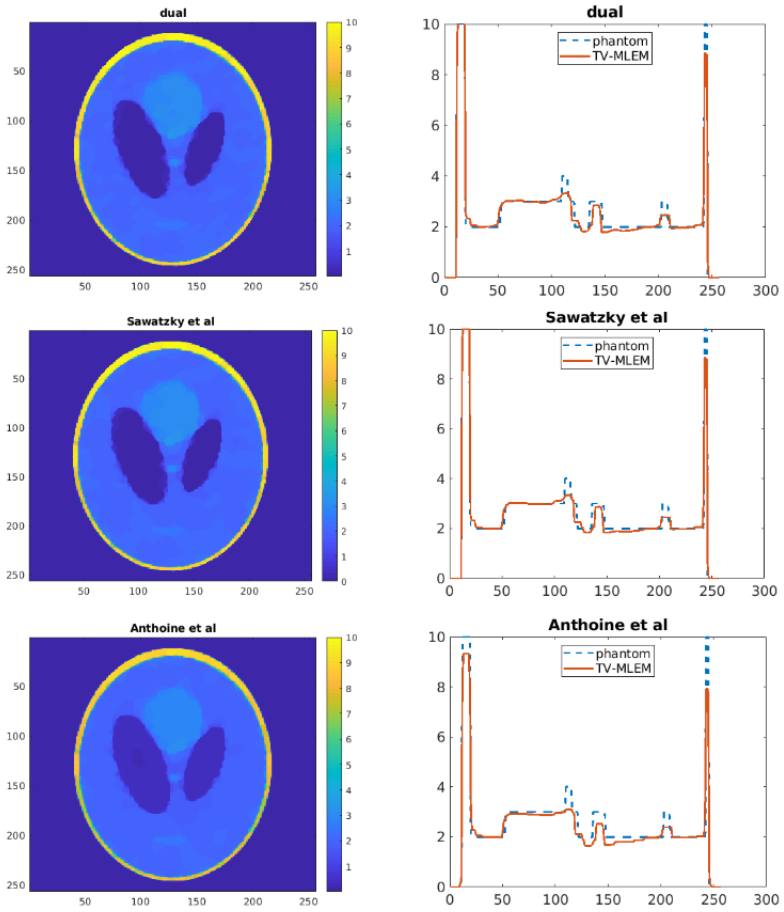

Figure 4.3: Comparison of the proposed dual methods, the methods in Sawatzky et al. [2008] and Anthoine et al. [2012] for MLEM reconstruction after 1×10^4 iterations. The right column are the central profiles plotted along the vertical direction of the images shown on the left.

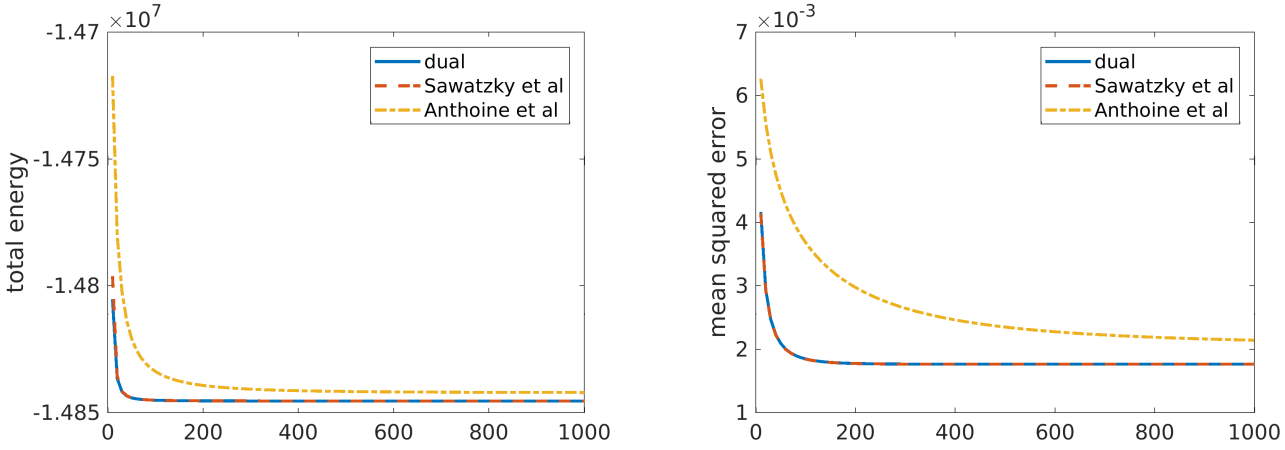

(a) Total energy

(b) MSE

Figure 4.4: Figures of merit for the comparison of the proposed dual method (blue line), Sawatzky et al. method (red line) and Anthoine et al. method (yellow line) for MLEM reconstruction after 1×10^3 iterations.

Algorithm 1 Dual TV-MAP-EM-FISTA, l^{th} iterations

MLEM step:

$$S = T^*\mathbf{1}; S_{\min} = \min(T^*\mathbf{1})$$

$$\lambda^{(\text{l, EM})} = \frac{\lambda^{(\text{l-1, TV-FISTA-EM})}}{S} T^* \frac{1}{[T\lambda^{(\text{l-1, TV-FISTA-EM})}]}$$

TV step:

$$\tau = \frac{S_{\mathbf{min}} - 6\alpha^2}{12 * \alpha * \mathbf{max}\{S\lambda^{(\text{l,EM})}\}}, \ \text{div}\psi^0 = 1$$

for $k = 1 : \text{nb\_iter\_TV}$

$$z^{(\text{k})} = \frac{S\lambda^{(\text{l, EM})}}{S + \alpha div\psi^{(\text{k})}}$$

$$\psi^{(\text{k+1})} = \frac{\psi^{(\text{k})} - \tau z^{(\text{k})}}{1 + \tau \| z^{(\text{k})} \|}$$

end

$$\lambda^{(\text{l, TV-EM})} = \frac{S\lambda^{(\text{l, EM})}}{S + \alpha div\psi^{(\text{nb\_iter\_TV})}}$$

FISTA step:

$$t^{(\text{l})} = \frac{1 + \sqrt{1 + 4(t^{(\text{l-1})})^2}}{2}$$

$$\lambda^{(\text{l, TV-FISTA-EM})} = \lambda^{(\text{l, TV-EM})} + \frac{t^{(\text{l-1})} - 1}{t^{(\text{l})}} (\lambda^{(\text{l, TV-EM})} - \lambda^{(\text{l-1, TV-EM})})$$

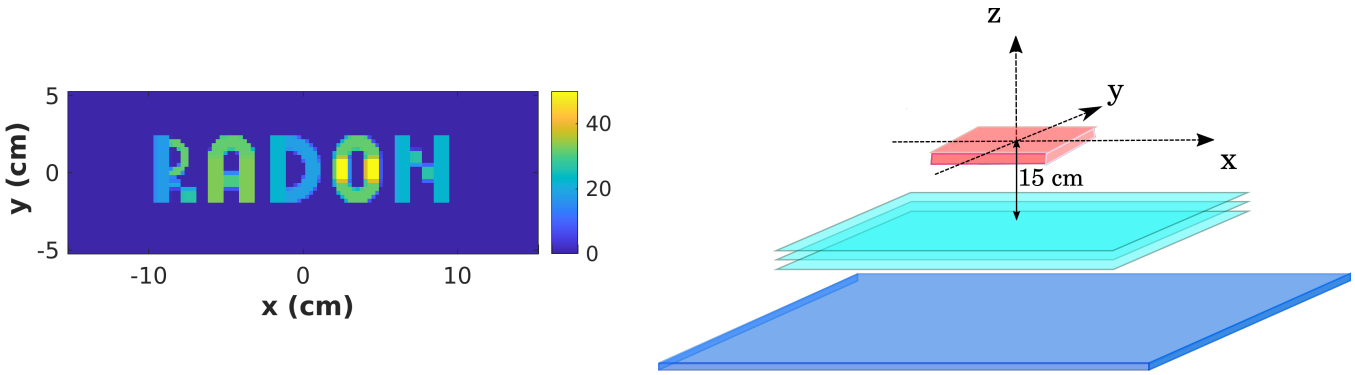

(a) Central slice of the ground truth

(b) Simulation geometry

Figure 4.5: Central slice of the simulated source (left) and the simulation geometry (right).

4.1.4 Results of dual TV-MAP-EM-FISTA reconstruction for Compton camera imaging

This section compares the results of reconstruction obtained by dual TV-MAP-EM-FISTA and MLEM for Compton camera imaging. A mono-energetic voxelized source was simulated with GATE. The source is composed of five letters with thickness 1 cm. The intensity was piecewise constant in each coronal plane and constant in the z direction. The center of the source is placed 15 cm to the first layer of camera. The reconstruction voxel size is 0.25 cm. In figure 4.5(a) the central coronal slice of the source is shown. During the simulation no uncertainty was added, neither measurement errors nor Doppler broadening, the data was supposed to be ideal. The simulation geometry is shown in figure 4.5(b). The camera prototype is same as the camera simulated in the previous chapter (3.3.1). 2×10^6 ideal events were used for reconstruction. The central slices in the coronal plane of reconstruction are shown in figure 4.6. Figure 4.7 compares the MSE calculated by (4.37) between the reconstructed image and the ground truth as a function of iteration.

The results with and without TV regularization at iteration 50 and 200 are compared in figure 4.6. The divergence of MLEM can be observed without TV regularization. On the contrary, the dual TV-MAP-EM-FISTA converges both visually and in MSE (see figure 4.7) and provides a better result even after 50 iterations. The reconstruction is smoother and closer to the ground truth when we compare the result of dual TV-MAP-EM-FISTA to MLEM.

Post smoothing is usually proposed for reducing the high frequency artifacts, figure 4.8 compares the post smoothing by median filter, post smoothing by TV dual method, and the dual TV-MAP-EM-FISTA. Results show that the TV post smoothing recovers the reconstructed distribution better than the median filter, and can be an optional noise control method for time saving, as the computation time is reduced compared to the dual TV-MAP-EM-FISTA.

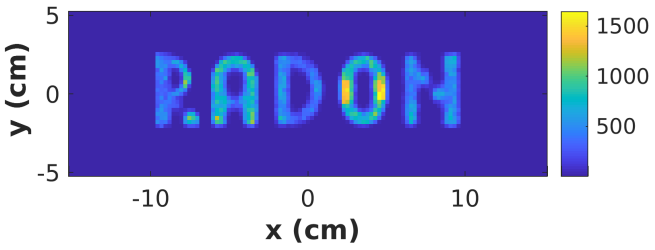

(a) MLEM, iteration 50

(b) Dual TV-MAP-EM-FISTA, iteration 50

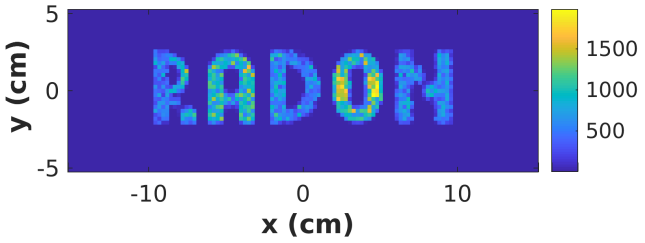

(c) MLEM, iteration 200

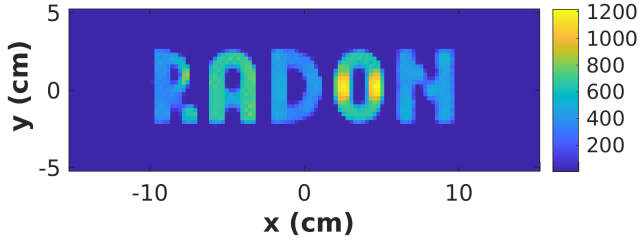

(d) Dual TV-MAP-EM-FISTA, iteration 200

Figure 4.6: Central slices of reconstruction for Compton camera imaging with 2x10^6 ideal events without Doppler broadening.

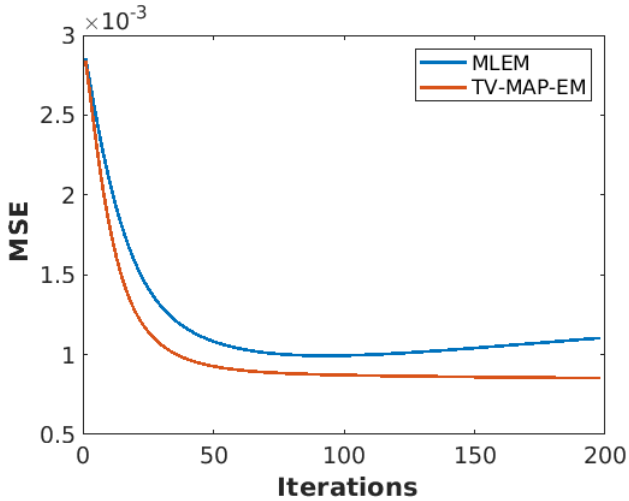

Figure 4.7: MSE of MLEM and dual TV-MAP-EM-FISTA.

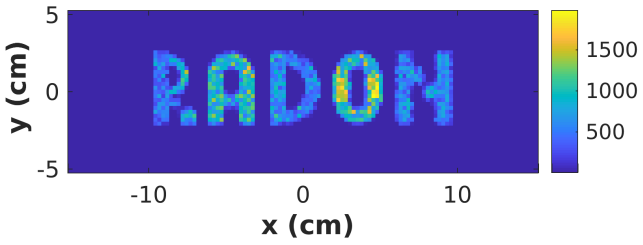

(a) MLEM, MSE = 0.0014

(b) Dual TV-MAP-EM-FISTA, MSE = 0.0011

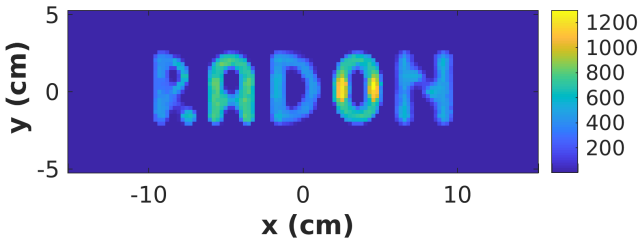

(c) MLEM with post median filter, MSE = 0.0012

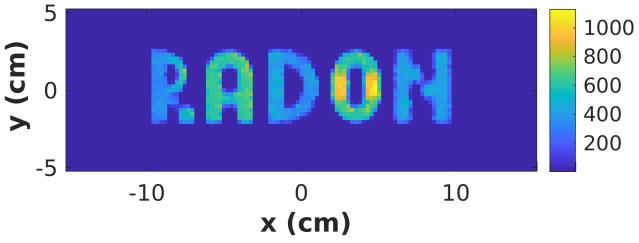

(d) MLEM with post TV smoothing, MSE = 0.0011

Figure 4.8: Central slices of reconstruction for Compton camera imaging with 2x10^6 ideal events without Doppler broadening. The reconstruction was stopped at 200 iteration, post smoothing by median filter (c) and TV dual method (d) were then added for comparaison.

4.2 Image-based PSF deconvolution

The originality of this section is a proposed resolution recovery method for Compton camera imaging which incorporates the PSF deconvolution into TV regularized EM reconstruction. The spatial resolution in Compton camera images often suffers from the uncertainties caused by the imperfect resolution of photon detection, mainly on the position and energy measurements. To correct the artifacts introduced by these uncertainties, we investigated the image-based PSF deconvolution. We first illustrate the Richardson-Lucy deconvolution algorithm introduced by Richardson [1972], Lucy [1974], then test the RL deconvolution on image deblurring with and without Poisson noise. Afterwards, we recall the PSF deconvolution method applied in resolution recovery for medical imaging, and illustrate the deconvolution on reconstruction algorithm. After investigating the deconvolution on reconstruction with the known convolution filter, we finally present the developed deconvolution method where we estimate the shift-variant PSF for Compton camera imaging reconstruction.

The original idea of applying the probability based deconvolution for restoring the noisy degraded image was proposed in Richardson [1972] and Lucy [1974]. This method based on Bayes's theorem can be applied to improve the quality of reconstructed images when the system matrix are not modeled accurately and when the data used for reconstruction has high noise level caused by low statistics. We will first illustrate this method in one dimension.

Denoting the transfer operator to obtain the observation z as $\mathbf{k}$. Denoting the value of the observed array at location m as z_m, the unknown true value at location i as u_i. $\mathbf{k}$, z and u can be taken as the entire set of discrete random variables. The numerical value of an element in $\mathbf{k}$, z and u can be considered as the measurement of the frequency that an event occurs at that position. We have $u = \sum_i u_i$, $z = \sum_m z_m$, $z_m = \sum_i \mathbf{k}_{i,m} u_i$, $\mathbf{k}_{i,m}$ corresponds to an element of transfer operator which transforms u_i to z_m. Units of energy (which can be considered as unique events) at an element in u are distributed at elements in z according to the frequencies indicated by $\mathbf{k}$. The restoration is a conservative process, in other words the total energy does not change, so $u = z$. In the following, the frequency function (in another word probability) is expressed by P. It is assumed that the problem to be solved can be expressed by the following equation:

$$z = \mathbf{k} * u, \tag{4.38}$$

where $*$ denotes the convolution.

The RL deconvolution is based on the Bayes's theorem. The conditional probability of an event at u_i given an event at z_m is:

$$P(u_i|z_m) = \frac{P(u_i, z_m)}{P(z_m)}. \tag{4.39}$$

Obviously $P(z_m) = \sum_j P(z_m|u_j)P(u_j)$, we thus have:

$$P(u_i|z_m) = \frac{P(z_m|u_i)P(u_i)}{\sum_j P(z_m|u_j)P(u_j)}. \tag{4.40}$$

Since z_m depends on all u_i in accordance with the point spread function $\mathbf{k}$, we have:

$$P(u_i) = \sum_m P(u_i, z_m) = \sum_m P(u_i|z_m)P(z_m). \tag{4.41}$$

Take (4.40) to (4.41):

$$P(u_i) = \sum_m \frac{P(z_m|u_i)P(u_i)}{\sum_j P(z_m|u_j)P(u_j)} P(z_m). \tag{4.42}$$

Often the estimation of probability $P(u_i)$ is solved by iterative methods with the initialization taken as a uniform distribution, so $P^0(u_i) = 1/I$ and $\widehat{P}^l(u_i)$ in l^{th} iteration is:

$$\widehat{P}^{(l)}(u_i) = \sum_m \frac{P(z_m|u_i)P(z_m)}{\sum_j P(z_m|u_j)\widehat{P}^{(l-1)}(u_j)}\widehat{P}^{(l-1)}(u_i), \tag{4.43}$$

since $u = \sum_i u_i$, $z = \sum_m z_m$ and $u = z$, we have:

$$P(z_m) = \frac{z_m}{z} = \frac{z_m}{u}, \tag{4.44}$$

$$P(u_i) = \frac{u_i}{u}. \tag{4.45}$$

since $z_m = \sum_i k_{i,m}u_i$, we also have:

$$P(z_m|u_i) = P(\mathbf{k}_{i,m}) = \frac{\mathbf{k}_{i,m}}{\mathbf{k}}, \tag{4.46}$$

where $\mathbf{k}_{i,m}$ corresponds to the element of transfer operator, in other words the application from element u_i to element z_m, $\mathbf{k}$ can also be taken as the entire set of applications. (4.43) then becomes to:

$$\frac{\widehat{u}_i^{(l)}}{u} = \frac{\widehat{u}_i^{(l-1)}}{u}\sum_m \frac{\frac{\mathbf{k}_{i,m}}{\mathbf{k}}\frac{z_m}{u}}{\sum_j \frac{\mathbf{k}_{j,m}}{\mathbf{k}}\frac{\widehat{u}_j^{(l-1)}}{u}}. \tag{4.47}$$

Finally, in order to estimate u given the observation z and a known $\mathbf{k}$, the RL deconvolution consists of the following iterative procedure where two convolution kernels are added:

$$\widehat{u}^{(l)} = \widehat{u}^{(l-1)} \bullet \left(\frac{z}{\widehat{u}^{(l-1)} \otimes \mathbf{k}} \otimes \mathbf{k}^*\right), \tag{4.48}$$

$\mathbf{k}^*$ here stands for the conjugate transpose of the PSF matrix $\mathbf{k}$.

4.2.1 Results of RL deconvolution on image deblurring

Before investigating the PSF deconvolution in EM reconstruction, we first investigated the RL deconvolution for image deblurring purely. The experiments in this section are divided into two steps: we first tested the RL deconvolution on image without noise, then tested the RL deconvolution on image with noise generated following the Poisson law. For both situations we further added TV regularization in a different experiment. We propose to apply the TV regularization for accelerating the convergence and reduce the negative influence of high frequencies when Poisson noise was included.

- **RL deconvolution on image without noise**

  This step aims to investigate the RL deconvolution in 3D with a known PSF and without noise. Two different volumes: a cube (thickness 1 cm) and an image "RADON" (thickness 1 cm) were convolved by a 3D Gaussian filter ($\sigma = 2$) without noise. The RL deconvolution was applied to the convolved 3D volume. Results in figures 4.9 and 4.10 show that with a known filter, RL deconvolution converges towards the undegraded image. In our example 1000 iterations are required to recover the cube and more iterations (about 2×10^4) are needed for the more complex image "RADON".

  We propose to apply total variation regularization to RL deconvolution for accelerating the convergence. The two slices in figure 4.11 are obtained after 200 iterations without

(central line) and with (last line) TV regularization. Figure 4.12 shows the central profile of slices in figure 4.11, one can tell the RL deconvolution has not converged. The slice in the center line of figure 4.11 has blurred edges because the RL deconvolution needs more iterations to converge. The last line in figure 4.10 is compared to the last line in figure 4.11, it may be seen that TV largely accelerates the RL deconvolution and helps to converge to an acceptable result. However, for an image convolved by a Gaussian filter, the TV regularized deconvolution will not give an exactly accurate recovery as the RL deconvolution do. The advantage of applying TV regularization is that it demands much less time to reach an acceptable result: not as exact as the ground truth but well deblurred visually. The MSE of deconvolution by TV-RL decreases faster than RL in the first iterations (see figure 4.11). The difference between MSE of each iteration is plotted in figure 4.13 to show the convergence. For TV-RL this value tends to zero earlier than RL, which proves that TV-RL converges faster.

- **RL deconvolution on Poisson distributed noisy image**

  In this step we investigated the RL deconvolution and TV regularized RL deconvolution on images with Poisson distributed noise. The 3D volume "RADON" was first convolved with a 3D Gaussian filter. The Poisson noisy volume is then generated by Matlab function *"poissrnd"* with mean value equals to the convolved 3D volume. Results show that with Poisson distributed noise the RL deconvolution will not be able to converge, and the TV regularization can effectively lead the deconvolution to a better recovery. The restoration is stable with TV regularization. The slices in figure 4.14 are obtained after 500 iterations of RL deconvolution with (below) and without (central) TV regularization, the TV weight $\alpha = 0.01$. The central profiles are presented in figure 4.15.

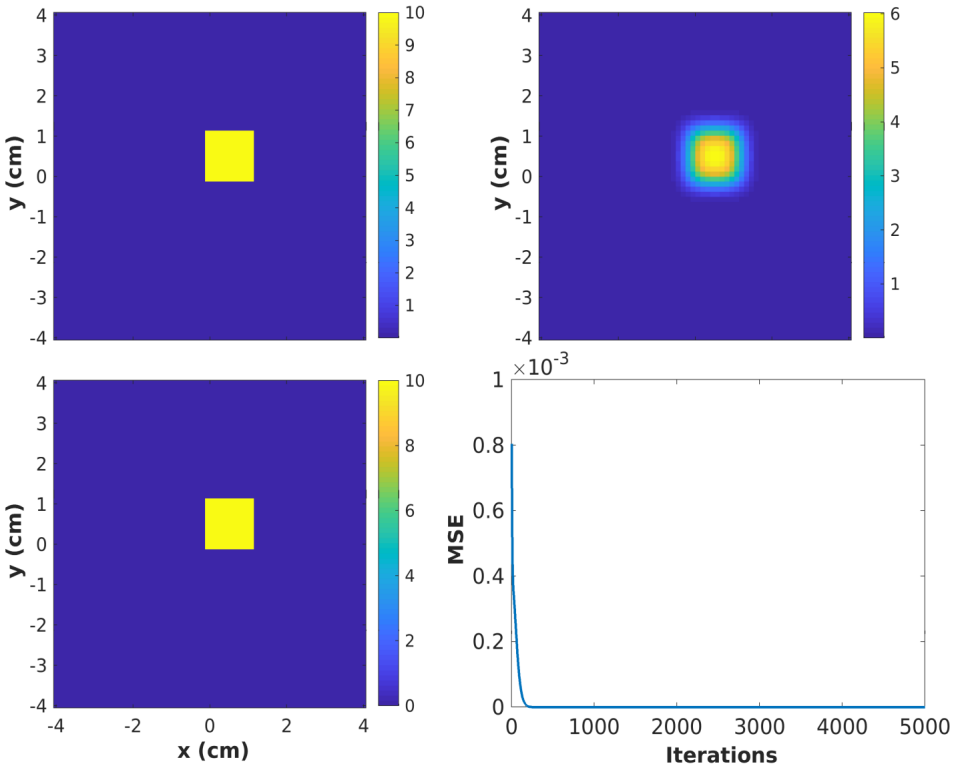

Figure 4.9: Central slices of the initial cube, convolved cube (without added noise) and deconvolved cube after 5,000 iterations and the mean squared error.

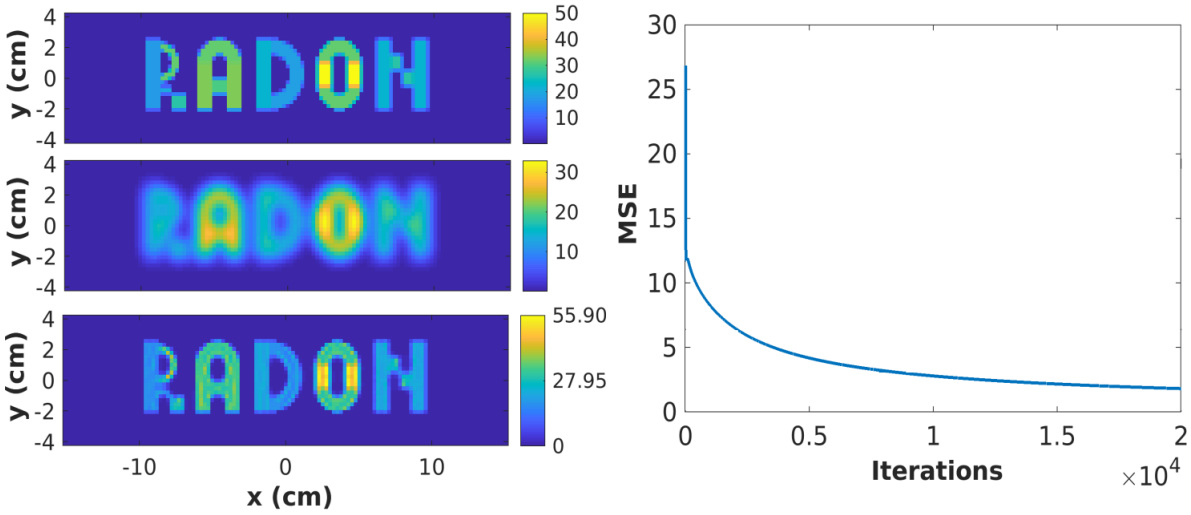

Figure 4.10: Central slices of the initial image, convolved image (without added noise) and deconvolved image after 20,000 iterations and the mean squared error.

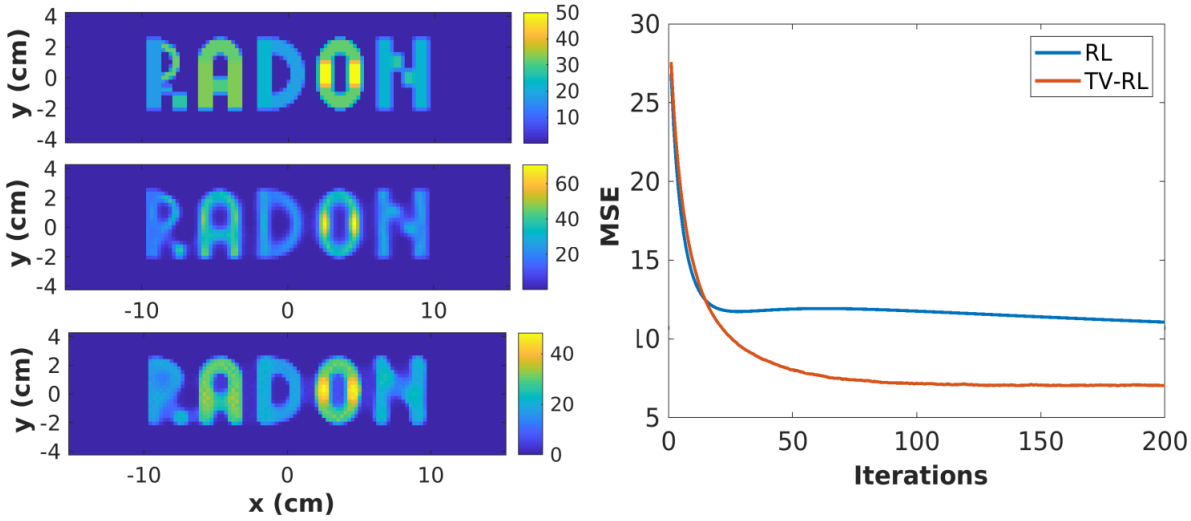

Figure 4.11: Central slices of the ground truth, the RL deconvolved image, the TV regularized RL deconvolved image (without noise) after 200 iterations and the mean squared error. The TV weight was set as $\alpha = 0.02$.

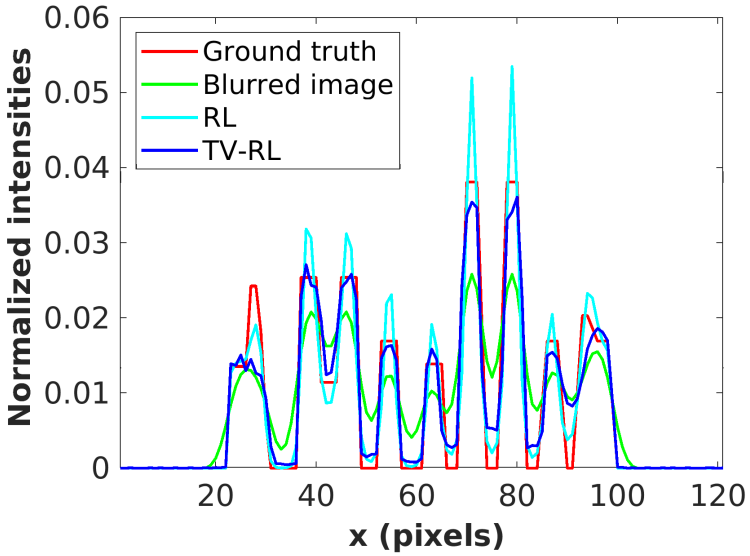

Figure 4.12: Central profiles of deconvolution for image without noise after 200 iterations.

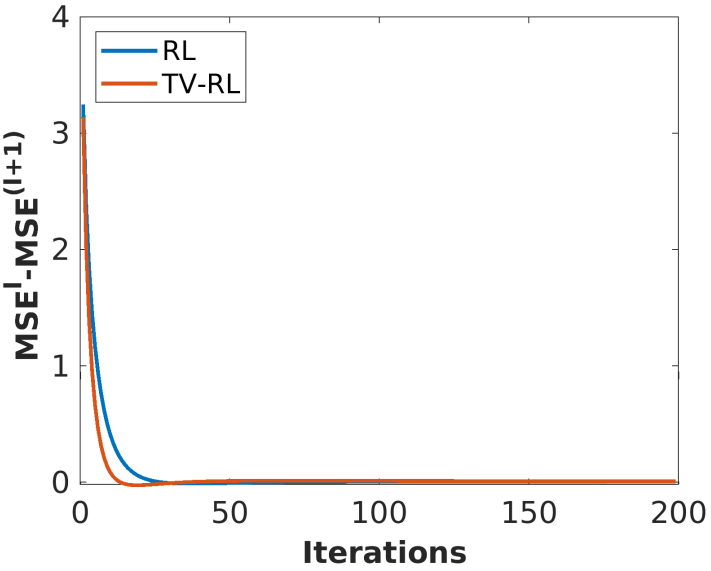

Figure 4.13: Difference of MSE between each iteration for deconvolved image (without noise).

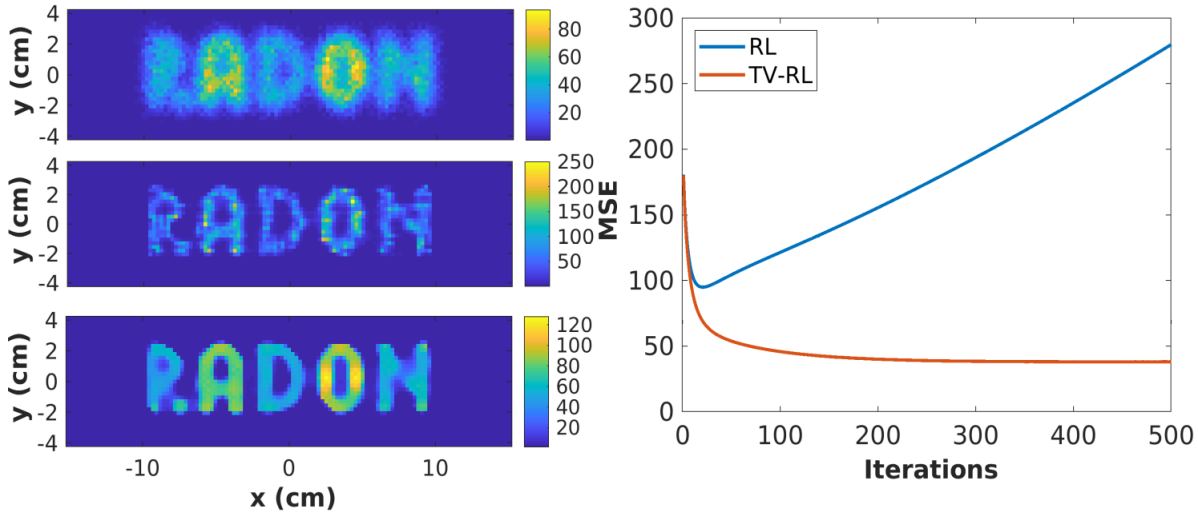

Figure 4.14: Central slices of the convolved image with Poisson distributed noise, the deconvolved volume with and without TV regularization after 500 iterations of RL deconvolution and the mean squared error. The TV weight was set as $\alpha = 0.01$.

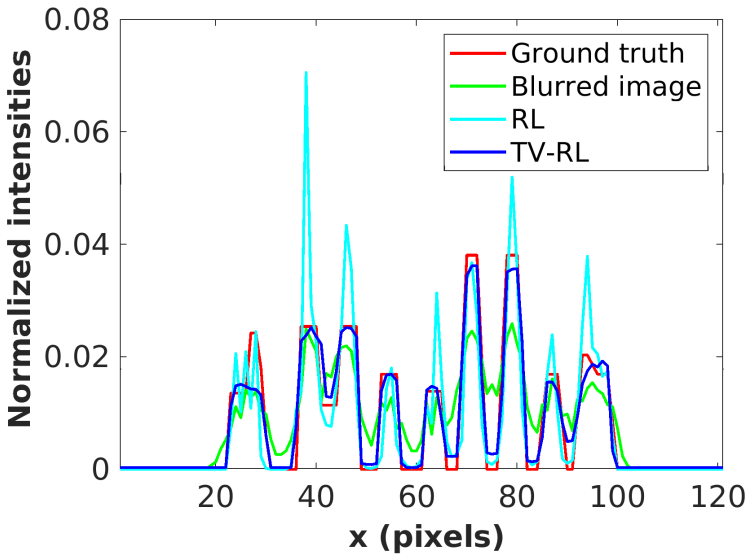

Figure 4.15: Central profiles of deconvolution for image with Poisson distributed noise after 500 iterations.

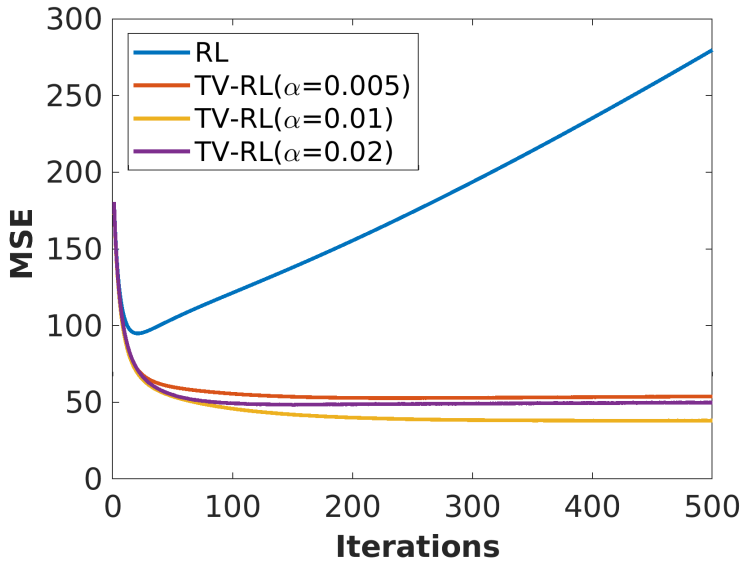

Figure 4.16: MSE with different TV weight α for deconvolution on Poisson distributed noisy image as function of RL iteration number.

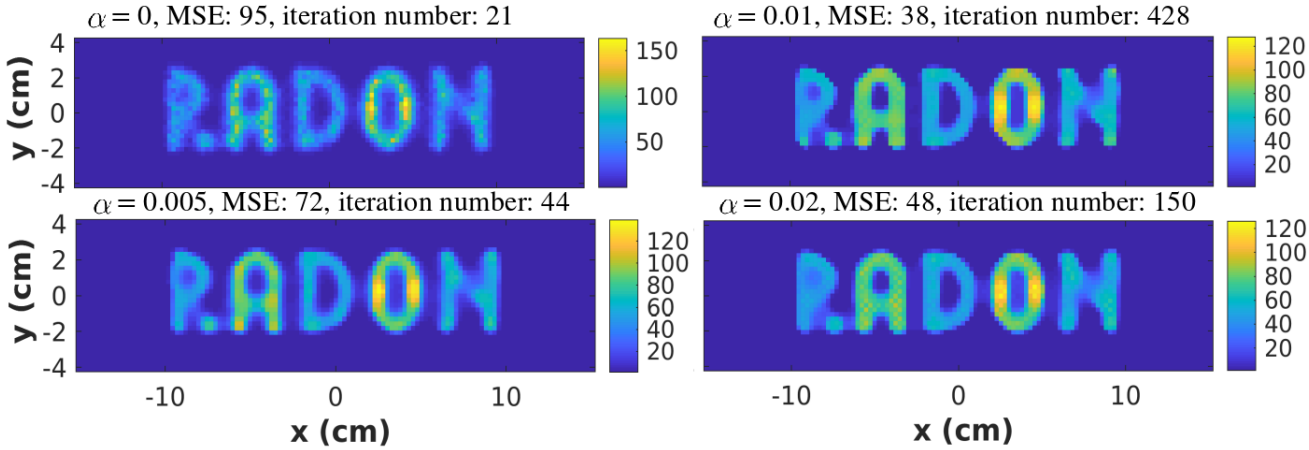

Figure 4.17: Central slices of the deconvolved images with different TV weights when MSE is minimum.

The choice of TV weight is essential to the result, a large α will yield the deconvolution to a solution too smooth and a small α will not help the deconvolution to converge. Figure 4.16 shows the details on the change of MSE with different TV weights. Figure 4.17 shows the central slices of recovery with different α. The experiments are summarized in table 4.2.1.

Parameters of TV-RL		
TV weight (α)	minimum of MSE	Iterations required
0	95	21
0.005	72	44
0.01	38	428
0.02	48	150

The investigation in this section shows that the RL method is a solution for resolution recovery in image space if the PSF is well known. Results also show that for Poisson noise, a regularization step is needed for deconvolution being able to converge. For a photon detection

imaging system, data are usually combined with Poisson noise, which gives us the reason to investigate the TV regularization on PSF-MLEM reconstruction. In the following we will first illustrate the state of the art of PSF deconvolution for Compton camera imaging reconstruction and then investigated the TV regularized PSF-MLEM. Usually, the PSF can be estimated or measured in medical imaging. Note that when the PSF can not be measured, TV regularization is worth investigated (Rudin and Osher [1994], Chan and Wong [1998], Chan et al. [1996], Carter [2001]) because some unknown PSFs might also have edges, which refers to blind deconvolution. However, we didn't investigate the blind deconvolution of TV because finding a proper regularization weight α can be difficult. We first estimated the PSF by simulation, then investigated the standard deconvolution with the estimated PSF, TV is then applied as regularization for reconstruction.

4.2.2 EM-RL reconstruction for Compton camera imaging

Applying the image-space PSF method to EM reconstruction for noise and edge artifacts reduction was originally introduced by Snyder et al. [1987]. Noise and edge artifacts are two fundamental features that impact the quality of the maximum likelihood tomographic reconstruction. The Poisson generated by photon counting and the unconstrained maximum likelihood estimation will cause the noise artifacts. During the past decades, many researchers have studied the possibility of resolution recovery for PET reconstruction by PSF deconvolution (Reader et al. [2003], Cloquet [2010], Rapisarda et al. [2010], Stute and Comtat [2013]). Incorporating the image-based shift-variant (SV) PSF into the expectation maximization (EM) algorithm for PET reconstruction was first proposed by Reader et al. [2003]. Their study compared the space variant (SV) and anisotropic PSF model to a shift-invariant and isotropic PSF model. The results proved that incorporating the convolution with adaptive SV and anisotropic PSF in reconstruction can help to ameliorate the resolution. Meanwhile, if the PSF is not well-adjusted the artifacts may arise. The Gibbs ringing may occur even with an appropriate model. These phenomena had latterly been observed and investigated by Stute and Comtat [2013]. In Stute and Comtat [2013] authors investigated the influence of different reconstruction parameters on the edge artifacts, for example the number of iterations, the non-negativity constraint, the PSF width and the numerical precision (e.g. float and double influence). Their study showed that the function form (e.g. Gaussian, Cauchy, etc.) used for PSF estimation will impact the result in terms of the resolution recovery but the most important factor is FWHM. Deconvolution will suppress the edge artifacts while the FWHM of the estimated PSF is as close as to the true PSF.

The use of PSF deconvolution for Compton camera imaging was first proposed by Kim et al. [2013]. They considered three different functions to model the 3D SV-PSF: Gaussian, Cauchy and general parametric functions. In Jan et al. [2018] authors evaluated the method on proton gamma beam, the tested SV-PSF model is presented as a 3D spatially variant Gaussian. The EM reconstruction aims to estimate iteratively the distribution of γ, and often the computation costs too much time. Adding the two convolution kernel in each iteration of MLEM will further increase the computation costs. In Jan et al. [2018], authors proposed to apply a post deconvolution after several iterations instead of inserting the deconvolution in each iteration. The obtained image by post RL deconvolution was not restored as well as the one obtained by EM-RL, but the quality was acceptable. The high frequencies increased in EM reconstruction will lead to unexpected peak and influence the estimation of PSF model. Most of the researchers proposed to add a post Gaussian convolution for smoothing the result (Stute and Comtat [2013], Kim et al. [2013], Jan et al. [2018]).

We investigate a TV-regularized EM reconstruction with PSF deconvolution method for the

data simulated with realistic detectors with a high level of noise caused by low statistics. Results show that the included deconvolution in each iteration of TV regularized MLEM, could be a possible solution for appropriate resolution recovery in Compton tomographic reconstruction, by reducing the ringing artifacts and the noise.

The MLEM algorithm consists in calculating, starting from some initial value $\widehat{\lambda}^0 \in (\mathbb{R}_+^*)^J$, the sequence:

$$\widehat{\lambda}_j^{(l+1)} = \frac{\widehat{\lambda}_j^{(l)}}{s_j} \sum_i \frac{t_{ij} y_i}{\sum_k t_{ik} \widehat{\lambda}_k^{(l)}}, \tag{4.49}$$

if the algorithm converges we will have:

$$\widehat{\lambda} = \lim_{l \to \infty} \widehat{\lambda}^{(l)}, \tag{4.50}$$

where $\widehat{\lambda}$ is the estimated average of emission defined in (4.19). We model the uncertainties of measurement by a convolution with $\mathbf{k}$, which means the measurement is now $T(\mathbf{k} \otimes \lambda)$. If the $\mathbf{k}$ is rotational invariant, the convolution with $\mathbf{k}$ is also the correlation with $\mathbf{k}$, the sequence in 4.49 can be expressed as:

$$\widehat{\lambda}^{(l+1)} = \frac{\widehat{\lambda}^{(l)}}{s}(R \otimes \mathbf{k}), \quad \text{with } R = T^T \left[\frac{1}{T(\widehat{\lambda}^{(l)} \otimes \mathbf{k})} \right]. \tag{4.51}$$

This modeling of uncertainties will introduce two additional convolutions during each iteration. The advantage of modeling the uncertainties in the image space is the simplicity of implementation for both projection and list-mode data based reconstruction. Since the SV-PSF is image-based and corresponds to the uncertainties caused by energy and position measurement, different camera geometries and different reconstruction geometries will certainly lead to different kernel $\mathbf{k}$. In the next section we investigated the SV-PSF deconvolution by Monte Carlo simulation with a fixed camera geometry used in the previous chapter (3.3.1). The first simulation was a voxelized source "RADON" convolved with a known PSF, a 3D Gaussian filter ($\sigma = 2$) same as the one used in the two previous sections, no uncertainty was considered during the simulation, even the Doppler broadening was disabled. The second simulation was obtained with unknown PSF, both uncertainties on the detection of energy and position were considered. The estimation of unknown PSF is detailed in section 4.2.4.

4.2.3 TV-EM-RL with known PSF

We first tested the RL-EM with a known PSF model. The simulated voxelized source is "RADON" convolved with a 3D Gaussian filter ($\sigma = 2$), corresponds to $\lambda * \mathbf{k}$. During the simulation no uncertainty was added and the measurement was supposed to be ideal. Results shown in figure 4.18 were obtained after 20 iterations with 2×10^5 detected events. The simulated geometry is presented in figure 4.5. The post-deconvolution without TV regularization will not help to compensate for the degraded reconstruction. The TV regularized post deconvolution ameliorates the reconstructed image, while the degradation is still stronger than the EM-RL and TV-EM-RL.

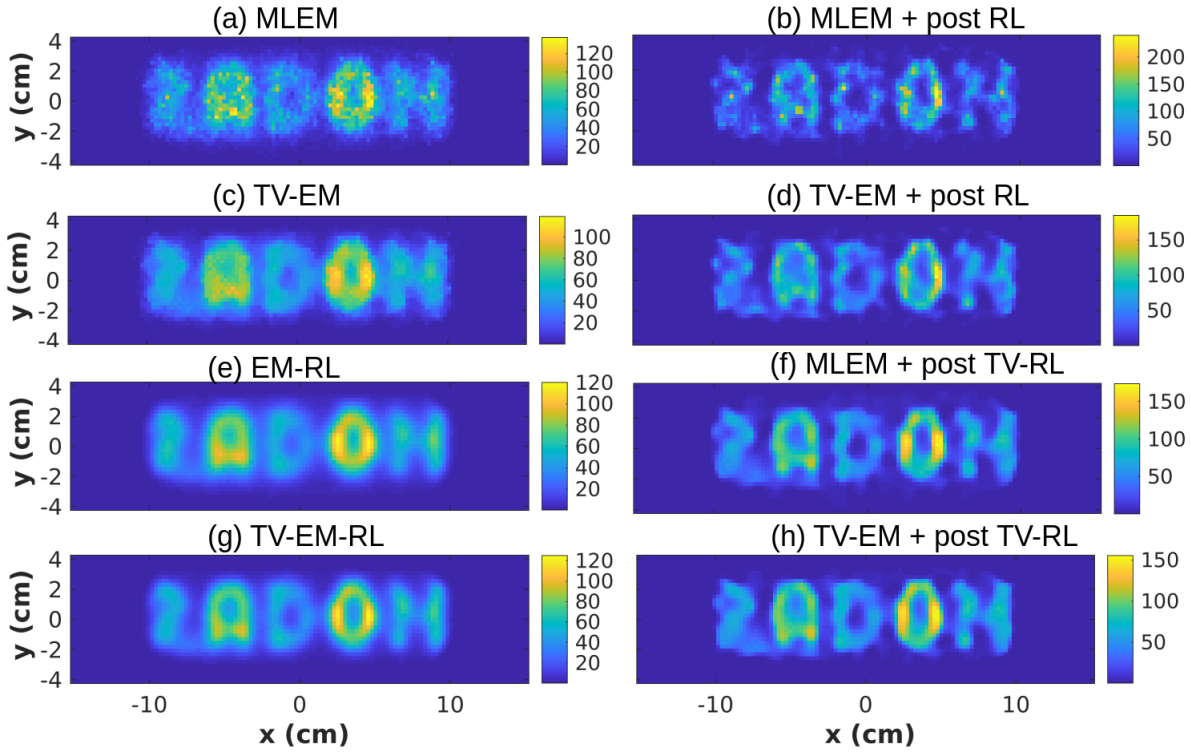

Figure 4.18: Central slices of reconstruction after 20 iterations. The tested methods are: (a) MLEM reconstruction, (b) previous reconstruction with a post RL deconvolution added in the 20th iteration, (c) TV regularized MLEM reconstruction, (d) previous reconstruction with a post RL deconvolution added in the 20th iteration, (e) MLEM reconstruction with deconvolution in each iteration, (f) MLEM reconstruction with a post RL deconvolution added in the 20th iteration, the post RL deconvolution is regularized by TV, (g) TV regularized MLEM reconstruction with RL deconvolution added in each iteration, (h) TV regularized MLEM reconstruction with a TV regularized post RL deconvolution added in the 20th iteration. All the RL iteration numbers were set to 20.

4.2.4 TV-EM-RL with unknown PSF

The PSF in this part is estimated by Monte Carlo simulation. We first estimate the PSF in different positions of a defined volume by reconstructing the point like sources simulated by MEGAlib. Then we reconstruct the image of a γ source by list-mode MLEM, EM-RL, and TV-EM-RL.

- **PSF estimation using Monte Carlo Simulation**

  Figure 4.19 represents the geometry of simulation. The center of the first scattering layer of the camera was located at (0, 0, −10) cm. The center of the reconstructed volume was located at (0, 0, −3) cm. The size of the reconstructed volume is $10 \times 10 \times 8$ cm^3 divided into $80 \times 80 \times 64$ voxels. We separately simulated sphere sources with 10^6 events emitted at each simulation, energy 511 keV, radius 1 mm. The distribution of sphere sources on one slice parallel to the camera is illustrated in figure 4.19 (c). Sources were simulated at different positions (x, y, z), x varies from −4 cm to 4 cm, y varies from −4 cm to 4 cm, z varies from −6 cm to −1 cm with a sampling of 1 cm.

  To investigate the shape of PSF, we reconstructed the image by methods validated in chapter 3 section 3.5. We took the reconstruction result after 50 MLEM iterations and

smoothed the result by convolving the result with a Gaussian filter ($\sigma_g = 2$ in pixels, FWHM = 6 mm). 2×10^5 detected events were used for reconstruction.

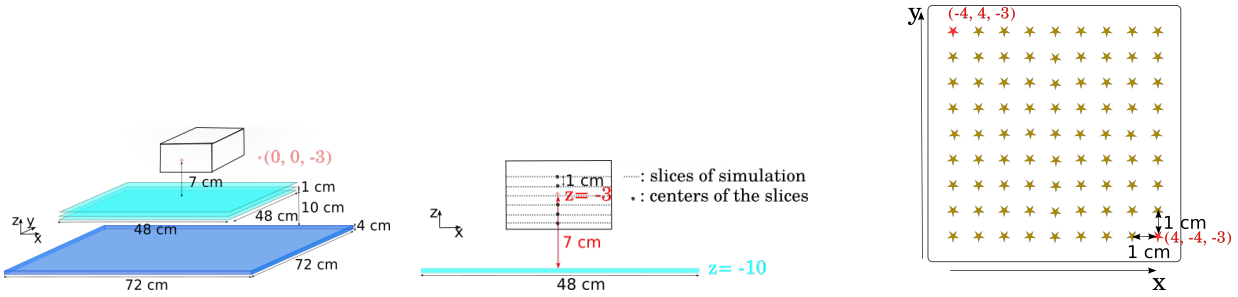

(a) simulation geometry (b) central cut of plane xz (c) simulated sources on (x, y, -3)

Figure 4.19: Illustration of the geometry of reconstruction for PSF estimation, the center of the reconstructed volume is located at (0, 0, −3) cm, distance 7 cm to the first scattering layer of the simulated Compton camera. The dashed lines in (b) correspond to the planes where the sphere sources were simulated. The plane closest to the camera is centered at (0, 0, −6). The distance between each plane is 1 cm. (c) illustrates the 81 sphere sources (represented by stars) simulated separately on the plane z = −3.

We modeled the PSF convolved with the smoothing filter by a 3D shift-variant Gaussian expressed as:

$$k_j(x,y,z) = -a \times \exp\Big\{ -0.5 \times \Big[\Big(\frac{x-\mu_x(j)}{\sigma_x(j)}\Big)^2 + \Big(\frac{y-\mu_y(j)}{\sigma_y(j)}\Big)^2 + \Big(\frac{z-\mu_z(j)}{\sigma_z(j)}\Big)^2\Big]\Big\} \quad (4.52)$$

where the standard deviation in each dimension is given as:

$$\sigma_x(j) = \begin{cases} \sigma_x^{\text{left}}(j) & x < \mu_x(j) \\ \sigma_x^{\text{right}}(j) & x > \mu_x(j) \end{cases} \quad (4.53)$$

and the estimated σ is calculated by:

$$\sigma_x(j) = \sqrt{\sigma_x(j)^2_{\text{estimated}} - \sigma_g^2} \quad (4.54)$$

In figure 4.20 we show profiles of the reconstruction PSF convolved with the smoothing filter (solid lines) together with profiles of the fitted Gaussian function (dashed lines). For the sources on the z axis, having coordinates (0, 0, z) with z = −6, ... −1, corresponds distance from 4 cm to 9 cm to the first layer of camera. The profiles are obtained from the vertical central rows from the volumes. The 3D Gaussian model is not well fitted when the distance to camera increases. The central slices of the reconstruction MLEM, MLEM with post smoothing and adjusted 3D Gaussian function for the central PSF (position (0, 0, −3) cm) are shown in figure 4.21. We interpolated the fitted parameters to get parameters in each voxel.

- **Results of TV-EM-RL on unknown PSF**

  We simulated the source in the form of letter "O" centered at (0, 0, −3) and placed parallel to the camera, the thickness of "O" in z direction was 1 cm. The event counts were 200,000. Figure 4.22 shows the central slices of the reconstruction obtained from Monte Carlo simulated realistic data. The PSF deconvolution is used for resolution recovery in the second and third line in figure 4.22.

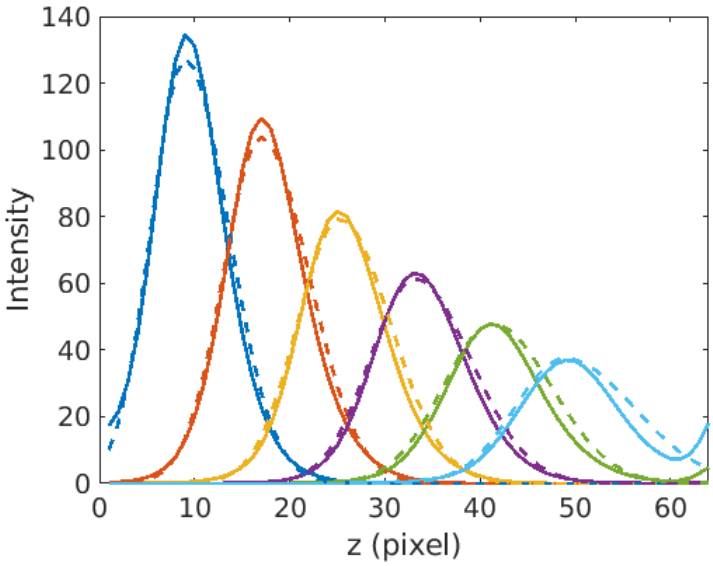

Figure 4.20: PSF reconstruction and fit along the vertical direction for sources placed on (0, 0, z), z varies from −6 to −1 cm, corresponds to the distance varying from 4 to 9 cm to the camera. The solid lines represent the reconstruction after 50 iterations of MLEM with post smoothing by a Gaussian filter (FWHM = 6 mm), the dashed lines represent the fitted 3D Gaussian in vertical direction. The size of the pixel is 1.25 mm.

4.3 Related publications

The proposed TV denoising method was applied in a study presented in appendix (see page 133), in which we aim to evaluate the imaging capabilities of the Compton camera independently of the detection technology, of the geometry or other factors that affect the results of a real detector. An ideal parallel hole collimated system was considered as reference. Both analytic (filtered backprojection) and iterative (maximum likelihood expectation maximization) algorithms were applied in conjunction with the TV denoising. A missing-angle acquisition for the collimated system was used in order to reproduce the covering angle of the simulated Compton camera. The results showed that Compton camera successfully competed against the missing angle collimated system in terms of uniformity in constant intensity regions. The results of this work cannot be extended directly to real detectors and clinical application. We can only infer that Compton cameras could be useful for configurations where a collimated detector cannot turn around the patient and thus missing angle data is generated. Besides, the advantage of Compton camera is more evident at high energies where the collimators become transparent, as it is the case in proton therapy.

A study on resolution recovery for Compton camera image reconstruction using more realistic data was presented at MIC 2018 (Feng et al. [2018]), where we focused on the PSF deconvolution and TV regularized MLEM reconstruction with low statistics. Results obtained with data simulated with ideal detectors and data simulated with more realistic detectors were compared. The study shows that TV a priori strongly improves the images when data are acquired in ideal conditions. For more realistic data, TV regularized MLEM reconstruction is not sufficient and the deconvolution with a pre-calculated image-space kernel should also be considered for properly recovering the reconstructed images.

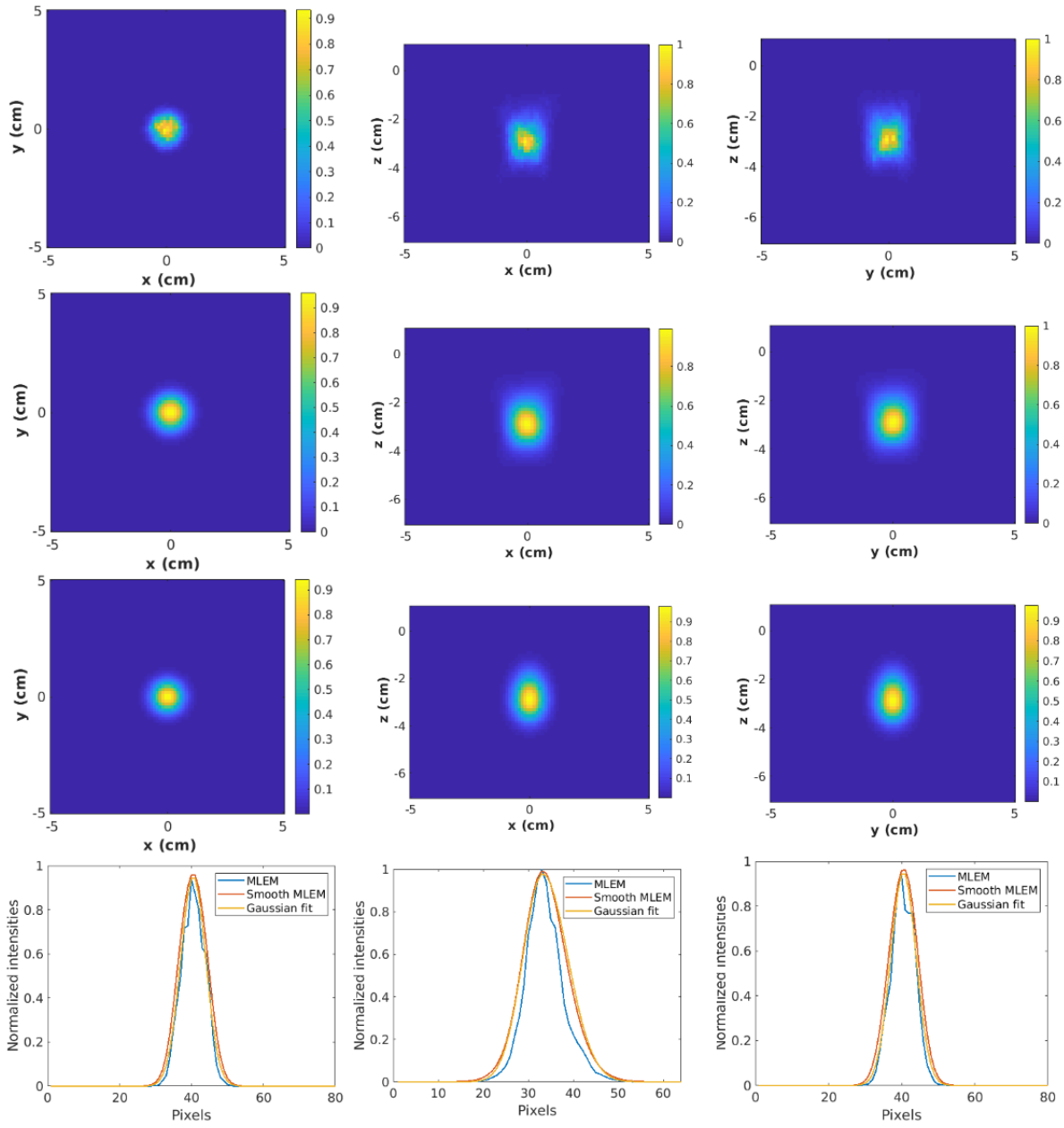

Figure 4.21: PSF calculated at the position (0, 0, −3). First line: central slices from the MLEM reconstruction of a spherical source of radius 1 mm centered at (0, 0, −3). Second line: central slices of the previous reconstruction with a post smoothing by Gaussian filter (FWHM = 6 mm). Third line: central slices of the adjusted 3D Gaussian function after the post smoothing. From the left to the right are slices on the plane: xy, xz, yz. Fourth line: central profiles along x axis, z axis, y axis.

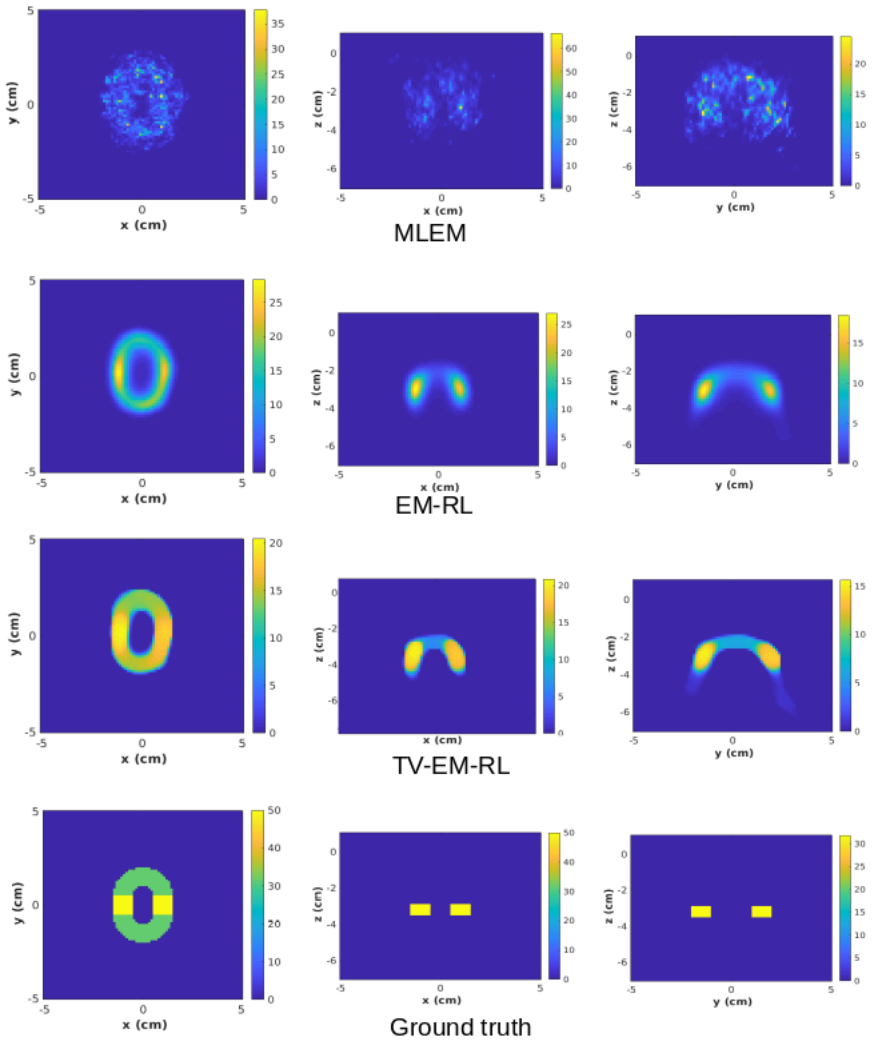

Figure 4.22: Illustration of resolution recovery with SV-PSF estimated from MC simulation. Reconstruction from data simulated with realistic detectors including measurement uncertainties. Images are obtained after 200 iterations, the first line is the result obtained by list-mode MLEM, the second line is obtained by EM-RL, the third line is obtained by TV-EM-RL, the last line is the reference image.

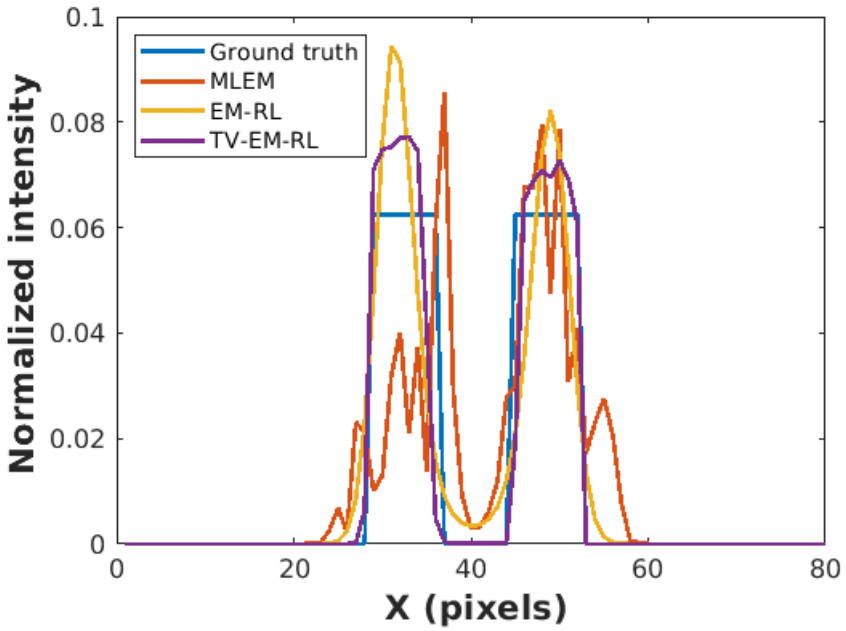

Figure 4.23: Central profiles of the reconstruction after 200 iterations.

4.4 Conclusion

In the reconstruction for Compton camera imaging which is based on the conical surface integration, due to the influence of the uncertainties in angular and position measurement, images often appear highly degraded and deformed. These uncertainties are difficult to model in the system matrix estimation. Besides, Poisson noise frequently appears when the reconstruction is generated by photon-counting devices. We investigated two methods for resolution recovery in image space to overcome the limited spatial resolution of reconstruction: TV denoising and PSF deconvolution. Several conclusion may be drawn from the obtained result.

Firstly, the TV regularized EM method largely helps the reconstruction to converge, and leads the reconstruction to a smooth denoised result while preserving the boundary information of the object. This advantage will be especially useful for proton therapy when the aim is to identify the falloff in the prompt γ profile at the end of the proton range. The disadvantage of TV-EM is that the choice of the parameter defining the regularization weight has a strong influence and is difficult to handle. Secondly, image-based PSF deconvolution might be a solution to recover the spatial resolution of blurred images. If the PSF is well known, without Poisson distributed noise, the RL deconvolution will converge to ground truth in image space. For Poisson distributed noised image the capability of deconvolution is limited, resolution recovery will diverge after several iterations and deblurred image will be over deconvolved. TV regularized deconvolution might be a solution for decreasing the Poisson distributed noise in image space. If the regularization weight is well chosen, TV-RL will produce an acceptable result. Thirdly, in the MLEM reconstruction, the deconvolution will not be able to converge to the ground truth even with a well known PSF. The post deconvolution can reduce the time cost but recovery is more limited compared to EM-RL. To balance the image denoising and deblurring while conserving the boundary of object, we propose to apply TV-EM-RL method for reconstruction. We believe that the TV-EM-RL is a proper option for spatial resolution recovery of MLEM reconstruction for Compton camera imaging. Since the computation of regularization and deconvolution is added in the image space, this method can be easily extended to other imaging modalities and adapted to other reconstruction algorithms (e.g. OSEM).

The inconvenient of TV-EM-RL is that the estimation of image-based PSF depends on the reconstruction set (reconstruction volume, event counts, etc.) and simulation geometry (material of camera, source energy, etc.). In practice the change of one of those factors will require the change of estimated PSF.

Part V

Reconstruction of prompt gamma ray in hadron therapy

Résumé en français

Le traitement par hadrons est une forme de radiothérapie qui utilise des particules lourdes appelées hadrons. Les particules lourdes les plus couramment utilisées sont les ions carbone et les protons. L'application des faisceaux d'hadrons dans le traitement des tumeurs radiorésistantes a été proposée par Robert R. Wilson en 1946 et a été utilisée pour la première fois pour traiter des patients en 1954 au laboratoire de Berkeley. Depuis lors, plusieurs centres ont été construits dans le monde, par exemple : NIRS-HIMAC (Japon), HIT (Allemagne), CNAO (Italie), Shanghai Proton and Heavy Ion Hospital (Chine), MedAustron (Autriche), Institut Paul Scherrer (Suisse), Centre de protonthérapie de l'Institut Curie (Paris, France), Institut Méditerranéen de ProtonThérapie (Nice, France), etc.

L'idée de l'hadronthérapie est d'utiliser les rayonnements ionisants pour tuer les cellules malignes lorsque les techniques classiques comme la chirurgie, la chimiothérapie, la radiothérapie classique ne peuvent être utilisées. La radiothérapie classique permet une diffusion non uniforme du flux de photons en utilisant les techniques de la radiothérapie à modulation d'intensité (IMRT). En utilisant un accélérateur linéaire à haute énergie (4-20 MeV), la dose d'irradiation peut être délivrée en différentes directions. Cependant, l'efficacité thérapeutique est limitée par le profil de dose en profondeur du photon. Cette contrainte limitera la précision d'irradiation d'une tumeur située profondément à l'intérieur de l'organe. Comme le profil de dose en profondeur est presque plat à l'exception de l'entrée, les tissus sains après la tumeur peuvent être irradiés. De plus, pour certaines tumeurs radiorésistantes, le carbone pourrait avoir une meilleure efficacité biologique. La thérapie par hadrons peut surmonter le manque de radiothérapie classique par une balistique améliorée grâce à la forme spécifique de la distribution de la dose déposée. A la fin de la portée du faisceau, un maximum d'énergie est fourni à l'objet. La région du pic de perte d'énergie pendant le trajet du rayonnement ionisant est appelée pic de Bragg. La position du pic de Bragg peut être décalée en profondeur en faisant varier l'énergie initiale des ions. Selon la vitesse et l'énergie, les ions ou protons chargés peuvent atteindre jusqu'à 30 cm de profondeur dans les tissus.

La détection précise du pic de Bragg est essentielle pour assurer la qualité du traitement en hadronthérapie. La plupart des techniques de vérification sont basées sur la détection du rayonnement secondaire généré par la réaction nucléaire pendant le déplacement des ions. Comme les réactions nucléaires peuvent se produire tout au long du trajet des ions jusqu'au pic de Bragg, l'émission de rayonnement secondaire est corrélée aux ions primaires. Il est prouvé que deux types de gamma peuvent être utilisés dans la pratique clinique pour les systèmes de surveillance de la dose : les paires gamma résultant de l'annihilation du positon, où la TEP est appliquée (Enghardt et al. [2004]) pour la détection ; et le rayon gamma dit prompt, où la caméra collimatée est utilisée (Min et al. [2006]). La caméra Compton est un autre appareil possible pour la surveillance de la dose en hadronthérapie. En utilisant la collimation électronique, la caméra Compton peut augmenter l'efficacité de détection. La simulation réalisée par Krimmer et al. [2015] a montré que l'efficacité de détection peut passer de 10^{-5} (caméras collimatées) à 10^{-4} (caméras Compton) pour les systèmes de balayage à faisceau crayon ou PBS (Pencil Beam Scanning). L'imagerie par caméra Compton nécessite des algorithmes spécifiques pour recons-

truire l'image de la source. Le faible nombre de comptages et les incertitudes d'acquisition imposent l'utilisation de l'information a priori. Dans ce chapitre, nous présenterons le résultat de la reconstruction sur les données des γ prompts simulés par l'IPNL et montrons le résultat obtenu à partir de l'algorithme présenté dans le chapitre précédent. Le résultat obtenu dans ce chapitre a été présenté dans la conférence PTCOG58.

Chapter 5

Compton camera imaging reconstruction for proton monitoring

5.1 Hadron therapy and Bragg peak identification

Hadron therapy is a form of radiotherapy that uses heavy particles called hadrons. The most commonly used heavy particles are carbon ions and protons. Applying hadron beams in cancer therapy for radio-resistant tumors was proposed by Robert R. Wilson in 1946 and was first used to treat patients in 1954 at Berkeley laboratory. Since then several centers have been built all over the world, e.g.: NIRS-HIMAC (Japan), HIT (Germany), CNAO (Italy), Shanghai Proton and Heavy Ion Hospital (China), MedAustron (Austria), Institut Paul Scherrer (Switzerland), Centre de protonthérapie de l'Institut Curie (Paris, France), Institut Méditerranéen de Proton-Thérapie (Nice, France), etc.

The idea of hadron therapy is to use ionizing radiation to kill malignant cells when classical techniques such as surgery, chemotherapy, classical radiotherapy cannot be used. Classical radiotherapy allows a non-uniform photon flux delivery by using the techniques of Intensity Modulated Radiotherapy (IMRT). By using high-energy (4-20 MeV) linear accelerator the irradiation dose can be delivered from different directions. However, the therapeutic effectiveness is limited by the depth dose profile of photons. This constraint will restrict the irradiation precision of tumor situated deep inner the organ. Since the depth dose profile is almost flat except the entrance, the healthy issues after the tumor might be irradiated. Besides, for some radioresistant tumors carbon might have better biological efficiency. Hadron therapy can overcome the shortage of classical radiotherapy by an improved ballistics through the specific shape of the distribution of the deposited dose. At the end of the beam range, a maximum of energy is delivered to the object. The region of energy loss peak during the travel of ionizing radiation is called Bragg peak. Fig. 5.1 shows the relative depth dose distribution of photons, protons and carbon ions with different initial energies in water. This figure is obtained from Grün [2014]. The Bragg peak position can be shifted in depth by varying the initial energy of the ions. Depending on speed and energy, charged ions or protons can reach up to 30 cm deep into the tissue. Usually a gantry is used for allowing direct rays at the patient from any direction. The system for quality assurance is usually composed of: an intensity-modulated raster scan procedure, assures the high-precision dose distribution; on-line therapy control that check up the rays. All those equipments and techniques assure the protons and carbon ions being directed with the highest precision. Figure 5.2 is a schematic demonstration of Heidelberg Ion Beam Therapy Center, source obtained from the site: [1].

[1] https://www.heidelberg-university-hospital.com/diseases-treatments/tumor-diseases/proton-therapy-and-carbon-ion-therapy/

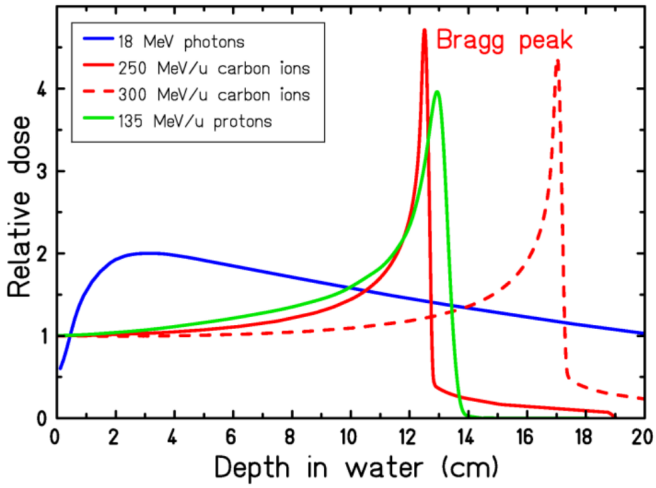

Figure 5.1: Relative depth dose distribution of photons, protons and carbon ions with different initial energies in water. Image source: Grün [2014].

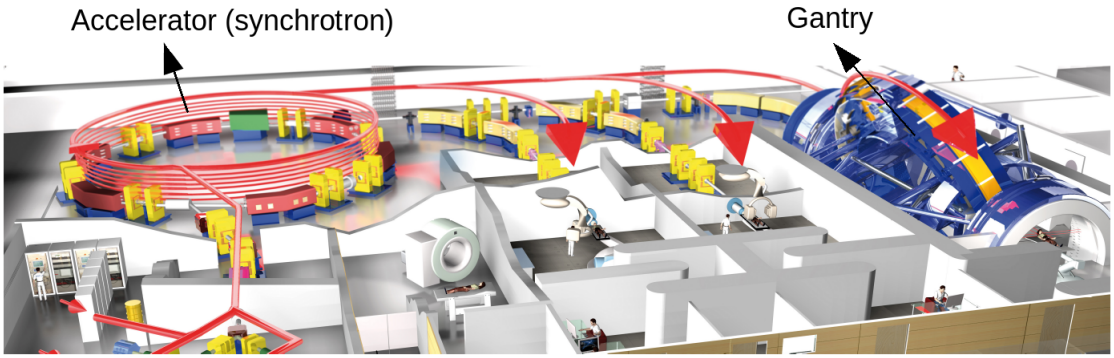

Figure 5.2: Schematic demonstration of Heidelberg Ion Beam Therapy Center.

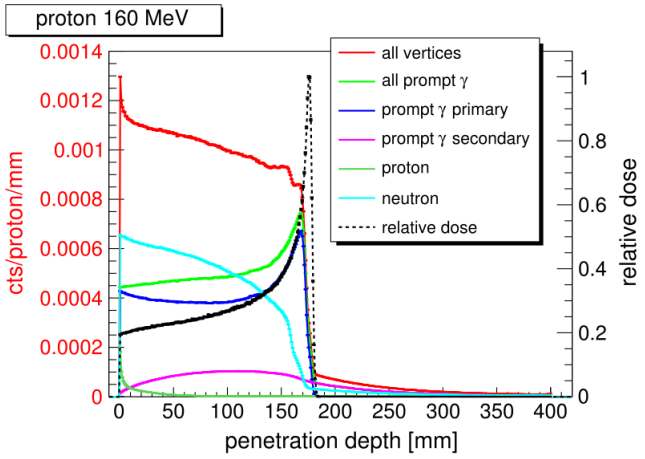

Figure 5.3: Emission vertices of secondaries emitting from a homogeneous water cylinder (15 cm diameter, 40 cm length) irradiated by a 160 MeV proton beam. Image source: Krimmer et al. [2018].

Accurate detection of Bragg peak is essential to assure the quality of treatment in hadron therapy. Most of the range verification techniques are based on the detection of secondary radiation generated by the nuclear reaction during the ions travel. Since the nuclear reactions may occur all along the ions travel path until the Bragg peak, secondary radiation emission is correlated to the primary ion range. It is proved that two kinds of gamma photons can be used for range monitoring system in clinical practice: the coincident gamma from positron annihilation, where PET is applied (Enghardt et al. [2004]) for the detection; and the so-called prompt gamma ray corresponding to a prompt emission of high-energy photons, where the γ camera can be used. The detection of prompt gamma for monitoring in hadron therapy is first proposed by Stichelbaut and Jongen [2003] and later be proved in many studies (Min et al. [2006], Testa et al. [2008], Krimmer et al. [2018]). Figure 5.3 illustrates the distribution of prompt secondary radiation emitting from a homogeneous water cylinder (15 cm diameter, 40 cm length) irradiated by a 160 MeV proton beam. This figure is obtained from the GEANT4 simulation in Krimmer et al. [2018], for practical reasons a threshold of 1 MeV for energy detection was set. One can notice the correlation between the prompt gamma peak and the relative dose peak.

Apart from the collimated camera, Compton camera is another possible prompt gamma imaging device for the dose monitoring in hadron therapy. By using the electronic collimation, Compton camera can increase the detection efficiency. The simulation realised by Krimmer et al. [2015] showed that the detection efficiency can rise from 10^{-5} (collimated cameras) to 10^{-4} (Compton cameras) for pencil beam scanning systems. Compton camera imaging requires specific algorithms for reconstructing the image of the source. The low number of counts and the acquisition uncertainties faced in prompt-gamma imaging imposes the use of a priori information. In this chapter we will present the reconstruction result for a proton therapy experiments simulated at IPNL during the thesis of Ley [2015]. This simulation is accomplished in a study of monitoring ion beam therapy with a Compton Camera in Fontana et al. [2019]. After illustration of the simulation setup, we show the result obtained from the algorithm introduced in the former chapter.

5.2 Methods

The simulation was performed with the GEANT4 toolkit, version 9.6.02. The simulated camera is the prototype under development within the French collaboration CLaRyS (Krimmer et al. [2015]). The Compton camera was composed of a stack of 7 double-sided silicon strip detectors (scatterer) and a plane of 100 single BGO blocks (absorber). The spatial resolution at 1 MeV was 0.9 mm for the scatterer and 5 mm for the absorber. The energy resolution was 11 keV at 1 MeV for the scatterer. For the absorber, the resolution was set at 20% FWHM at the reference energy of 662 keV. A cylindrical PMMA phantom (15 cm diameter and 20 cm length) was placed 20 cm in front of the camera. The 160 MeV proton beam range of interest was 15.2 cm in the phantom. The beam time structure was 1 proton per bunch, 1 bunch every 10 ns. The considered time structure is related to IBA C230 cyclotron [2], which has been used in 16 clinical centers worldwide. The simulation features are summarized below:

Hadronic models in GEANT4	Electromagnetic Inelastic Elastic	G4BinaryCascade G4LElastic
Clinical feature	Facility Clinical intensity Energy	IBA Cyclotron C230 2 x 10^{10} p/s 160 MeV
Beam structure	Bunch time [ns] Period [ns] Primaries/bunch	3.2 9.4 217

Figure 5.4 illustrates the simulation geometry. The center of the camera is set to where the prompt γ is expected to stop, in other words where the Bragg peak is supposed to be. Only the events with two interactions are selected for reconstruction. The initial energy E_0 of detected event is unknown, and we assume that the relation $E_0 = E_1 + E_2$ holds, with E_1 and E_2 the energies deposited in the first and second interactions. 50 keV and 100 keV were set as lower thresholds for the energy deposited in a single scatterer layer and BGO block. A total absorbed energy lower limit is set to 1 MeV. Three techniques for reconstruction were tested:

1. MLEM reconstruction with n iterations

2. previous result with TV denoising added after the n^{th} iteration

3. TV regularized EM reconstruction (TV-MAP-EM)

5.3 Results and discussions

Images in figure 5.5, 5.6 and 5.7 were obtained from 1×10^3 detected events corresponding to the expected number of counts for the acquisition of a single spot in proton therapy (10^8 protons at 160 MeV). The central profiles are normalized by the maximum. The reconstructed volume was $(20 \times 40 \times 5)$ cm^3 divided into $(100 \times 200 \times 25)$ voxels. The calculation time for 20 iterations are 225.92 seconds for TV regularized EM (TV-MAP-EM) and 213.27 seconds for list-mode MLEM. The TV denoising on the previous result takes 0.65 seconds. We show the results obtained with $n = 1, 10, 20$, the expected Bragg peak is indicated by the red line.

[2]IBA Cyclotron C230: one of the accelerators produced by company Ion Beam Applications (IBA) in Belgium, for more information, see: Jongen et al. [2004].

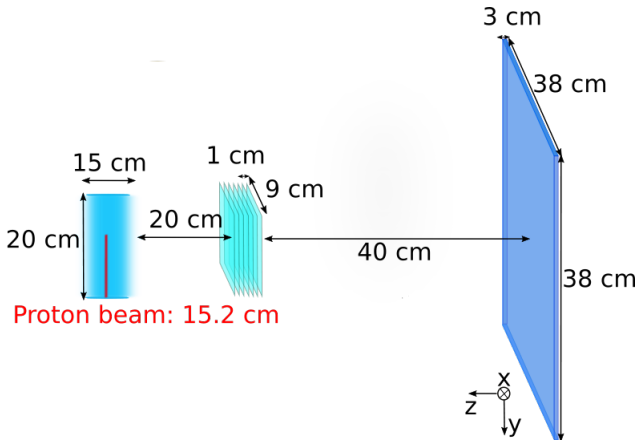

Figure 5.4: Simulation geometry of the Compton camera prototype developed by IPNL.

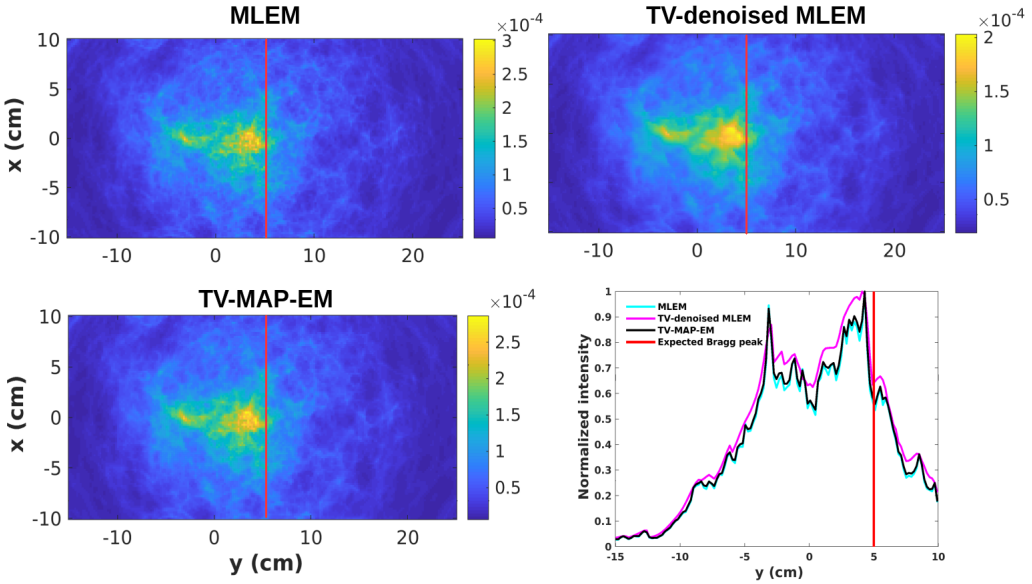

Figure 5.5: Central slices and the profile at the first iteration.

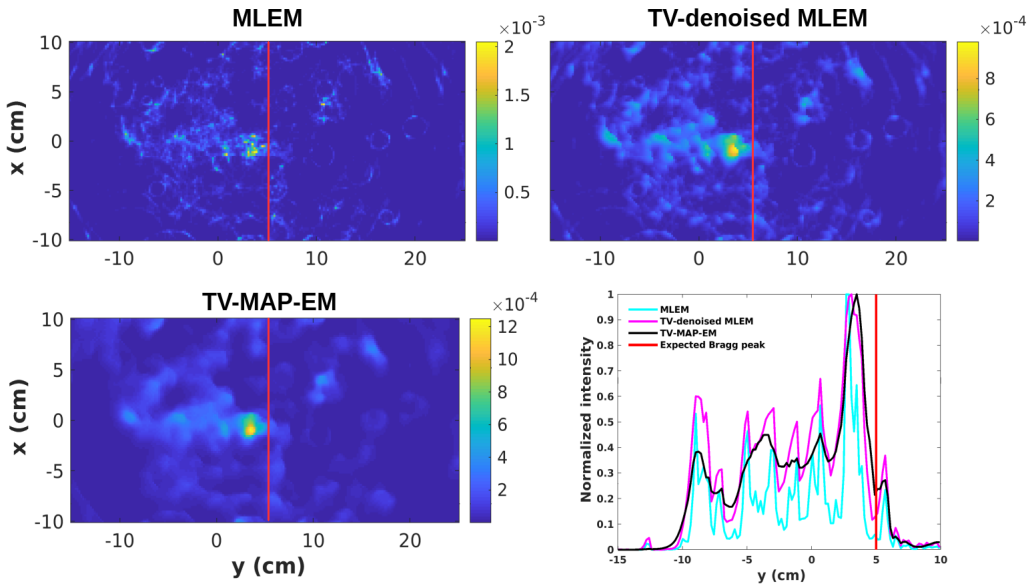

Figure 5.6: Central slices and the profile after 10 iterations.

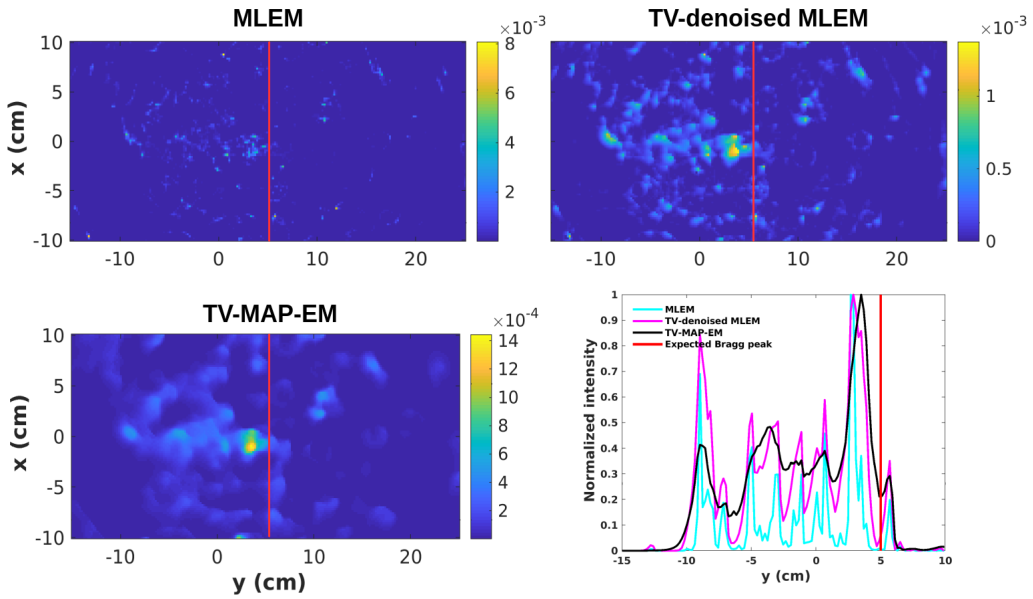

Figure 5.7: Central slices and the profile after 20 iterations.

Comparing figure 5.6 to figure 5.5, too much high frequency is introduced after 10 iterations of MLEM, which makes it difficult to distinguish the dose fall-off and might mislead the evaluation of dose profile. Comparing the result of TV-MAP-EM to the result of MLEM, the dose profile is more homogeneous, and the Bragg peak is more evident. Post TV denoising is less effective than TV-MAP-EM, but can visually ameliorate the reconstructed image, and might be a solution for time-saving. From these results, TV-MAP-EM strongly reduces the noise, largely helps the reconstruction converge and facilitates the detection of Bragg peak. These results were presented at PTCOG58 conference.

Part VI

Conclusion

Conclusion et perspectives

Tout d'abord, nous avons étudié les différents modèles mathématiques pour le calcul de la matrice de sensibilité et de le matrice de système. Les résultats obtenus sur des données sans erreur de mesure supplémentaire ont prouvé qu'avec un modèle plus adapté et un calcul de matrice de sensibilité plus précis, nous pouvons s'attendre à une haute résolution dans la reconstruction LM-MLEM. Les artefacts courants tels que le flou et l'allongement à la verticale vers la caméra ont été largement diminués. La conclusion que l'on peut tirer de cette partie est qu'une modélisation inadéquate des processus physiques pendant la reconstruction pourrait contribuer à l'amélioration de la qualité de la reconstruction. Deuxièmement, nous avons mis en œuvre une méthode de débruitage par la technique de variation totale que nous avons introduite dans le MLEM, ce qui permet d'améliorer la qualité de l'image dans les expériences de faible comptage. Nous avons montré qu'avec la régularisation de TV, l'imagerie par caméra Compton peut produire des images à haute résolution avec des détecteurs idéaux. Pour des données plus réalistes en tenant compte des erreurs de mesure, nous avons proposé d'appliquer la déconvolution de la PSF. Enfin, le résultat sur la source simulée en protonthérapie, obtenu par le MLEM régularisé par TV a prouvé qu'avec certaines améliorations, l'imagerie par caméra Compton peut fournir des images plus précises. Cela nous ramène à un des premiers essais sur l'application de la caméra Compton en hadronthérapie.

Dans cette étude, plusieurs méthodes d'amélioration de la reconstruction par l'algorithme MLEM ont été étudiées. Les méthodes mises en œuvre pour l'estimation de la matrice de système et de la matrice de sensibilité ne sont pas exactement adaptés à la simulation Monte Carlo. La méthode de déconvolution est dépendante de l'environnement donc demande une estimation de la PSF chaque fois que le géomètre est changé. De plus, le MLEM avec la régularisation de TV ne peut conduire à un résultat stable que si le poids de régularisation est bien choisi. Les approches basées sur l'apprentissage machine pourraient être l'une des options pour résoudre la difficulté de l'ensemble des paramètres et même pour réaliser l'estimation de la matrice système et de la matrice de sensibilité.

D'ailleurs, le code de reconstruction a été parallélisé par nos collègues. Cependant, le temps de calcul reste un problème à résoudre. Pour en savoir plus sur la capacité de l'imagerie par caméra Compton, d'autres techniques de reconstruction comme le OSEM devraient également être explorées car elles sont plus rapides. Par rapport à la déconvolution de la PSF comprise dans chaque itération de LM-MLEM, la post-déconvolution est moins performante mais conduit à un résultat acceptable, ce qui peut être une solution pour diminuer le temps de calcul. L'implémentation sur GPU contribuant largement à réduire le temps de calcul peut être aussi une option. En dehors des perspectives mentionnées, des nouvelles configurations de l'acquisition pour améliorer les statistiques devraient aussi être développées dans la prochaine étape.

Chapter 6

Conclusion and perspectives

This thesis aims to investigate the capability of Compton camera imaging by improving the reconstruction algorithm LM-MLEM. We investigated several mathematical models used in the MLEM algorithm and proposed a TV regularized PSF deconvolution for improving the image quality. The investigations of this study were validated by Monte Carlo simulation. This chapter summarizes our contributions and proposes some of the perspectives of Compton camera imaging in nuclear medicine.

6.1 Conclusion

Firstly, we investigated the different mathematical models for sensitivity matrix calculation and system matrix estimation. The sensitivity matrix calculation is well adapted against the Monte Carlo simulation. Results on data simulated with ideal detector without added measurement errors proved that with a more adapted model and a more accurate sensitivity matrix calculation, high resolution of reconstruction can be expected. Common artifacts often observed in Compton camera imaging such as blurring and elongation in the vertical direction to the camera were largely decreased with a more adapted model validated on ideal detector. The conclusion we might draw from this part of work is that improper modeling of the physical processes during the reconstruction will contribute to the elongation artifacts. These artifacts can be reduced by more accurate modeling.

Secondly, we implemented a total variation denoising method that we introduced in the MLEM algorithm as a regularization step for reconstruction of Poisson distributed data, which allows to improve the image quality in low-counts experiments, and can be easily extended to other imaging modalities and adapted to other reconstruction algorithms (e.g. OSEM). We showed that with this regularization the Compton camera imaging can provide high resolution images with ideal detectors. For more realistic data with measurement errors considered, we proposed to apply PSF deconvolution for resolution recovery in the image space that ameliorates the conditioning of the inverse problem. The proposed TV regularized MLEM with PSF deconvolution method improves the quality of reconstruction compared to LM-MLEM without regularization.

Finally, results on the clinically relevant simulated prompt gamma ray source obtained by GEANT4 proved that with some improvements Compton camera imaging can provide acceptable images for monitoring in hadron therapy. The capability of Compton camera to reproduce images for clinical uses needs more experiments, these results are one of the first attempts to explore the Compton camera imaging in hadron therapy.

6.2 Perspectives

In this study several methods for ameliorating the reconstruction by algorithm MLEM were realized. All the data used in this thesis were simulated at energy 511 keV, other energies should also be tested on the proposed TV regularized PSF deconvolution method. The validated calculation of system matrix is only for 511 keV, a more general model should be developed for multi-energies sources and energy selection methods should also be considered. The implemented methods for the estimation of system matrix and sensitivity matrix are still not exactly adapted to Monte Carlo simulation. The PSF deconvolution method is environment dependent and should be further studied to provide clinically relevant images. Besides, the implemented TV regularized MLEM can lead to a smoothing and stable result only if the regularization weight is well chosen. Machine learning based approaches might be one of the options to solve the difficulty of parameter set and even, to achieve the system matrix and sensitivity matrix estimation.

The computation time is still an problem to be solved. To accelerate the reconstruction the code has been parallelized by our colleagues, a GPU implementation will further largely help to reduce the time consumption. Apart from accelerating the code of reconstruction, acceleration from the algorithms might also be considered. Compared to PSF deconvolution involved in each iteration of MLEM, a post PSF deconvolution can reduce the computation time and provide an acceptable result. To investigate the capability of Compton camera imaging, other reconstruction algorithms such as OSEM should also be implemented.

Our study was based on Monte Carlo simulation. Although clinically relevant simulated data was used at the end of this thesis, whether the Compton camera devices can be used in hadron therapy still needs more experiments. GATE can serve as a proper toolkit to compare the capability of imaging by Compton camera and collimated camera in patient dose monitoring. Investigations on simulated data against realistic data are required for further evaluation. Apart from the above perspectives, in aspects of new configurations of geometry, multiple cameras covering a larger solid angle should also be considered for improving the statistics and better recovering the isotropic 3D PSF. The use of Compton cameras in tomographic mode can be an option for saving the commercial cost.

Publications

International conference

[1] **Y. Feng**, A. Etxebeste, J.M. Létang, D. Sarrut, V. Maxim, “Total variation and point spread function priors for MLEM reconstruction in Compton camera imaging”, NSS-MIC IEEE International Conference, Sydney-Australia, 2018

[2] **Y. Feng**, M. Fontana, A. Etxebeste, D. Dauvergne, J.M. Létang, E. Testa, D. Sarrut, V. Maxim, “A maximum-a-posteriori EM reconstruction method based on total variation regularization for Compton camera imaging”, PTCOG58, Manchester-UK, 2019

[3] **Y. Feng**, A. Etxebeste, J.M. Létang, D. Sarrut, V. Maxim, “Influence of the model in Compton camera MLEM reconstruction”, NSS-MIC IEEE International Conference, Manchester-UK, 2019

International journal

[1] V. Maxim, **Y. Feng,** H. Banjak, E. Bretin. “Tomographic reconstruction from Poisson distributed data: a fast and convergent EM-TV dual approach”, preprint HAL, https://hal.archives-ouvertes.fr/hal-01892281, 2018

[2] **Y. Feng**, A. Etxebeste, J.M. Létang, D. Sarrut, V. Maxim, “3D reconstruction benchmark of a Compton camera against a parallel hole gamma-camera on ideal data”, revised, IEEE Transactions on Radiation and Plasma Medical Sciences

[3] **Y. Feng**, J.M. Létang, D. Sarrut, V. Maxim, “Influence of Doppler broadening model accuracy in Compton camera list-mode MLEM reconstruction”, in preparation

[4] **Y. Feng**, J.M. Létang, D. Sarrut, V. Maxim, “Resolution recovery by PSF deconvolution and TV regularization on MLEM algorithm in Compton camera imaging”, in preparation

Bibliography

A. Zoglauer. *First Light for the Next Generation of Compton and Pair Telescope*. PhD thesis, Technische Universität Munchen, 2005.

S Aldawood, PG Thirolf, A Miani, M Böhmer, G Dedes, R Gernhäuser, C Lang, S Liprandi, L Maier, T Marinšek, et al. Development of a Compton camera for prompt-gamma medical imaging. *Radiation Physics and Chemistry*, 140:190–197, 2017.

Anders H Andersen and Avinash C Kak. Simultaneous algebraic reconstruction technique (SART): a superior implementation of the ART algorithm. *Ultrasonic imaging*, 6(1):81–94, 1984.

Andriy Andreyev, Arkadiusz Sitek, and Anna Celler. Stochastic image reconstruction method for Compton camera. In *2009 IEEE Nuclear Science Symposium Conference Record (NSS/MIC)*, pages 2985–2988. IEEE, 2009.

H.O. Anger. Use of a gamma ray pinhole camera for in-vivo studies. *Use of a gamma ray pinhole camera for in-vivo studies*, 1952.

Francis J Anscombe. The transformation of Poisson, binomial and negative-binomial data. *Biometrika*, 35(3/4):246–254, 1948.

Sandrine Anthoine, Clothilde Melot, Yannick Boursier, and Jean-François Aujol. Some proximal methods for Poisson intensity CBCT and PET. *Inverse problems and Imaging*, 6(4):p–565, 2012.

Elena Aprile, A Curioni, Karl-Ludwig Giboni, M Kobayashi, UG Oberlack, and S Zhang. Compton imaging of MeV gamma-rays with the liquid xenon gamma-ray imaging telescope (lxegrit). *Nuclear Instruments and Methods in Physics Research Section A: Accelerators, Spectrometers, Detectors and Associated Equipment*, 593(3):414–425, 2008.

MS Bandstra, EC Bellm, SE Boggs, D Perez-Becker, A Zoglauer, H-K Chang, J-L Chiu, J-S Liang, Y-H Chang, Z-K Liu, et al. Detection and imaging of the Crab Nebula with the nuclear Compton telescope. *The Astrophysical Journal*, 738(1):8, 2011.

Roman Basko, Gengsheng L Zeng, and Grant T Gullberg. Application of spherical harmonics to image reconstruction for the Compton camera. *Physics in Medicine & Biology*, 43(4):887, 1998.

A Beck and M Teboulle. A fast iterative shrinkage-thresholding algorithm for linear inverse problems. *SIAM J.Imaging SCIENCES*, 2(1), 2009.

Thomas Beyer, David W Townsend, Tony Brun, Paul E Kinahan, Martin Charron, Raymond Roddy, Jeff Jerin, John Young, Larry Byars, Ronald Nutt, et al. A combined PET/CT scanner for clinical oncology. *Journal of nuclear medicine*, 41(8):1369–1379, 2000.

SE Boggs and P Jean. Event reconstruction in high resolution Compton telescopes. *Astronomy and Astrophysics Supplement Series*, 145(2):311–321, 2000.

Ronald N Bracewell. Strip integration in radio astronomy. *Australian Journal of Physics*, 9(2): 198–217, 1956.

Jamylle Laurice Carter. *Dual methods for total variation-based image restoration*. PhD thesis, UCLA Los Angeles, CA, USA:, 2001.

A Chambolle. An algorithm for total variation minimization and applications. *Journal of Math. Imaging and Vision*, 20:89–97, 2004.

Antonin Chambolle and Thomas Pock. A first-order primal-dual algorithm for convex problems with applications to imaging. *Journal of Mathematical Imaging and Vision*, 40(1):120–145, May 2011. doi: 10.1007/s10851-010-0251-1.

Tony F Chan and Chiu-Kwong Wong. Total variation blind deconvolution. *IEEE transactions on Image Processing*, 7(3):370–375, 1998.

Tony F Chan, HM Zhou, and Raymond Hon-fu Chan. Continuation method for total variation denoising problems. In *Advanced Signal processing algorithms*, volume 2563, pages 314–326. International Society for Optics and Photonics, 1995.

Tony F Chan, Gene H Golub, and Pep Mulet. A nonlinear primal-dual method for total variation-based image restoration. In *ICAOS'96*, pages 241–252. Springer, 1996.

Ramesh Chandra and Arman Rahmim. *Nuclear medicine physics: the basics*. Lippincott Williams & Wilkins, 2017.

Simon R. Cherry, James A. Sorenson, and Michael E. Phelps. chapter 17 - single photon emission computed tomography. In Simon R. Cherry, James A. Sorenson, and Michael E. Phelps, editors, *Physics in Nuclear Medicine (Fourth Edition)*, pages 279 – 306. W.B. Saunders, Philadelphia, fourth edition edition, 2012. ISBN 978-1-4160-5198-5. doi: https://doi.org/10.1016/B978-1-4160-5198-5.00017-4. URL `http://www.sciencedirect.com/science/article/pii/B9781416051985000174`.

Cloquet. Non-Gaussian space-variant resolution modeling for list-mode reconstruction. *Physics in Medicine & Biology*, 2010.

M. J. Cree and P. J. Bones. Towards direct reconstruction from a gamma camera based on Compton scattering. *IEEE Transactions on Medical Imaging*, 13(2):398–407, June 1994. ISSN 1558-254X. doi: 10.1109/42.293932.

Michael J Cree and Philip J Bones. Towards direct reconstruction from a gamma camera based on Compton scattering. *IEEE transactions on medical imaging*, 13(2):398–407, 1994.

Arthur P Dempster, Nan M Laird, and Donald B Rubin. Maximum likelihood from incomplete data via the EM algorithm. *Journal of the royal statistical society. Series B (methodological)*, pages 1–38, 1977.

David L Donoho. Nonlinear wavelet methods for recovery of signals, densities, and spectra from indirect and noisy data. In *In Proceedings of Symposia in Applied Mathematics*. Citeseer, 1993.

YF Du, Z He, GF Knoll, DK Wehe, and W Li. Evaluation of a Compton scattering camera using 3-D position sensitive CdZnTe detectors. *Nuclear Instruments and Methods in Physics Research Section A: Accelerators, Spectrometers, Detectors and Associated Equipment*, 457 (1-2):203–211, 2001.

Jesse WM Du Mond. Compton modified line structure and its relation to the electron theory of solid bodies. *Physical Review*, 33(5):643, 1929.

Roger Eckhardt. Stan ulam, john von neumann, and the Monte Carlo method. *Los Alamos Science*, 15(131-136):30, 1987.

W Enghardt, P Crespo, F Fiedler, R Hinz, K Parodi, J Pawelke, and Falk Poenisch. Charged hadron tumour therapy monitoring by means of PET. *Nuclear Instruments and Methods in Physics Research Section A: Accelerators, Spectrometers, Detectors and Associated Equipment*, 525(1-2):284–288, 2004. doi: 10.1016/j.nima.2004.03.128.

A Etxebeste, D Dauvergne, M Fontana, J.M Létang, G Llosá, E Muñoz, J.F Oliver, É Testa, and D Sarrut. A GATE module for Compton camera imaging simulation. *Physics in Medicine & Biology*, 2019.

Y. Feng, A. Etxebeste, J. M. Létang, D. Sarrut, and V. Maxim. Total variation and point spread function priors for MLEM reconstruction in Compton camera imaging. In *2018 IEEE Nuclear Science Symposium and Medical Imaging Conference Proceedings (NSS/MIC)*, pages 1–3, Nov 2018.

Mattia Fontana, Denis Dauvergne, Jean Michel Létang, Jean-Luc Ley, and É Testa. Compton camera study for high efficiency SPECT and benchmark with Anger system. *Physics in Medicine & Biology*, 62(23):8794, 2017.

Mattia Fontana, J.-L Ley, Denis Dauvergne, N Freud, J Krimmer, Jm Létang, V Maxim, M.-H Richard, Ilaria Rinaldi, and Etienne Testa. Monitoring ion beam therapy with a Compton camera: simulation studies of the clinical feasibility. *IEEE Transactions on Radiation and Plasma Medical Sciences*, PP:1–1, 08 2019. doi: 10.1109/TRPMS.2019.2933985.

Mirela Frandes, Andreas Zoglauer, Voichita Maxim, and Rémy Prost. A tracking compton-scattering imaging system for hadron therapy monitoring. *IEEE Transactions on Nuclear Science*, 57(1):144–150, 2010.

Piotr Fryzlewicz and Guy P Nason. A Haar-Fisz algorithm for Poisson intensity estimation. *Journal of computational and graphical statistics*, 13(3):621–638, 2004.

R Gariod, R Allemand, E Cormoreche, M Laval, and M Moszynski. The LETI positron tomograph architecture and time of flight improvements. In *Proceedings of The Workshop on Time of Flight Tomography*, pages 25–29, 1982.

Peter Gilbert. Iterative methods for the three-dimensional reconstruction of an object from projections. *Journal of theoretical biology*, 36(1):105–117, 1972.

Richard Gordon, Robert Bender, and Gabor T Herman. Algebraic reconstruction techniques (ART) for three-dimensional electron microscopy and X-ray photography. *Journal of theoretical Biology*, 29(3):471–481, 1970.

Jerome Edward Gormley, WL Rogers, NH Clinthorne, DK Wehe, and GF Knoll. Experimental comparison of mechanical and electronic gamma-ray collimation. *Nuclear Instruments and Methods in Physics Research Section A: Accelerators, Spectrometers, Detectors and Associated Equipment*, 397(2-3):440–447, 1997.

P. J. Green. Bayesian reconstructions from emission tomography data using a modified EM algorithm. *IEEE Transactions on Medical Imaging*, 9(1):84–93, March 1990. ISSN 1558-254X. doi: 10.1109/42.52985.

Rebecca Antonia Grün. Impact of tissue specific parameters on the predition of the biological effectiveness for treatment planning in ion beam therapy. 2014.

Li Han, W Leslie Rogers, Sam S Huh, and Neal Clinthorne. Statistical performance evaluation and comparison of a Compton medical imaging system and a collimated anger camera for higher energy photon imaging. *Physics in Medicine & Biology*, 53(24):7029, 2008.

Atsushi Harayama, Yuto Ichinohe, Hirokazu Odaka, Shin Watanabe, Tadayuki Takahashi, Hiroyasu Tajima, Kei Genba, Daisuke Matsuura, Hiroshi Ikebuchi, Yoshikatsu Kuroda, et al. A portable Si/CdTe Compton camera and its applications to the visualization of radioactive substances. *Nuclear Instruments and Methods in Physics Research Section A: Accelerators, Spectrometers, Detectors and Associated Equipment*, 787:207–211, 2015.

M Hirasawa and T Tomitani. An analytical image reconstruction algorithm to compensate for scattering angle broadening in Compton cameras. *Physics in Medicine & Biology*, 48(8): 1009, 2003.

Jean-Baptiste Hiriart-Urruty and Claude Lemaréchal. *Convex analysis and minimization algorithms I: Fundamentals*, volume 305. Springer science & business media, 2013.

H. M. Hudson and R. S. Larkin. Accelerated image reconstruction using ordered subsets of projection data. *IEEE Transactions on Medical Imaging*, 13(4):601–609, Dec 1994. ISSN 1558-254X. doi: 10.1109/42.363108.

F Hueso-González, G Pausch, J Petzoldt, KE Römer, and W Enghardt. Prompt gamma rays detected with a BGO block Compton camera reveal range deviations of therapeutic proton beams. *IEEE Transactions on Radiation and Plasma Medical Sciences*, 1(1):76–86, 2016.

Takahiro Ida, Shinji Motomura, Masashi Ueda, Yasuyoshi Watanabe, and Shuichi Enomoto. Accurate modeling of event-by-event backprojection for a germanium semiconductor Compton camera for system response evaluation in the LM-ML-EM image reconstruction method. *Japanese Journal of Applied Physics*, 58(1):016002, 2018.

A Iltis, H Snoussi, L Rodrigues de Magalhaes, MZ Hmissi, C Tata Zafiarifety, G Zeufack Tadonkeng, and C Morel. Temporal imaging CeBr3 Compton camera: A new concept for nuclear decommissioning and nuclear waste management. In *EPJ Web of Conferences*, volume 170, page 06003. EDP Sciences, 2018.

Meei-Ling Jan, Ming-Wei Lee, and Hsuan-Ming Huang. PSF reconstruction for Compton-based prompt gamma imaging. *Physics in Medicine & Biology*, 63(3):035015, 2018.

Y Jongen, W Kleeven, and S Zaremba. New cyclotron developments at IBA. *Proc. of the Cyclotrons*, 2004.

Soo Mee Kim, Hee Seo, Jin Hyung Park, Chan Hyeong Kim, Chun Sik Lee, Soo-Jin Lee, Dong Soo Lee, and Jae Sung Lee. Resolution recovery reconstruction for a Compton camera. *Physics in Medicine & Biology*, 58(9):2823, 2013.

Aya Kishimoto, Jun Kataoka, Takanori Taya, Leo Tagawa, Saku Mochizuki, Shinji Ohsuka, Yuto Nagao, Keisuke Kurita, Mitsutaka Yamaguchi, Naoki Kawachi, et al. First demonstration of multi-color 3-D in vivo imaging using ultra-compact Compton camera. *Scientific reports*, 7(1):2110, 2017.

Tommy Knöös, Mats Nilsson, and Lars Ahlgren. A method for conversion of Hounsfield number to electron density and prediction of macroscopic pair production cross-sections. *Radiotherapy and Oncology*, 5(4):337–345, 1986.

J Krimmer, J-L Ley, C Abellan, J-P Cachemiche, L Caponetto, Xiushan Chen, M Dahoumane, D Dauvergne, N Freud, Baptiste Joly, et al. Development of a Compton camera for medical applications based on silicon strip and scintillation detectors. *Nuclear Instruments and Methods in Physics Research Section A: Accelerators, Spectrometers, Detectors and Associated Equipment*, 787:98–101, 2015.

J Krimmer, D Dauvergne, JM Létang, and É Testa. Prompt-gamma monitoring in hadrontherapy: A review. *Nuclear Instruments and Methods in Physics Research Section A: Accelerators, Spectrometers, Detectors and Associated Equipment*, 878:58–73, 2018.

RA Kroeger, WN Johnson, JD Kurfess, BF Phlips, and EA Wulf. Three-compton telescope: theory, simulations, and performance. *IEEE Transactions on Nuclear Science*, 49(4):1887–1892, 2002.

P. Kuchment and F. Terzioglu. Inversion of weighted divergent beam and cone transforms. *Inverse Problems & Imaging*, 11(6):1071–1090, 2017. doi: 10.3934/ipi.2017049.

Kenneth Lange and Richard Carson. EM reconstruction algorithms for emission and transmission tomography. *J. Comput. Assist. Tomogr*, 8(2):306–316, 1984.

W. Lee, A. Bolotnikov, T. Lee, G. Camarda, Y. Cui, R. Gul, A. Hossain, U. Roy, G. Yang, and R. James. Mini Compton camera based on an array of Frisch-grid CdZnTe detectors. In *2014 IEEE Nuclear Science Symposium and Medical Imaging Conference (NSS/MIC)*, pages 1–7, Nov 2014.

Tom K Lewellen. Time-of-flight PET. In *Seminars in nuclear medicine*, volume 28-3, pages 268–275. Elsevier, 1998.

Jean-Luc Ley. *Mise en oeuvre d'un démonstrateur de caméra Compton pour l'imagerie en médecine nucléaire et pour le contrôle en temps réel de l'hadronthérapie à l'aide des rayonnements gamma prompts*. PhD thesis, 2015.

Lefteris Livieratos. *Basic principles of SPECT and PET imaging*, pages 345–359. 09 2012. ISBN 978-3-642-02399-6. doi: 10.1007/978-3-642-02400-9_12.

G. Llosá, J. Barrio, C. Lacasta, S. Callier, C. de La Taille, and L. Raux. Characterization of a detector head based on continuous LaBr3 crystals and SiPM arrays for dose monitoring in hadron therapy. In *IEEE Nuclear Science Symposuim Medical Imaging Conference*, pages 2148–2150, Oct 2010. doi: 10.1109/NSSMIC.2010.5874160.

Leon B Lucy. An iterative technique for the rectification of observed distributions. *The astronomical journal*, 79:745, 1974.

Florian Luisier, Cédric Vonesch, Thierry Blu, and Michael Unser. Fast interscale wavelet denoising of Poisson-corrupted images. *Signal Processing*, 90(2):415–427, 2010.

Florian Luisier, Thierry Blu, and Michael Unser. Image denoising in mixed Poisson–Gaussian noise. *IEEE Transactions on image processing*, 20(3):696–708, 2011.

Markku Makitalo and Alessandro Foi. Optimal inversion of the Anscombe transformation in low-count Poisson image denoising. *IEEE transactions on Image Processing*, 20(1):99–109, 2011.

V. Maxim. Filtered backprojection reconstruction and redundancy in Compton camera imaging. *IEEE Transactions on Image Processing*, 23(1):332–341, Jan 2014. ISSN 1941-0042. doi: 10.1109/TIP.2013.2288143.

Voichiţa Maxim. Enhancement of compton camera images reconstructed by inversion of a conical radon transform. *Inverse Problems*, 35(1):014001, nov 2018. doi: 10.1088/1361-6420/aaecdb. URL `https://doi.org/10.1088%2F1361-6420%2Faaecdb`.

Voichiţa Maxim, Mirela Frandeş, and Rémy Prost. Analytical inversion of the Compton transform using the full set of available projections. *Inverse Problems*, 25(9):095001, 2009.

Voichita Maxim, Xavier Lojacono, Estelle Hilaire, Jochen Krimmer, Etienne Testa, Denis Dauvergne, Isabelle Magnin, and Rémy Prost. Probabilistic models and numerical calculation of system matrix and sensitivity in list-mode MLEM 3D reconstruction of Compton camera images. *Physics in Medicine & Biology*, 61(1):243–264, 2016. doi: doi:10.1088/0031-9155/61/1/243.

Voichita Maxim, Yuemeng Feng, Hussein Banjak, and Elie Bretin. Tomographic reconstruction from Poisson distributed data: a fast and convergent EM-TV dual approach. submitted, https://hal.archives-ouvertes.fr/hal-01892281, 2018.

B Mazoyer, R Trebossen, C Schoukroun, B Verrey, A Syrota, J Vacher, P Lemasson, O Monnet, A Bouvier, and JL Lecomte. Physical characteristics of TTV03, a new high spatial resolution time-of-flight positron tomograph. *IEEE Transactions on Nuclear Science*, 37(2):778–782, 1990.

Michael Miller, Jun Zhang, Katherine Binzel, Jerome Griesmer, Thomas Laurence, Manoj Narayanan, Deepa Natarajamani, Sharon Wang, and Michael Knopp. Characterization of the vereos digital photon counting PET system. *Journal of Nuclear Medicine*, 56(supplement 3):434–434, 2015.

Chul-Hee Min, Chan Hyeong Kim, Minyoung Youn, and Jong-Won Kim. Prompt gamma measurements for locating the dose falloff region in the proton therapy. *Applied Physics Letters*, 89:183517–183517, 11 2006. doi: 10.1063/1.2378561.

Shinji Motomura, Yousuke Kanayama, Makoto Hiromura, Tomonori Fukuchi, Takahiro Ida, Hiromitsu Haba, Yasuyoshi Watanabe, and Shuichi Enomoto. Improved imaging performance of a semiconductor Compton camera GREI makes for a new methodology to integrate biometal analysis and molecular imaging technology in living organisms. *Journal of Analytical Atomic Spectrometry*, 28(6):934–939, 2013.

Enrique Muñoz, John Barrio, Ane Etxebeste, Pablo G Ortega, Carlos Lacasta, Josep F Oliver, Carles Solaz, and Gabriela Llosá. Performance evaluation of MACACO: a multi-layer Compton camera. *Physics in Medicine & Biology*, 62(18):7321–7341, aug 2017. doi: 10.1088/1361-6560/aa8070. URL `https://doi.org/10.1088%2F1361-6560%2Faa8070`.

Enrique Muñoz, John Barrio, José Bernabéu, Ane Etxebeste, Carlos Lacasta, Gabriela Llosá, Ana Ros, Jorge Roser, and Josep F Oliver. Study and comparison of different sensitivity models for a two-plane Compton camera. *Physics in Medicine & Biology*, 63(13):135004, 2018.

Takashi Nakano, Makoto Sakai, Kota Torikai, Yoshiyuki Suzuki, Shin ei Noda, Mitsutaka Yamaguchi, Shin'ichiro Takeda, Yuto Nagao, Mikiko Kikuchi, Hirokazu Odaka, Tomihiro Kamiya, Naoki Kawachi, Shin Watanabe, Kazuo Arakawa, and Tadayuki Takahashi. Imaging of 99m Tc-DMSA and 18 F-FDG in humans using a Si/CdTe Compton camera. *Physics in Medicine & Biology*, 2019. doi: 10.1088/1361-6560/ab33d8.

Robert D Nowak and Mario AT Figueiredo. Unsupervised progressive parsing of Poisson fields using minimum description length criteria. In *Proceedings 1999 International Conference on Image Processing (Cat. 99CH36348)*, volume 2, pages 26–30. IEEE, 1999.

Robert D Nowak and Eric D Kolaczyk. A statistical multiscale framework for Poisson inverse problems. *IEEE Transactions on Information Theory*, 46(5):1811–1825, 2000.

C. E. Ordonez, A. Bolozdynya, and W. Chang. Dependence of angular uncertainties on the energy resolution of Compton cameras. In *IEEE Nuclear Science Symposium*, volume 2, November 1997.

P G Ortega, I Torres-Espallardo, F Cerutti, A Ferrari, J. E Gillam, C Lacasta, G Llosá, J. F Oliver, P. R Sala, P Solevi, and M Rafecas. Noise evaluation of Compton camera imaging for proton therapy. *Physics in Medicine & Biology*, 2015.

Palamodov. Reconstruction from cone integral transforms. *Inverse Problem*, 2017.

VY Panin, GL Zeng, and GT Gullberg. Total variation regulated EM algorithm [SPECT reconstruction]. *IEEE Transactions on Nuclear Science*, 46(6):2202–2210, 1999.

Lucas C Parra. Reconstruction of cone-beam projections from Compton scattered data. *IEEE Transactions on Nuclear Science*, 47(4):1543–1550, 2000.

Guntram Pausch, Christian Golnik, Alexander Schulz, and Wolfgang Enghardt. A novel scheme of Compton imaging for nuclear medicine. In *2016 IEEE Nuclear Science Symposium, Medical Imaging Conference and Room-Temperature Semiconductor Detector Workshop (NSS/MIC/RTSD)*, pages 1–5. IEEE, 2016.

E Rapisarda, V Bettinardi, K Thielemans, and M C Gilardi. Image-based point spread function implementation in a fully 3D OSEM reconstrcution algorithm for PET. *Physics in Medicine & Biology*, July 2010.

A J Reader, P J Julyan, H Williams, D L Hastings, and J Zweit. EM algorithm system modeling by image-space techniques for PET reconstruction. *IEEE Transactions on Nuclear Science*, 50(5), 2003.

M. . Richard, M. Dahoumane, D. Dauvergne, M. De Rydt, G. Dedes, N. Freud, J. Krimmer, J. M. Letang, X. Lojacono, V. Maxim, G. Montarou, C. Ray, F. Roellinghoff, E. Testa, and A. H. Walenta. Design study of the absorber detector of a Compton camera for on-line control in ion beam therapy. *IEEE Transactions on Nuclear Science*, 59(5):1850–1855, Oct 2012. ISSN 1558-1578. doi: 10.1109/TNS.2012.2206053.

William Hadley Richardson. Bayesian-based iterative method of image restoration. *Journal of the Optical Society of America*, 62(1):55–59, 1972.

DWO Rogers. Fifty years of Monte Carlo simulations for medical physics. *Physics in Medicine & Biology*, 51(13):R287, 2006.

H Rohling, M Priegnitz, S Schoene, A Schumann, W Enghardt, F Hueso-Gonzalez, G Pausch, and F Fiedler. Requirements for a Compton camera for in vivo range verification of proton therapy. *Physics in Medicine & Biology*, 62(7):2795, 2017.

L Rudin and S Osher. Total variation based image restoration with free local constraints. *Image Processing, Proceedings. ICIP-94.IEEE International Conference*, 1994.

L Rudin, S Osher, and E Fatemi. Nonlinear total variation based noise removal algorithms. *Physica D: Nonlinear Phenomena*, 60, 1992.

A. C. Sauve, A. O. Hero, W. L. Rogers, S. J. Wilderman, and N. H. Clinthorne. 3D image reconstruction for a Compton SPECT camera model. *IEEE Transactions on Nuclear Science*, 46(6):2075–2084, 1999.

Alex Sawatzky, Christoph Brune, Frank Wubbeling, Thomas Kosters, Klaus Schafers, and Matin Burger. Accurate EM-TV algorithm in PET with low SNR. *Nuclear Science Symposium Conference Record, IEEE*, 2008.

Stephen M Schindler, Walter R Cook, Jeffrey Hammond, Fiona A Harrison, Thomas A Prince, Song Wang, Stéphane Corbel, and William A Heindl. GRIP-2: A sensitive balloon-borne imaging gamma-ray telescope. *Nuclear Instruments and Methods in Physics Research Section A: Accelerators, Spectrometers, Detectors and Associated Equipment*, 384(2-3):425–434, 1997.

S. Schoene, W. Enghardt, F. Fiedler, C. Golnik, G. Pausch, H. Rohling, and T. Kormoll. An image reconstruction framework and camera prototype aimed for Compton imaging for in-vivo dosimetry of therapeutic ion beams. *IEEE Transactions on Radiation and Plasma Medical Sciences*, 1(1):96–107, Jan 2017. ISSN 2469-7303. doi: 10.1109/TNS.2016.2623220.

Sebastian Schoene, Wolfgang Enghardt, Fine Fiedler, Christian Golnik, Guntram Pausch, Heide Rohling, and Thomas Kormoll. An image reconstruction framework and camera prototype aimed for Compton imaging forin-vivodosimetry of therapeutic ion beams. *IEEE Transactions on Radiation and Plasma Medical Sciences*, 1(1):96–107, 2016.

V Schonfelder, R Diehl, GG Lichti, H Steinle, BN Swanenburg, AJM Deerenberg, H Aarts, J Lockwood, W Webber, J Macri, et al. The imaging Compton telescope COMPTEL on the gamma ray observatory. *IEEE Transactions on Nuclear Science*, 31(1):766–770, 1984.

Volker Schönfelder, Andreas Hirner, and K Schneider. A telescope for soft gamma ray astronomy. *Nuclear Instruments and Methods*, 107(2):385–394, 1973.

Lawrence A Shepp and Yehuda Vardi. Maximum likelihood reconstruction for emission tomography. *IEEE transaction on medical imaging*, 1(2):113–122, 1982.

Manbir Singh and David Doria. An electronically collimated gamma camera for single photon emission computed tomography. part II: Image reconstruction and preliminary experimental measurements. *Medical Physics*, 10(4):428–435, 1983.

J Skilling, AW Strong, and K Bennett. Maximum-entropy image processing in gamma-ray astronomy. *Monthly Notices of the Royal Astronomical Society*, 187(2):145–152, 1979.

Bruce Smith. Reconstruction methods and completeness conditions for two Compton data models. *J. Opt. Soc. Am. A*, 22(3):445–459, Mar 2005. doi: 10.1364/JOSAA.22.000445. URL `http://josaa.osa.org/abstract.cfm?URI=josaa-22-3-445`.

D. L. Snyder, M. I. Miller, L. J. Thomas, and D. G. Politte. Noise and edge artifacts in maximum-likelihood reconstructions for emission tomography. *IEEE Transactions on Medical Imaging*, 6(3), 1987.

Donald L Snyder and David G Politte. Image reconstruction from list-mode data in an emission tomography system having time-of-flight measurements. *IEEE transaction on medical imaging*, 30(3):1843–1849, 1983.

F Stichelbaut and Y Jongen. Verification of the proton beam position in the patient by the detection of prompt gamma-rays emission. In *39th PTCOG meeting, San Francisco*, 2003.

Simon Stute and Claude Comtat. Practical considerations for image-based PSF and blobs reconstruction in PET. *Physics in Medicine & Biology*, 58(11):3849, 2013.

J.P. Sullivan, S.R. Tornga, and M.W. Rawool-Sullivan. Extended radiation source imaging with a prototype Compton imager. *Applied Radiation and Isotopes*, 67:617–624, 2009.

Suleman Surti. Update on time-of-flight PET imaging. *Journal of Nuclear Medicine*, 56(1): 98–105, 2015.

Shin'ichiro Takeda, Hirokazu Odaka, Shin-nosuke Ishikawa, Shin Watanabe, Hiroyuki Aono, Tadayuki Takahashi, Yousuke Kanayama, Makoto Hiromura, and Shuichi Enomoto. Demonstration of in-vivo multi-probe tracker based on a Si/CdTe semiconductor Compton camera. *IEEE Transactions on Nuclear Science*, 59(1):70–76, 2012.

V Tatischeff, M Tavani, P Von Ballmoos, L Hanlon, U Oberlack, A Aboudan, A Argan, D Bernard, A Brogna, A Bulgarelli, et al. The e-ASTROGAM gamma-ray space mission. In *Space Telescopes and Instrumentation 2016: Ultraviolet to Gamma Ray*, volume 9905, page 99052N. International Society for Optics and Photonics, 2016.

Takanori Taya, J Kataoka, A Kishimoto, Y Iwamoto, A Koide, T Nishio, S Kabuki, and T Inaniwa. First demonstration of real-time gamma imaging by using a handheld Compton camera for particle therapy. *Nuclear Instruments and Methods in Physics Research Section A: Accelerators, Spectrometers, Detectors and Associated Equipment*, 831:355–361, 2016.

Michel M Ter-Pogossian, David C Ficke, Mikio Yamamoto, and John T Hood. Super PETT I: a positron emission tomograph utilizing photon time-of-flight information. *IEEE transactions on medical imaging*, 1(3):179–187, 1982.

E Testa, M Bajard, M Chevallier, D Dauvergne, F Le Foulher, N Freud, J-M Létang, J-C Poizat, C Ray, and M Testa. Monitoring the Bragg peak location of 73 MeV/ u carbon ions by means of prompt γ-ray measurements. *Applied physics letters*, 93(9):093506, 2008.

RW Todd, JM Nightingale, and DB Everett. A proposed γ camera. *Nature*, 251(5471):132, 1974.

T Tomitani and M Hirasawa. Image reconstruction from limited angle Compton camera data. *Physics in Medicine & Biology*, 47(12):2129, 2002.

Wm J Veigele. Photon cross sections from 0.1 keV to 1 MeV for elements Z= 1 to Z= 94. *Atomic Data and Nuclear Data Tables*, 5(1):51–111, 1973.

Curtis R Vogel and Mary E Oman. Iterative methods for total variation denoising. *SIAM Journal on Scientific Computing*, 17(1):227–238, 1996.

Christopher G. Wahl, Willy R. Kaye, Weiyi Wang, Feng Zhang, Jason M. Jaworski, Alexis King, Y. Andy Boucher, and Zhong He. The Polaris-H imaging spectrometer. *Nuclear Instruments and Methods in Physics Research Section A: Accelerators, Spectrometers, Detectors and Associated Equipment*, 784:377 – 381, 2015. ISSN 0168-9002. doi: https://doi.org/10.1016/j.nima.2014.12.110. Symposium on Radiation Measurements and Applications 2014 (SORMA XV).

Scott J Wilderman, NH Clinthorne, Jeffrey A Fessler, C-H Hua, and WL Rogers. List mode EM reconstruction of Compton scatter camera images in 3-D. In *2000 IEEE Nuclear Science Symposium. Conference Record (Cat. No. 00CH37149)*, volume 2, pages 15–292. IEEE, 2000.

S.J. Wilderman, N.H. Clinthorne, J.A. Fessler, and W.L. Rogers. List-mode maximum likelihood reconstruction of Compton scatter camera images in nuclear medicine. In *IEEE Nuclear Science Symposium*, pages 1716–1720, November 1998.

S.J. Wilderman, J.A. Fessler, N.H. Clinthorne, J.W. LeBlanc, and W.L. Rogers. Improved modeling of system response in list mode EM reconstruction of Compton scatter camera images. *IEEE Transactions on Nuclear Science*, 48:111–116, 2001.

Rebecca M Willett and Robert D Nowak. Platelets: a multiscale approach for recovering edges and surfaces in photon-limited medical imaging. *IEEE Transactions on Medical Imaging*, 22 (3):332–350, 2003.

Dan Xu and Zhong He. Gamma-ray energy-imaging integrated spectral deconvolution. *Nuclear Instruments and Methods in Physics Research Section A: Accelerators, Spectrometers, Detectors and Associated Equipment*, 574(1):98–109, 2007.

Ming Yan and Luminita A. Vese. Expectation maximization and total variation based model for computed tomography reconstruction from undersampled data. *Medical Imaging 2011: Physics of Medical Imaging*, 2011.

YF Yang, Y Gono, S Motomura, S Enomoto, and Y Yano. A Compton camera for multitracer imaging. *IEEE Transactions on Nuclear Science*, 48(3):656–661, 2001.

Bo Zhang, Jalal M Fadili, and Jean-Luc Starck. Wavelets, ridgelets, and curvelets for Poisson noise removal. *IEEE Transactions on Image Processing*, 17(7):1093–1108, 2008.

Andreas Zoglauer, Michelle Galloway, Mark Amman, Steven E Boggs, Julie S Lee, Paul N Luke, Lucian Mihailescu, Kai Vetter, and Cornelia B Wunderer. First results of the high efficiency multi-mode imager (HEMI). In *2009 IEEE Nuclear Science Symposium Conference Record (NSS/MIC)*, pages 887–891. IEEE, 2009a.

Andreas Zoglauer, Georg Weidenspointner, Michelle Galloway, Steven E Boggs, and Cornelia B Wunderer. Cosima—the cosmic simulator of MEGAlib. In *2009 IEEE Nuclear Science Symposium Conference Record (NSS/MIC)*, pages 2053–2059. IEEE, 2009b.

Appendix

3D reconstruction benchmark of a Compton camera against a parallel hole gamma-camera on ideal data

Yuemeng Feng, Ane Etxebeste, David Sarrut, Jean Michel Létang, Voichiţa Maxim

***Abstract*—Compton cameras and collimated gamma cameras are competing devices suitable for prompt gamma detection in range verification of particle therapy. In this study, we evaluate the first approach from the point of view of the tomographic reconstruction step by comparing it to the second. We clear any technological constraints by considering a simple geometry, ideal detecting stages, a mono-energetic synthetic phantom. To this end, both analytic (filtered back-projection) and iterative (list-mode maximum likelihood expectation maximization) algorithms are applied in conjunction with total variation denoising. It was shown in previous studies that compared to the mechanically collimated camera, the Compton camera has a higher efficiency. Factors between ten and one hundred were reported. Meanwhile, for each detected event the emission position of the original photon lies on a conical surface for Compton cameras, instead of a line for collimated cameras. This leads to a supplementary degree of freedom that logically calls during image reconstruction for a larger data set and may cancel out the benefits of the superior efficiency. We consider here a static Compton camera and a rotating collimated camera with similar angular coverage. We show empirically that reconstruction from conical projections requires ten times more detected events to obtain at least the same image quality. In some experiments, the Compton camera allows to avoid severe artefacts produced by the limited-angle geometry of the collimated camera. In addition, the Compton camera should be better suited for imaging high-energy and poly-energetic sources.**

***Index Terms*—Compton camera imaging, SPECT, gamma ray, maximum likelihood, maximum a posteriori, total variation**

I. Introduction

The Compton camera was proposed during 70's simultaneously for astronomical ([1]) and nuclear medicine ([2]) imaging applications. Several prototypes ([3], [4], [5], [6], [7]) have been built and exploited for the observation of cosmic γ sources, or for monitoring nuclear plants and waste with the development of hand-held γ-detectors boosted by the recent accident in Fukushima, Japan ([8], [9], [10], [11], [12]). Although Compton cameras should have superior efficiency ([13], [14], [15], [16], [17], [18], [19]), imaging of γ sources in nuclear medicine is still carried out with collimator-based gamma cameras. Compton cameras have recently regained interest as they may allow ion-range monitoring in proton and hadron-therapy using prompt-γ emission generated by nuclear interactions of the ions with tissue ([20], [21], [22], [23], [24], [25], [26], [27], [28], [29]). The energies of the prompt-γ rays are too large to cope with parallel hole acquisition and require hard collimation ([30], [31]). Three-dimensional imaging is then challenging, taking into account the low emission rates. To completely sample the projection space, multi-slit collimators combined with detectors rotating around the patient might be designed but they would trigger significant burden. Compact detectors for range verification are also under study ([32], [33], [34]).

The specificity of the Compton camera is to have a large acceptance angle and to identify the direction of an incoming ray without mechanical collimation, with a coincidence strategy based on Compton scattering followed by photoelectric absorption. However, the set of possible emission points can only be restricted to a conical surface unless the direction of the Compton electron is known, by contrast with the parallel hole geometry where the restriction to a line is possible. The analytic image reconstruction process is therefore relatively complex. As a consequence, analytic methods were initially available for subsets of data only: cone axis perpendicular to the detector in [35], point-like scatterer in [36], [37], two dimensions in [38]. Lately, methods accepting a much larger part of the data were developed ([39], [40], [41], [42]). The conical Radon transform is born and is receiving much interest ([43], [44], [45], [46], [47], [48], [49], [50]).

This conical projection pattern raises concerns about the quality that the reconstructed images can ever reach. Will it be possible, with both competitive detectors and reconstruction algorithms to obtain one day clinically acceptable images? Previous works attempted to benchmark the Compton camera with respect to the Anger camera from the point of view of detection efficiency and imaging capabilities. It is widely acknowledged that at energies superior to three or four hundreds of keV, Compton camera devices allow an increase in efficiency of one or two orders of magnitude ([51], [52]). Recently, a factor of 20 was found in simulations when compared the single particle emission computed tomography (SPECT) General Electric HealthCare Infinia system with a Compton camera prototype currently under development ([19]). These studies concentrate on the physical aspects and get rid as much as possible of the influence of one particular reconstruction algorithm. Our purpose is on the contrary to avoid as much as possible the influence of a particular geometry or physical effects and to concentrate on the image reconstruction capabilities, as function of the

The authors acknowledge financial support of the French National Research Agency through the ANR project 3DCLEAN (ANR-15-CE09-0009) and LABEX PRIMES (ANR-11-IDEX-0007) of Université de Lyon. This work was performed within the framework of the SIRIC LYriCAN Grant INCa_INSERM_DGOS_12563. The first author is supported by a PhD grant from the China Scholarship Council.

The authors are with Université de Lyon, INSA-Lyon, Université Claude Bernard Lyon 1, UJM-Saint Etienne, CNRS, Inserm, CREATIS UMR 5220, U1206, F69621, Villeurbanne, France, e-mail: {yuemeng.feng, ane.etxebeste, david.sarrut, jean-michel.letang, voichita.maxim}@creatis.insa-lyon.fr

Manuscript received September 6, 2019.

number of events. It is widely recognized that the Compton camera allows to significantly increase the detection efficiency. However, one might wonder if the more complex projection geometry and the supplementary degree of freedom due to conical surfaces is compatible with high quality images. In the final result, this supplementary degree of freedom could eventually completely cancel out the benefit of the superior efficiency. On the other side, Compton camera imaging can be done with a single stationary planar detector. This can be an advantage when the motion of the collimated camera is restricted by physical obstacles.

The purpose of this work was to investigate the limits of the "ideal" Compton camera imaging capabilities, with the best reconstruction algorithms available in our team. As reference for the 3D reconstruction benchmark we took the "ideal" Anger camera with parallel holes in a missing angle configuration. We put aside the efficiency of the cameras to focus on reconstruction issues: virtual experiments where a relatively low number of counts were considered, with the lower bound set to 2×10^4 measured events for the Compton camera and 2×10^3 measured events for the missing angle Anger camera.

The geometry of acquisition as well as data selection and pre-processing strategies have a major impact on the resulting Compton camera images (see *e.g.*, [53], [14], [22], [54], [55], [26]). The spatial resolution of reconstruction can be improved by more accurate modeling of the physical effects ([56], [24] [57], [58]) and by deconvolution methods in data space for energy spectrum ([59]) or in spatial domain ([60], [61]). Imaging performance of conventional collimated Anger camera systems is primarily determined by properties of the collimator. At energies above 300 keV, the collimator septal thickness must be increased to reduce penetration and scattering at the price of a reduced sensitivity. The choice of the hole diameter is thus a trade-off between sensitivity and resolution. On the opposite side, the Compton camera resolution increases with the energy as the Doppler broadening and detector noise decrease. However, as the energy increases above 1 MeV, the probabilities for multiple interactions, pair productions and electron escape increase, too. This may lead to false coincidences and requires specific algorithms for the identification of the interaction sequence [62]. In this work, the energy of the γ-rays has no influence on the Anger camera data and images as the data are Poisson-realisations from ideal parallel-line projections. For the Compton camera, three energies were considered: 511 keV, 2 MeV and 4 MeV. This choice influences the result through the Klein-Nishina differential cross-section which gives the probability for the scattering angle value. At low energies as the ones currently used in SPECT, high scattering angles are dominant. As the energy increases, forward scattering prevails. In theory, this might have an influence on the missing-data artefacts. However, we deliberately chose here a large camera that limit as much as possible data truncation. Note that out-of-field activity could also be a source of noise in Compton camera imaging, where it has no influence on Anger camera acquisitions.

II. The two simulated setups

A. Compton camera (CC)

1) Device description: CCs detect the γ photons on the basis of a coincidence process. The photon needs to hit the camera twice: once in the scatterer stage, once in the absorber stage. The first interaction has to be a Compton scattering. During this inelastic interaction the photon transfers part of its incident energy to an electron as kinetic energy E_1, which is ideally totally released in the detector at V_1 (see figure 1). The scattered photon, deviated by scattering angle β, has to interact with the camera at least once again at some position V_2. The quantities of interest are the positions of the two first hits, the energy E_1 and the total energy of the photon, E_0, that can be estimated by summing up the energies deposited in sensitive material. The scattering angle β may be deduced through the Compton kinematics.

To achieve both high Compton-to-photoelectric interaction ratio and low Doppler broadening, materials with low-Z elements as Silicon are often chosen for the scatterer. At high energies, scattering detectors made of Ge ([63]), CZT ([64]), $LaBr_3$ ([65]) might be preferred to reach a high efficiency of detection. Meanwhile the Doppler broadening will be increased and the Compton-to-photoelectric ratio will be reduced ([66]), which leads to a more noisy dataset for imaging. Several layers of scatterer can be ranged in a stack and the furthest detector is usually made of scintillating crystals, similar to the detector of the Anger camera. Its role is to completely stop the photon by photoelectric absorption, hence the term absorber (see figure 1).

In the absence of noise, the point where the gamma ray was emitted lies on the surface of the cone having its apex at the first interaction, its axis directed by the line defined by the first two interactions and its half-opening angle β. As a consequence, data acquired with a CC having ideal position and energy resolutions are usually modelled as integrals of the weighted activity of the source on conical surfaces. These models are gathered under the name of weighted conical Radon transforms, cone transforms or Compton transforms.

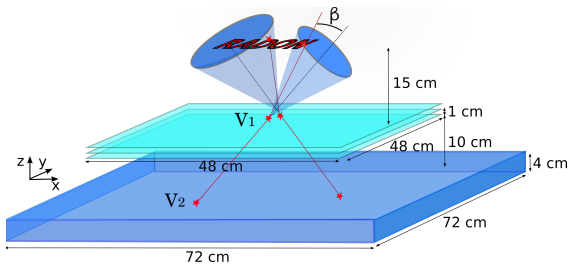

Fig. 1. Schematic representation of a CC composed of a three-layer scatterer (light blue) and an absorber (dark blue). The source is represented as the word RADON. Photons emitted from the source are first scattered then absorbed in the detector, and the position where they were emitted can only be determined at this stage as belonging to conical surfaces. The scattering and absorption positions are respectively noted V_1 and V_2. The scattering angle is noted β.

2) Monte Carlo simulated data: Each Compton cone is characterised by the coordinates of the apex, the two angular coordinates of the axis and the half-opening angle. The dimension of the data space is thus 5 or 6, and simulation

of deterministic conical projections on a sufficiently fine grid is prohibitive. Moreover, for e.g. 10^5 counts, most of the projections would be empty. Thus, Monte Carlo data have to be produced event by event.

Simulations were performed with a new CC module ([67]) developed within GATE/Geant4 ([68]) simulation platform. The simulated Compton camera is shown in figure 1. The scatterer detector was composed of three parallel silicon layers with $48\times48\times0.2$ cm^3 in size separated by 1 cm distance from each other. The absorber was made of a $72.96\times72.96\times4$ cm^3 $LaBr_3$ pixelated scintillator matrix composed of 128×128 pixels with $0.5\times0.5\times4$ cm^3 in size. The distance between the last silicon layer (center) and the center of the absorber was 10 cm. The source was placed parallel to the camera at a distance of 15 cm from the first scatterer layer. All the coincidences with at least one interaction in each detector type (scatterer and absorber) were accepted. In order to recover the ideal Compton kinematics, the positions of the first two primary interactions were stored together with the initial energy and the energy of the first Compton scattered photon. In addition, the *option 1* of the standard electromagnetic physics list, which does not include Doppler broadening, was activated.

B. Anger camera (AC)

1) Device description: To be detected by the AC, a γ photon emitted by the source must pass through a hole of the collimator then interact with the sensitive material. Usually, the detection is based on photoelectric absorption of the photon in a scintillating crystal, followed by measurement of visible light. The efficiency of the system is relatively low, as a considerable fraction of photons hits the collimators and are either absorbed or scattered. The scattered photons, whose incoming direction is uncertain, are discarded on the basis of their lower energy. ACs are usually designed for relatively low energies, in the order of tens until few hundreds of keV. For higher energies, collimators need to be thicker reducing significantly the efficiency. For instance, knife-edge ([30]) and slit ([31]) cameras were proposed for the detection of the prompt-γ emission that has an energy spectrum going up to a few MeVs. This type of detector provides a 1D signal that might be sufficient for on-line range monitoring purposes. However, 3D images would provide more extensive information on the irradiated area and even on the tissue composition.

2) Simulated data: In this work we do not deal with issues related to collimators. Parallel line projections were taken for each YZ slice from the source with the `radon` function from Matlab. The spacing between the centres of two adjacent holes was 0.25 cm, the same as the thickness of a slice, and the angular step was 6°. The energy of the source was not taken into account. From these deterministic exact projections, Poisson measures were then simulated. The total number of counts was a random number with given mean. This mean will be loosely referred in the text as the number of counts, as the small variation of its value do not significantly affect the results. The AC turns around the x axis as indicated in figure 3 with the green arrow. At 90° the camera is perpendicular to the z axis. We considered a limited angle configuration [30,150] degrees, for a total angle of 120° and a missing angle of 60°. The choice of the missing angle value was motivated by the similar missing angle in the Compton camera configuration, where the solid angle covered by the first scatterer layer at the center of the source, in the plane yOz, was slightly less than 120°. We neglect the loss of data in the plane xOz, despite the fact that this loss will have the most severe consequences, especially at the extremities of the source.

C. The source

We simulated a mono-energetic source consisting of five letters with the coronal plane identical to the one shown in figure 2, the coordinates represent centimeters. The source is 1 cm thick, 20 cm long and 4 cm high. The activity is piecewise constant in all letters which are composed of boxes and parts of hollow cylinders. For instance, the letter "O" can be seen as a source containing two hot inserts (activity ratio $\sim$1.6) and one cold insert. The ratio between the the maximum activity in letter "O" and the rounded component of the letter "D" is $\sim$2.7. The maximum activity is normalized. For the Compton camera simulations, the isotropic source was let to emit photons at three energies, 511 keV, 2 MeV and 4 MeV respectively. For the AC, the energy was not modelled in the simulation.

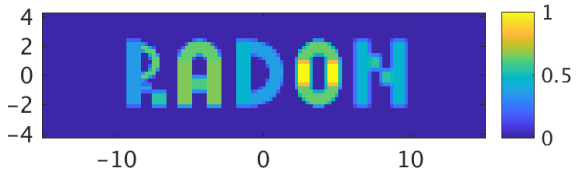

Fig. 2. Simulated source. The colorbar shows the normalized activity.

Three placements of the source were considered allowing to evaluate the quality of the reconstruction in the direction orthogonal to the camera for thin (C1), intermediate (C2) and thick sources (C3) as shown in figure 3. The center of the volume is at the center of the coordinate system and thus at 15 cm from the Compton camera. The distance to the AC is not modeled.

With the TV-MAP-EM algorithm described hereafter, we reconstructed images from 2×10^4, 2×10^5 and 2×10^6 counts.

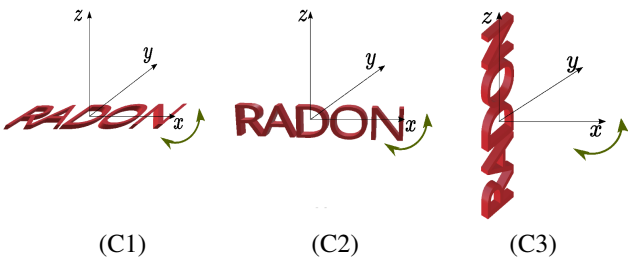

Fig. 3. Positions of the source, represented as red letters. The source remains identical in all three configurations, only the orientation differs. (C1) Letters parallel to the CC plane. (C2) Letters perpendicular to the CC plane. (C3) Letters at increasing distance from the CC plane. The AC rotates around the x axis as indicated by the arrows and the CC plane is parallel to the xy-plane.

For the CC analytic algorithm more events were necessary. From 25×10^6 simulated events, only one half were usable as a valid Compton cone should not intersect the detector in more than one point, the apex (for details, see reference [49]). A number of 12.5×10^6 counts were then simulated for the Anger camera with limited angular coverage.

III. Image reconstruction methods

The image of the source can be reconstructed from the measured data either analytically, with a filtered back-projection algorithm, or by iterative algorithms. Among iterative algorithms, the most widely employed is the maximum likelihood expectation maximization algorithm (MLEM), common to all emission tomography modalities ([69], [70]) and formally described for general distributions in the seminal paper [71]. Its specificity lies in the proper modelling of the Poisson nature of the data and in providing positive solutions without the need of additional projection steps. MLEM has several variants, among which OSEM ([72]) and list-mode MLEM ([73], [74]). When prior information on the solution is necessary to compensate for the low number of counts and to reduce the noise, maximum a posteriori (MAP) EM algorithms can be used.

A. Filtered back-projection

In this work, we applied the filtered back-projection algorithm developed for CC image reconstruction in [49]. It was shown in [35] that an infinitely large planar detector offers a complete geometry, and the source can be perfectly reconstructed even from only events corresponding to cones with axes perpendicular to that plane. A method allowing to consider arbitrary axis directions was proposed in [41], and the supplementary data is used for noise reduction. For each element of scatterer, the integrals of the source activity on half-lines can be obtained from the set of conical projections composed of all possible axis directions and scattering angle in some interval $[\beta_1, \beta_2]$. At sufficiently high energy and thus for low scattering angles, most of these cones can be measured with a camera with scatterer as large as the source and a sufficiently large absorber. By letting the camera turn around the source, a complete set of cone-beam projections can thus be obtained. We do not chose this solution for several reasons. First, at low emission rates, very few events that scatter for the first time in a particular detector element will be measured. The computation of the cone-beam projections will be then compromised. Second, the cost of such a device would be high. Finally, our aim is to test a limited-scan geometry, where an AC could not complete a 180°-trip around the source, and thus 3D imaging with a CC covering a limited angle would be of interest. Some attempts to find a complete acquisition geometry and associated analytic reconstruction algorithms can be found in [39], [42], [47]. Similar to the missing angle parallel-ray acquisitions, any planar finite CC will lead to artefacts in the reconstructed images. These artefacts increase as the solid angle covered by the detector at the source position decreases. Prior to reconstruction, a sort of sinogram has to be completed by binning the data with respect to the coordinates of the cone apex, the axis angular parameters in spherical coordinates and the scattering angle β. The resulting array has five or six dimensions, depending on the number of scatterers of the camera. This binning reduces the precision on the data and the effect on the image can be remarkable. For instance, a systematic error of 2.5° on the axis inclination will alter the point spread function (PSF) as one moves far from the detector ([49], figure 7). The same error on the scattering angle will additionally cause displacement of the source and even prevent reconstruction. These results were obtained with the MLEM algorithm (in its classical variant, not in list-mode), from deterministic projections and perfect knowledge of the system matrix.

For the collimated camera, filtered back-projection implemented in Matlab as the `iradon` function was applied to each slice of the volume.

When the images were reconstructed by filtered back-projection, a smoothing filter was always applied in order to counterbalance the ramp filter at the higher frequencies and thus reduce the noise. These filters smooth the image and blur the edges. Total variation denoising ([75]) might be better suited at least for piecewise constant images. We therefore applied the total variation denoising method from [75], implemented following [76]. The analytic methods are fast, but work properly only for high number of counts where, in addition, list-mode MLEM algorithms exhibit prohibitive computing times. For this reason, we have only shown the analytic reconstruction results in the experiment of high number of counts.

B. Maximum likelihood expectation maximization algorithm

Let t_{ij} denote the probability for a photon emitted in voxel j to be detected as event i and let λ_j be the mean number of photons emitted in voxel j. The number of photons detected by the i^{th} element of detector also follows a Poisson law, with mean $\mu_i = \sum_j t_{ij}\lambda_j$. Note that for the CC, the index j has to account not only for positions, as it is the case for the Anger camera, but also for the polar and azimuthal angles of the axis of the cone and for the Compton scattering angle. The reconstruction problem might be seen as a linear inverse problem,

$$\boldsymbol{\mu} = T\boldsymbol{\lambda}, \tag{1}$$

where $\boldsymbol{\lambda}$ has positive values and the measured vector $\boldsymbol{y}$ follows a Poisson distribution with mean $\boldsymbol{\mu}$. The matrix $T = (t_{ij})$ is often called system matrix. The logarithm of the likelihood of a measurement $\boldsymbol{y}$ generated from the emission $\boldsymbol{\lambda}$ can be formulated as:

$$L(\boldsymbol{\lambda}|\boldsymbol{y}) = \sum_i (-\sum_j t_{ij}\lambda_j + y_i \ln(\sum_j t_{ij}\lambda_j) - \ln(y_i!)) \tag{2}$$

Let $s = (s_j)$ be the sensitivity vector, containing the detection probabilities for photons emitted from voxels j. The MLEM algorithm consists in calculating, starting from some initial value $\widehat{\boldsymbol{\lambda}}^0 \in (\mathbb{R}_+^*)^J$, the sequence

$$\widehat{\lambda}_j^{l+1} = \frac{\widehat{\lambda}_j^l}{s_j} \sum_i \frac{t_{ij} y_i}{\sum_k t_{ik}\widehat{\lambda}_k^l}, \tag{3}$$

solves the minimization problem:

$$\min\{-L(\boldsymbol{\lambda}|\boldsymbol{y}) : \boldsymbol{\lambda} \in (\mathbb{R}_+)^J\}. \quad (4)$$

In the list-mode version, the data space is highly sampled in order to have $y_i \in \{0, 1\}$. The main differences are that each measured event becomes a "bin", only non-empty bins are used in the reconstruction, and the sensitivity calculation changes. The sensitivity is related to the system matrix through the relation $s_j = \sum_i t_{ij}$. In list-mode, the sampling of the data space is huge, therefore only the elements corresponding to measured events are calculated for the system matrix. Consequently a different strategy has to be employed for the calculation of the sensitivity. List-mode is indispensable for CC imaging for at least three reasons. First, the huge dimension of the data space (indexed on five or six parameters) that would require huge storage capacities or coarse sampling in each direction. Second, the CC is expected to make the difference in conditions where the number of counts is relatively low. Regarding the first argument, it is likely that the number of events should be lower than the number of bins for reasonable sampling rates. Third, sampling induces some reduction in the precision of the data. This reduction does not excessively penalize modalities where the acquisition is made on lines, but even mild errors on the angular parameters have significant consequences on the reconstructed images of the CC (see discussion in section III-A).

MLEM algorithm was used for the first time for Compton camera imaging in [74]. Currently there is no established model for the calculation of the system matrix, but several proposals have been made in the literature ([77], [78], [79]). In [24], a MLEM based reconstruction framework together with an imaging prototype were presented and the proposed system matrix was tested on measured data. Monte Carlo simulations can help to choose and validate a model, but probably only up to some approximations induced by data binning. We used the approach detailed in [56], where it was demonstrated that the elements of the system matrix can be approximated up to a constant factor as

$$t_{ij} = \int_{M \in v_j} K(\beta_M, E_0) \frac{\cos\theta_{\overrightarrow{V_1M}}}{\|\overrightarrow{V_1M}\|^2} h_i(M) dv, \quad (5)$$

where $K(\beta_M, E_0)$ is the Klein-Nishina Compton scattering cross-section ([80]), M is a point in the voxel v_j, $\theta_{\overrightarrow{V_1M}}$ is the angle made by $\overrightarrow{V_1M}$ with the axis of the camera and h_i is a spatial kernel modelling the cone and the uncertainties on the Compton angle β. For ideal data, h_i is the Dirac distribution on the cone associated to the i^{th} event. For the calculation of the sensitivity we generalized the formula from [78] to several scatterers.

The statistical noise and sometimes the ill-conditioned nature of the problem may lead to significant noise in the reconstructed images. As a consequence, the iterations of the MLEM algorithm have to be stopped at some point that is difficult to anticipate and in clinical routine the images use to be post-smoothed. Choosing a post-smoothing filter is a key issue as the noise in the MLEM images is not uniform but spatially variant with standard-deviation depending on the intensity ([81], [82]).

A better choice, allowing a balance between the data fidelity constrain represented by the log-likelihood (2) and some a priori, consists in including both of them in a penalized optimization problem. The ML-EM algorithm becomes the maximum a posteriori or MAP-EM algorithm. The second is sometimes implemented as appropriate smoothing of the solution between each two iterations of the first. The positivity of the solution can be easily ensured and the relative fast convergence of MLEM is preserved and even reinforced. Maximum a posteriori method brings general information about the source that allows to search for the solution in a smaller space. Often some regularity of the intensity function is imposed. In this work, we applied a non-smooth and spatially variant penalty: the total variation norm of the solution. For strong noise, corresponding to low statistics, total variation might be a good choice for classes of images more general than the piecewise constant class ([83]).

C. Total variation prior

Adding total variation regularization to Poisson-distributed data tomography aims to reconstruct the image with both minimal total variation and maximal log-likelihood through the resolution of the minimization problem:

$$\min\{-L(\boldsymbol{\lambda}|\boldsymbol{y}) + \alpha G(\boldsymbol{\lambda}) : \boldsymbol{\lambda} \in (\mathbb{R}_+)^J\}. \quad (6)$$

Here $\alpha \geq 0$ is the weight of TV regularization and G denotes the discrete version of the L_1-norm of the gradient in the image:

$$G(\lambda) = \int_\Omega |\nabla\lambda(x)| dx. \quad (7)$$

We used the method proposed in [84] for solving the MAP-TV regularization problem within EM iterations. The method is based on the Fenchel-Rockafellar duality theorem and on the dual formulation of the (M) step from the EM algorithm. A fast iterative shrinkage-thresholding algorithm (FISTA) was used to speed up the convergence ([85]).

D. Figures of merit

To evaluate the reconstruction quality we calculated the structural similarity (SSIM) index between the reconstructed image and the reference normalized to their maximum of intensity ([86]). As the images were smoothed with the total variation prior, we expect a low variation for this maximum. Compared to peak signal to noise ratio (PSNR) and root mean square error (RMSE) which evaluate two images on a pixel-by-pixel basis, SSIM is closer to visual perception. However, it remains a global measure which is barely affected by localized differences in the images.

IV. Results

In this section we evaluate with simulated data how the TV-MAP-EM reconstructed Compton camera images are affected by (A) the energy at which the source emits, (B) the number of acquired events and (C) the thickness of the source in the direction orthogonal to the camera. For (B) and (C) we perform a comparison with the Anger camera with angular coverage

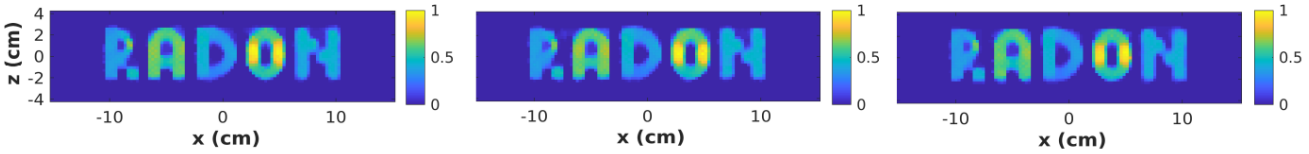

(a) 511 keV (b) 2 MeV (c) 4 MeV

Fig. 4. Images reconstructed from Compton camera data, as a function of the energy. From the left to the right the simulated energies are 511 keV, 2 MeV, 4MeV. The word-shaped source was placed perpendicular to the camera in configuration (C2). Central slices from the volumes reconstructed from 2×10^6 detected events at the 200th TV-MAP-EM iteration are shown.

limited to 120°. A final test concerns high statistics experiments and analytic, filtered back-projection reconstruction. For both cameras, we reconstructed volumes having $121 \times 34 \times 34$ voxels for the (C1) and (C2) configurations. For the (C3) configuration, the volume has $34 \times 34 \times 113$ voxels, in order to avoid intersection between the volume and the CC. Each cubic voxel has a size of 0.25^3 cm^3. The total volume is thus about $30 \times 8 \times 8$ cm^3 for the (C1) and (C2) configurations and $8 \times 8 \times 28$ cm^3 for (C3). For each test, we show one of the two central slices of the word-shaped source (the word is composed originally of four slices).

A. Influence of the emission energy

In figure 4 we show the Compton camera images for the source emitting successively at energies 511 keV, 2 MeV and 4 MeV. The source was placed in configuration (C2) (see figure 3). We used 2×10^6 measured events for each reconstruction.

B. Compton camera against limited angle Anger camera

The CC is expected to have an efficiency one or two orders of magnitude superior to the AC and to be used in applications where the counts are very low. The source, emitting at 511 keV, was placed perpendicular to the CC in configuration (C1). For the AC, at half-course the word is perpendicular to the detector. The AC is considered in a 120°-limited angle configuration. We then reconstructed the volumes for a number of detected events ranging from 2×10^4 to 2×10^6 for the CC and from 2×10^3 to 2×10^6 for the AC. The SSIM index comparing the reconstructed volumes to the reference image was calculated as function of the iteration number and plotted in figure 5.

Figure 6 compares the regularized iterative reconstructions from CC and AC for different counts. The source was placed in configuration (C1). For the CC simulation, the photons were emitted at energy 511 keV. The image on the top-left is the reference. The results for the CC reconstruction are shown on the left side from the second line to the last, for respectively 2×10^6, 2×10^5 and 2×10^4 measured events. The results for the missing angle AC configuration with projections measured on 120° in the range [30°,150°] are shown on the right from the top to the end, for respectively 2×10^6, 2×10^5, 2×10^4 and 2×10^3 measured events.

C. Position of the source

The CC has lower resolution in the direction orthogonal to the detector. The position of the source also affects the AC

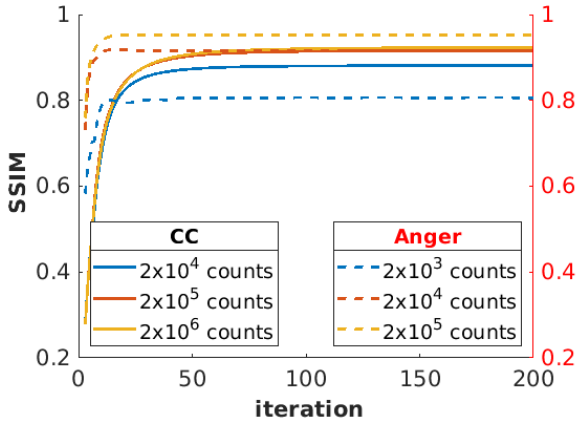

Fig. 5. Structural similarity between the reconstructed image and the reference. The images are normalized by their maximum.

images in a limited-angle configuration. In figure 7 we show the iterative reconstruction from 2×10^6 measured events for the three position (C1)-(C3) shown in figure 3. The source was let to emit at 511 keV and the result is shown at the 200th iteration for 2×10^6 measured events. Results for the CC and the AC are shown for comparison.

D. Analytic reconstruction from high counts

When the number of detected events is high, analytic reconstruction methods can be applied. Figure 8 compares filtered back-projection reconstructions from CC and from missing angle AC acquisitions, for 1.25×10^7 valid counts (see section II-C for details). TV-denoising was applied to the reconstructed volumes.

V. Discussions

The energy of the photons influence the shape of the Compton cones through the Klein-Nishina cross-section in CC imaging. At low energies, high scattering angles are favoured. As the energy increase, small angles related to almost forward scattering prevail. The data become then more and more close to the linear projection model. On the one hand, if the camera is small and is not let to turn around the source, missing angle artefacts would be expected. On the other hand, for large cameras an improvement could be expected as the surface of uncertainty decrease with the half-opening angle of the cone. From the results of the iterative reconstruction shown in figure

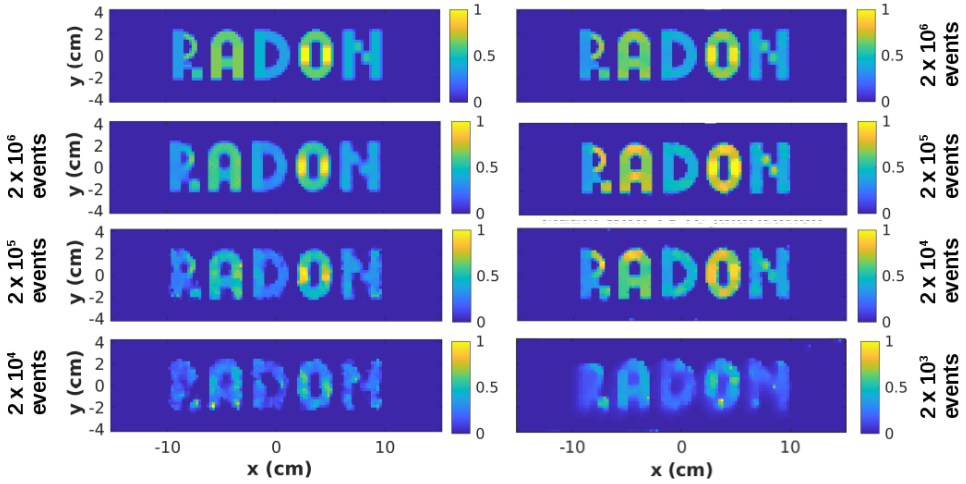

(a) Compton camera (b) Missing angle Anger camera

Fig. 6. Iterative reconstruction from Compton camera (left) and limited angle Anger camera (right) as a function of counts. The simulated source was placed parallel to the Compton camera in configuration (C1). Central slices from the reconstructed volumes are shown for the 200th TV-MAP-EM iteration.

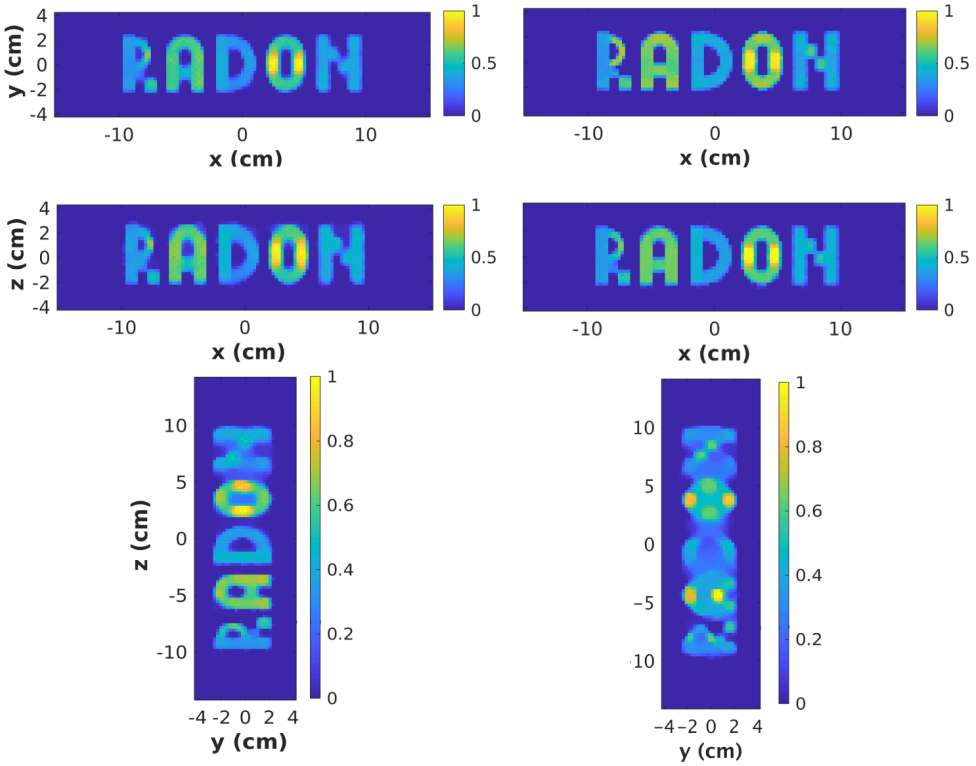

(a) Compton camera (b) Missing angle Anger camera

Fig. 7. Images reconstructed from Compton camera (left) and missing angle Anger camera (right), as a function of source position. Form the top to the bottom the source placement corresponds to the configuration denoted respectively as (C1), (C2) and (C3) in figure 3. Central slices from the volumes reconstructed from 2×10^6 detected events at the 200th TV-MAP-EM iteration are shown.

4, the influence of the energy on the image is not evident. The reason might be the large angular acceptance of the simulated geometry. These conclusions are not applicable to realistic data where the energy has a determinant influence on the results both for the CC (see for instance [54]) and the AC.

One conclusion that might be drawn from the comparison at different counts, is that at equal statistics, the AC is superior to the CC except for the missing angle artefacts that can be seen in the right column from figure 6. If we consider for the CC an efficiency ten times larger than for the AC, the images become visually comparable and even better for the CC as they are less affected by artefacts. As a rule of thumb, this factor of ten seems to be the price to pay when switching from linear to conical projections. In a comparison study not

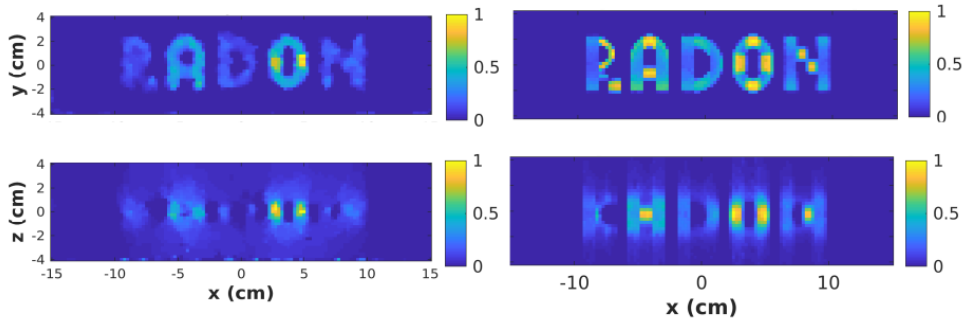

(a) Compton analytic reconstruction (b) Anger analytic reconstruction

Fig. 8. Filtered back-projection reconstruction from Compton camera and from missing angle collimated camera data. Total variation denoising was applied to the reconstructed volumes.

included here, we observed a factor somewhere between 10 and 100 for the full 180° with the AC. The second conclusion is that remarkably good images can be reconstructed from CC *ideal* data even at very low statistics. The shape of the source we considered is complex compared to point-sources, spheres or box sources, and the activity is not uniform. The shape of the letters is identifiable even with 2×10^4 detected events and the intensities are approximately well reproduced with 2×10^5 detected events. The third conclusion is that when comparing the SSIM indexes, the AC images seem more close to the original than the CC images, despite the missing angle artefacts that the eye can identify in the first ones.

Usually the resolution in CC images is lower in the orthogonal direction and degrades with the distance. In figure 7, central slices for different positions of the source are compared. The differences between (C1) and (C2) are relatively mild. However, for the configuration (C3), the letter "N" is obviously blurred compared to the letter "R", which is placed 15 cm closer to the camera. This blur could be due to modelling inaccuracies in the system matrix from (3) and in the sensitivity but also to the finite extent of the camera and the resultant missing data. In real acquisitions, several factors further degrade image quality especially for distant sources. Detection uncertainties, due either to intrinsic Doppler broadening or to the detection process, can be at some extent be modelled in the system matrix and corrected for. Correcting for random coincidences, incomplete absorption and wrong sequencing of the hits can be more tricky. Furthermore, the uncertainties of the angular parameters, *i.e.*, Compton scattering angle and axis direction in spherical coordinates, will have severe consequences (for more details, see discussions in section III-A).

The reconstruction time of iterative methods become prohibitive for large CC data sets and analytic methods could be an alternative as they are much faster. With an optimal implementation, real time reconstruction could probably be reached. However, analytic methods cannot account for the detection model, for statistical noise and for the missing projections, giving less precise results. They still may give a coarse identification of the source when the number of counts is too low to for a precise reconstruction (see [49] for more details). The comparison in figure 8 shows that filtered back-projection gives poor results compared to iterative methods for both acquisition systems. Some artefacts that might be misleading for a quantitative evaluation of the images can be observed in the parallel missing angle acquisition. Compared to figure 6, figure 8 shows that the impact of missing data on the analytic reconstruction is higher even at a number of detected events increased by a factor of more than 10. Binning could be another factor of degradation for CC analytic reconstruction as it introduces errors on the measures. For a real AC the collimators allow for some broadening and the projections are not measured on straight lines as it was done here. The influence of the binning in the collimated system cannot be measured in our set-up.

VI. Conclusions

The aim of this work was to evaluate the imaging capabilities of the Compton camera independently of the detection technology, of the geometry or other factors that affect the results of a real detector. As reference we considered an ideal parallel hole collimated system. We focused on the reconstruction algorithms, both analytic and iterative, and on the evolution of the visual quality of the images as function of the number of events. We investigated a missing-angle configuration for the collimated system reproducing the covering angle of the simulated Compton camera. To obtain approximately the same quality at visual inspection, we found that the CC should acquire about ten times more events than the AC because of the conical uncertainty. This factor is also the lower bound reported in the literature for the efficiency increase allowed by the first compared to the second. As a consequence, with an efficiency ten times larger, the CC would not allow to reduce the clinical acquisition time. However, the Compton camera successfully competed against the missing angle collimated system in terms of uniformity in constant activity regions.

Generally, a list-mode TV-MAP-EM reconstruction algorithm will give better results than list-mode MLEM or analytic algorithms. In particular, the missing angle geometry has a stronger impact on the images reconstructed by filtered back-projection compared to iterative algorithms. This can be seen from the Anger camera images at high statistics. The much

faster filtered back-projection is still an appealing alternative for Compton camera high statistics data.

The results of this work cannot be extended directly to real detectors and clinical application. We can only infer that Compton cameras could be useful for configurations where a collimated detector cannot turn around the patient and thus missing angle data is generated. Besides, the advantage of Compton camera is more evident at high energies where the collimators become transparent, as it is the case in proton therapy.

REFERENCES

[1] M. Schönfelder, A. Hirner, and K. Schneider, "A telescope for soft gamma ray astronomy," *Nuclear Instruments and Methods*, vol. 107, no. 2, pp. 385–394, 1973.

[2] R. Todd, J. Nightingale, and D. Everett, "A proposed γ camera," *Nature*, vol. 251, pp. 132–134, 1974.

[3] V. Schonfelder, R. Diehl, G. G. Lichti, H. Steinle, B. N. Swanenburg, A. J. M. Deerenberg, H. Aarts, J. Lockwood, W. Webber, J. Macri, J. Ryan, G. Simpson, B. G. Taylor, K. Bennett, and M. Snelling, "The imaging Compton telescope COMPTEL on the gamma ray observatory," *IEEE Transactions on Nuclear Science*, vol. 31, no. 1, pp. 766–770, Feb 1984.

[4] S. M. Schindler, W. R. Cook, J. Hammond, F. A. Harrison, T. A. Prince, S. Wang, S. Corbel, and W. A. Heindl, "GRIP-2: A sensitive balloon-borne imaging gamma-ray telescope," *Nuclear Instruments and Methods in Physics Research Section A: Accelerators, Spectrometers, Detectors and Associated Equipment*, vol. 384, no. 2-3, pp. 425–434, 1997.

[5] A. Zoglauer, M. Galloway, M. Amman, S. E. Boggs, J. S. Lee, P. N. Luke, L. Mihailescu, K. Vetter, and C. B. Wunderer, "First results of the high efficiency multi-mode imager (HEMI)," in *2009 IEEE Nuclear Science Symposium Conference Record (NSS/MIC)*, Oct 2009, pp. 887–891.

[6] M. Bandstra, E. Bellm, S. Boggs, D. Perez-Becker, A. Zoglauer, H.-K. Chang, J.-L. Chiu, J.-S. Liang, Y.-H. Chang, Z.-K. Liu *et al.*, "Detection and imaging of the Crab Nebula with the nuclear Compton telescope," *The Astrophysical Journal*, vol. 738, no. 1, p. 8, 2011.

[7] V. Tatischeff, M. Tavani, P. Von Ballmoos, L. Hanlon, U. Oberlack, A. Aboudan, A. Argan, D. Bernard, A. Brogna, A. Bulgarelli *et al.*, "The e-ASTROGAM gamma-ray space mission," in *Space Telescopes and Instrumentation 2016: Ultraviolet to Gamma Ray*, vol. 9905. International Society for Optics and Photonics, 2016, p. 99052N.

[8] L. Mihailescu, K. Vetter, M. Burks, E. Hull, and W. Craig, "SPEIR: a Ge Compton camera," *Nuclear Instruments and Methods in Physics Research Section A: Accelerators, Spectrometers, Detectors and Associated Equipment*, vol. 570, no. 1, pp. 89–100, 2007.

[9] J. Sullivan, S. Tornga, and M. Rawool-Sullivan, "Extended radiation source imaging with a prototype Compton imager," *Applied Radiation and Isotopes*, vol. 67, pp. 617–624, 2009.

[10] S. Takeda, A. Harayama, Y. Ichinohe, H. Odaka, S. Watanabe, T. Takahashi, H. Tajima, K. Genba, D. Matsuura, H. Ikebuchi, Y. Kuroda *et al.*, "A portable Si/CdTe Compton camera and its applications to the visualization of radioactive substances," *Nuclear Instruments and Methods in Physics Research Section A: Accelerators, Spectrometers, Detectors and Associated Equipment*, vol. 787, pp. 207–211, 2015.

[11] C. Wahl, W. Kaye, W. Wang, F. Zhang, J. Jaworski, A. King, Y. Boucher, and Z. He, "The Polaris-H imaging spectrometer," *Nuclear Instruments and Methods in Physics Research Section A: Accelerators, Spectrometers, Detectors and Associated Equipment*, vol. 784, pp. 377–381, 2015.

[12] A. Iltis, H. Snoussi, L. Magalhaes, M. Hmissi, C. Tata Zafiarifety, G. Tadonkeng, and C. Morel, "Temporal imaging $CeBr_3$ Compton camera: A new concept for nuclear decommissioning and nuclear waste management," in *EPJ Web of Conferences*, vol. 170, 01 2018, p. 06003.

[13] M. Singh and D. Doria, "An electronically collimated gamma camera for single photon emission computed tomography. Part II: Image reconstruction and preliminary experimental measurements," *Medical physics*, vol. 10, no. 4, pp. 428–435, 1983.

[14] S. Takeda, H. Odaka, S. Ishikawa, S. Watanabe, H. Aono, T. Takahashi, Y. Kanayama, M. Hiromura, and S. Enomoto, "Demonstration of in-vivo multi-probe tracker based on a Si/CdTe semiconductor Compton camera," *IEEE Transactions on Nuclear Science*, vol. 59, no. 1, pp. 70–76, Feb 2012.

[15] S. Motomura, Y. Kanayama, M. Hiromura, T. Fukuchi, T. Ida, H. Haba, Y. Watanabe, and S. Enomoto, "Improved imaging performance of a semiconductor Compton camera GREI makes for a new methodology to integrate bio-metal analysis and molecular imaging technology in living organisms," *Journal of Analytical Atomic Spectrometry*, vol. 28, pp. 934–939, 2013.

[16] J. Krimmer, J.-L. Ley, C. Abellan, J.-P. Cachemiche, L. Caponetto, X. Chen, M. Dahoumane, D. Dauvergne, N. Freud, B. Joly, D. Lambert, L. Lestand, J. Létang, M. Magne, H. Mathez, V. Maxim, G. Montarou, C. Morel, M. Pinto, C. Ray, V. Reithinger, E. Testa, and Y. Zoccarato, "Development of a Compton camera for medical applications based on silicon strip and scintillation detectors," *Nuclear Instruments and Methods in Physics Research Section A: Accelerators, Spectrometers, Detectors and Associated Equipment*, vol. 787, no. 0, pp. 98 – 101, 2015.

[17] G. Pausch, C. Golnik, A. Schulz, and W. Enghardt, "A novel scheme of Compton imaging for nuclear medicine," in *2016 IEEE Nuclear Science Symposium, Medical Imaging Conference and Room-Temperature Semiconductor Detector Workshop (NSS/MIC/RTSD)*, Oct 2016, pp. 1–5.

[18] A. Kishimoto, J. Kataoka, T. Taya, L. Tagawa, S. Mochizuki, S. Ohsuka, Y. Nagao, K. Kurita, M. Yamaguchi, N. Kawachi, K. Matsunaga, H. Ikeda, E. Shimosegawa, and J. Hatazawa, "First demonstration of multi-color 3-D in vivo imaging using ultra-compact Compton camera," *Scientific Reports*, vol. 7, 2017.

[19] M. Fontana, D. Dauvergne, J. Letang, J. Ley, and É.. Testa, "Compton camera study for high efficiency SPECT and benchmark with Anger system," *Physics in Medicine & Biology*, vol. 62, no. 23, p. 8794, 2017.

[20] M. Frandes, A. Zoglauer, V. Maxim, and R. Prost, "A tracking Compton-scattering imaging system for hadron therapy monitoring," *IEEE Transactions on Nuclear Science*, vol. 57, no. 1, pp. 144–150, Feb 2010.

[21] M.-H. Richard, M. Dahoumane, D. Dauvergne, M. De Rydt, G. Dedes, N. Freud, J. Krimmer, J. M. Letang, X. Lojacono, V. Maxim, G. Montarou, C. Ray, F. Roellinghoff, E. Testa, and A. H. Walenta, "Design study of the absorber detector of a Compton camera for on-line control in ion beam therapy," *IEEE Transactions on Nuclear Science*, vol. 59, no. 5, pp. 1850–1855, Oct 2012.

[22] P. G. Ortega, I. Torres-Espallardo, F. Cerutti, A. Ferrari, J. E. Gillam, C. Lacasta, G. Llosà, J. F. Oliver, P. R. Sala, P. Solevi, and M. Rafecas, "Noise evaluation of Compton camera imaging for proton therapy," *Physics in Medicine & Biology*, vol. 60, pp. 1845–63, 2015.

[23] T. Taya, J. Kataoka, A. Kishimoto, Y. Iwamoto, A. Koide, T. Nishio, S. Kabuki, and T. Inaniwa, "First demonstration of real-time gamma imaging by using a handheld Compton camera for particle therapy," *Nuclear Instruments and Methods in Physics Research Section A: Accelerators, Spectrometers, Detectors and Associated Equipment*, vol. 831, pp. 355–361, 2016.

[24] S. Schoene, W. Enghardt, F. Fiedler, C. Golnik, G. Pausch, H. Rohling, and T. Kormoll, "An image reconstruction framework and camera prototype aimed for compton imaging for in-vivo dosimetry of therapeutic ion beams," *IEEE Transactions on Radiation and Plasma Medical Sciences*, vol. 1, no. 1, pp. 96–107, Jan 2017.

[25] S. Aldawood, P. Thirolf, A. Miani, M. Böhmer, G. Dedes, R. Gernhäuser, C. Lang, S. Liprandi, L. Maier, T. Marinšek *et al.*, "Development of a Compton camera for prompt-gamma medical imaging," *Radiation Physics and Chemistry*, vol. 140, pp. 190–197, 2017.

[26] H. Rohling, M. Priegnitz, S. Schoene, A. Schumann, W. Enghardt, F. Hueso-González, G. Pausch, and F. Fiedler, "Requirements for a Compton camera for in vivo range verification of proton therapy," *Physics in Medicine & Biology*, vol. 62, no. 7, p. 2795–2811, 2017.

[27] F. Hueso-González, G. Pausch, J. Petzoldt, K. E. Römer, and W. Enghardt, "Prompt gamma rays detected with a BGO block Compton camera reveal range deviations of therapeutic proton beams," *IEEE Transactions on Radiation and Plasma Medical Sciences*, vol. 1, no. 1, pp. 76–86, Jan 2017.

[28] J. Krimmer, D. Dauvergne, J. M. Létang, and É. Testa, "Prompt-gamma monitoring in hadrontherapy: A review," *Nuclear Instruments and Methods in Physics Research Section A: Accelerators, Spectrometers, Detectors and Associated Equipment*, vol. 878, pp. 58–73, 2018.

[29] M. Fontana, J.-L. Ley, D. Dauvergne, N. Freud, J. Krimmer, J. M. Létang, V. Maxim, M.-H. Richard, I. Rinaldi, and É. Testa, "Monitoring ion beam therapy with a Compton camera: simulation studies of the clinical feasibility," *IEEE Transactions on Radiation and Plasma Medical Sciences*, 2019.

[30] M. Priegnitz, S. Barczyk, L. Nenoff, C. Golnik, I. Keitz, T. Werner, S. Mein, J. Smeets, F. V. Stappen, G. Janssens, L. Hotoiu, F. Fiedler, D. Prieels, W. Enghardt, G. Pausch, and C. Richter, "Towards clinical application: prompt gamma imaging of passively scattered proton fields

with a knife-edge slit camera," *Physics in Medicine & Biology*, vol. 61, no. 22, p. 7881, 2016.

[31] J. Krimmer, M. Chevallier, J. Constanzo, D. Dauvergne, M. De Rydt, G. Dedes, N. Freud, P. Henriquet, C. La Tessa, J. M. Létang *et al.*, "Collimated prompt gamma TOF measurements with multi-slit multi-detector configurations," *Journal of Instrumentation*, vol. 10, no. 01, p. P01011, 2015.

[32] J. M. Verburg, K. Riley, T. Bortfeld, and J. Seco, "Energy-and time-resolved detection of prompt gamma-rays for proton range verification," *Physics in Medicine & Biology*, vol. 58, no. 20, p. L37, 2013.

[33] P. C. Lopes, P. Crespo, J. Huizenga, and D. R. Schaart, "Optimization of the signal-to-background ratio in prompt gamma imaging using energy and shifting time-of-flight discrimination: Experiments with a scanning parallel-slit collimator," *IEEE Transactions on Radiation and Plasma Medical Sciences*, vol. 2, no. 5, pp. 510–519, 2018.

[34] F. Hueso-González and T. Bortfeld, "Compact method for proton range verification based on coaxial prompt gamma-ray monitoring: a theoretical study," *IEEE Transactions on Radiation and Plasma Medical Sciences*, pp. 1–1, 2019.

[35] M. J. Cree and P. J. Bones, "Towards direct reconstruction from a gamma camera based on compton scattering," *IEEE Transactions on Medical Imaging*, vol. 13, no. 2, pp. 398–407, June 1994.

[36] L. C. Parra, "Reconstruction of cone-beam projections from compton scattered data," *IEEE Transactions on Nuclear Science*, vol. 47, no. 4, pp. 1543–1550, Aug 2000.

[37] T. Tomitani and M. Hirasawa, "Image reconstruction from limited angle Compton camera data," *Physics in Medicine & Biology*, vol. 47, pp. 2129–2145, 2002.

[38] R. Basko, G. L. Zeng, and G. T. Gullberg, "Analytical reconstruction formula for one-dimensional Compton camera," *IEEE Transactions on Nuclear Science*, vol. 44, no. 3, pp. 1342–1346, June 1997.

[39] B. Smith, "Reconstruction methods and completeness conditions for two Compton data models," *Journal of the Optical Society of America A*, vol. 22, pp. 445–459, March 2005.

[40] V. Maxim, M. Frandes, and R. Prost, "Analytical inversion of the Compton transform using the full set of available projections," *Inverse Problems*, vol. 25, no. 9, pp. 1–21, 2009.

[41] V. Maxim, "Filtered backprojection reconstruction and redundancy in Compton camera imaging," *IEEE Transactions on Image Processing*, vol. 23, no. 1, pp. 332–341, 2014.

[42] P. Kuchment and F. Terzioglu, "Inversion of weighted divergent beam and cone transforms," *Inverse Problems & Imaging*, vol. 11, no. 6, pp. 1071–1090, 2017.

[43] R. Gouia-Zarrad and G. Ambartsoumian, "Exact inversion of the conical Radon transform with a fixed opening angle," *Inverse Problems*, vol. 30, no. 4, p. 045007, 2014.

[44] M. Haltmeier, "Exact reconstruction formulas for a Radon transform over cones," *Inverse Problems*, vol. 30, no. 3, p. 035001, 2014.

[45] C.-Y. Jung and S. Moon, "Exact inversion of the cone transform arising in an application of a Compton camera consisting of line detectors," *SIAM Journal on Imaging Sciences*, vol. 9, no. 2, pp. 520–536, 2016.

[46] S. Moon, "Inversion of the conical Radon transform with vertices on a surface of revolution arising in an application of a Compton camera," *Inverse Problems*, vol. 33, no. 6, p. 065002, 2017.

[47] V. Palamodov, "Reconstruction from cone integral transforms," *Inverse Problems*, vol. 33, no. 10, p. 104001, 2017.

[48] D. Schiefeneder and M. Haltmeier, "The Radon transform over cones with vertices on the sphere and orthogonal axes," *SIAM Journal on Applied Mathematics*, vol. 77, no. 4, pp. 1335–1351, 2017.

[49] V. Maxim, "Enhancement of Compton camera images reconstructed by inversion of a conical Radon transform," *Inverse Problems*, vol. 35, no. 1, p. 014001, 2019.

[50] F. Terzioglu, "Some analytic properties of the cone transform," *Inverse Problems*, vol. 35, no. 3, 2019.

[51] J. E. Gormley, W. Rogers, N. Clinthorne, D. Wehe, and G. Knoll, "Experimental comparison of mechanical and electronic gamma-ray collimation," *Nuclear Instruments and Methods in Physics Research Section A: Accelerators, Spectrometers, Detectors and Associated Equipment*, vol. 397, no. 2-3, pp. 440–447, 1997.

[52] L. Han, W. L. Rogers, S. S. Huh, and N. Clinthorne, "Statistical performance evaluation and comparison of a Compton medical imaging system and a collimated Anger camera for higher energy photon imaging," *Physics in Medicine & Biology*, vol. 53, no. 24, p. 7029, 2008.

[53] M.-H. Richard, M. Chevallier, D. Dauvergne, N. Freud, P. Henriquet, F. Le Foulher, J. Letang, G. Montarou, C. Ray, F. Roellinghoff *et al.*, "Design guidelines for a double scattering compton camera for prompt-γ imaging during ion beam therapy: A monte carlo simulation study," *IEEE Transactions on Nuclear Science*, vol. 58, no. 1, pp. 87–94, Feb 2011.

[54] E. Hilaire, D. Sarrut, F. Peyrin, and V. Maxim, "Proton therapy monitoring by Compton imaging: influence of the large energy spectrum of the prompt-γ radiation," *Physics in Medicine & Biology*, vol. 61, no. 8, p. 3127, 2016.

[55] E. Draeger, S. Peterson, D. Mackin, H. Chen, S. Beddar, and J. C. Polf, "Feasibility studies of a new event selection method to improve spatial resolution of compton imaging for medical applications," *IEEE Transactions on Radiation and Plasma Medical Sciences*, vol. 1, no. 4, pp. 358–367, July 2017.

[56] V. Maxim, X. Lojacono, E. Hilaire, J. Krimmer, E. Testa, D. Dauvergne, I. Magnin, and R. Prost, "Probabilistic models and numerical calculation of system matrix and sensitivity in list-mode MLEM 3D reconstruction of Compton camera images," *Physics in Medicine & Biology*, vol. 61, no. 1, pp. 243–264, 2016.

[57] E. Muñoz, J. Barrio, J. Bernabéu, A. Etxebeste, C. Lacasta, G. Llosá, A. Ros, J. Roser, and J. F. Oliver, "Study and comparison of different sensitivity models for a two-plane compton camera," *Physics in Medicine & Biology*, vol. 63, no. 13, p. 135004, jun 2018. [Online]. Available: https://doi.org/10.1088%2F1361-6560%2Faac8cd

[58] T. Ida, S. Motomura, M. Ueda, Y. Watanabe, and S. Enomoto, "Accurate modeling of event-by-event backprojection for a germanium semiconductor Compton camera for system response evaluation in the LM-ML-EM image reconstruction method," *Japanese Journal of Applied Physics*, vol. 58, no. 1, p. 016002, 2018.

[59] D. Xu and Zhong He, "Gamma-ray energy-imaging integrated deconvolution," vol. 2, pp. 882–886, Oct 2005.

[60] S. M. Kim, H. Seo, J. H. Park, C. H. Kim, C. S. Lee, S.-J. Lee, D. S. Lee, and J. S. Lee, "Resolution recovery reconstruction for a compton camera," *Physics in Medicine & Biology*, vol. 58, no. 9, p. 2823, 2013.

[61] M.-L. Jan, M.-W. Lee, and H.-M. Huang, "PSF reconstruction for Compton-based prompt gamma imaging," *Physics in Medicine & Biology*, vol. 63, no. 3, p. 035015, 2018.

[62] A. Zoglauer, R. Andritschke, and G. Kanbach, "Data analysis for the MEGA prototype," *New Astronomy Reviews*, vol. 48, no. 1-4, pp. 231–235, Feb. 2004.

[63] Y. F. Yang, Y. Gono, S. Motomura, S. Enomoto, and Y. Yano, "A compton camera for multitracer imaging," *IEEE Transactions on Nuclear Science*, vol. 48, no. 3, pp. 656–661, June 2001.

[64] T. Kormoll, F. Fiedler, C. Golnik, K. Heidel, M. Kempe, S. Schoene, M. Sobiella, K. Zuber, and W. Enghardt, "A prototype compton camera for in-vivo dosimetry of ion beam cancer irradiation," in *2011 IEEE Nuclear Science Symposium Conference Record*. IEEE, Oct 2011, pp. 3484–3487.

[65] G. Llosá, J. Barrio, C. Lacasta, S. Callier, C. de La Taille, and L. Raux, "Characterization of a detector head based on continuous labr3crystals and sipm arrays for dose monitoring in hadron therapy," in *IEEE Nuclear Science Symposuim Medical Imaging Conference*. IEEE, Oct 2010, pp. 2148–2150.

[66] D. Robertson, J. C. Polf, S. W. Peterson, M. T. Gillin, and S. Beddar, "Material efficiency studies for a compton camera designed to measure characteristic prompt gamma rays emitted during proton beam radiotherapy," *Physics in Medicine & Biology*, vol. 56, no. 10, p. 3047, 2011.

[67] A. Etxebeste, Y. Feng, J. M. Létang, V. Maxim, É. Testa, and D. Sarrut, "An extension of the GATE Monte Carlo simulation toolkit to model Compton camera systems," in *Third Geant4 International User Conference*, 2018. [Online]. Available: https://hal.archives-ouvertes.fr/hal-01926614

[68] D. Sarrut, M. Bardiès, N. Boussion, N. Freud, S. Jan, J. Létang, G. Loudos, L. Maigne, S. Marcatili, T. Mauxion, P. Papadimitroulas, Y. Perrot, U. Pietrzyk, C. Robert, D. Schaart, D. Visvikis, and I. Buvat, "A review of the use and potential of the gate monte carlo simulation code for radiation therapy and dosimetry applications," *Medical physics*, vol. 41, p. 064301, 06 2014.

[69] L. Shepp and Y. Vardi, "Maximum likelihood reconstruction for emission tomography," *IEEE Transactions on Medical Imaging*, vol. 1, no. 2, pp. 113–122, 1982.

[70] K. Lange and R. Carson, "EM reconstruction algorithms for emission and transmission tomography," *Journal of computer assisted tomography*, vol. 8, no. 2, pp. 306–316, 1984. [Online]. Available: http://pascal-francis.inist.fr/vibad/index.php?action=getRecordDetail&idt=9717742

[71] A. Dempster, N. Laird, and D. Rubin, "Maximum likelihood from incomplete data via the EM algorithm," *Journal of the Royal Statistical Society. Series B (Methodological)*, vol. 39, pp. 1–38, 1977.

[72] H. Hudson and R. Larkin, "Accelerated image reconstruction using ordered subsets of projection data," *IEEE transactions on medical imaging*, vol. 13, no. 4, pp. 601–609, 1994.
[73] H. H. Barrett, T. White, and L. C. Parra, "List-mode likelihood," *Journal of the Optical Society of America. A*, vol. 14, no. 11, pp. 2914–2923, 1997.
[74] S. J. Wilderman, N. H. Clinthorne, J. A. Fessler, and W. L. Rogers, "List-mode maximum likelihood reconstruction of Compton scatter camera images in nuclear medicine," in *1998 IEEE Nuclear Science Symposium Conference Record. 1998 IEEE Nuclear Science Symposium and Medical Imaging Conference (Cat. No.98CH36255)*, vol. 3, Nov 1998, pp. 1716–1720 vol.3.
[75] L. Rudin, S. Osher, and E. Fatemi, "Nonlinear total variation based noise removal algorithms," *Physica D: nonlinear phenomena*, vol. 60, no. 1-4, pp. 259–268, 1992.
[76] A. Chambolle, "An algorithm for total variation minimization and applications," *Journal of Mathematical imaging and vision*, vol. 20, no. 1-2, pp. 89–97, 2004.
[77] A. C. Sauve, A. O. Hero, W. L. Rogers, S. J. Wilderman, and N. H. Clinthorne, "3D image reconstruction for a Compton SPECT camera model," *IEEE Transactions on Nuclear Science*, vol. 46, no. 6, pp. 2075–2084, Dec 1999.
[78] S. J. Wilderman, J. A. Fessler, N. H. Clinthorne, J. W. LeBlanc, and W. L. Rogers, "Improved modeling of system response in list mode EM reconstruction of Compton scatter camera images," *IEEE Transactions on Nuclear Science*, vol. 48, no. 1, pp. 111–116, Feb 2001.
[79] S. R. Tornga, M. W. Rawool Sullivan, and J. P. Sullivan, "Three-dimensional Compton imaging using list-mode maximum likelihood expectation maximization," *IEEE Transactions on Nuclear Science*, vol. 56, no. 3, pp. 1372–1376, June 2009.
[80] O. Klein and Y. Nishina, "Über die streuung von strahlung durch freie elektronen nach der neuen relativistischen quantendynamik von dirac," *Zeitschrift für Physik*, vol. 52, no. 11-12, pp. 853–868, 1929.
[81] J. Nuyts and J. A. Fessler, "A penalized-likelihood image reconstruction method for emission tomography, compared to postsmoothed maximum-likelihood with matched spatial resolution," *IEEE transactions on medical imaging*, vol. 22, no. 9, pp. 1042–1052, 2003.
[82] J. W. Stayman and J. A. Fessler, "Compensation for nonuniform resolution using penalized-likelihood reconstruction in space-variant imaging systems," *IEEE Transactions on Medical Imaging*, vol. 23, no. 3, pp. 269–284, March 2004.
[83] A. Sawatzky, C. Brune, F. Wubbeling, T. Kosters, K. Schafers, and M. Burger, "Accurate EM-TV algorithm in PET with low SNR," in *2008 IEEE Nuclear Science Symposium Conference Record*, Oct 2008, pp. 5133–5137.
[84] V. Maxim, Y. Feng, H. Banjak, and E. Bretin, "Tomographic reconstruction from Poisson distributed data: a fast and convergent EM-TV dual approach," INSA Lyon, preprint, 2018. [Online]. Available: https://hal.archives-ouvertes.fr/hal-01892281/
[85] A. Beck and M. Teboulle, "A fast iterative shrinkage-thresholding algorithm for linear inverse problems," *SIAM journal on imaging sciences*, vol. 2, no. 1, pp. 183–202, 2009.
[86] Zhou Wang, A. C. Bovik, H. R. Sheikh, and E. P. Simoncelli, "Image quality assessment: from error visibility to structural similarity," *IEEE Transactions on Image Processing*, vol. 13, no. 4, pp. 600–612, April 2004.

FOLIO ADMINISTRATIF

THESE DE L'UNIVERSITE DE LYON OPEREE AU SEIN DE L'INSA LYON

NOM : FENG — DATE de SOUTENANCE : 25/10/2019

Prénoms : Yuemeng

TITRE : Modélisation et régularisation en reconstruction tomographique pour l'imagerie par caméra Compton

NATURE : Doctorat — Numéro d'ordre : 2019LYSEI084

Ecole doctorale : Electronique, Electrotechnique, Automatique

Spécialité: STIC Santé

RESUME : La caméra Compton est un dispositif d'imagerie gamma pour la tomographie par émission monophotonique (TEMP). Les améliorations qu'elle pourrait apporter aux applications médicales font l'objet de nombreuses études. Elles dépendent à la fois des développements instrumentaux et des techniques de traitement des données, dont la reconstruction tomographique est une étape-clé. Le but de cette thèse est d'améliorer les performances des algorithmes de reconstruction itératifs calculant le maximum de vraisemblance en mode liste (LM-MLEM). En imagerie avec une caméra Compton, le modèle d'acquisition est basé sur l'intégrale de l'intensité de la source sur des projections coniques. La modélisation des incertitudes de mesure influence fortement le résultat de LM-MLEM. L'une des contributions de cette étude est de montrer qu'un modèle plus précis de l'élargissement Doppler, validé avec la simulation Monte-Carlo, conduit à des images plus quantitatives. Une autre contribution est une méthode de régularisation par contrôle de la variation totale (TV) pour des données distribuées selon une loi de Poisson. La régularisation TV permet d'améliorer fortement la qualité des images pour les acquisitions à faible statistique rencontrées dans les applications de ce type d'imagerie. Nous avons également étudié l'apport de la déconvolution avec la fonction d'étalement du point dans le domaine de l'image, en conjonction avec la régularisation. Cette approche est utilisée pour corriger les effets physiques trop difficile à modéliser dans la fonction de transfert. Toutes les méthodes ont été validées avec des simulations Monte-Carlo.

MOTS-CLÉS : Imagerie Compton, reconstruction tomographique, MLEM, TV régularisation, PSF déconvolution

Laboratoire (s) de recherche : Centre de Recherche et d'Application en Traitement de l'Image et du Signal (CREATIS), Unité CNRS UMR 5220 – INSERM U1206 – Université Lyon 1 – INSA Lyon - Université Jean Monnet Saint-Etienne.

Directeur de thèse: David Sarrut, DR CNRS, INSA-LYON, CREATIS, Unité CNRS UMR 5220 – INSERM U1206 – Université Lyon 1 – INSA Lyon - Université Jean Monnet Saint-Etienne.
Co-Directeur de thèse: Voichiţa Maxim, Maître de Conférences HDR, INSA-LYON, CREATIS, Unité CNRS UMR 5220 – INSERM U1206 – Université Lyon 1 – INSA Lyon - Université Jean Monnet Saint-Etienne.

Président de jury :
Composition du jury :

RAFECAS Magdalena	Professeur, Institute of Medical Engineering	Rapporteure
IDIER Jérôme	DR CNRS, Ecole Centrale de Nantes	Rapporteur
RESMERITA Elena	Associate Professor, Alpen-Adria University of Klagenfurt	Examinatrice
MOREL Christian	Professeur, Université de Aix-Marseille	Examinateur
LETANG Jean Michel	Maître de Conférences, INSA-LYON	Examinateur
SARRUT David	DR CNRS, INSA-LYON	Directeur de thèse
MAXIM Voichiţa	Maître de Conférences HDR, INSA-LYON	Co-directrice de thèse